THE UNIVERSITY OF CHICAGO

ORGANIZATION OF A PLANAR SIGNALING SYSTEM THAT ORCHESTRATES COLLECTIVE EPITHELIAL CELL MIGRATION IN DROSOPHILA

A DISSERTATION SUBMITTED TO
THE FACULTY OF THE DIVISION OF THE BIOLOGICAL SCIENCES
AND THE PRITZKER SCHOOL OF MEDICINE
IN CANDIDACY FOR THE DEGREE OF
DOCTOR OF PHILOSOPHY

GRADUATE PROGRAM IN CELL AND MOLECULAR BIOLOGY

BY
AUDREY MILLER WILLIAMS

CHICAGO, ILLINOIS
AUGUST 2023

Copyright © 2023 by Audrey Miller Williams

All Rights Reserved

For my moms, for all your love and encouragement

TABLE OF CONTENTS

LIST OF FIGURES vi

LIST OF TABLES viii

ACKNOWLEDGMENTS ix

ABSTRACT x

1 INTRODUCTION 1
- 1.1 Preface 1
- 1.2 Crawling cell motility 1
- 1.3 Collective cell migration 5
- 1.4 Motility coordination at cell-cell interfaces 11
- 1.5 Planar cell polarity 14
- 1.6 Fat-like cadherins 19
- 1.7 Rotational collective migration of the *Drosophila* follicular epithelial cells . . 25

2 FAT2 POLARIZES THE WAVE COMPLEX IN TRANS TO ALIGN CELL PROTRUSIONS FOR COLLECTIVE MIGRATION 36
- 2.1 Preface 36
- 2.2 Abstract 36
- 2.3 Introduction 37
- 2.4 Results 41
- 2.5 Discussion 65
- 2.6 Methods 69

3 FAT2 POLARIZES LAR AND SEMA5C TO COORDINATE THE MOTILITY OF COLLECTIVELY MIGRATING EPITHELIAL CELLS 87
- 3.1 Preface 87
- 3.2 Abstract 87
- 3.3 Introduction 88
- 3.4 Results 92
- 3.5 Discussion 114
- 3.6 Methods 116

4 TRANSIENT EXTRACELLULAR CALCIUM CHELATION REVERSES FOLLICLE CELLS' POLARITY AND MIGRATION DIRECTION 133
- 4.1 Preface 133
- 4.2 Introduction 133
- 4.3 Results 136
- 4.4 Discussion 149
- 4.5 Methods 154

5 CONCLUSIONS, DISCUSSION, AND FUTURE DIRECTIONS 160
5.1 Conclusions 160
5.2 Future Directions 173

BIBLIOGRAPHY 185

A ADDITIONAL FINDINGS ON THE SPATIAL ORGANIZATION AND FUNCTION OF FAT2, LAR, AND SEMA5C IN FOLLICLE CELLS. 217
A.1 Introduction 217
A.2 Results 218
A.3 Discussion 222
A.4 Methods 225

B TRICORNERED AND FURRY ARE REQUIRED IN FOLLICLE CELLS FOR THEIR ROTATIONAL MIGRATION AND MEMBRANE HOMEOSTASIS . . . 228
B.1 Introduction 228
B.2 Results 229
B.3 Discussion 240
B.4 Methods 242

LIST OF FIGURES

1.1 Polarity modes in collective cell migration 8
1.2 Structure of the egg chamber during follicle cell migration 27
1.3 Domain organization of Fat2, Lar, Sema5c, and PlexA 33

2.1 Introduction to egg chamber rotation and follicle cell protrusions 39
2.2 Method used to segment and measure membrane protrusions 42
2.3 Fat2 increases and polarizes follicle cell protrusivity 43
2.4 Membrane extension length and protrusion orientation in individual egg chambers 45
2.5 Actin protrusions are reduced and unpolarized without Fat2 and further reduced without the WAVE complex 47
2.6 Fat2 acts locally across the cell interface to orient membrane protrusions 49
2.7 Fat2 in each cell concentrates the WAVE complex at the leading edge of the cell behind 50
2.8 Evaluation of endogenous Sra1-GFP functionality 52
2.9 Fat2 concentrates the WAVE complex at cell-cell interfaces and polarizes it across the epithelium 53
2.10 Fat2 stabilizes a region of WAVE complex enrichment in each cell 56
2.11 The WAVE complex is still associated with protrusions in the absence of Fat2 . 58
2.12 Fat2 stabilizes a protrusive region in each cell 59
2.13 Fat2 colocalizes with the WAVE complex across leading-trailing cell-cell interfaces 61
2.14 Ena and Lar are not required for colocalization between Fat2 and the WAVE complex 63

3.1 Introduction to the organization of Fat2, Lar, and Sema5c at the follicle cell basal surface 90
3.2 Fat2, Lar, and Sema-5c are enriched at actin protrusion tips away from the basal surface 94
3.3 Lar remains largely functional with an endogenous 3xGFP tag 96
3.4 Fat2 concentrates Sema5c in trans at the leading edge 98
3.5 Calcium chelation causes rapid loss of Lar and Sema5c from the leading edge . . 100
3.6 Fat2 is not sufficient to relocalize Lar away from the basal surface or tricellular junctions 102
3.7 Fat2's enrichment at interfaces shows only a mild dependence on Lar and Sema5c 104
3.8 Sema5c contributes to the localization of Fat2 105
3.9 Sema5c does not regulate the localization of Lar or the WAVE complex 107
3.10 Fat2 is relatively stable at the trailing edge, and slows the departure of Lar and Sema5c from the leading edge 108
3.11 Lar and Sema5c act in parallel to polarize cell migratory machinery and promote collective migration 111
3.12 Loss of either Fat2, Lar, or Sema5c have different effects on the polarity of membrane protrusions 113

4.1 Calcium chelation with EGTA rapidly, reversibly stops follicle cell migration . . 137

4.2 Transient EGTA treatment, but not CK-666 treatment, consistently reverses the direction of follicle cell migration . . . 139
4.3 The polarity of Fat2 and Lar reverses along with migration following transient EGTA treatment . . . 143
4.4 The planar-polarization of microtubules and Rab10+ compartments is progressively lost when migration is stopped, and reversed along with migration reversal 146
4.5 EGTA treatment alters tissue architecture and cytoplasmic calcium dynamics . 148

A.1 Removal of Fat2's intracellular domain sharply increases its levels throughout the cell . . . 219
A.2 Unlike Sema5c overexpression, Lar overexpression does not inhibit protrusion . . 221
A.3 Tissue-wide depletion of Lar with RNAi suppresses the cell mixing phenotype of $Sema5c^{K175}$ mosaic epithelia . . . 223

B.1 Loss of Trc, Fry, or GCKIII causes changes in basal F-actin organization . . . 231
B.2 Mosaicism for *trc* or *fry* mutations decreases the persistence and coordination of follicle cell migration . . . 232
B.3 Fat2 and Lar are still able to localize to leading-trailing interfaces in the absence of Trc or Fry . . . 233
B.4 Loss of Trc or Fry does not disrupt polarized secretion of Collagen IV . . . 235
B.5 Loss of Trc, Fry, or GCKIII causes defects in stalk and polar cells . . . 236
B.6 Loss of Trc or Fry causes excess membrane accumulation between cells' basal surfaces and the basement membrane . . . 237
B.7 Depletion of Mob4 causes a range of egg chamber morphology defects . . . 246
B.8 The Mob4 antibody stains large, sparse planar-polarized filamentous structures that do not contain Mob4 or microtubules . . . 247
B.9 Loss of Atg6 causes protrusions to persist into Stage 9 . . . 249

LIST OF TABLES

2.1 Experimental genotypes for Chapter 2 82
2.2 *Drosophila* culture conditions for Chapter 2 86

3.1 Experimental genotypes for Chapter 3 128
3.2 *Drosophila* culture conditions for Chapter 3 132

4.1 Experimental genotypes for Chapter 4 158
4.2 *Drosophila* culture conditions for Chapter 4 159

A.1 Experimental genotypes for Appendix A 227

B.1 Experimental genotypes for Appendix B 243

ACKNOWLEDGMENTS

I'd like to thank my advisor, Sally Horne-Badovinac, committee members Ellie Heckscher, Michael Glotzer, and Ed Munro, the whole Munro lab, Allison Zajac, Seth Donoughe, Kristin Sherrard, Sierra Schwabach, Claire Stedden, Mitch Anderson, Sherzod Tokamov, Ashley Rich, Graduate Students United comrades, Adam Peller, Carmen Williams, Ann Miller, Beverley Anderson, and in the home stretch Evan Edwards. You variously improved the quality of my work and helped me sustain and enjoy the process of doing it.

ABSTRACT

Collective cell migrations are a major means by which animals' epithelial tissues move, reorganize, and remodel their environment. Epithelial cells are tightly adhered to one another in a continuous tissue sheet, so for a cell in the interior to move it must displace a neighboring cell. In this confined context, cells and their neighbors must coordinate their motility behaviors to move in concert rather than pushing and pulling one another unproductively. However, we have limited examples of the cellular and molecular mechanisms underpinning that coordination and do not know if they are generalizable. The follicular epithelium of *Drosophila melanogaster* offers an opportunity to test the generality of these mechanisms in vivo and to identify new ones. Follicle cells undergo a highly persistent collective migration that can be observed live with subcellular resolution as it occurs in an intact tissue and with its physiological substrate. This migration is made possible by an unconventional planar signaling system that couples the trailing edge of each cell to the leading edge of the cell behind. Several proteins in this system—Fat2, Lar, Sema5c, and Plexin A—have been identified. However, they have primarily been studied as discrete Fat2-Lar and Sema5c-Plexin A pairs, and the mechanisms by which they become planar-polarized and polarize the cells' motility machinery are still largely unknown. I investigated how molecular interactions within and between these protein pairs maintain their polarized distributions, and how they work together to regulate the cells' motility machinery, with a focus on their lamellipodia.

I have organized my work into three data chapters (Chapters 2-4). In Chapter 2, I show that trailing edge-enriched Fat2 acts in trans to polarize the protrusive activity of the following cell, and that it accomplishes this by concentrating the lamellipoda-templating WAVE complex in puncta just across the interface from Fat2-containing puncta. In Chapter 3, I expand my focus to include Lar and Sema5c. Fat2 was previously shown to localize Lar in trans to leading edges, and I show that it does the same for Sema5c. From there, Lar and Sema5c signal in parallel to regulate migration. Fat2 therefore polarizes two arms of a planar

signaling system, one including Lar and the other Sema5c and Plexin A, each with distinct outputs to the cell motility machinery. Previous phenotypic data and my own findings support a model in which Lar acts as an attractive cue by regulating protrusion at leading edges, and Sema5c and Plexin A signal repulsively to trailing edges. In Chapter 4, I present a new method for acutely inhibiting Fat2 and inducing disassembly of the Fat2-based puncta, and show that it can be used to follow puncta reassembly and the onset of collective migration ex vivo. Altogether, I find that Fat2 polarizes and aligns follicle cells' motility machinery using a multi-output planar signaling system with attractive and repulsive signaling arms. My work demonstrates how coordination strategies can be deployed combinatorially to give rise to emergent collective behaviors. It also highlights the overlapping challenges that tissues must overcome to achieve planar cell polarity and collective cell migration.

CHAPTER 1

INTRODUCTION

1.1 Preface

The properties of animal tissues emerge from the behaviors of their constituent cells and interactions among those cells. One such property is the migratory state of the tissue—whether its cells remain stationary, rearrange locally, or undergo longer-range movement. Another is the presence or absence of planar cell polarity, in which individual cells are polarized in the plane of the sheet-like tissue and those polarities are aligned in a common direction. I use the *Drosophila* egg chamber's follicular epithelium as a model in which to study these two tissue states and how they are influenced by signaling interactions among neighboring cells. Follicle cells' planar polarity and collective migration are inextricable from one another, with planar-polarized signaling orchestrating collective migration and collective migration stabilizing planar polarity. In this chapter, I introduce the concepts and findings that have informed my dissertation. First, I provide an overview of collective cell migrations and the signaling mechanisms that coordinate them, building up from a description of crawling motility in individual animal cells. I then discuss planar cell polarity and the architecture of protein signaling systems that orchestrate it in different tissues. Finally, I introduce the *Drosophila* egg chamber and our current understanding of the planar-polarization and rotational collective migration of its follicle cells.

1.2 Crawling cell motility

During crawling, or mesenchymal, migration, cells extend F-actin-rich protrusions from their leading edges, increase F-actin contractility at their trailing edges, and dynamically form and disassemble focal adhesions or other transmembrane protein assemblies that adhere them to their substrate (Bodor et al., 2020). The composition and properties of protrusions,

contractile F-actin networks, and adhesions vary among different types of cells, and a within a single cell they can reorganize to accommodate diverse substrates, but the basic motile force generation mechanism remains similar (Bodor et al., 2020). One widely-deployed type of protrusion is the lamellipodium, which is formed by a polymerizing network of branched actin that grows towards and pushes against the plasma membrane (Graziano & Weiner, 2014; Krause & Gautreau, 2014; Mullins et al., 2018). The membrane's advancement creates a new region of cell-substrate contact that can be stabilized by the formation of adhesions within this region. Behind the advancing lamellipodium, F-actin is organized into contractile actomyosin networks including the mesh-like F-actin cortex or bundled F-actin stress fibers. The gradient of greater actin polymerization in the lamellipodium to greater myosin-driven network contraction elsewhere results in a rearward ("retrograde") flow of the entire network (Welch et al., 1997). Cell-substrate adhesions such as integrin-based focal adhesions bind to that F-actin network, and their frictional resistance to its flow channels some of the energy of F-actin polymerization and contraction in the forward direction, allowing it to push the cell's leading edge forward (Case & Waterman, 2015). Focal adhesions placed under tension by F-actin flow are stabilized and strengthened, whereas those that are not under tension are rapidly disassembled, so the strength and distribution of adhesions adapts to the tension load and allows cells' motile force generation to be responsive to their internal state and environment (Burridge & Guilluy, 2016; Gardel et al., 2008; Wehrle-Haller, 2012a). Finally, adhesions that reach the trailing edge are detached from the substrate and disassembled, allowing the trailing edge of the cell to release and move forward (Wehrle-Haller, 2012b).

Lamellipodium assembly by the WAVE complex

The branched actin networks of lamellipodia are templated by the heteropentameric WASP family verprolin homolog regulatory complex (WAVE complex) (Steffen et al., 2004; Weiner et al., 2006), whose biochemical activities and localization tendencies position these networks

and contribute to their sheet-like shape and physical adaptivity (Miki et al., 1998; Miki et al., 2000; Pipathsouk et al., 2019). The WAVE complex localizes in linear hetero-oligomers along the plasma membrane (Pipathsouk et al., 2019), where it feeds actin monomers into growing actin filaments and activates Arp2/3 to form new branches on those filaments (Bieling et al., 2018; Machesky et al., 1999; Mullins et al., 2018). Together, these activities result in a highly branched, sheet-like F-actin network with its growing ends oriented towards and pushing against the plasma membrane. The WAVE complex is localized by binding to Rac and Arf GTPases and phosphatidylinositol (3,4,5)-triphosphate (PIP_3) at the plasma membrane (Humphreys et al., 2012; Koronakis et al., 2011; Lebensohn & Kirschner, 2009; Oikawa et al., 2004; Sossey-Alaoui et al., 2005), and also exhibits cooperative localization dynamics such that gradients of Rac or PIP_3 can result in sharp boundaries between regions of high and low WAVE complex accumulation (Graziano & Weiner, 2014; Weiner et al., 2007). The WAVE complex exhibits a preference for accumulation at regions of high positive membrane curvature as are found at the tips of lamellipodia (Pipathsouk et al., 2019), and this preference may contribute to its cooperative localization. Binding to Rac at the membrane relieves inhibition of the Arp2/3-activating and G-actin-binding domains within the WAVE complex's Scar/WAVE subunit, restricting the activity of the complex to sites of membrane and Rac binding (Chen et al., 2010). The WAVE complex is inactivated by dissociation from the plasma membrane, and F-actin network polymerization contributes to this dissociation, such that the activity of the WAVE complex contributes to its own inactivation (Graziano & Weiner, 2014; Huang et al., 2013; Millius et al., 2012; Weiner et al., 2007). The combination of cooperative localization, negative feedback from actin polymerization, and the dynamical properties of its activators discussed in the subsequent section leads the WAVE complex to exhibit excitable dynamics, accumulating and templating lamellipodia in bursts, oscillations, or traveling waves.

Directionality and persistence in cell migration

The direction of motile force generation and cell crawling is determined by the distribution of regions of F-actin network polymerization and contraction, which sets the direction of the tensile force that the network exerts on cell-substrate adhesions, and by the distribution of those adhesions, which shapes the resistance to that force that converts rearwards network flow into forwards pushing against the plasma membrane (Barnhart et al., 2011; Yolland et al., 2019). Migration direction and speed can therefore be regulated by modulation of F-actin polymerization, contractility, or cell-substrate adhesion, which I refer to collectively as the "motility machinery". Regulation can come from a cell's environment or from cell-intrinsic, self-organized polarity networks. In this section, I focus on cell-intrinsic polarity during cell migration. In subsequent sections, I will return to motility regulation by extrinsic signals.

Many cells are capable of polarizing their motility machinery through networks of positive and negative feedback that stabilize different cytoskeletal architectures in different regions of the cell (Devreotes & Horwitz, 2015; Li et al., 2020; Stock & Pauli, 2021). These polarity circuits commonly include Rac and Rho GTPases, phosphoinositides, F-actin networks, and mechanical features such as membrane tension. Mutual antagonism between the phosophoinositide PI(3,4,5)P_3 and its phosphatase PTEN can generate a bistable state with PI(3,4,5)P_3 and PTEN partitioned into separate regions (Matsuoka & Ueda, 2018). Similarly, mutual antagonism between Rac and Rho GTPases mediated by effectors of each protein can contribute to partitioning of zones of high Rac and Rho activity. Rac and PI(3,4,5)P_3 activate the WAVE complex and promote protrusive, leading edge-like states, whereas Rho increases myosin activity and promotes a contractile, trailing edge-like state. In addition to circuits built around mutual antagonism among leading and trailing edge constituents, polarization can be driven by networks of local excitation and global inhibition (Xiong et al., 2010). For example, excitation of WAVE complex-dependent protrusion at

one site along the membrane can raise membrane tension around the entire cell, creating a higher barrier to the formation of additional protrusions (Diz-Muñoz et al., 2013; Houk et al., 2012). In some cells and contexts, local excitation/global inhibition or mutually-inhibiting polarity networks can be excited or polarized by stochastic fluctuations in the cell state, and so will drive cell polarization with no extrinsic directional inputs. For example, in uniform ex vivo or cell culture environments, fish keratocytes and vertebrate neutrophils are still able to polarize and migrate in a random walk (Servant et al., 2000; Yam et al., 2007). In other contexts, an extrinsic directional cue such as a chemokine or substrate stiffness gradient is necessary to push the cell into a regime where the polarized state is stabilized, but cells' ability to self-organize sharpens and stabilizes its response to that cue, increasing its sensitivity and directional persistence (Stock & Pauli, 2021). In vivo, cells are typically integrating many extrinsic and intrinsic mechanical and biochemical cues that influence whether, and in what direction, they polarize and migrate.

1.3 Collective cell migration

Cells elaborate the bodies of animals using a wide array of collective behaviors—groups of cells contract to make folds and boundaries, intercalate between one another to elongate tissues, and remodel extracellular matrices through patterned tensile forces. Cell migrations are frequently also a collective process. Nearly all animal cell migrations are collective events not reducible to the behaviors of each cell in isolation. For example, fibroblasts align extracellular matrix fibers as they crawl along them, and subsequent cells follow the path of fiber alignment, such that groups of fibroblasts both align and are aligned by their extracellular matrixes (Park et al., 2020). In an example of biochemical coordination, cells generate chemokine concentration gradients by metabolizing nearby chemokine molecules, and they simultaneously move up the gradients they have generated, such that the group will tend to move together towards regions of lower cell density (Tweedy et al., 2020). Collective

cell migrations are usually defined more narrowly as migrations of groups of adherent cells in the same direction and aided by interactions within the group. These too are common in animals. They underlie a host of developmental processes including the well-studied examples of fish gastrulation and lateral line formation, vertebrate neural crest cell migration, the outgrowth of vertebrate vasculature, and the branching of mammalian mammary gland tissue (Anon et al., 2012; Arima et al., 2011; Ewald et al., 2008; Friedl & Gilmour, 2009; Olson & Nechiporuk, 2018; Scarpa & Mayor, 2016; Schumacher, 2019; Shellard & Mayor, 2019b; Tada & Heisenberg, 2012). They are also part of homeostatic processes such as the turnover of the epithelial cells that line the mammalian intestine and the closure of wounds after injury (Friedl & Gilmour, 2009; Krndija et al., 2019). As evidence for the ubiquity of these events, the rotational collective migration of *Drosophila* follicle cells that is the focus of my dissertation research is only one of at least three different collective migrations undertaken by these cells as they form an egg (Haigo & Bilder, 2011; Horne-Badovinac & Bilder, 2005).

Scales of polarity in collective cell migration

As in individual cell migration, collective cell migration depends on the polarization of motility machinery along a front-rear axis, without which no net force is exerted on the cells' environment. However, the sites and scales at which polarity is present vary among collective migrations. In some cases, cells at either end of the migrating group have distinct organizations of their motility machinery, adopting specialized roles as "leaders" and "followers" respectively (Campanale & Montell, 2023) (Fig. 1.1). This "supracellular polarity" contributes to the directionality of group movement (Shellard & Mayor, 2019a). Cranial neural crest cells in *Xenopus* are an example of this migration mode—the cells at the rear form a multicellular actin cable that restricts rearward protrusion and maintains group cohesion, and those at the front exhibit higher protrusivity (Shellard et al., 2018). Often (as in the

cranial neural crest), leaders and followers are not permanent cell differentiation states, but rather cells move in and out of these roles as their position in the group changes (Shellard & Mayor, 2019a; Shellard et al., 2018). Supracellular polarity is not always present—in some collective migrations, cells throughout the group each adopt the same morphology, polarizing along cell-scale leading-trailing axes (Cetera & Horne-Badovinac, 2015; Shellard & Mayor, 2019a) (Fig. 1.1). In these cases, directional group movement hinges on the alignment of the cells' leading-trailing axes with those of their neighbors such that there is a net directional force exerted by the group. This organization is an example of planar cell polarity, a topic I will return to in a later section. It is exemplified by the rotational migrations of topologically closed epithelia such as the follicle cells, which lack any global front or rear that could give rise to supracellular polarity. However, degrees of this egalitarian collective organization are more widespread, and it is possible (and perhaps the norm) for polarity to be present simultaneously at cellular and supracellular scales. For example, in the *Drosophila* border cells, there are supracellular gradients of Rac activity and protrusivity across the cell cluster, but Rac activity is also polarized within individual cells, and both of these scales contribute to polarized protrusion and collective movement (Campanale et al., 2022). Supracellular polarity and the behaviors of cells at the periphery of migrating groups are often easier to observe experimentally than those of the cells in the group interior, so cases of planar alignment of the cell motility machinery are likely to be underrepresented in the collective migration literature.

Epithelial collective migration

Epithelial cells are well known for their ability to adhere to one another and polarize along an apical-basal axis, and we now know that this does not preclude them from migrating in a variety of contexts and in various geometries (Theveneau & Mayor, 2013). Clusters or ducts of epithelial cells can migrate together along extracellular matrices or other cells,

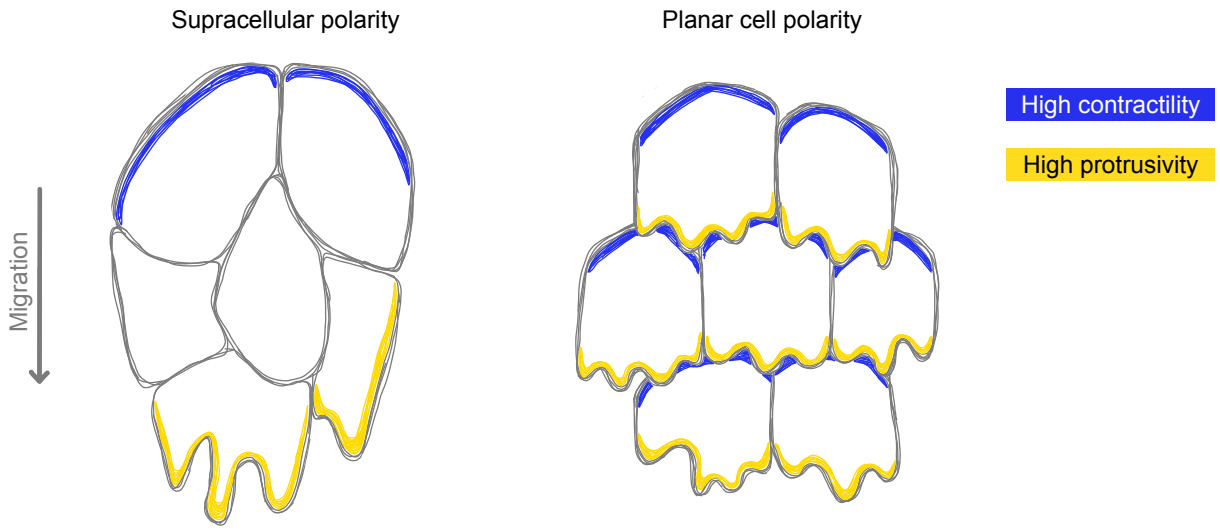

Figure 1.1: **Polarity modes in collective cell migration.** Diagrams of clusters of collectively-migrating cells. In migrations that exhibit supracellular polarity, leading and following cells adopt distinct morphologies and behaviors. In planar-polarized, egalitarian collective migrations, each cell polarizes along a leading edge-trailing edge axis, and these axes are aligned in the direction of migration. These represent two extremes of a continuum of polarity modes—supracellular polarity and planar cell polarity can also coexist. Adapted from Shellard and Mayor, 2019a.

as occurs in the migrations of the *Drosophila* border cells, zebrafish kidney tubules, and growing vascular endothelium (Friedl & Gilmour, 2009; Vasilyev et al., 2009). In addition, epithelia can undergo collective migrations within largely two-dimensional epithelial planes, moving along a largely two-dimensional basement membranes or other sheet-like substrates (Theveneau & Mayor, 2013).

Many epithelial cell types are capable of migrating in this manner under the right conditions, but a number of different factors determine whether any particular epithelium will be migratory and the mode in which that migration will occur. Epithelia can undergo solid-like collective migrations (a.k.a. solid flocking) in which the movements of cells across the tissue are highly correlated with one another at both short and long length scales such that the entire group moves together with minimal rearrangement among neighboring cells. They can also undergo liquid-like migration (a.k.a. liquid flocking), in which cells movements remain correlated at long distances but less so at short distances due to frequent neighbor

rearrangements. In the absence of long-range movement correlation, cell layers can again be in either solid-like or liquid-like states depending on the degree of cell movement and neighbor rearrangement. These four states can be though of as regions within an epithelial migration phase space, with the position of an epithelium within that space influenced by a number of different factors (Atia et al., 2021; Trepat & Sahai, 2018). For example, high cell density makes neighbor rearrangements difficult and favors solid-like states whether migratory or non-migratory. A tendancy of neighboring cells to align with one another favors solid-like migration over the other states. This can result from tissue-extrinsic influences like an axial strain on the epithelium that elongates all the cells in the same direction, or by the traits of the cells themselves, like the presence signaling systems that couple the polarities of neighbors. Other factors such as the cells' propulsive force magnitude, their migration persistence, and the strength of their adhesion to the substrate can also all influence the migratory state of an epithelium (Atia et al., 2021; Trepat & Sahai, 2018).

Another important factor in epithelial migrations is their boundary conditions—whether the epithelium is free to move or expand into adjacent open space, is confined by barriers like other tissues, or is topologically-closed (picture a sphere) and so lacks either extrinsic barriers or free space (Vecchio et al., 2023; Vedula et al., 2012). One of the best studied boundary configurations is the epithelial wound (or in vitro wound models) in which the epithelium has one free edge it can move into. This relieves a constraint on the cells' movement and introduces a directional cue that guides them, and it also creates an asymmetry between cells at the free edge and ones deeper within the tissue (Chepizhko et al., 2018). Cells at the edge of the wound respond by forming lamellipodia along their free edges and exerting stronger traction forces on their substrate, contributing to the spreading of the epithelium into the open space (Kim et al., 2013; Mayor & Etienne-Manneville, 2016). Although it was previously thought that the cells at the wound edge were largely responsible for generating the motile forces that moved the sheet, with other cells being carried along, measurements of

traction forces show that cells throughout the epithelium contribute to the force generation that drives wound closure (Trepat et al., 2009). In keeping with this, cells several rows back from the wound edge also extend lamellipodia between the basal surfaces of their neighbors and the underlying substrate (Farooqui & Fenteany, 2005). Because these are often obscured by the overlying neighboring cells and so are harder to identify than protrusions at free edges, they have been termed "cryptic" lamellipodia (Farooqui & Fenteany, 2005). Further evidence for wound closure being a collective process comes from studies of ERK signaling, with which some epithelia orchestrate propagating waves of cell contraction and polarization that allow the cells to move together more efficiently (Hino et al., 2020).

Although free edges can encourage and guide collective epithelial cell migrations, they are not required for migration to occur. Epithelia bounded on all sides by immovable barriers can still undergo liquid-like rearrangements with no net collective movement, and topologically-closed epithelia can undergo liquid-like or solid-like migrations. In cell culture, airway endothelial cells enter a liquid-like state upon introduction of asthma-mimicking compressive stresses (Park et al., 2015). Topologically-closed mammary gland organoids, intestinal organoids, and kidney epithelial cell cysts all undergo rotational collective migrations when grown in three-dimensional culture (Hirata et al., 2018; Tanner et al., 2012; Wang et al., 2013; Yang et al., 2021). These migrations are not simply phenomena of cell culture, but also occur in developmental and homeostatic contexts—although the geometry of rotating kidney and intestinal cells is not found in vivo, mammary gland organoids do reproduce the tissue's in vivo geometry, and it may be the case that their rotation is not an artifact of culture and contributes to the morphogenesis of these structures (Fernández et al., 2021). In addition, during zebrafish eye development, retinal pigmented epithelial cells extend lamellipodia and migrate towards the rim of the optic cup, and epithelial cells of the intestinal villi migrate from villus crypt to tip despite the absence of a free edge in either case (Krndija et al., 2019; Soans et al., 2022).

1.4 Motility coordination at cell-cell interfaces

An important factor in whether, and how, groups of cells migrate is how their motility behavior is affected by contact with one another (Trepat & Sahai, 2018). A cell's response to contact with other cells is shaped in part by signaling systems that operate at cell-cell interfaces (Mishra et al., 2019). Signaling systems can be grouped into attractive and repulsive categories, with attractive ones promoting movement toward the cell-cell contact site and repulsive ones either preventing movement or promoting movement in a different direction. Although these systems are highly salient to collective migration, much of our knowledge about them comes from other contexts such as the collision of two individually-migrating cells or the behaviors of axon growth cones as they migrate through different tissues and choose synaptic partners (Robichaux & Cowan, 2014). I will first describe some of these systems and the cell responses they cause, and their relationship to collective cell migration.

Repulsive signals

When two migrating cells colide with one another, stop migrating, and repolarize away from a site of cell-cell contact (and sometimes detach and migrate away), that behavior is termed "contact inhibition of locomotion" (CIL) or "contact repulsion" (Roycroft & Mayor, 2015, 2016). This avoidant behavior was first characterized phenomenologically in cells migrating in at low densities in culture (Abercrombie & Heaysman, 1954). Since then, it has since been shown to influence the migrations of both individual cells and adherent cell groups in vivo (Carmona-Fontaine et al., 2008; Hayakawa et al., 2020; Stedden et al., 2019; Stramer & Mayor, 2017). For example, CIL causes hemocytes to spread apart from one another to evenly tile the developing *Drosophila melanogaster* embryo and Cajal–Retzius cells to do so in the mouse cerebral cortex (Davis et al., 2012; Stramer et al., 2010; Villar-Cerviño et al., 2013).

CIL behavior can be induced by a variety of protein signaling systems. For all of these, the first step is the formation of a cell-cell adhesion, often through classical cadherins, which brings the CIL-inducing transmembrane receptor proteins into proximity with one another (Roycroft & Mayor, 2016; Stramer & Mayor, 2017). Receptors are then activated by binding and induce local changes in the cell motility machinery. These systems can be symmetrical (typically upon homotypic collision) or they can induce changes in just one of the cells (upon heterotypic collision)(Roycroft & Mayor, 2016; Stramer & Mayor, 2017). Although the upstream components of CIL signaling are diverse, many converge on regulation of small GTPases. Activation of Rho increases contractility and collapses protrusions; inhibition of Rap1 reduces integrin-based cell-ECM adhesion; and inhibition of Rac1 reduces lamellipodial protrusion, each of which favor trailing edge-like states at the collision site (Roycroft & Mayor, 2016; Stramer & Mayor, 2017). A far-from-exhaustive list of CIL-inducing receptors includes semaphorins and plexins, which inhibit Rap1 through the Rap1 GAP activity of the plexin (among other outputs); the Slit-Robo pathway, which inhibits Rac through the BAR domain-containing srGAP proteins; and Eph-Ephrin signaling, which activates Rho through the RhoGEF Vav2 (Batson et al., 2014; Fritz et al., 2015; Hu & Zhu, 2018). Proteins of the core planar cell polarity can also mediate contact inhibition of locomotion. During the migration of the mesenchymal neural crest cells, cells exhibit CIL upon collision with one another, and this is dependent both on N-cadherin-based adhesion and on proteins of the core planar cell polarity pathway. They concentrate Rho at the contact site, causing repulsion. Collectively, this behavior causes the cells to spread apart from one another and to move away from their initial position, where their density is high. In combination with guidance by other signaling pathways, this results in efficient directional migration of the group (Carmona-Fontaine et al., 2008; Mayor & Theveneau, 2013; Shellard & Mayor, 2019b; Szabó et al., 2019). Interestingly, that signaling includes other repulsive cues including from semaphorins, which help constrain the migration to a narrow strip (Szabó et al., 2019).

CIL is most readily observable in the context of collisions of individual cells, but it also plays a key role in the emergent behaviors of epithelia and other stably-adherent cell groups (Camley et al., 2014; Smeets et al., 2016; Zimmermann et al., 2016). Depending on the specifics of the CIL mechanism and other properties of the cells, it is possible for a behavior called "contact following" to emerge (Desai et al., 2013; Hayakawa et al., 2020). In these cases, one cell polarizes away from a cell-cell contact, but the other continues in the same direction, and the cells' adhesion to one another is maintained. In simulations and in cell culture, this can give rise to cell alignment and persistent migration in "trains" when they are confined to narrow strips, or to persistent rotational motion when they are arranged in rings or discs using micropatterns or spheres in 3D culture (Camley et al., 2014; Desai et al., 2013; Jain et al., 2020; Kulawiak et al., 2016). It also shapes the response of epithelia to the presence of a free edge: in cell culture wound healing models, the cells at the wound edge are typically more protrusive than the surrounded cells. They also polarize those protrusions in the direction of the free edge and exert greater traction forces on their substrate, both behaviors that can be caused by the relief of contact inhibition at this edge (Mayor & Etienne-Manneville, 2016; Zimmermann et al., 2016). In simulations, CIL greatly increases the efficiency of wound closure (Smeets et al., 2016).

Attractive signals

Cells can regulate one another's polarity through a variety of attractive cues that cause one cell to orient its leading edge and move towards another cell. For example, in a cultured endothelial cell model, cadherin "fingers" extend from the highly-contractile trailing edge of one cell and are engulfed by the less-contractile leading edge of the cell behind. This promotes Rac activation downstream of recruitment of a BAR domain containing protein that detects the resulting change in membrane curvature (Hayer et al., 2016). In a cultured epithelial cell model, pulling forces from the trailing edge of one cell evict cortical Merlin from

the neighboring cell, and this leads to Rac activation and protrusion (Das et al., 2015). Both of these systems result in the alignment of the followers leading edge towards the trailing edge of its neighbor, contributing to persistent collective movement.

Mechanical and geometric coupling

The polarity of neighboring cells is not only coordinated through biochemical signaling, but also through physical interactions. Cells migrating collectively are mechanically coupled to one another through their adhesions (Gupta & Yap, 2021), and they also compete with one another for occupation of their shared space and substrate. This competition can act as a source of polarity relay across cell groups. For example, in cultured kidney epithelial cells grown on one-cell-wide micropatterns, when two cells collide, the one whose leading edge is more lamellar often "wins," extends lamellipodia under the other cell, and continues migrating in the same direction. Those lamellipodia create a barrier between the other cell and the substrate that prevents it from continuing forward, favoring polarity reversal. This gives rise to the formation of trains of cells migrating in the same direction (Jain et al., 2020). Pulling forces from following cells can also polarize leading cells in the other direction. In a cultured cell model of wound healing, contraction of cells behind the wound margin "elect" leader cells, causing them to polarize protrusions and traction forces towards their free edge (Vishwakarma et al., 2018). Similar types of physical coupling likely act as near-ubiquitous aspects of collective migration coordination, influencing and being influenced by the biochemical signaling described above such that the distinction between these categories blurs.

1.5 Planar cell polarity

The epithelial cells of many animal tissues are polarized not only along an apical-basal axis, but also within the epithelial plane and in alignment with one another. This depends on cou-

pling of the in-plane polarities of neighboring cells, and depends on transmembrane proteins that bind one another in trans across cell-cell interfaces (Lavalou & Lecuit, 2022). Planar cell polarity systems allow cells to transduce tissue-scale polarity into the polarization of protein composition across individual cells, or in some cases to drive cell polarization and neighboring cell alignment through their own self-organization. Where planar cell polarity has been studied, it is typically orchestrated by one (or both) of two widely-deployed pathways: the "core" planar cell polarity pathway and the Fat/Dachsous pathway, which I discuss in more detail in the next sections. These sets of proteins transduce a tissue coordinate system into polarization of a variety of cell structures and behaviors. In Drosophila epithelia, they are used to position cuticle elaborations such as hairs, denticles, and bristles, as well as eye ommatidia, and the ease of screening for defects in these external structures has made them some of the best studied examples (Adler, 2012; Goodrich & Strutt, 2011; Harrison et al., 2020). In addition to these cell extensions, planar cell polarity regulates the positioning of cilia in multiciliated cells, enabling them to generate the fluid flows that clear debris from the mammalian airway and propel sperm and eggs through the oviduct. It also controls the orientation of stereocilia bundles of the inner ear, enabling hearing (Butler & Wallingford, 2017; Wallingford, 2010). Planar cell polarity pathways also orchestrate cell rearrangements. Most notably, through asymmetric recruitment of myosin to a subset of junctions, they can bias cell intercalations along one axis and cause a tissue to become longer and narrower. This is necessary for the elongation of the many tissues including mammalian brain ventricles, oviduct, and trachea (Butler & Wallingford, 2017). Multicellular rearrangements driven by planar cell polarity pathways also tilt the follicles of the vertebrate epidermis that form fur and feathers (Cetera et al., 2018; Cetera et al., 2017; Lin & Yue, 2018). Collective epithelial cell migrations also meet the organizational definition of planar cell polarity: cells polarize along leading edge-trailing edge axes within the plane of the epithelium, and do so in alignment with their neighboring cells. This organization often has distinct molecular

origins, and is not typically considered under the same framework. However, the striking planar-polarization of follicle cells' motility machinery and of the proteins that regulate it invites this comparison. I will discuss the basic mechanisms that underpin the emergence of planar polarity in the better-studied core and Fat/Dachsous pathways, and then return to these ideas during later discussion of collective migration of follicle cells.

The core planar cell polarity pathway

The founding planar cell polarity pathway, and the most widely studied one, is the core planar cell polarity pathway. It has been most extensively studied in the *Drosophila* wing disc epithelium, and this summary draws mainly on that literature, but this pathway is also deployed widely through animal tissues to polarize a range of different cell structures and behaviors. At its core is the atypical cadherin/adhesion G-protein-coupled receptor Flamingo, which binds homophilically across cell-cell interfaces. The core asymmetry comes from two additional transmembrane protein, Van Gogh and Frizzled, which bind to the Flamingo proteins on opposite sides of the interface (the proximal and distal sides respectively in the wing disc), and have been proposed to alter the conformation of Flamingo. Several additional cytoplasmic proteins bind to these core complexes, including Prickle on the proximal side and Disheveled and Diego on the distal side (Adler, 2012; Goodrich & Strutt, 2011). Through competitive binding interactions, they stabilize transmembrane complexes that are oriented in the same direction as one another and make ones that are oriented in opposite directions more prone to endocytic turnover (Harrison et al., 2020; Strutt et al., 2019; Strutt & Strutt, 2008; Strutt et al., 2011; Warrington et al., 2017). This favors the formation of interface regions with many complexes aligned in the same direction. The core planar polarity proteins localize in clusters in the plane of the adherens junctions, and that clustering appears to be necessary for polarity sorting to occur efficiently, possibly because it concentrates the molecules and causes them to come into more frequent contact with one another (Strutt

et al., 2016).

In addition to interface-level polarity sorting, there are also cell- and tissue-scale inputs to the core planar cell polarity pathway. In fact, in the absence of longer-range polar inputs, mathematical modeling and experimental findings agree that local polarity is still possible, but will tend to decay over several cell lengths (Ma et al., 2003; Zhu & Owen, 2013). The nature of the long-range polar input(s) has been controversial, although it now appears that part of the reason for this controversy is that there are multiple factors involved (Lavalou & Lecuit, 2022). Proteins implicated as long-range cues included a number of morphogens with graded expression in the wing disc such as Wnts, Notch, Wingless, Hedgehog, and others (Lavalou & Lecuit, 2022). In each case, their removal or misexpression changes the planar polarity of the Drosophila wing. The Fat/Dachsous complex discussed in the following section has also been proposed to act as the long-range polar cue, as components of this pathway have graded expression, and changes to these gradients change the distributions of core planar cell polarity pathway members (Lavalou & Lecuit, 2022). However, these proteins all share the attribute that they regulate wing morphogenesis, and more recently it has been shown that tissue strain and cell rearrangement can themselves align and re-align core planar polarity proteins (Aigouy et al., 2010; Aw et al., 2016; Chien et al., 2015; Eaton & Jülicher, 2011). Several mechanisms have been proposed for this, multiple of which could contribute in parallel. For one, oriented neighbor exchange can influence the distribution of core planar polarity complexes simply by patterning the time-since-formation of junctions with different orientations. The cells of the wing epithelium respond to axial tissue strain by undergoing biased intercalation orthogonal to that axis, meaning that on average the interfaces that run parallel to the axis of strain will have formed more recently and had less time for the core planar polarity complex to form, polarizing its distribution (Aigouy et al., 2010; Aw & Devenport, 2017; Eaton & Jülicher, 2011; Lavalou & Lecuit, 2022). Microtubules have also been proposed to couple tissue mechanics and planar polarity.

They tend to align along cells' long axes, which are often the axes in which the cells are experiencing greatest stress, and have been shown to mediate plus end-directed transport of Frizzled towards the distal side of wing disc cells (Lavalou & Lecuit, 2022; Shimada et al., 2006). Microtubules could therefore help transduce tissue mechanics into cell-scale asymmetries in protein distribution. Interestingly, the Fat/Dachsous pathway has also been shown to contribute to microtubule polarity (Shimada et al., 2006), so it is also possible that microtubules are a point of intersection of the two pathways. Effectors of the core planar cell polarity pathway vary widely and are often tissue-specific. They include a number of actin-regulatory proteins including RhoA, Drok, Fuzzy and MYO1D, and the cilia-associated protein SPAG6 (Adler, 2012; Butler & Wallingford, 2017; Goodrich & Strutt, 2011).

The Fat/Dachsous planar cell polarity pathway

The heart of the Fat/Dachsous planar cell polarity pathway is again an asymmetric molecular bridge, in this case formed by heterotypic binding between the massive atypical cadherins Fat and Dachsous. Another important pathway member is the Golgi-resident kinase Four-jointed, which phosphorylates portions of the extracellular cadherin domains of both Fat and Dachsous that mediate their binding to one another. Curiously, Fat phosphorylation increases its binding affinity for Dachsous, but phosphorylation of Dachsous decreases its binding affinity for Fat. Although these properties alone would not give rise to polarized protein distributions, they are able to transduce tissue-wide gradients in the expression of the components into cell-scale polarity. Four-jointed and Dachsous are expressed in opposing gradients in the wing, and the difference in protein concentration/binding affinity between each pair of neighboring cells favors the formation of complexes with one orientation over the other. Flattening these protein gradients (not just removing constituents) abolishes the planar polarity of the pathway, suggesting that graded expression is solely responsible for local as well as long-range polarity of this pathway and that there are not strong feedback am-

plification mechanisms at work. Effectors of the Fat/Dachsous pathway include the myosin Dachs, microtubules and the mitotic spindle, and the Hippo signaling pathway (Fulford & McNeill, 2020).

Comparison of the core and Fat/Dachsous planar cell polarity pathways

The core and Fat/Dachsous planar polarity pathways share interesting core features and also have revealing differences. At the core of both lies asymmetric molecular bridges that relay polarity information between neighboring cells. This seems to be the minimal ingredient of all planar polarity systems, and is also found in the recently-described Toll-8/Cirl pathway (Lavalou et al., 2021), and in the follicle cells' Fat2-based pathway. In addition, both rely on a source of tissue-scale, axial or vectorial information such as graded expression of a pathway component or axis of tissue strain in order to achieve long-range planar polarity. However, the relative dependence of the two pathways on tissue-scale polarity differs. The core planar polarity system can use local feedback amplification mechanisms to amplify weak cues, or to achieve local polarity (e.g. swirls) in the absence of tissue-scale cues. The Fat-Dachsous pathway, which does not seem to involve any interface-level feedback amplification, is entirely reliant on tissue polarity and can be thought of as a system for reading out this polarity, rather than a self-organizing system entrained to it.

1.6 Fat-like cadherins

The planar polarity of the *Drosophila* follicular epithelium does not depend on the proteins of either the core or Fat/Dachsous planar cell polarity pathways, but it does require the presence of the Fat-like cadherin Fat2, a relative of Fat (Viktorinová & Dahmann, 2013; Viktorinová et al., 2009). In this section, I will discuss the domain organization and function

of Fat-like cadherins, occasionally drawing comparisons to Fat cadherins.

Fat-like cadherins, like their relatives the Fat cadherins, are giant (500 kDa) atypical cadherins with extracellular and intracellular domains and a single pass transmembrane domain. The largest portion of these proteins is extracellular, including their 34 cadherin repeats followed by one laminin G motif and several EGF-like motifs close to the transmembrane domain. These are the same motifs found in the extracellular domains of Fat cadherins, but Fat cadherins have two laminin G motifs and a different arrangement of the laminin G and EGF-like motifs. The intracellular domains of Fat-like cadherins have sequences that are more divergent from one another (and especially from Fat cadherins) and are not predicted to form any known tertiary structure (Fulford & McNeill, 2020; Sadeqzadeh et al., 2014; Sharma & McNeill, 2013). Fat-like cadherins have primarily been studied in mammals, which have three of them (Fat1-3) and *Drosophila melanogaster*, which as one (Fat2) (Fulford & McNeill, 2020; Sadeqzadeh et al., 2014; Sharma & McNeill, 2013). To distinguish between mammalian and *Drosophila* proteins in this section, I will referring to them as mFat1-3 and dFat2 respectively. Both Fat and Fat-like cadherins predate the origin of bilaterian animals, as the cnidarian *Nematostella vectensis* has both. Putative Fat or Fat-like cadherins are also present in animals that diverged from bilaterians even earlier, but these have highly variable domain structures including dramatic variation in their number of cadherin repeats (from 9 in *Trichoplax adherens* to 37 in *Monosiga brevicolis*) (Brooun et al., 2020; Hulpiau et al., 2013).

Protein interactions of the Fat-like extracellular domain

Compared to the better-studied Fat cadherins, we know little about the binding partners and cell-biological functions of Fat-like cadherins. This is particularly true of functions mediated by their extracellular domains, whose huge size makes biochemical approaches difficult. The extracellular domains of cadherin proteins are structured in part by calcium binding in the

linking regions between their extracellular cadherin repeats, which reduce their flexibility and cause the chain of cadherin repeats to have a more rod-like structure. In the Fat cadherin mFat4, calcium binding sites are absent in several of the linking regions, and this creates kinks in the extracellular domain that allow it to fit within the space of the cell-cell interface (Tsukasaki et al., 2014). It is likely that the extracellular domains of Fat-like cadherins have similarly-kinked conformations. The larger category of atypical cadherins generally bind other atypical cadherins using several cadherin repeats close to their N-termini, as do Fat and Dachsous using their four N-terminal-most repeats (Medina et al., 2023; Sotomayor et al., 2014). However, no known cadherin (or non-cadherin) extracellular binding partners have been identified for Fat-like cadherins. There is one cell aggregation assay-based report that mFat2 undergoes homophilic trans binding (Nakayama et al., 2002), but this remains to be confirmed under more physiological binding conditions. In the *Drosophila* follicle cells, dFat2 is tightly polarized to trailing edges only (Viktorinová & Dahmann, 2013), making homophilic trans binding very unlikely. Although binding partners have yet to be identified, protein interactions have been identified that are mediated by the extracellular domain of Fat-like cadherins. In the *Drosophila* follicle cells, dFat2 localizes the transmembrane protein Lar in trans to the adjacent leading edge, and this activity is not affected by deletion of dFat2's intracellular domain (Barlan et al., 2017). It is plausible that Fat2 and Lar bind one another directly, or this could be an indirect recruitment interaction. Through this trans recruitment, dFat2 promotes protrusion in the Lar-containing cell (Barlan et al., 2017). Intriguingly, in the context of Q neuroblast migration in *Caenorhabditis elegans*, the Lar homolog PTP-3 is required in the neuroblast and the Fat-like cadherin CDH-4 in the surrounding cells for anterior migration to occur (Sundararajan & Lundquist, 2012; Sundararajan et al., 2014). This suggests that trans interaction between Fat-like cadherins and receptor tyrosine phosphatases may extend beyond the Drosophila follicle cells.

Protein interactions of the Fat-like intracellular domain

More progress has been made understanding Fat-like cadherins' regulation of cell morphology and behavior through their intracellular domains. These domains contain a number of functionally-annotated regions, although not all are conserved across all Fat-like cadherins. One of the most extensively validated is their EVH1 motifs, which mediate binding to the actin elongation factor Ena/VASP and participate in mFat1 functions in several cell types (Moeller et al., 2004; Schreiner et al., 2006; Tanoue & Takeichi, 2005). mFat3 also contains EVH1 motifs, and these mediate a subset of the proteins cell migration and morphology-regulating functions in the retinal amacrine neurons (Avilés et al., 2022; Cheng et al., 2016; Krol et al., 2016). dFat2 lacks an EVH1 motif but contains multiple WIRS motifs that can mediate WAVE complex binding, so it may interact with the actin cytoskeleton through a different effector (Squarr et al., 2016). The intracellular domain of dFat2 is partially required for the polarization of the protein to trailing edges (Barlan et al., 2017), but whether the WIRS motifs specifically contribute to this or other dFat2 functions remains to be determined. Along with these, an immunoprecipitation-mass spectrometry study of the mFat3 intracellular domain identified several additional physically-associated proteins. These include the actin-interacting protein Raptor, the microtubule associated protein CLASP1/2, the kinesin 1 Kif5B, and the post-synaptic scaffold protein PSD95 (Avilés et al., 2022). The conservation of these proteins' binding in other Fat-like cadherins has not been tested, although a very similar Kif5B binding motif is present in mFat1 (Cheng et al., 2016). The intracellular domains of mFat1 and mFat3 both undergo alternative splicing that affects the binding domains present in their intracellular domains (Braun et al., 2007; Cheng et al., 2016).

Functions of Fat-like cadherins in development and disease

Fat-like cadherins have been implicated in several diseases and developmental defects, which offer clues about their function. Mutations in Fat-like cadherins or changes in their expression levels contribute to neurological diseases, glomerulotubular nephropathy (a disease of the kidney filtration barrier), and numerous cancers (Chen et al., 2022; Gee et al., 2016; Lahrouchi et al., 2019; Pastushenko et al., 2020). Each of these diseases involve highly polarized and/or motile cell types, and generally support roles for these proteins in the morphology and motility of cells. mFat1 in particular is frequently mutated in many cancers, and has been shown to act as a tumor suppressor by regulating Wnt and Hippo pathway activity and mitochondrial activity (Cao et al., 2016; Morris et al., 2013; Nishikawa et al., 2011). In the context of tissue development, dFat2 regulates the planar cell polarity of the follicular epithelial cells (Viktorinová et al., 2009) (discussed further in a later section), but in mammals no planar cell polarity defects have been reported upon removal of individual Fat-like cadherins. However, removal of one copy of mFat1 in mice homozygous for mFat4 loss-of-function mutations display more severe planar cell polarity-related phenotypes in the cochlea, renal tubule, neural tube, and caudal vertebrae (Badouel et al., 2015; Saburi et al., 2012). These include reduced tissue elongation, a process that is driven by cell intercalation biased along one axis (termed "convergent extension"). mFat1 may regulate tissue planar polarity and/or downstream aspects of convergent extension in a manner partially redundant with mFat4.

A role for mFat1 in regulation of the actin cytoskeleton is supported by studies of cultured mammalian kidney epithelial cells. mFat1 regulates actin organization cell-autonomously through its binding interaction with Ena/VASP. Depletion of mFat1 reduces stress fiber formation and cell-cell adhesion, and also reduces the cells' ability to planar-polarize and migrate to close a gap in the epithelium in a scratch wound (Moeller et al., 2004; Tanoue & Takeichi, 2004). When Fat1 is depleted, the orientation of the cells' Golgi-nucleus axis is

randomized with respect to the wound edge, and the cells form fewer lamellipodial protrusions along the wound edge (Moeller et al., 2004). mFat1 localizes to lamellipodia tips at free edges as well as to cell-cell interfaces close to the basal surface (Moeller et al., 2004; Tanoue & Takeichi, 2004). The population of mFat1 that localizes to lamellipodia tips appears to be a distinct Fat1 isoform from the interface-localized population, and to be responsible for lamellipodium dynamics, planar polarity, and scratch wound healing roles (Braun et al., 2007). mFat1 exhibits a similar localization to free leading edges and cell-cell adhesions, and a similar pro-migratory role, in vascular smooth muscle cells (Hou et al., 2006). This suggests that the protrusion and migration-regulating function of mFat1 may be widespread among mFat1-expressing tissues. Although many of these functions appear to be cell autonomous and mediated by motifs within the intracellular domain, contributions of the extracellular domain and non-cell-autonomous roles have remained largely untested. The other mammalian Fat-like cadherins have also been shown to promote cell protrusion and migration. High mFat2 expression in clusters of basal-like breast cancer cells increases their protrusivity and invasive behavior (Dang et al., 2016), and mFat3 regulates the migration of amacrine cells in the developing retina discussed below(Deans et al., 2011).

Roles for Fat-like cadherins in neuronal morphology and migration have been identified in both *C. elegans* and in mammals (Deans et al., 2011; Krol et al., 2016; Okajima et al., 2020; Schmitz et al., 2008; Sundararajan et al., 2014; Yip & Heiman, 2018). The roles of CDH-4 in the *C. elegans* nervous system, discussed above, suggest that it acts in trans to allow neuroblasts to polarize along a stable leading edge-trailing edge axis and migrate directionally (Sundararajan et al., 2014). In mammals, mFat3 expression is largely restricted to the nervous system. Its functions have been studied most extensively in the amacrine cells of the developing retina, where it regulates the amacrine cells' migration into the correct retinal layer as well as the architecture of the synapses they form there (Avilés et al., 2022; Cheng et al., 2016; Deans et al., 2011). These functions depend on distinct regions of the mFat3

intracellular domain, with WAVE complex and kinesin 1-binding motifs contributing most strongly to cell migration, and WAVE complex and Ena/VASP-binding motifs to synapse regulation (Avilés et al., 2022). mFat3 localizes to the amacrine cells' neurites, from which synapses form, and it prevents excess synapse formation in a manner that is autonomous to the amacrine cells (Avilés et al., 2022; Deans et al., 2011). However, is not yet known whether intercellular interactions among amacrine cells contribute to mFat3 function.

Altogether, it appears that Fat-like cadherins regulate cell morphology and motility, and accomplish this through regulation of the actin (and perhaps microtubule) cytoskeleton within restricted regions of polarized cell types. Where their localization has been evaluated, Fat-like cadherins are present only in portions of the cell (e.g. lamellipodia, trailing edges, or the neurites) (Avilés et al., 2022; Moeller et al., 2004; Tanoue & Takeichi, 2004; Viktorinová & Dahmann, 2013). This ability to polarize appears to be the most consistent feature of Fat-like cadherins, enabling them to regulate the actin cytoskeleton and perhaps other proteins and structures through a set of less-conserved, modular intracellular protein-binding motifs. It is likely that the extracellular domains of these proteins, and cell-cell interactions mediated by them, are central to their localization and perhaps other aspects of their function.

1.7 Rotational collective migration of the *Drosophila* follicular epithelial cells

For my dissertation research, I have investigated the rotational collective migration of the *Drosophila melanogaster* follicle cells, and the unconventional planar polarity system that orchestrates it. These cells are part of the multicellular structure called the egg chamber (or follicle) which gives rise to an egg. The egg chamber has been an important model of many aspects of cell and developmental biology, such as stem cell niche maintenance (Kirilly & Xie, 2007; Xie & Spradling, 1998; Zhang & Kalderon, 2001), germline development (Forbes & Lehmann, 1998; Spradling et al., 1997; Styhler et al., 1998), epithelial apical-basal

polarity and barrier function (Benton & Johnston, 2003; Isasti-Sanchez et al., 2021; Lu & Bilder, 2005; Tanentzapf et al., 2000), unconventional genome duplication strategies (Deng et al., 2001; Hammond & Laird, 1985; Maines et al., 2004; Royzman & Orr-Weaver, 1998), basement membrane secretion (Devergne et al., 2017; Devergne et al., 2014; Isabella & Horne-Badovinac, 2015, 2016; Lerner et al., 2013; Zajac & Horne-Badovinac, 2021), and of course collective cell migration (Bai et al., 2000; Cetera & Horne-Badovinac, 2015; Haigo & Bilder, 2011; Montell et al., 1992; Parsons et al., 2023; Prasad & Montell, 2007). I will first describe the structure of the egg chamber and outline some major events in its development. Then I will outline our understanding of the follicle cells' planar polarity and collective migration on which my has research built.

Structure and development of the egg chamber

The insect egg chamber is a multicellular unit within the ovary that plays a functionally analogous role to the ovarian follicles of vertebrates, supporting the development of an oocyte/egg (Horne-Badovinac & Bilder, 2005; McLaughlin & Bratu, 2015). The interior of each egg chamber contains one oocyte and 15 germline "nurse cells" that remain connected to the oocyte by cytoplasmic bridges following four rounds of cell division with incomplete cytokinesis. The oocyte is largely transcriptionally silent throughout egg chamber development, and the nurse cells support its growth in part by supplying much of the cytoplasmic contents of the eventual egg. Surrounding the germline cells is the follicular epithelium, a monolayer tissue that supports oocyte development, patterns egg morphogenesis, and finally secretes the material of the eggshell before being shed as the egg is laid. Surrounding the entire egg chamber is a basement membrane extracellular matrix. The follicle cells' apical surfaces face inward and adhere to the germline cells, and their basal surfaces face outward and adhere to the encapsulating basement membrane.

Egg chambers develop in assembly line-like chains, termed ovarioles (McLaughlin &

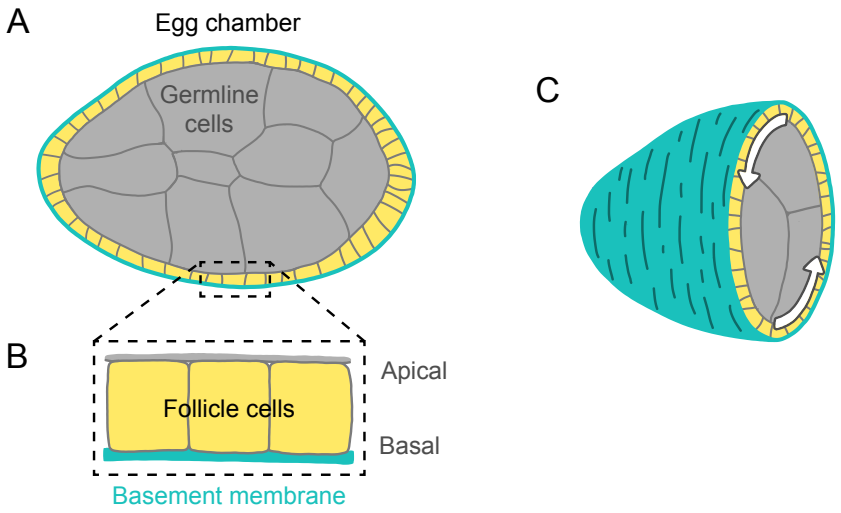

Figure 1.2: **Structure of the egg chamber during follicle cell migration.** Follicle cells are in yellow, germline cells gray, and the basement membrane cyan. **A**, Diagram of a stage 6 egg chamber sectioned along the anterior-posterior axis. Posterior is to the right. The posterior-most germline cell is the oocyte, others are nurse cells. **B**, Close-up view of three follicle cells. Their apical surfaces adhere to the germline cells and their basal surfaces adhere to the basement membrane. **C**, Diagram of the anterior half of an egg chamber sectioned through the medial plane. Arrows indicate the rotation of the egg chamber caused by follicle cell migration, which can occur in either the clockwise or counterclockwise direction.

Bratu, 2015). Their development has been divided into 14 stages based on morphological criteria that I will refer to here (Spradling, 1993). Egg chambers first form in structures called germaria (singular: germarium), which contain the germline and follicle stem cells niches that supply the initial complement of cells (McLaughlin & Bratu, 2015). Follicle cell precursors encapsulate newly-formed cysts of germline cells, polarize along apical-basal axes, and then the whole unit buds from the posterior end of the germarium. A subset of follicle cells differentiate into stalk cells, and these maintain the egg chamber's attachment to the germarium (and subsequently to the next egg chamber that buds from it). As new egg chambers form, older ones move progressively posterior-wards toward the oviduct, through which the egg is ultimately laid. Follicle cells are initially cuboidal and all share similar gene expression profiles, with the exception of several (eventually two) cells at the anterior and posterior-most poles (the polar cells) (Horne-Badovinac & Bilder, 2005). The polar cells

secrete the JAK/STAT pathway ligand Unpaired, and pathway activation in nearby follicle cells causes them to further differentiate into anterior and posterior terminal domain cells (González-Reyes & Johnston, 1998; Horne-Badovinac & Bilder, 2005; McGregor et al., 2002; McLaughlin & Bratu, 2015). Follicle cells continue to proliferate until stage 7, contributing to egg chamber growth and ultimately reaching approximately 650 cells (Horne-Badovinac & Bilder, 2005). After cell division ceases, the cells continue to endoreplicate, and further oocyte growth is accommodated by follicle cell growth and shape changes (Horne-Badovinac & Bilder, 2005). Between stages 8 and 10, subsets of follicle cells differentiate and change shape, with the anterior-most ones in contact with nurse cells becoming squamous and the rest columnar (Horne-Badovinac & Bilder, 2005). At the end of this shape transition, the squamous cells will all be in contact with nurse cells and the columnar cells with the oocyte. The nurse cells transfer their contents to the oocyte, first through directed transport and then by contracting and squeezing out most of their cytoplasm in a process called "nurse cell dumping" (McLaughlin & Bratu, 2015). The nurse cells are then phagocytosed by the squamous cells, leaving the egg chamber interior mostly occupied by the oocyte (Lebo & McCall, 2021). As the oocyte grows, the columnar cells reorganize to replace the squamous cell side of the epithelium, becoming squamous themselves in the process (Horne-Badovinac & Bilder, 2005). Subsets of them undergo additional shape changes and movements to pattern additional structures within the eggshell. These include the dorsal appendages, which are long projections that mediate gas exchange; the micropyle, the pore through which the sperm travels to fertilize the egg; and the operculum, hatch-like eggshell region through which the larvae eventually hatches (Horne-Badovinac & Bilder, 2005). As oocyte growth is completing, follicle cells secrete the material of the eggshell apically into the space between themselves and the oocyte. They are then shed during the passage of the egg chamber through the oviduct and the egg is fertilized by sperm released from the spermatheca and laid (Bloch Qazi et al., 2003; Deady et al., 2015).

Egg chamber elongation

As the egg chamber grows, it undergoes a number of morphogenetic changes including a dramatic elongation from spherical to ellipsoidal with a length more than twice its width (Gates, 2012). This seemingly-simple morphological change is actually orchestrated by multiple cell/tissue-biological processes at different stages of egg chamber development. First, there is an early phase of elongation that is orchestrated by JAK/STAT signaling from the polar cells (Alégot et al., 2018). Subsequent egg elongation depends on follicle cell migration along the basement membrane (Haigo & Bilder, 2011). This migration causes the entire egg chamber to rotate within the stationary basement membrane. As the cells migrate, they secrete new basement membrane material, and their migration movement patterns the deposition of this material (and perhaps also remodels existing material) (Chlasta et al., 2017; Crest et al., 2017; Isabella & Horne-Badovinac, 2016). This gives the basement membrane a polarized, fibrillar structure aligned with the axis of migration, and it also imparts a symmetric stiffness gradient in the basement membrane that is highest around the medial circumference and lowest at the anterior and posterior poles. As the egg chamber grows, the basement membrane resists that expansion anisotropically as a result of its mechanical patterning. It funnels growth primarily along the anterior-posterior axis, causing the egg chamber to elongate (Ramos-Lewis & Page-McCaw, 2019). Genetic manipulations that prevent follicle cell migration result in eggs with normal volumes but near-spherical shapes. The polarized basement membrane structure continues to serve as long-term record of polarity after migration has stopped, causing the follicle cells' contractile actomyosin stress fibers to re-align circumferentially along the medial axis and drive further tissue elongation (Campos et al., 2020).

Follicle cell migration

Follicle cells migrate by crawling along the basement membrane using motility machinery at their basal surfaces. Each cell forms protrusions at its leading edge and an array of aligned stress fibers coupled to focal adhesions along its length (Sherrard et al., 2021). The leading edge-trailing edge axes of all the cells are aligned with one another, giving rise to a chiral circumferential planar-polarity across the epithelium (Cetera et al., 2014; Gutzeit et al., 1991; Haigo & Bilder, 2011). The integrin-based focal adhesions form behind the leading edge and remain stationary with respect to the basement membrane as the cell moves forward, mediating force transmission between the cell and its substrate. Focal adhesions that persist until the trailing edge of the cell has reached them are detached from the substrate, allowing the cell to advance (Sherrard et al., 2021). Focal adhesions are coupled to stress fibers that are aligned in the direction of cell movement. Unlike most stress fibers documented in cell culture, follicle cells' stress fibers add new segments bounded by new focal adhesions as the cell advances, such that there are focal adhesions along the lengths of stress fibers as well as at their two ends (Sherrard et al., 2021). This treadmilling behavior allows individual stress fibers to persist for longer than it takes for the cell to advance its own length, and has been proposed to contribute to the high directional persistence of the cells' migration (Sherrard et al., 2021). Appropriate levels of adhesion and contractility, and dynamic turnover of adhesions, are all necessary for efficient migration (Dent et al., 2019; Lewellyn et al., 2013). Follicle cells' leading edge protrusions are composed of filopodia embedded within a wider lamellipodium (Cetera et al., 2014). The WAVE complex, which builds the branched actin network of the lamellipodium, localizes along the leading edge of the cell (Cetera et al., 2014). Enabled (Ena), the actin elongation factor that builds the filopodia, localizes in puncta at the filopodia tips (Cetera et al., 2014). Removal of WAVE complex subunits prevents the formation of both filopodia and lamellipodia (Cetera et al., 2014), suggesting that the filopodial actin network is built from the underlying lamellipodial actin network.

This also prevents migration (Cetera et al., 2014). Loss of Ena removes filopodia but does not affect follicle cells' migration speed (Cetera et al., 2014), showing that the lamellipodia are responsible for pushing the leading edge forward.

Follicle cells begin to migrate just as the egg chamber buds from the germarium, causing the egg chamber to rotate in place around the axis bounded by the anterior and posterior polar cells (Cetera et al., 2014; Chen et al., 2016). This migration continues for approximately two days of egg chamber development, gaining speed gradually through stages 6-7 and then slowing to a halt during stage 8, concurrent with the cells' transition into stretch and columnar cells (Cetera et al., 2014). Although the axis around which migration occurs is fixed, migration can proceed with either chirality along that axis, imparting the basement membrane with the same polarized structure (Haigo & Bilder, 2011). Half of all egg chambers rotate clockwise, and the other half counterclockwise, irrespective of the rotation direction of other egg chambers in the ovariole (Haigo & Bilder, 2011). This indicates that the direction of migration is set by a stochastic symmetry-breaking process that occurs during egg chamber formation. No spontaneous reversal events have been observed either ex vivo or using in vivo tracking approaches, suggesting that once migration has begun, its directionality is stable for its duration, a fairly remarkable feat of migration persistence. Persistent collective migration depends on the planar-polarization of the cell motility machinery described above. Interestingly, cell migration is also required to maintain that planar polarity, as all known genetic conditions that prevent one also prevent the other (Cetera et al., 2014). This has led to the model that symmetry breaking is mediated by positive feedback between planar polarity and tissue motion (Haigo & Bilder, 2011). However, the microtubule network of the follicle cell precursors exhibits a chirality prior to the onset of migration that is predictive of the migration direction, and microtubule disruptions prevent symmetry breaking, so it has also been proposed that microtubules are part of a feedback loop that causes symmetry breaking (Chen et al., 2016; Viktorinová & Dahmann, 2013).

Planar signaling during follicle cell migration

The planar alignment of cells' motility machinery and their migration depend on a set of transmembrane proteins that localize to leading-trailing interfaces, and I have focused my research on the question of how these proteins are organized at this site, and how they polarize the cell motility machinery. The best studied of these is Fat2, a 500 kDa atypical cadherin with an extracellular domain composed of 34 N-terminal cadherin domains, and one laminin G and five EGF-like domains close to the transmembrane domain (Horne-Badovinac, 2017; Sharma & McNeill, 2013; Tanoue & Takeichi, 2005) (Fig. 1.3). It also has a single-pass transmembrane domain and a short intracellular domain with no clear domain structure homology. Fat2 localizes in puncta along the trailing edge of each follicle cell, where it acts cell-autonomously to promote retraction of the trailing edge, and non-cell-autonomously to promote the formation of protrusions at the leading edge of the cell behind (Barlan et al., 2017; Viktorinová & Dahmann, 2013). In the absence of Fat2, leading edge protrusions are reduced and epithelia are non-migratory (Barlan et al., 2017; Squarr et al., 2016; Viktorinová & Dahmann, 2013). A truncated Fat2 that lacks the intracellular domain is able to rescue protrusion formation, and epithelia are migratory (but slow) in this context (Barlan et al., 2017), showing that much of Fat2's function is mediated by its extracellular domain. The intracellular domain contains a WIRS motif that has been shown to interact with the WAVE complex (Chen, Brinkmann, et al., 2014; Squarr et al., 2016), but the functional significance of this physical interaction is not clear. No other proteins that physically interact with Fat2 have been identified.

Fat2 regulates migration in part through the receptor tyrosine phosphatase Lar (Barlan et al., 2017). Lar contains extracellular immunoglobulin and fibronectin type III domains, and two intracellular protein tyrosine phosphatase domains (Krueger et al., 1996) (Fig. 1.3). One of these exhibits phosphatase activity and the other is thought to be enzymatically inactive (Krueger et al., 2003), but whether Lar's phosphatase activity plays a role in follicle cell

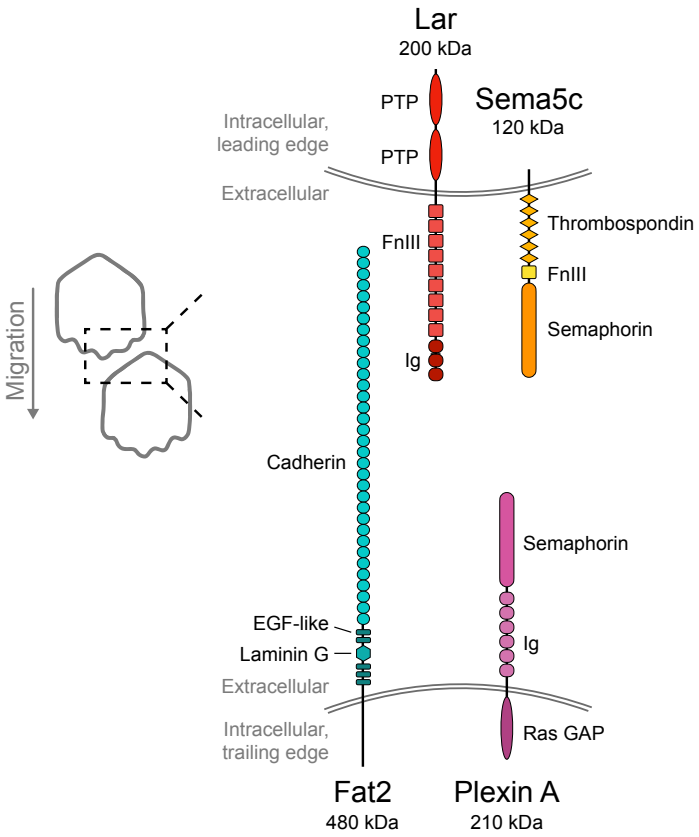

Figure 1.3: **Domain organization of Fat2, Lar, Sema5c, and PlexA.** Predicted domains are shown with the same shape and color Proteins are not drawn to scale. EGF-like: epidermal growth factor-like. FnIII: fibronectin type III. Ig: immunoglobulin. PTP: protein tyrosine phosphatase.

migration has not been determined. Fat2 acts in trans to localize Lar to the leading edge, in the same non-cell-autonomous pattern in which it promotes leading edge protrusions (Barlan et al., 2017). This is independent of Fat2's intracellular domain and is not a reciprocal localizing interaction, as Lar plays little or no role in the localization of Fat2 (Barlan et al., 2017). This results in the colocalization of Fat2 and Lar in polar, interface-spanning puncta (Barlan et al., 2017). From the leading edge, Lar promotes protrusive F-actin enrichment in cis and trailing edge retraction in trans, in the reciprocal pattern to Fat2 (Barlan et al., 2017). Although loss of Fat2 and Lar cause qualitatively similar phenotypes in reciprocal patterns, the effects of Lar loss are milder and follicle cells lacking Lar still migrate, albeit

slowly (Barlan et al., 2017). Because of this, it has been proposed that Fat2 signals in parallel through Lar and an as-yet-unidentified second effector (Barlan et al., 2017).

In addition to Fat2 and Lar, follicle cell migration is also regulated by the ligand-receptor pair Semaphorin 5c (Sema5c) and Plexin A (PlexA) (Stedden et al., 2019). Sema5c is a transmembrane semaphorin that localizes to the leading edge of each cell, and PlexA is enriched at trailing edges (Stedden et al., 2019) (Fig. 1.3). In vitro binding and functional studies support PlexA's role as a Sema5c receptor (Stedden et al., 2019). Although antibody staining of PlexA suggests that it only weakly colocalizes with puncta of Sema5c, loss of PlexA reduces the enrichment of Sema5c at leading edges, further supporting their relationship as ligand and receptor (Stedden et al., 2019). Removal of either protein from follicle cells delays the onset of migration until stage 5 and also slows it (Stedden et al., 2019). Semaphorin-plexin signaling has been most extensively studied in the context of neuronal guidance, where semaphorins in the environment of plexin-expressing neuron cause the neuron's growth cone to collapse and its extending axon to turn away (Hung & Terman, 2011). Activated PlexA has been shown to exhibit GAP activity toward the small GTPase Rap1, and to relieve autoinhibition of the F-actin disassembly protein MICAL (Schmidt et al., 2008; Terman et al., 2002; Wang et al., 2018; Zhao et al., 2018). In the follicle cells, overexpressed Sema5c causes a reduction in the F-actin protrusions of adjacent cells whose leading edges contact the cell containing excess Sema5c, and this phenotype is dependent on the presence of PlexA (Stedden et al., 2019). This has led to the model that Sema5c signals in trans through PlexA to restrict protrusive activity at trailing edges (Stedden et al., 2019). This could be accomplished through direct regulation of protrusion-related proteins, but it could also be an indirect consequence of regulation of Rap1, MICAL, or proteins involved in other aspects of cell motility.

There are indications that the Fat2-Lar and Sema5c-PlexA signaling systems do not work entirely independently of one another. Lar and Sema5c colocalize with one another in

puncta and the absence of Lar reduces Sema5c levels at leading edges (Stedden et al., 2019), suggesting that Lar contributes to the localization of Sema5c. Somewhat contradictorily, removal of one copy of Lar partially suppresses the round egg phenotype of Sema5c mutant egg chambers (Stedden et al., 2019), suggesting an antagonistic relationship between the two proteins. These proteins could directly antagonize one another at the level of the puncta in which they colocalize, or they could have functional outputs that must be appropriately balanced with one another for egg chamber elongation.

CHAPTER 2

FAT2 POLARIZES THE WAVE COMPLEX IN TRANS TO ALIGN CELL PROTRUSIONS FOR COLLECTIVE MIGRATION

2.1 Preface

This chapter includes work published with the following citation:

Williams, A. M., Donoughe, S., Munro, E., & Horne-Badovinac, S. (2022). Fat2 polarizes the WAVE complex in trans to align cell protrusions for collective migration. *eLife*, *11*, e78343. https://doi.org/10.7554/eLife.78343

This was a collaboration with Seth Donoughe, who developed methods for automated segmentation of cells and their membrane protrusions and for measuring protrusion traits.

2.2 Abstract

For a group of cells to migrate together, each cell must couple the polarity of its migratory machinery with that of the other cells in the cohort. Although collective cell migrations are common in animal development, little is known about how protrusions are coherently polarized among groups of migrating epithelial cells. We address this problem in the collective migration of the follicular epithelial cells in *Drosophila melanogaster*. In this epithelium, the cadherin Fat2 localizes to the trailing edge of each cell and promotes the formation of F-actin-rich protrusions at the leading edge of the cell behind. We show that Fat2 performs this function by acting in *trans* to concentrate the activity of the WASP family verprolin homolog regulatory complex (WAVE complex) at one long-lived region along each cell's leading edge. Without Fat2, the WAVE complex distribution expands around the cell perimeter and fluctuates over time, and protrusive activity is reduced and unpolarized. We further show that Fat2's influence is very local, with sub-micron-scale puncta of Fat2 enriching the WAVE

complex in corresponding puncta just across the leading-trailing cell-cell interface. These findings demonstrate that a trans interaction between Fat2 and the WAVE complex creates stable regions of protrusive activity in each cell and aligns the cells' protrusions across the epithelium for directionally persistent collective migration.

2.3 Introduction

Collective cell migration is essential for a variety of morphogenetic processes in animals (Friedl & Gilmour, 2009; Norden & Lecaudey, 2019; Perez-Vale & Peifer, 2020; Scarpa & Mayor, 2016). As with individual cell migrations, adherent collective migrations are driven by the concerted action of cell protrusions, contractile actomyosin networks, and adhesions to a substrate (Bodor et al., 2020; Buttenschön & Edelstein-Keshet, 2020; Scarpa & Mayor, 2016). To move forward, individual cells polarize these structures along a migratory axis, and to move persistently in one direction, they need to maintain that polarity stably over time (Stock & Pauli, 2021). Collective cell migrations introduce a new challenge: to move together, the group of migrating cells must be polarized in the same direction (Stock & Pauli, 2021). Otherwise, they would exert forces in different directions and move less efficiently, separate, or fail to migrate altogether.

The epithelial follicle cells of the *Drosophila melanogaster* ovary are a powerful experimental system in which to investigate how local interactions among migrating cells establish and maintain group polarity. Follicle cells are arranged in a continuous, topologically closed monolayer epithelium that forms the outer cell layer of the ellipsoidal egg chamber—the organ-like structure that gives rise to the egg (Duhart et al., 2017) (Fig. 2.1A-C). The apical surfaces of follicle cells adhere to a central germ cell cluster, and their basal surfaces face outward and adhere to a surrounding basement membrane extracellular matrix. The follicle cells migrate along this stationary basement membrane, resulting in rotation of the entire cell cluster (Haigo & Bilder, 2011). As the cells migrate, they secrete additional basement

membrane proteins (Haigo & Bilder, 2011). The coordination of migration with secretion causes the cells to produce a basement membrane structure that channels tissue growth along one axis (Crest et al., 2017; Gutzeit et al., 1991; Haigo & Bilder, 2011; Isabella & Horne-Badovinac, 2016). Follicle cell migration lasts for roughly two days, and the migration direction—and resulting direction of egg chamber rotation—is stable throughout (Chen et al., 2017; Stedden et al., 2019). The edgeless geometry of the epithelium means cells are not partitioned into "leader" and "follower" roles, and there is no open space, chemical gradient, or other external guidance cue to dictate the migration direction. Instead, this feat of stable cell polarization and directed migration is accomplished through local interactions between the migrating cells themselves (Barlan et al., 2017; Stedden et al., 2019).

Follicle cell migration is driven, in part, by lamellipodial protrusions that extend from the leading edge of each cell (Cetera et al., 2014; Gutzeit et al., 1991). Lamellipodia are built by the WASP family verprolin homolog regulatory complex (WAVE complex) (Miki et al., 1998; Miki et al., 2000), which is a protein assembly composed of five subunits: SCAR/WAVE, Abi, Sra1/Cyfip, Hem/Nap1, and HSPC300 (Chen et al., 2010). The WAVE complex adds branches to actin filaments by activating the Actin-related proteins-2/3 complex (Arp2/3) and elongates existing filaments, building the branched actin network that pushes the leading edge forward (Bieling et al., 2018; Machesky et al., 1999; Mullins et al., 2018). Embedded within the lamellipodia are Enabled (Ena)-dependent filopodia, which are visually prominent with F-actin labeling but dispensable for migration (Cetera et al., 2014) (Fig 2.1D,E). Removal of filopodia reveals the underlying lamellipodial actin network, whereas removal of WAVE complex subunits eliminates all protrusive structures (Cetera et al., 2014) (Fig 2.1F). We use the term "protrusions" to encompass both of these F-actin networks and the membrane deformations they cause.

The follicle cells align their protrusions across the tissue, a form of planar polarity (Cetera et al., 2014; Gutzeit et al., 1991). The atypical cadherin Fat2 is required both for this

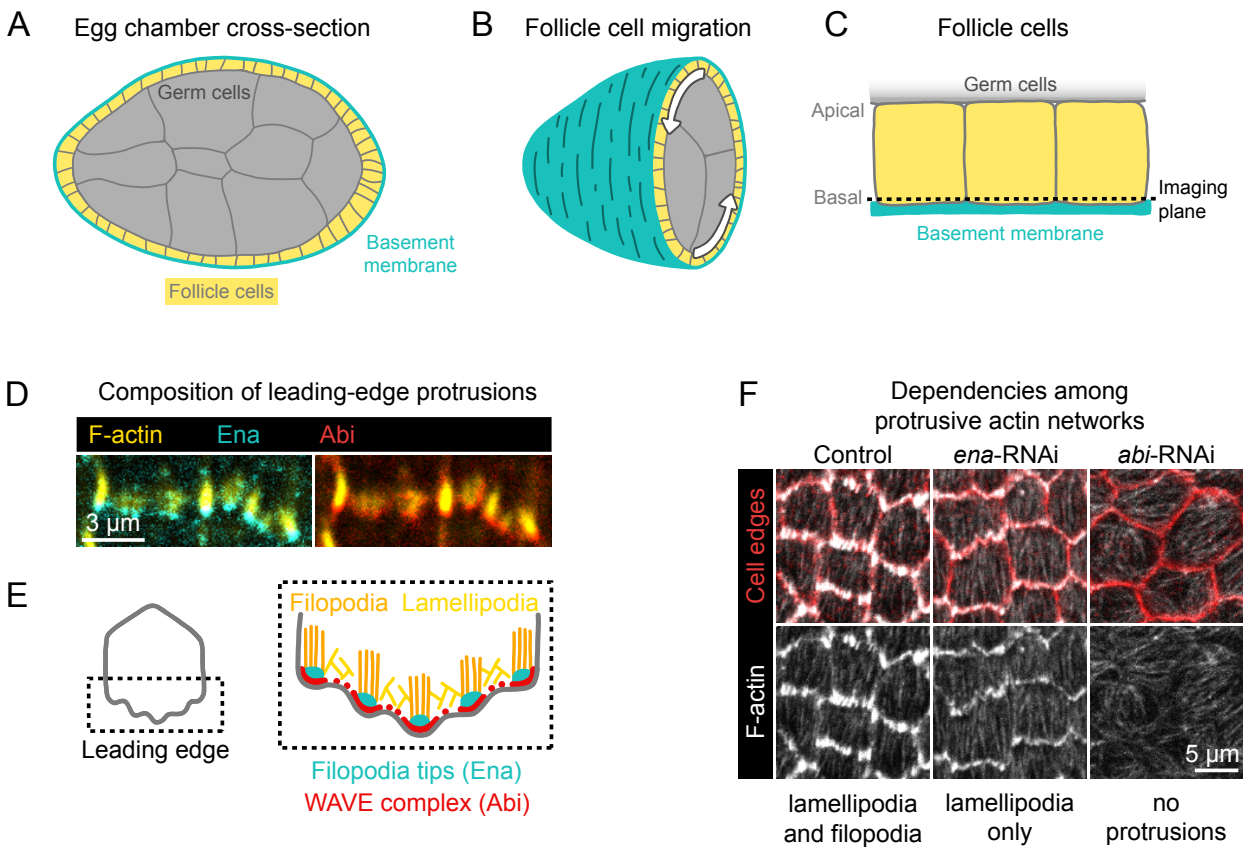

Figure 2.1: **Introduction to egg chamber rotation and follicle cell protrusions.** **A**, Diagram of a stage 6 egg chamber in cross-section. Anterior is left, posterior right. **B**, Three-dimensional diagram of an egg chamber with the anterior half shown. Arrows indicate the migration of follicle cells along the basement membrane and the resulting rotation of the egg chamber around its anterior-posterior axis. **C**, Diagram of three follicle cells. Their apical surfaces adhere to the germ cells and their basal surfaces adhere to the basement membrane. The dashed line represents the basal imaging plane used throughout this study except where indicated. **D**, Images of the leading edges of two cells expressing Ena-GFP and WAVE complex label Abi-mCherry, and with F-actin stained with phalloidin. **E**, Diagrams showing the organization of F-actin and its regulators at the leading edge. The WAVE complex builds a lamellipodial actin network, within which Ena builds filopodia. **F**, Images of F-actin (phalloidin) and cell interfaces (anti-Discs Large) in control, *ena*-RNAi, and *abi*-RNAi backgrounds. Expression of *ena*-RNAi strongly depletes filopodia, revealing the less-prominent lamellipodial actin network, whereas *abi*-RNAi expression removes both filopodia and lamellipodia.

planar polarity and for collective migration to occur (Horne-Badovinac, 2017; Viktorinová & Dahmann, 2013; Viktorinová et al., 2009). Fat2 is planar polarized to the trailing edge of each cell (Viktorinová & Dahmann, 2013), where it promotes the formation of protrusions at the leading edge of the cell immediately behind (Barlan et al., 2017). Interestingly, in addition to migration depending on polarized Fat2 activity, Fat2's planar polarity also depends on epithelial migration (Barlan et al., 2017). It is not known how Fat2 regulates lamellipodia or cell polarity, or how these processes influence one another. We hypothesized that Fat2 acts as a coupler between tissue planar polarity and cell protrusion by polarizing WAVE complex activity to the leading edge of each cell. To test this, we used genetic mosaic analysis and quantitative imaging of fixed and live tissues to dissect Fat2's contributions to protrusivity and protrusion polarity at cell and tissue scales.

We show that Fat2 signals in *trans*, entraining WAVE complex activity to one long-lived region along each cell's leading edge. Without Fat2, the WAVE complex accumulates transiently at different regions around the cell perimeter, and cell protrusivity is reduced and unpolarized. The interaction between Fat2 and the WAVE complex is non-cell-autonomous but very local, with sub-micron-scale puncta of Fat2 along the trailing edge concentrating the WAVE complex just across the cell-cell interface, at the tips of filopodia embedded within the lamellipodium. These findings demonstrate how an intercellular interaction between Fat2 and the WAVE complex promotes cell protrusivity, stabilizes regions of protrusive activity along the cell perimeter, and aligns protrusions across the epithelium by coupling leading and trailing edges. Fat2-WAVE complex interaction thereby stabilizes the planar polarity of protrusions for directionally persistent collective migration.

2.4 Results

Fat2 increases and polarizes protrusions at the basal surface of the follicular epithelium

Recent work has shown that Fat2 regulates migration of the follicular epithelium by polarizing F-actin-rich protrusions; specifically, Fat2 at the trailing edge of each cell causes protrusions to form at the leading edge of the cell behind it, and without Fat2, protrusions are reduced or lost (Barlan et al., 2017; Squarr et al., 2016). Beyond this qualitative description, it is not known how Fat2 modulates cell protrusion.

We sought to obtain a deeper, time-resolved view of the role of Fat2 in regulating protrusivity and protrusion distribution. To do so, we developed methods to segment cell membrane extensions and measure their lengths and orientations, and applied these methods to timelapse movies of the basal surface of control and $fat2^{N103\text{-}2}$ epithelia (a null allele, hereafter referred to as *fat2*) (Figs. 2.2, 2.3). A detailed description of the segmentation approach is included in the Methods. To analyze these data, we first measured the average lengths of membrane extensions from all cell-cell interfaces (Fig. 2.3A,B). The distribution of measured lengths was unimodal, with no natural division between protrusive and non-protrusive interfaces. Therefore, to establish an empirically-grounded cutoff between these categories, we recorded timelapse movies of control epithelia treated with the Arp2/3 inhibitor CK-666, which are non-migratory and almost entirely non-protrusive (Cetera et al., 2014). We used measurements from CK-666-treated epithelia to set a cutoff for the minimum length of a protrusion: any edges with membrane extensions longer than the 98th percentile of those in CK-666-treated epithelia were considered *protrusive* for subsequent analysis (Fig. 2.3B).

Using this quantification approach, we first asked how tissue protrusivity was affected by the loss of Fat2. We found that the protrusivity of *fat2* epithelia was lower than that of control epithelia on average, but highly variable, with overlap between the protrusivity

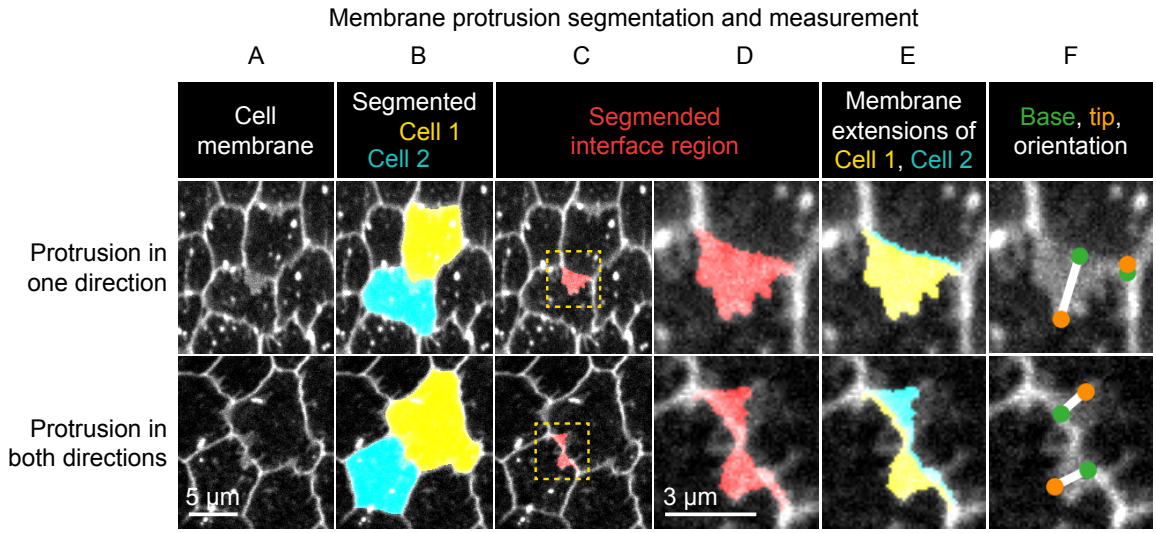

Figure 2.2: **Method used to segment and measure membrane protrusions.** Top row shows an example of a pair of neighboring cells in which one cell is protruding across their shared interface. Bottom row shows a case in which both cells are protruding across the interface. **A**, Cell interfaces and protrusions were labeled with a membrane dye and timelapses of the basal surface were collected. **B**, Cells were automatically segmented with a watershed-based method, and segmentation errors were hand-corrected. **C**, The bright interface region between each pair of neighboring cells was identified using a watershed-based method. This region includes the interface and any membrane protrusions that extend across it. **D**, An enlargement of the boxed regions of (C). **E**, The interface region was divided into two parts by the shortest path from vertex to vertex within the region, which approximates the true cell-cell interface position. The two resulting regions were then assigned to the cell from which they each extended. The area of these regions and the length of the interface between them were used to define average membrane extension length (as described in Methods). **F**, The tip and base of each region were identified, and then used to measure lengths and orientations (see Methods).

distributions of both untreated and CK-666-treated epithelia (Fig. 2.3B,C; 2.4A,B). As a complementary method, we also measured protrusivity via F-actin labeling in fixed and live tissues, using *abi*-RNAi-expressing epithelia as a nearly non-protrusive benchmark. The results largely paralleled those seen with membrane labeling (Fig. 2.5A-D); however, the disparity in protrusivity between *fat2* and control epithelia appeared larger when measured using F-actin labeling than when measured with membrane labeling (Figs. 2.3C; 2.5C). Images of follicle cell protrusions visualized by F-actin staining are dominated by fluorescence

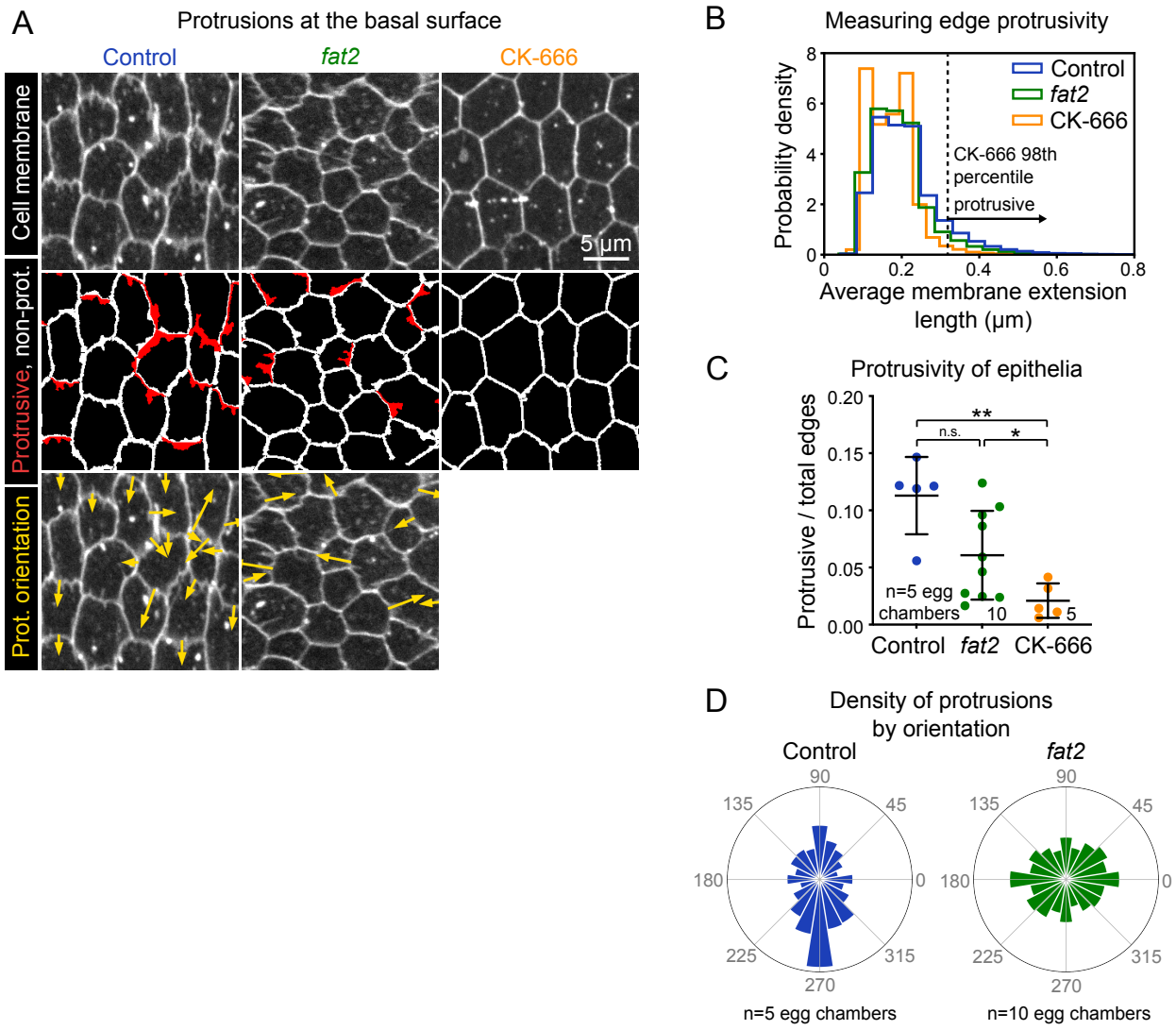

Figure 2.3: **Fat2 increases and polarizes follicle cell protrusivity.** Continued on next page.

Figure 2.3: **Fat2 increases and polarizes follicle cell protrusivity (continued).** **A**, Timelapse frames of control, *fat2*, and CK-666-treated epithelia labeled with a membrane dye. Middle row shows segmented edges. Protrusive edges, defined as edges with average membrane extension lengths longer than the 98th percentile of those of CK-666-treated epithelia, are shown in red. Non-protrusive edges are white. Bottom row shows arrows indicating the orientation of each protrusion overlaid on labeled cell membrane. Arrows originate at protrusion bases and have lengths proportional to protrusion lengths. **B**, Histogram showing the distribution of average membrane extension lengths. The 98th percentile length threshold for CK-666-treated epithelia is indicated. **C**, Plot showing the ratio of protrusive to total edges. The protrusivity of *fat2* epithelia is variable, with a distribution overlapping with control and CK-666-treated epithelia. Counts of protrusive and total edges are listed in Table 1. Welch's ANOVA ($W(2,9.3)=15.89$, $p=0.0012$) with Dunnet's T3 multiple comparisons test; n.s. $p=0.07$, *$p=0.04$, **$p=0.004$. Bars indicate mean ± SD. **D**, Polar histograms of the distribution of protrusion orientations in control and *fat2* epithelia. Anterior is left, posterior is right, and in control epithelia images were flipped as needed so that migration is always oriented downward. Bar areas scale with the fraction of protrusions. Protrusion numbers are listed are in Table 1. Control protrusions point predominantly in the direction of migration, whereas *fat2* protrusions are less polarized.

from filopodia (Fig. 2.1F). The appearance of lower protrusivity of *fat2* epithelia as measured with an F-actin label may therefore indicate that filopodia are disproportionately reduced by loss of Fat2. Altogether, these data show that *fat2* epithelia are less protrusive than control epithelia, but do retain some protrusive activity.

These results raised an important question—if some *fat2* epithelia have levels of membrane protrusivity comparable to that of control epithelia, then why do all *fat2* epithelia fail to migrate (Barlan et al., 2017; Chen et al., 2017; Viktorinová & Dahmann, 2013)? We hypothesized that the mispolarization of protrusions across the tissue contributes to *fat2* migration failure. In control epithelia, the majority of protrusions were polarized in the direction of migration, orthogonally to the egg chamber's anterior-posterior axis (Fig. 2.3A,D; 2.4C). In contrast, in *fat2* epithelia, protrusions were fairly uniformly distributed in all directions or biased in two opposite directions (Fig. 2.3A,D; 2.4C). Where an axial bias was present, the axis was inconsistent between egg chambers. We also confirmed this finding using F-actin labeling of protrusions. To compare the planar polarity of F-actin protrusions

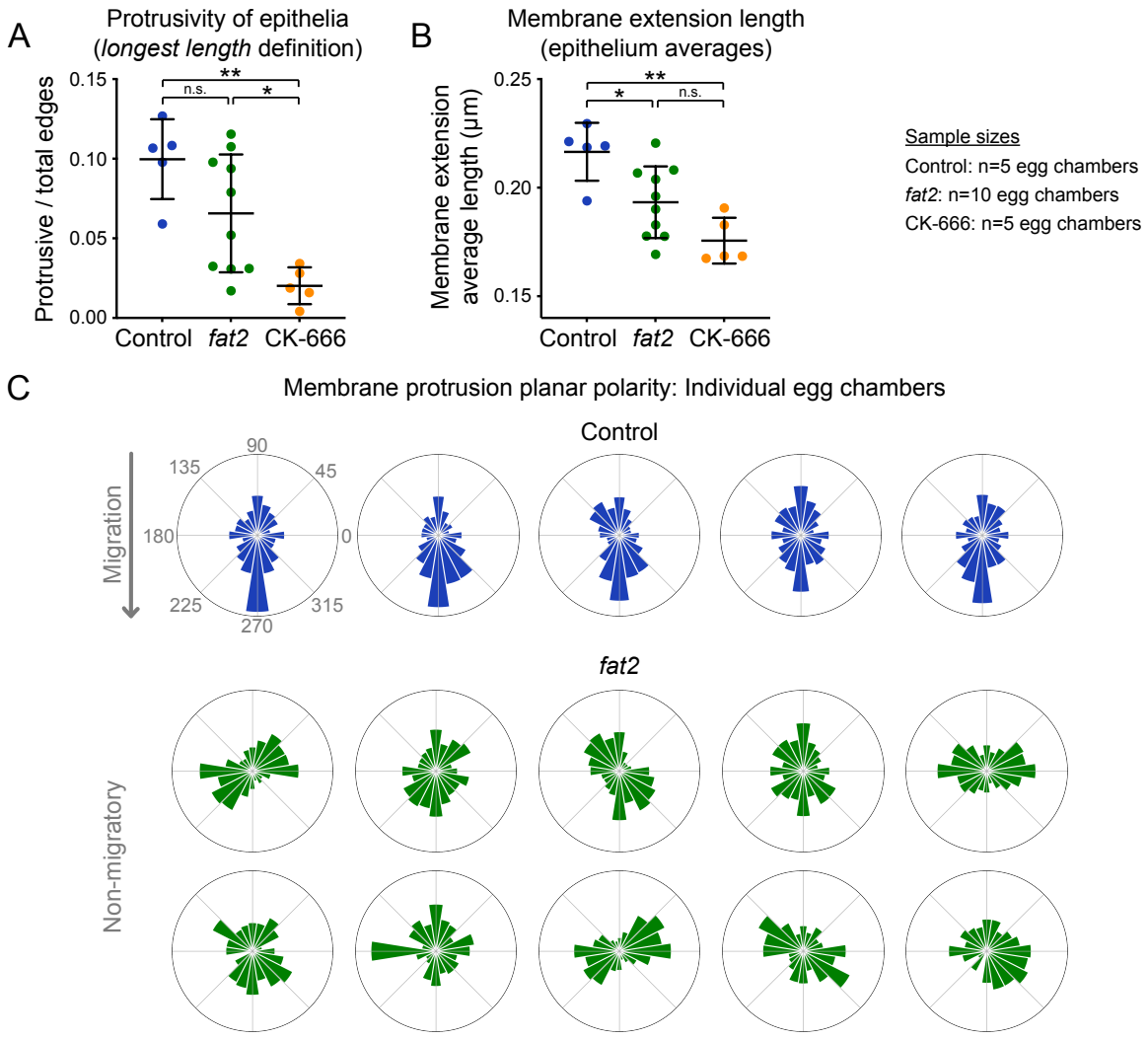

Figure 2.4: **Membrane extension length and protrusion orientation in individual egg chambers.** Continued on next page.

between control and *fat2* epithelia, we measured F-actin enrichment at cell-cell interfaces as a function of the angle of the interface relative to the egg chamber's anterior-posterior axis. We again saw that protrusions were planar-polarized in control epithelia and unpolarized in *fat2* epithelia (Fig. 2.5A,E,F). These data show that Fat2 is required to polarize protrusions in a common direction across the epithelium.

Because Fat2 regulates both follicle cell migration and planar polarity, and migration and planar polarity are interdependent (Barlan et al., 2017; Cetera et al., 2014; Viktorinová

Figure 2.4: **Membrane extension length and protrusion orientation in individual egg chambers (continued). A**, Plot showing the ratio of protrusive to total edges, with protrusivity defined in terms of membrane extension *longest length* (see Methods). In agreement with the *average length* definition, the protrusivity of *fat2* epithelia is variable, with a distribution overlapping with control and CK-666-treated epithelia. Counts of protrusive and total edges are listed in Table 1. Welch's ANOVA (W(2,9.4)=22.25, p=0.0003) with Dunnet's T3 multiple comparisons test; n.s. p=0.16, *p=0.011, **p=0.0019. **B**, Plot showing the mean membrane extension lengths of control, *fat2*, and CK-666-treated egg chambers, with membrane extension length defined as *average length* (see Methods). With this cutoff-independent protrusivity measurement, the protrusivity of *fat2* egg chambers is intermediate between control and CK-666, with a wider distribution that overlaps both. Welch's ANOVA (W(2,9.7)=13.59, p=0.0015) with Dunnet's T3 multiple comparisons test; n.s. p=0.076, *p=0.042, **p=0.0019. **A,B**, Bars indicate mean ± SD. **C**, Polar histograms showing the distribution of membrane protrusion orientations in individual control and *fat2* egg chambers. Anterior is left, posterior is right, and images were flipped as needed so that migration is downward for control epithelia, in which membrane protrusions are biased in the direction of migration. Bar areas scale with the fraction of protrusions. Protrusion numbers are listed are in Table 1. In *fat2* epithelia, protrusions have varying levels of axial bias and little or no vectorial bias.

& Dahmann, 2013; Viktorinová et al., 2009), the unpolarized protrusions of *fat2* epithelia could be a cause or a consequence of inability of *fat2* epithelia to migrate. To distinguish between these possibilities, we exploited the fact that small groups of *fat2* cells can be carried along by neighboring non-mutant, migratory cells (Viktorinová & Dahmann, 2013), allowing us to evaluate polarity of protrusions from *fat2* cells in a migratory context. We generated *fat2* mosaic tissues that had sufficiently small fractions of mutant cells that the tissue as a whole still migrated, and found that *fat2* cells in these tissues were often protrusive, but their protrusions were not polarized in the direction of migration (Fig. 2.6). This demonstrates that Fat2 does not simply polarize protrusions indirectly by maintaining tissue-wide migration. Rather, Fat2 is required at the scale of groups of cells to polarize those cells' protrusions in alignment with the direction of collective migration.

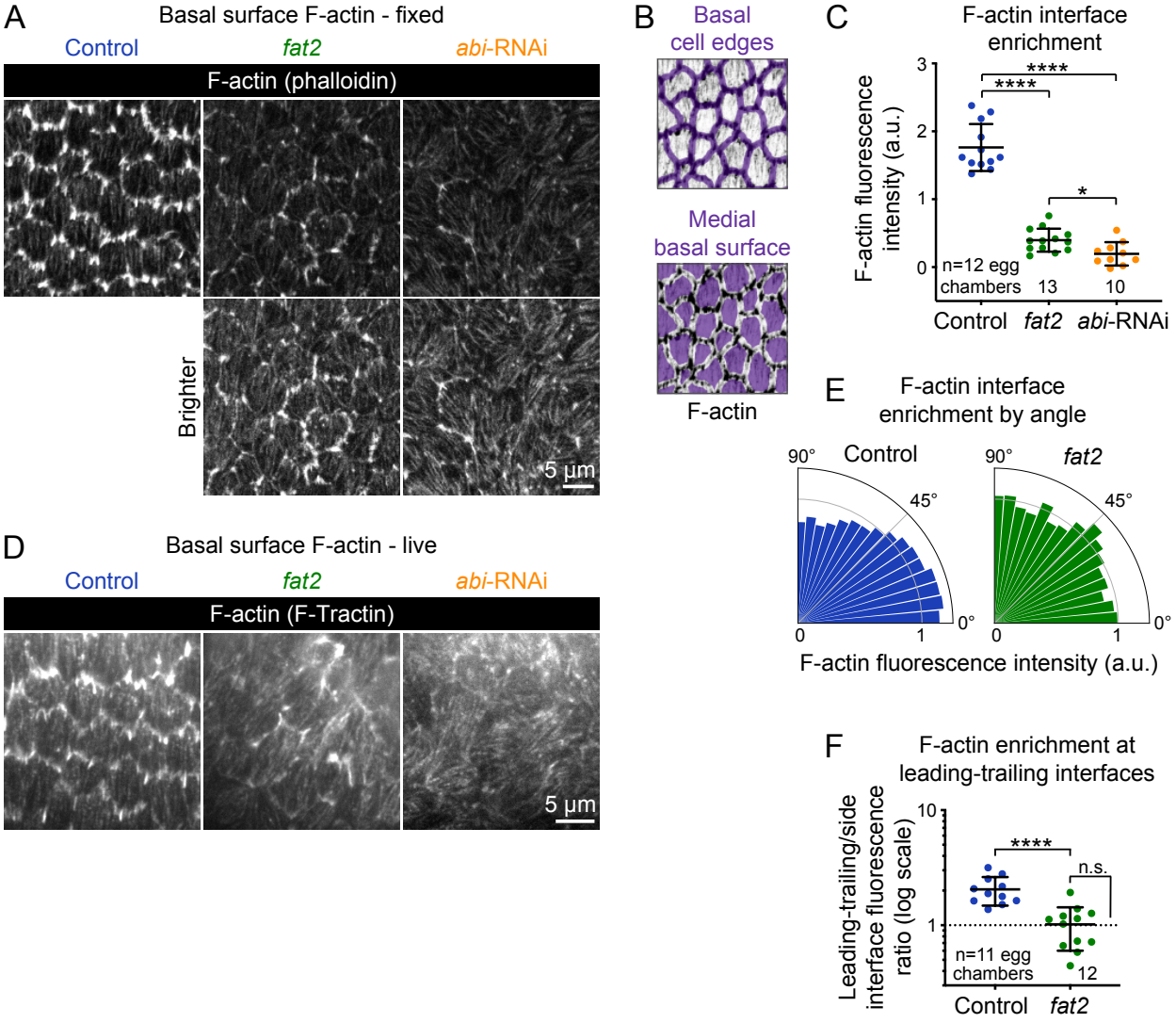

Figure 2.5: **Actin protrusions are reduced and unpolarized without Fat2 and further reduced without the WAVE complex.** Continued on next page.

Figure 2.5: **Actin protrusions are reduced and unpolarized without Fat2 and further reduced without the WAVE complex (continued).** **A**, Images showing phalloidin staining of F-actin in control, *fat2*, and *abi*-RNAi-expressing epithelia. Bottom row shows the same images with displayed brightness increased. **B**, Examples of segmented cell-cell interfaces or medial basal surfaces overlayed on F-actin. **C**, Plot of the difference in F-actin fluorescence intensity between cell interfaces and medial basal surfaces shows that while *fat2* and *abi*-RNAi epithelia have less F-actin interface enrichment than control epithelia, F-actin interface enrichment remains higher in *fat2* epithelia than *abi*-RNAi epithelia. Welch's ANOVA ($W(2, 19.84)=94.68$, $p<0.0001$) with Dunnet's T3 multiple comparisons test; *$p=0.033$, ****$p<0.0001$. **D**, Frames from timelapse movies of control, *fat2*, and *abi*-RNAi epithelia with F-actin labeled with F-Tractin-tdTomato. As with phalloidin staining, the protrusivity of *fat2* epithelia is intermediate between that of control and *abi*-RNAi epithelia. Brightness display settings vary between genotypes to correct for variability in F-Tractin-tdTomato expression levels. **E**, Plot of F-actin fluorescence intensity at cell interfaces as a function of interface angular distance from horizontal. Bar areas are rescaled so that the mean in each condition is one. **F**, Plot of the F-actin fluorescence intensity ratio between near-horizontal (0°-10°) and near-vertical (80°-90°) interfaces, corresponding with leading-trailing and side interfaces, respectively, in migratory control epithelia. F-actin is enriched along near-horizontal interfaces in control, but not *fat2*, egg chambers. Control-*fat2* comparisons: unpaired t-test, ****$p<0.0001$. Comparison between *fat2* and one (dashed line, the expectation if there is no enrichment): one sample t-test, n.s. $p=0.88$.

Fat2 increases and polarizes the WAVE complex at the basal surface of the follicular epithelium

Follicle cell protrusions are built by the WAVE complex (Cetera et al., 2014), which commonly acts in a circuit with active Rac and PI(3,4,5)P3. We hypothesized that Fat2 polarizes protrusions by polarizing the distribution of one of these circuit components. To visualize their activity, we focused on the WAVE complex, whose localization most closely determines and reports sites of protrusion. Using CRISPR/Cas9, we endogenously tagged the WAVE complex subunit Sra1 with eGFP (hereafter: Sra1-GFP), allowing us to visualize its localization and dynamics at endogenous levels.

We confirmed that Sra1-GFP flies are viable and fertile when the tagged allele is homozygous, Sra1-GFP localizes to follicle cell leading edges like other WAVE complex labels (Cetera et al., 2014; Squarr et al., 2016), its localization depends on WAVE complex subunit

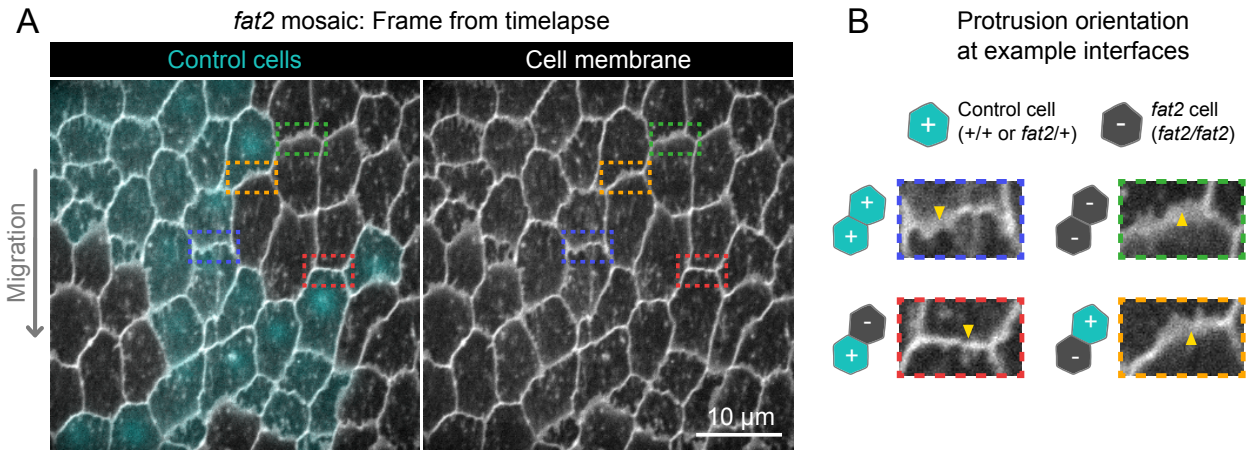

Figure 2.6: **Fat2 acts locally across the cell interface to orient membrane protrusions. A**, Timelapse frame of a *fat2* mosaic epithelium with cell membrane labeled, used to evaluate protrusion orientations in control or *fat2* cells within a migratory context. Boxes indicate examples of leading-trailing interfaces between neighbor pairs with each possible combination of genotypes. Representative of 10 similar timelapse movies. **B**, Larger images of the interfaces boxed in (A), showing that protrusions are misoriented when *fat2* cells are ahead of the interface regardless of the genotype of the cell behind the interface. Arrows point in the direction of protrusion.

Abi, and F-actin protrusions appear normal (Figs. 2.7A,B; 2.8A-C). Migration was slower when Sra1-GFP was present in two copies (Fig. 2.8D), so we performed all subsequent experiments with one copy of Sra1-GFP.

With an endogenous WAVE complex label in hand, we investigated how Fat2 affects WAVE complex localization. Previous work has shown that WAVE complex levels are reduced at the basal surface of follicle cells lacking Fat2 (Squarr et al., 2016). Consistent with this result, we found that Sra1-GFP levels were lower along cell-cell interfaces at the basal surface of *fat2* epithelia than of control epithelia (Fig. 2.9A-C). Planar polarity of Sra1-GFP across the epithelium was also lost in the absence of Fat2 (Fig. 2.9D,E). Fat2 acts non-cell-autonomously to cause protrusions to form at the leading edge of the cell just behind (Barlan et al., 2017) (Fig. 2.7C), so we next tested the hypothesis that Fat2 localizes the WAVE complex to the leading edge in the same non-cell-autonomous pattern. We did this using *fat2* mosaic epithelia, in which we could measure Sra1-GFP levels at leading-trailing

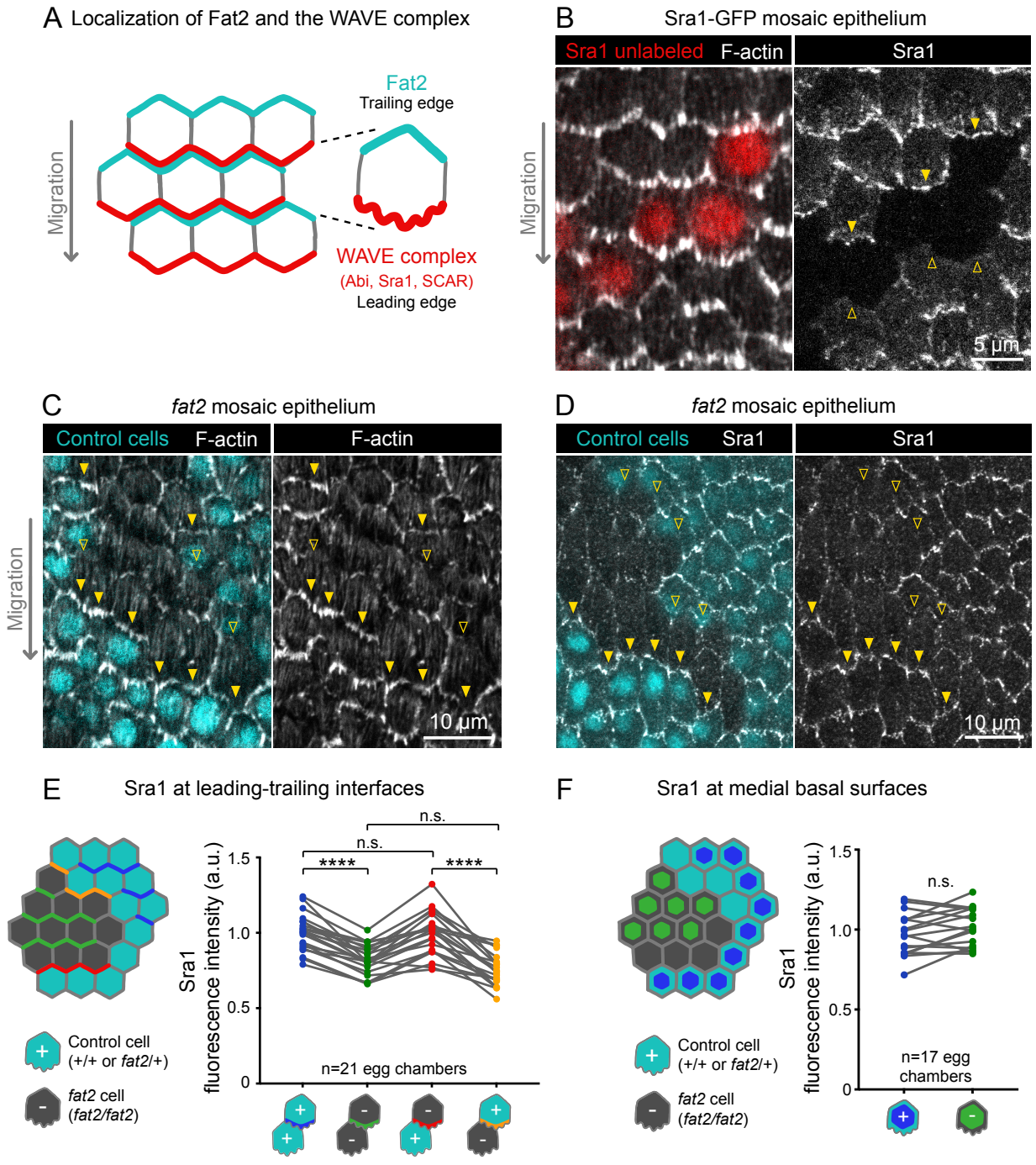

Figure 2.7: **Fat2 in each cell concentrates the WAVE complex at the leading edge of the cell behind.** Continued on next page.

Figure 2.7: **Fat2 in each cell concentrates the WAVE complex at the leading edge of the cell behind (continued).** **A**, Diagram showing Fat2 localization at the trailing edge and WAVE complex at the leading edge of the basal surface of follicle cells. The WAVE complex subunits referenced in this paper listed. **B**, Images of an Sra1-GFP mosaic epithelium with phalloidin-stained F-actin, showing Sra1-GFP enrichment at leading edges (filled arrows) and not trailing edges (open arrows). **C**, Images of a *fat2* mosaic epithelium with phalloidin-stained F-actin. Filled arrows indicate leading edges of *fat2* cells behind control cells, where protrusions are present. Open arrows indicate leading edges of control cells behind *fat2* cells, where protrusions are reduced. **D**, Images of a *fat2* mosaic epithelium expressing Sra1-GFP. Filled arrows indicate leading edges of *fat2* cells behind control cells. Open arrows indicate leading edges of control cells behind *fat2* cells. **E,F**, Quantification of Sra1-GFP mean fluorescence intensity in *fat2* mosaic epithelia along leading-trailing interfaces (E) or medial basal surfaces (F). Diagrams to the left of plots show the measured regions with respect to control (cyan) and *fat2* (gray) cells. The genotype(s) of cells in each measured category are shown below the x-axis. Lines connect measurements from the same egg chamber. **E**, Sra1-GFP is reduced at the leading edge of cells of any genotype behind *fat2* cells. Repeated measures ANOVA ($F(3,80)=22.77$, $p<0.0001$) with post-hoc Tukey's test; n.s. (left to right) $p=0.99$, 0.24, ****$p<0.0001$. **F**, Sra1-GFP is not significantly changed at the medial basal surface of *fat2* cells. Paired t-test; n.s. $p=0.08$.

interfaces shared by control and *fat2* cells. We found that Sra1-GFP levels were normally-enriched along the leading edges of *fat2* cells if control cells were present immediately ahead, showing that Sra1 can still localize to the leading edge of cells lacking Fat2. Conversely, Sra1-GFP levels were reduced along the leading edge of control cells if *fat2* cells were immediately ahead (Figs. 2.7D,E; 2.9F). We also observed a corresponding non-autonomous pattern of membrane protrusion polarity in timelapse movies of *fat2* mosaic epithelia (Fig. 2.6). We conclude that Fat2 acts non-cell-autonomously to localize the WAVE complex to leading edges, resulting in tissue-wide planar polarization of protrusive activity, and thereby in collective cell migration.

We next asked if, by recruiting the WAVE complex to the leading edge, Fat2 was reducing its levels at other membrane sites, and thereby suppressing mispolarized protrusion. To test whether Fat2 was measurably depleting the non-leading-edge WAVE complex pool, we compared the level of Sra1-GFP at the medial basal surfaces of cells in control or *fat2* epithelia, or between control and *fat2* cells in mosaic epithelia (see diagram in Fig. 2.7F). In

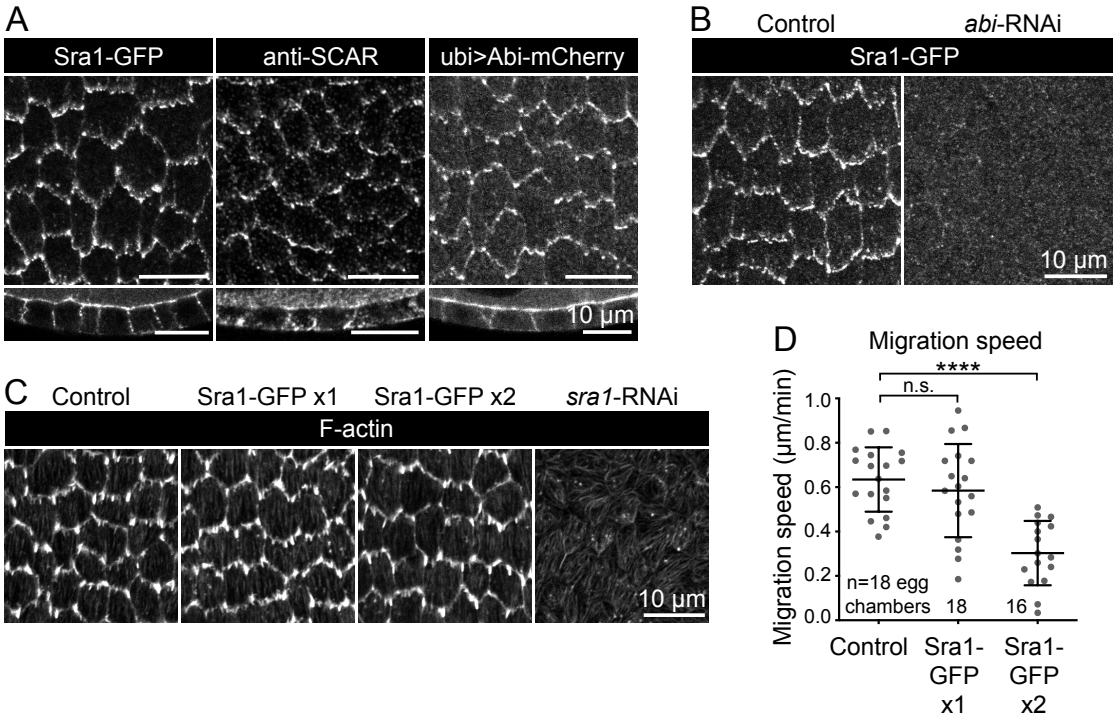

Figure 2.8: **Evaluation of endogenous Sra1-GFP functionality. A**, Images comparing the localization of markers of WAVE complex subunits: Sra1-GFP, Scar antibody, and Abi-mCherry, at the basal surface (top row) and in cross-section (bottom row). **B**, Images of Sra1-GFP localization in control and *abi*-RNAi-expressing epithelia. Sra1-GFP is dispersed in the absence of Abi. **C**, Images showing phalloidin-stained F-actin in epithelia with wild-type Sra1, one or two copies of Sra1-GFP, or expressing *sra1*-RNAi, used to assess the appearance of protrusions in each condition. **D**, Plot of migration speed of epithelia with wild-type Sra1 or one or two copies of Sra1-GFP. Migration speed is reduced when both Sra1 copies are GFP-tagged. One-way ANOVA ($F(2,49)=18.37$, $p<0.0001$) with post-hoc Tukey's test; n.s. 0.66, ****$p<0.0001$. Bars indicate mean ± SD.

both cases we measured small increases in mean Sra1-GFP in *fat2* cells compared to control cells, but these were not statistically significant (Figs. 2.7D,F; 2.9C,G). Our measurements may not be sensitive enough to detect redistribution of Sra1-GFP occurring across a broad membrane area, or the Sra1-GFP population may be redistributing away from the basal surface. It therefore remains to be determined whether by concentrating the WAVE complex at the leading edge, Fat2 also depletes the WAVE complex from other membrane sites, and thereby suppresses mispolarized protrusions.

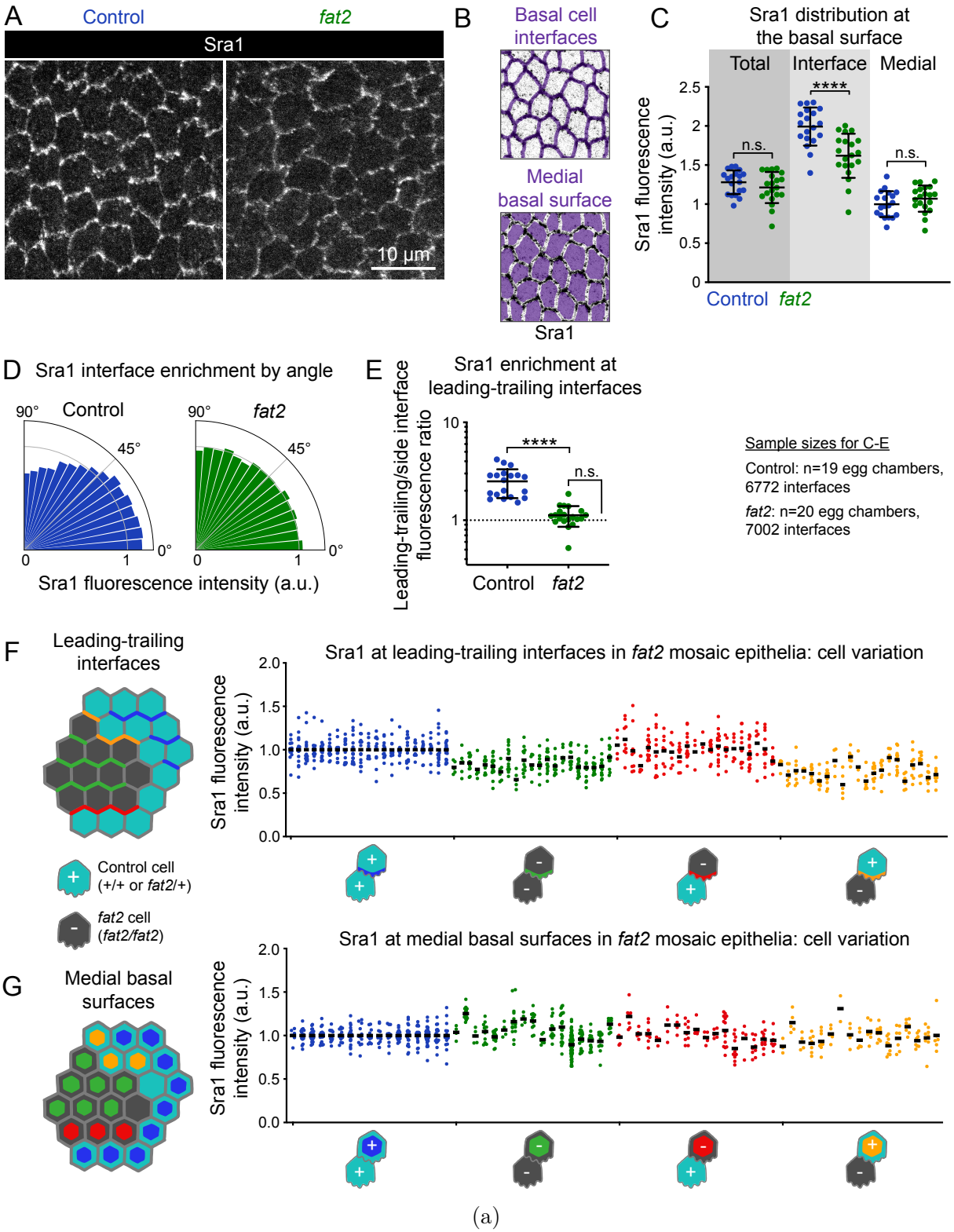

(a)

Figure 2.9: **Fat2 concentrates the WAVE complex at cell-cell interfaces and polarizes it across the epithelium.** Continued on next page.

Figure 2.9: **Fat2 concentrates the WAVE complex at cell-cell interfaces and polarizes it across the epithelium (continued).** **A**, Images of Sra1-GFP at the basal surface in control and *fat2* epithelia. **B**, Examples of segmented cell-cell interfaces or medial basal surfaces overlaid on Sra1-GFP images. **C**, Plot of mean Sra1-GFP fluorescence intensity across the entire basal surface (total), at cell-cell interfaces, and at medial basal surfaces in control and *fat2* epithelia. One-way ANOVA ($F(5,111)=63.22$, $p<0.0001$) with post-hoc Šidák's test; n.s. (left to right) p=0.67, 0.64, ****$p<0.0001$. **D**, Plot of Sra1-GFP fluorescence at cell-cell interfaces as a function of interface angular distance from horizontal. Bar areas are rescaled so that the mean in each condition is one. **E**, Plot of the Sra1-GFP fluorescence intensity ratio between near-horizontal (0°-10°) and near-vertical (80°-90°) interfaces, corresponding with leading-trailing and side interfaces, respectively, in migratory control epithelia. Sra1-GFP is enriched along near-horizontal interfaces in control, but not *fat2*, egg chambers. Control-*fat2* comparison: unpaired t-test, ****$p<0.0001$. Comparison between *fat2* and one (dashed line, the expectation if there is no enrichment): one sample t-test, n.s. p=0.052. **C,E**, Bars indicate mean ± SD. **F,G**, Quantification of Sra1-GFP mean fluorescence intensity in *fat2* mosaic epithelia along leading-trailing interfaces (F) or medial basal surfaces (G). Diagrams to the left of plots show the measured regions with respect to control (cyan) and *fat2* (gray) cells. The genotype(s) of cells in each measured category are shown below the x-axis. Each column shows data from one egg chamber with points from individual cells. Bars indicate mean. Tissue summary plots in Fig. 2.7E,F.

Fat2 stabilizes a region of WAVE complex enrichment and protrusivity in *trans*

In individually migrating cells, the excitable dynamics of the WAVE complex and its regulators enable it to form transient zones of enrichment along the cell perimeter even in the absence of a directional signal (Iglesias & Devreotes, 2012; Stock & Pauli, 2021; Weiner et al., 2007). Although the planar-polarized distribution of the WAVE complex across the epithelium was lost in *fat2* mutant tissue, we wondered (1) whether the WAVE complex could still form regions of enrichment in individual cells and (2) whether these WAVE complex-enriched regions were active and responsible for templating unpolarized protrusions. To evaluate the WAVE complex distribution along the edges of individual cells, we generated entirely *fat2* mutant epithelia in which patches of cells expressed Sra1-GFP. At cell-cell interfaces along Sra1-GFP expression boundaries, we found that the boundary cells often had cortical re-

gions devoid of Sra1-GFP (Fig. 2.10A). This observation shows that the WAVE complex is not uniformly localized around the cortex and can form regions of enrichment without Fat2. We also saw that Sra1-GFP enrichment coincided with the presence of F-actin protrusions (Fig. 2.10A), indicating that the WAVE complex in these regions is active. To confirm that the WAVE complex builds the protrusions in *fat2* epithelia, we co-imaged Sra1-GFP and a membrane label, and found that Sra1-GFP was enriched at the tips of membrane protrusions (Fig. 2.11). These data indicate that the WAVE complex can still accumulate and build protrusions in the absence of Fat2, tissue-wide planar polarity, and collective cell migration.

A striking feature of migrating follicle cells is the stable polarization of their protrusive leading edges. It is not known whether Fat2 contributes to the stabilization of protrusive regions in addition to positioning them. If so, the positions of WAVE complex-enriched, protrusive regions of *fat2* epithelia should fluctuate more than those of control epithelia, in addition to being less well-polarized at the tissue level. To see if this is the case, we acquired timelapse movies of Sra1-GFP and monitored its distribution along cell perimeters over time. In control epithelia, Sra1-GFP was strongly enriched along leading-trailing interfaces relative to side interfaces over the 20-minute timelapse. Side interfaces were mostly devoid of Sra1-GFP, except for infrequent Sra1-GFP accumulations that persisted for several minutes (Fig. 2.10B-D). In contrast, in *fat2* epithelia, the regions of greatest Sra1-GFP enrichment along the cell perimeter changed substantially over the 20-minute timelapse and multiple Sra1-GFP-enriched regions were often present simultaneously in individual *fat2* cells. Sra1-GFP accumulated in these regions, typically spreading outward along the membrane as it did so, and then dissipated. These events had a duration that was comparable to the transient accumulations of Sra1-GFP at side interfaces in control cells (Fig. 2.10B-D). Because all cell-cell interfaces in *fat2* epithelia and side interfaces in control epithelia lack Fat2, this suggests a several-minutes timescale over which regions of WAVE complex enrichment can persist without stabilization by Fat2. Live imaging of Sra1-GFP in *fat2* mosaic epithelia

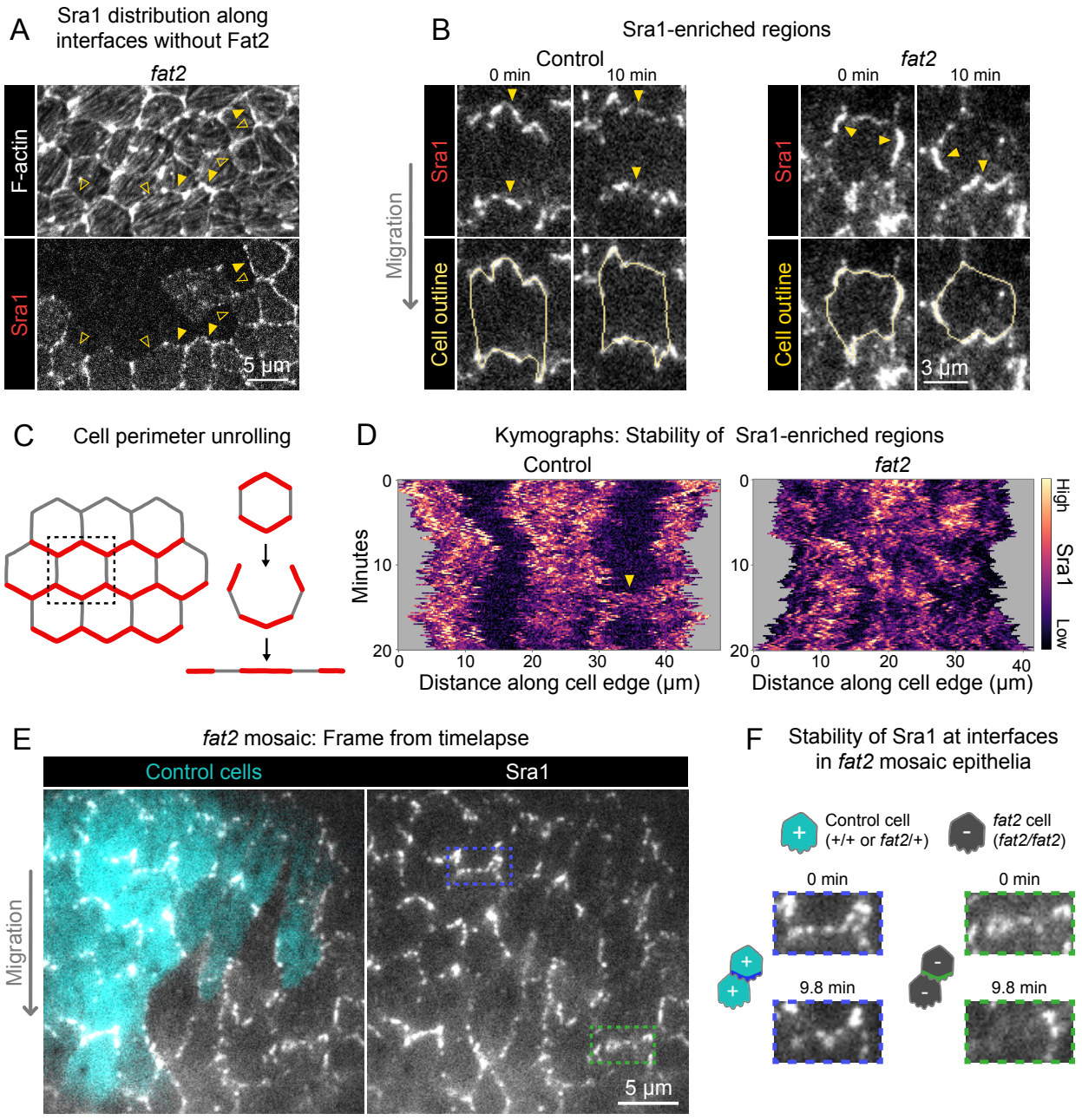

Figure 2.10: **Fat2 stabilizes a region of WAVE complex enrichment in each cell.** Continued on next page.

Figure 2.10: **Fat2 stabilizes a region of WAVE complex enrichment in each cell (continued). A**, Images of phalloidin-stained F-actin and mosaically-expressed Sra1-GFP in an entirely *fat2* mutant epithelium. Filled and open arrows indicate genotype boundary interfaces with and without Sra1-GFP enrichment, respectively. Sra1-GFP enrichment is heterogeneous, and interfaces with Sra1-GFP enrichment have more F-actin protrusions. **B**, Timelapse frames of Sra1-GFP in control and *fat2* epithelia. Top row shows Sra1-GFP with arrows indicating regions of Sra1-GFP enrichment; bottom row shows Sra1-GFP and outlines of cell perimeters used to make kymographs. Laser intensity and brightness display settings differ between genotypes. **C**, Diagram of cell perimeter unrolling for kymograph generation. Red represents planar-polarized Sra1 as distributed before and after unrolling. **D**, Kymographs of Sra1-GFP fluorescence intensity along cell perimeter outlines exemplified in (C). The y-axis length of regions of high Sra1-GFP enrichment reports their stability over time. Control cells have Sra1-GFP regions along leading-trailing interfaces that are stable over 20 minutes. In *fat2* cells, Sra1-GFP-enriched regions are less stable. The arrow indicates a transient accumulation of Sra1-GFP at a control cell side. These occur occasionally, and their stability is similar to Sra1-GFP regions in *fat2* cells. **E**, Timelapse frame of a *fat2* mosaic epithelium in which all cells express Sra1-GFP, used to evaluate Sra1-GFP dynamics in control or *fat2* cells within a migratory context. Boxes indicate a leading-trailing interface between two control cells (blue) or *fat2* cells (green). Representative of 9 similar timelapse movies. **F**, Larger images of the interfaces boxed in (E), taken 9.8 minutes apart. Sra1-GFP is initially enriched along both interfaces. It remains enriched in the control interface throughout, but loses enrichment along the *fat2* interface.

yielded similar information—Sra1-GFP enrichment fluctuated more at interfaces between *fat2* cells than interfaces between control cells despite both being in a migratory tissue (Fig. 2.10E,F).

To see if Fat2's role stabilizing the WAVE complex distribution translates to a role stabilizing protrusive regions, we returned to our timelapse movies of membrane protrusions in control and *fat2* epithelia, this time focusing on the protrusions' dynamics rather than their distribution. In control cells, protrusion polarity appeared largely stable over the 20 minute duration of our timelapse movies, whereas in *fat2* cells it often shifted substantially. In some *fat2* epithelia, protrusion positions shifts were largely restricted to two opposite-facing cell edges, whereas in others, protrusions positions shifted seemingly at random (Fig. 2.12A). To evaluate the stability of protrusion polarity quantitatively, we measured the frequency of interface protrusion polarity "switches," in which first one cell and then its

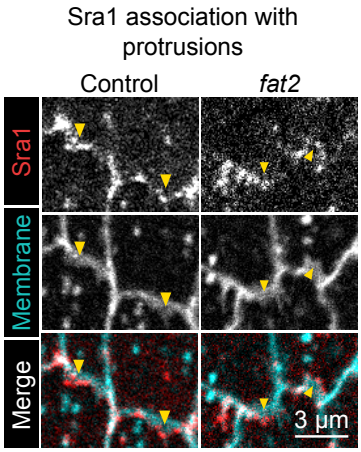

Figure 2.11: **The WAVE complex is still associated with protrusions in the absence of Fat2.** Timelapse frames showing pairs of cell interfaces from control or *fat2* epithelia expressing Sra1-GFP and labeled with a membrane dye. Arrows indicate membrane protrusions. Sra1-GFP is enriched at protrusion tips in both control and *fat2* epithelia.

neighbor protruded across their shared interface (Fig. 2.12B). These events were rare in control epithelia, with ∼2% of interfaces switching polarity per hour. In contrast, they were more common in *fat2* epithelia, with ∼60% of interfaces switching polarity per hour (Fig. 2.12C). Together, these observations show that, in addition to polarizing the WAVE complex and protrusive activity to the leading edge, Fat2 stabilizes their distributions for repeated cycles of protrusion from one long-lived cell region (Fig. 2.12D).

Fat2 and the WAVE complex colocalize across leading-trailing cell-cell interfaces

Finally, we explored how Fat2 recruits the WAVE complex across the cell-cell interface. To constrain the set of possible mechanisms, we assessed the spatial scale of their interaction. Fat2 has a punctate distribution along each cell's trailing edge (Barlan et al., 2017; Viktorinová & Dahmann, 2013), so we asked whether Fat2 recruits the WAVE complex locally to these sites, or recruits it more broadly to the entire interface. We evaluated the colocalization between Fat2 and the WAVE complex along leading-trailing interfaces, visu-

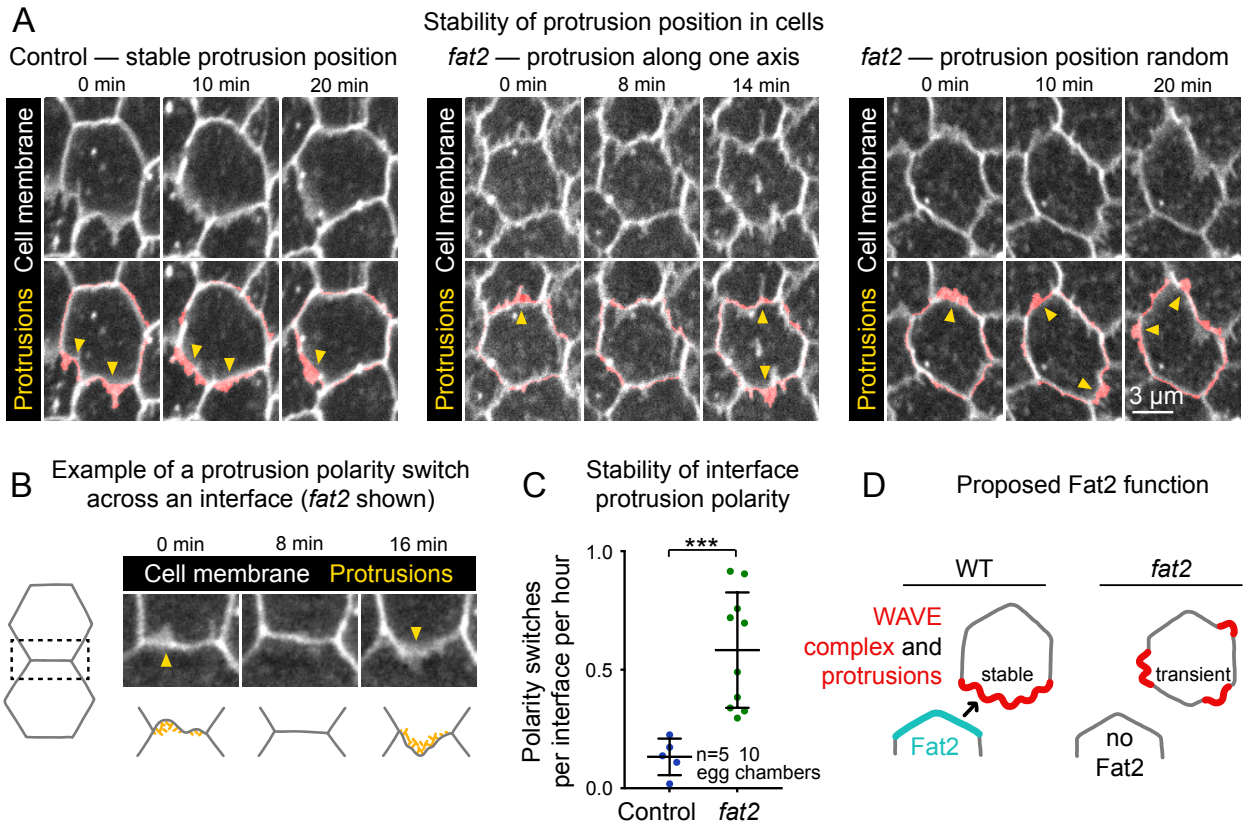

Figure 2.12: **Fat2 stabilizes a protrusive region in each cell. A**, Timelapse frames of control and *fat2* epithelia labeled with a membrane dye, showing the position of a cell's protrusions over time. Top row shows the interfaces and protrusions of one cell and its neighbors. Segmented membrane extensions originating from the center cell (red) are overlaid in the bottom row. Arrows indicate sites of membrane protrusion. In the control cell, protrusion position is stable, whereas in *fat2* cells it shifts either along a fixed axis (middle) or seemingly at random (right). **B**, Example in which one cell and then its neighbor protrudes across a shared interface (a "polarity switch"). The row shows timelapse frames of an interface and associated protrusions from a *fat2* epithelium labeled with membrane dye. Arrows originate in the protruding cell and point in the direction of protrusion. The bottom row shows corresponding diagrams of the interface with F-actin-rich protrusions illustrated in yellow. **C**, Plot showing the frequency of interface protrusion polarity switches (exemplified in (B)) in timelapse movies of control and *fat2* epithelia. Polarity switches occur more frequently at *fat2* interfaces than control ones. Unpaired t-test; ***p=0.0002. Bars indicate mean ± SD. **D**, Diagram showing the proposed role of Fat2 stabilizing a region of WAVE complex enrichment and protrusivity. Without Fat2, WAVE complex-enriched, protrusive regions are reduced and more transient.

alizing Fat2 with an endogenous 3xeGFP tag (Fat2-3xGFP) and the WAVE complex with mCherry-tagged Abi under control of the ubiquitin promoter (Abi-mCherry). Like Fat2-3xGFP, Abi-mCherry formed puncta, and Abi-mCherry and Fat2-3xGFP puncta strongly colocalized (Spearman's r = 0.71±0.04; Fig. 2.13A-E). Abi-mCherry colocalized significantly less strongly with uniformly-distributed E-cadherin-GFP (Spearman's r = 0.49±0.07; Fig. 2.14A,B), indicating that Fat2-3xGFP-Abi-mCherry colocalization was not simply a byproduct of curved membrane morphology or our measurement approach. In timelapse movies, Fat2-3xGFP and Abi-mCherry puncta moved together through cycles of protrusion extension and retraction (Fig. 2.13B). Short-lived Abi-mCherry accumulations formed infrequently at cell sides away from Fat2, similar to the Sra1-GFP side accumulations we described earlier (Figs. 2.10D; 2.14C). Together, these findings suggest that Fat2 recruits the WAVE complex locally, at the scale of individual puncta, with the WAVE complex occasionally "escaping" Fat2-dependent concentration at the leading edge.

If Fat2 puncta locally recruit the WAVE complex, changing the distribution of Fat2 puncta should cause corresponding changes to the distribution of the WAVE complex. To test this, we examined follicle cells expressing an endogenous Fat2 truncation that lacks the intracellular domain (Fat2$^{\Delta ICD}$-3xGFP), which distributes more broadly around the cell perimeter than wild-type Fat2 (Aurich & Dahmann, 2016; Barlan et al., 2017), but remains punctate. The distribution of Abi-mCherry expanded around the cell perimeter in the Fat2$^{\Delta ICD}$-3xGFP background (Fig. 2.13A) as was previously reported for protrusions (Barlan et al., 2017). Despite their altered distributions, Abi-mCherry puncta colocalized just as well with Fat2$^{\Delta ICD}$-3xGFP puncta as with Fat2-3xGFP puncta (Spearman's r = 0.71±0.04 vs. 0.71±0.05; Figs. 2.13E; 2.14B). From these data we conclude that Fat2 controls the distribution of the WAVE complex by concentrating the WAVE complex in adjacent puncta. These findings also demonstrate that the Fat2 intracellular domain is dispensable for Fat2-WAVE complex interaction in collectively migrating follicle cells.

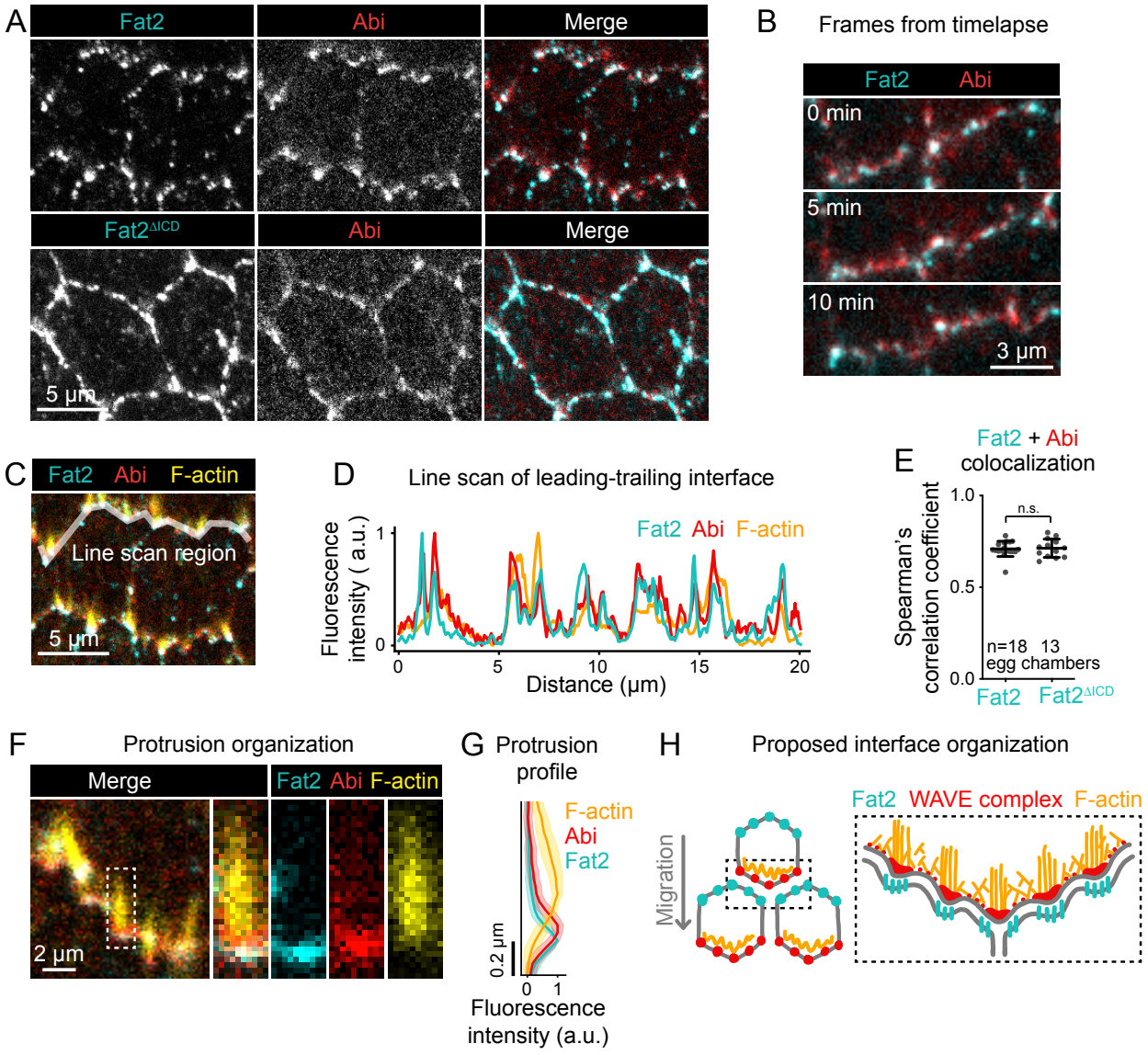

Figure 2.13: **Fat2 colocalizes with the WAVE complex across leading-trailing cell-cell interfaces.** Continued on next page.

Figure 2.13: **Fat2 colocalizes with the WAVE complex across leading-trailing cell-cell interfaces (continued).** **A**, Images of cells expressing Abi-mCherry and endogenous full-length Fat2-3xGFP or endogenous Fat2-3xGFP lacking the intracellular domain (Fat2$^{\Delta ICD}$), used to assess colocalization. **B**, Timelapse frames showing the leading-trailing interfaces of two cells expressing Fat2-3xGFP and Abi-mCherry, showing their colocalization over time. **C**, Image showing the leading-trailing interface region used in (D); it is also an example of a region used in (E). **D**, Line scan showing the fluorescence intensity of Fat2-3xGFP, Abi-mCherry, and F-actin (phalloidin) along the leading-trailing interfaces of the two cells in (C), showing their corresponding peaks of enrichment. **E**, Plot of Spearman's correlation coefficients of Fat2-3xGFP or Fat2$^{\Delta ICD}$-3xGFP and Abi-mCherry showing no significant difference in colocalization. Bars indicate mean ± SD. One-way ANOVA ($F(5,81)=44.86$, $p=0.0164$ with Fig. 2.14B) with post-hoc Tukey's test; n.s. $p>0.99$. **F**, Image showing the distribution of Fat2-3xGFP, Abi-mCherry, and F-actin (phalloidin) at the leading-trailing interface and along the boxed filopodium. **G**, Plot showing fluorescence intensity of traces of F-actin, Abi-mCherry, and Fat2-3xGFP showing their relative sites of enrichment along the length of filopodia. Lines and shaded regions indicate mean ± SD. n=74 protrusions (used for SD), 18 cells, 1 cell/egg chamber. **H**, Diagram of proposed organization of Fat2, the WAVE complex, and F-actin along the leading-trailing interface based on the present data and previously published work (Barlan et al., 2017; Cetera et al., 2014; Viktorinová & Dahmann, 2013). Fat2 puncta at the trailing edge colocalize with WAVE complex puncta at the leading edge, ahead of filopodia embedded within the lamellipodium.

Ena-dependent filopodia are embedded within and grow from the lamellipodia (Cetera et al., 2014). The WAVE complex interacts with Ena and is required for the filopodia to form (Cetera et al., 2014; Chen, Squarr, et al., 2014), so we asked whether the distribution of Fat2-WAVE complex puncta is related to the distribution of filopodia. Labeling filopodia tips with a GFP-tagged Ena transgene (GFP-Ena) and comparing the localization of Abi-mCherry and F-actin to either GFP-Ena or to Fat2-3xGFP, we found that the sites of highest Fat2-3xGFP and Abi-mCherry enrichment coincided with filopodia tips (Figs. 2.13C,D,F; 2.14D,E). Fluorescence intensity profiles along filopodia lengths showed that Fat2-3xGFP and Abi-mCherry were enriched just ahead of the F-actin-rich region (Fig. 2.13F,G). Fat2-3xGFP was shifted slightly forward from Abi-mCherry, consistent with the separation of Fat2-3xGFP and Abi-mCherry fluorophores by a cell-cell interface (Figs. 2.13F,G; 2.14E,F). This analysis demonstrates a stereotyped organization in which Fat2 and the WAVE complex

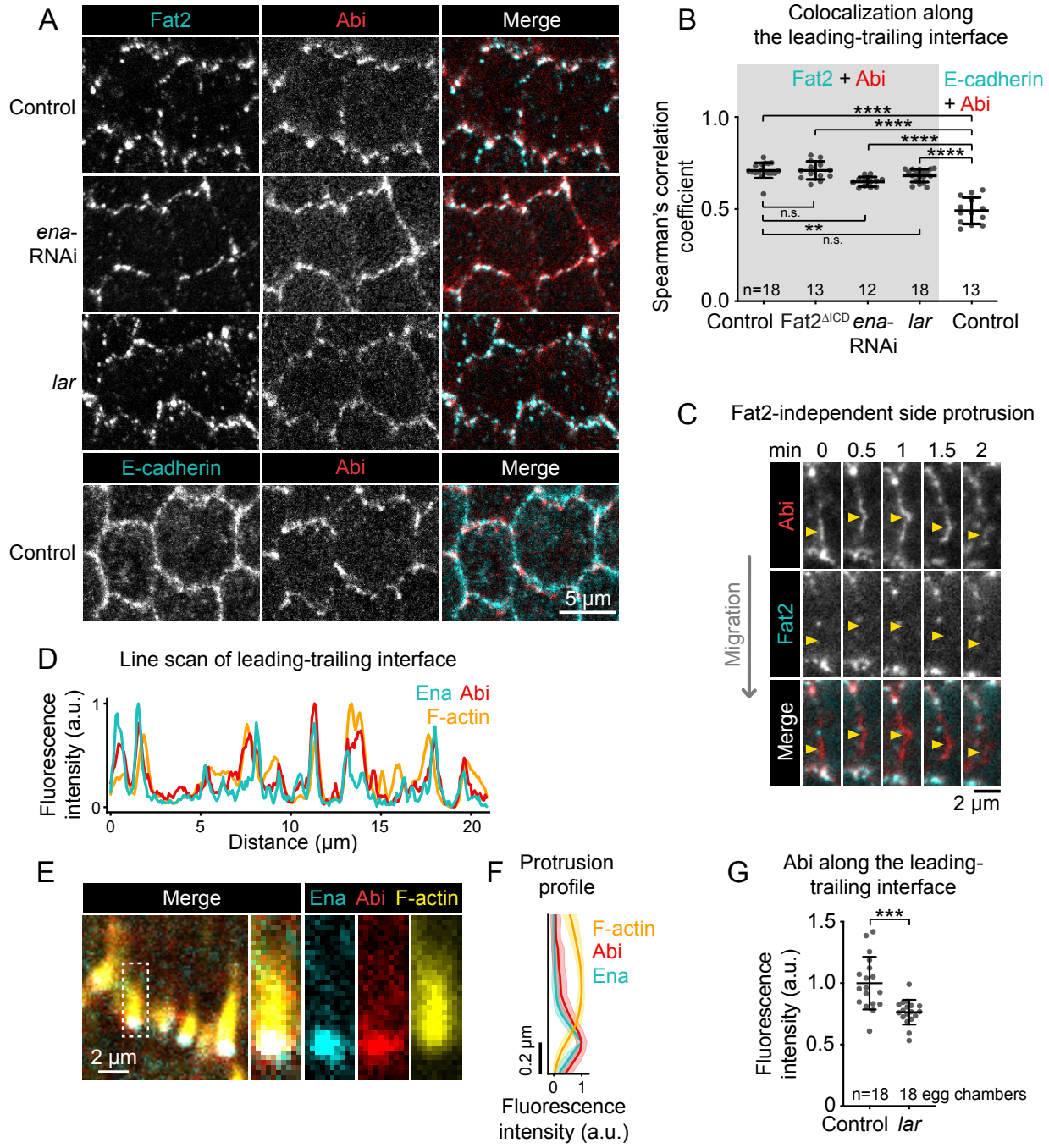

Figure 2.14: **Ena and Lar are not required for colocalization between Fat2 and the WAVE complex.** Continued on next page.

Figure 2.14: **Ena and Lar are not required for colocalization between Fat2 and the WAVE complex (continued).** **A**, Images of cells expressing Fat2-3xGFP and Abi-mCherry in control, *lar*, and *ena*-RNAi backgrounds (top 3 rows) or E-cadherin-GFP and Abi-mCherry (bottom row, negative control for colocalization measurements). **B**, Plot of Spearman's correlation coefficients of Abi-mCherry and Fat2-3xGFP (or Fat2$^{\Delta ICD}$-3xGFP) (gray background) or E-cadherin-GFP (white background) along leading-trailing interfaces show that Fat2 and Abi colocalize in all four conditions more strongly than E-cadherin and Abi. One-way ANOVA ($F(5,81)=44.86$, $p=0.0164$) with post-hoc Tukey's test; n.s. (left to right) $p>0.99$, $p=0.41$, $^{**}p<0.0046$, $^{****}p<0.0001$. **A,B**, Control, Fat2-3xGFP, and Abi-mCherry images and Spearman's coefficients are also in Fig. 2.13A,E. **C**, Timelapse frames of a side-facing cell-cell interface from an epithelium expressing Abi-mCherry and Fat2-3xGFP. Arrows indicate a site of transient Abi-mCherry accumulation, protrusion, and dissipation with no corresponding Fat2-3xGFP enrichment. **D**, Line scan of GFP-Ena, Abi-mCherry, and F-actin (phalloidin) fluorescence intensity along a leading-trailing interface region, showing their corresponding peaks of enrichment. **E**, Image showing the GFP-Ena, Abi-mCherry, and F-actin (phalloidin) at the leading edge and in the boxed filopodium. **F**, Plot of mean fluorescence intensity of F-actin, Abi-mCherry, and GFP-Ena along the length of filopodia showing their relative distribution. Lines and shaded regions indicate mean ± SD. n=54 filopodia (used for SD), 39 cells from 2 egg chambers. **G**, Plot of mean fluorescence intensity of Abi-mCherry along leading-trailing interfaces in control epithelia or similarly-oriented interfaces in *lar* epithelia, some of which are non-migratory. **B,F,G**, Bars (B,G) or lines and shaded regions (F) indicate mean ± SD.

are concentrated with Ena near the tips of the filopodia, with Fat2 at the trailing edge across the cell-cell interface from the leading edge components (Fig. 2.13H).

We considered two explanations for the close spatial relationship between Fat2 puncta, WAVE complex puncta, and filopodia. Fat2 could recruit the WAVE complex locally to puncta, and WAVE complex puncta shape the distribution of filopodia. Alternatively, Fat2 could recruit the WAVE complex to the leading edge, but their colocalization in puncta be a secondary effect of the filopodia, perhaps caused by the known interaction between Ena and Abi (Chen, Squarr, et al., 2014) or by deformation of the leading-trailing interface. To rule out a dependence on filopodia, we measured colocalization between Fat2-3xGFP and Abi-mCherry in *ena*-RNAi-expressing epithelia, in which filopodia are strongly depleted (Cetera et al., 2014) (Fig. 2.1F). Despite the loss of filopodia, both Fat2-3xGFP and Abi-mCherry remained punctate, and their colocalization was only slightly reduced (Spearman's

r = 0.71±0.04 vs. 0.65±0.03, Fig. 2.14A,B). We therefore rule out Ena or the filopodia themselves as required mediators of the spatial relationship between Fat2 and the WAVE complex, and infer that Fat2-WAVE complex colocalization is indicative of Fat2 recruitment of the WAVE complex locally to these sites.

Altogether, we propose that Fat2 acts locally, at the scale of individual Fat2 puncta, to concentrate the WAVE complex in adjacent puncta across the cell-cell interface. Because Fat2 puncta are distributed along the trailing edge, this has the broader effect of stabilizing a region of WAVE complex enrichment at the leading edge.

2.5 Discussion

This work demonstrates that a *trans* interaction between the atypical cadherin Fat2 and the WAVE complex can stabilize WAVE complex polarity for directed cell migration. Fat2, localized to the trailing edge of each cell, recruits the WAVE complex to the leading edge of the cell behind, just across their shared interface. By concentrating WAVE complex activity in a restricted region, Fat2 strongly biases lamellipodia and filopodia to form at these leading edge sites, stably polarizing overall cell protrusive activity to one cell side. Because the Fat2-WAVE complex signaling system is deployed at each leading-trailing interface in a planar-polarized manner, it both polarizes protrusions within individual cells and aligns these individual cell polarities across the epithelium. This allows the cells to exert force in a common direction and achieve a highly coordinated collective cell migration.

While the molecular players differ, local coupling of leading and trailing edges through asymmetric interactions across their shared interface is a recurring motif in studies of epithelial collective cell migrations. In an epithelial cell culture model of collective migration, asymmetric pulling forces across cell-cell interfaces polarize Rac1 activity and cell protrusion (Das et al., 2015). In another model, one cell's lamellipodium is stabilized by confinement under the trailing edge of the cell ahead, reinforcing interface asymmetry (Jain et al., 2020).

In an endothelial collective cell migration model, asymmetric membrane "fingers" containing VE-cadherin extend from the trailing edge and are engulfed by the leading edge of the cell behind, whose movement they help guide (Hayer et al., 2016). These types of leading-trailing edge coupling systems could operate together with longer-range cues to reinforce the planar polarity of cells' migratory structures. In migrations with a closed topology and no extrinsic directional cues, such as that of the follicle cells, local polarity coupling may be especially critical for collective migration.

Our development of new computational tools to segment and quantify membrane protrusion dynamics in a collectively-migrating epithelium has led to new insights into how Fat2 regulates protrusions. We found that without Fat2, protrusivity was reduced, and the distribution of remaining protrusions expanded around the cell periphery. Therefore, Fat2 not only promotes protrusion at the leading edge, but also restricts protrusion to that edge. Analysis of *fat2* mosaic epithelia revealed that Fat2 acts locally to enforce this restriction—even in the context of a globally planar-polarized, migratory epithelium, cells lacking input from Fat2 in the cell ahead were unable to polarize their protrusions in the direction of migration. Although protrusions were no longer biased in one direction without Fat2, the presence of axial orientation bias in a subset of *fat2* epithelia indicates that some form of Fat2-independent planar polarity was still present. This could be mediated by undiscovered planar signaling molecules or by a mechanical cue such as tension transmitted between cells. Investigating the cell-cell communication that gives rise to this layer of planar polarity will be an interesting area for future research.

Excitable WAVE complex activity underlies lamellipodial protrusion (Graziano & Weiner, 2014; Weiner et al., 2007; Xiong et al., 2010), and WAVE complex activity is often entrained by directional cues from the environment (Hayashi et al., 2014; Huang et al., 2013; Millius et al., 2009; Xiong et al., 2010). We hypothesize that Fat2 acts as a similar activity-entraining directional cue in follicle cells. Excitable WAVE complex dynamics were especially apparent

in our data in contexts where Fat2 was absent from the cell-cell interface—either at interfaces between cells in *fat2* epithelia, or at protrusive side interfaces we observed with low frequency in control cells. In both contexts, the WAVE complex accumulated at an edge region, spread laterally along the membrane, and then dissipated. This corresponded with the initiation, growth, and collapse of a protrusion. Where Fat2 was present, the WAVE complex distribution along the cell perimeter stayed more constant and WAVE complex levels fluctuated in place, but did not appear to spread laterally. These findings, along with the loss of cell and tissue-scale WAVE complex polarization in the absence of Fat2, suggest that Fat2 acts by concentrating WAVE complex activity in a narrow region, thereby polarizing protrusions to a single leading edge.

How might Fat2 locally concentrate the WAVE complex? The WAVE complex is activated by recruitment to the plasma membrane (Chen et al., 2010; Lebensohn & Kirschner, 2009; Oikawa et al., 2004). Positive regulators of WAVE complex accumulation include active Rac, phosphatidylinositol (3,4,5)-triphosphate (PIP_3), membrane-localized proteins that directly bind the WAVE complex, and the WAVE complex itself (Chen, Brinkmann, et al., 2014; Graziano & Weiner, 2014; Miki et al., 1998; Nakao et al., 2008; Namekata et al., 2010; Oikawa et al., 2004; Sossey-Alaoui et al., 2005; Steffen et al., 2004; Weiner et al., 2006). We propose that Fat2 promotes WAVE complex accumulation within a stable region by acting through one or more of these positive regulators, thereby controlling the site where the WAVE complex excitation threshold is crossed and a protrusion is formed. Under this model, in the absence of Fat2, this site selection instead becomes more stochastic and therefore long-lasting protrusive regions cannot form. If part of the WAVE complex circuit is limiting for protrusion formation, this could also account for Fat2's ability to suppress protrusion formation away from the leading edge. However, there are other possible suppression mechanisms. For example, in neutrophils, protrusions have been shown to increase membrane tension and thereby suppress distant protrusion, enforcing the selection of a single

protrusive region (Houk et al., 2012).

Fat2 acts at the trailing edge of each cell to recruit the WAVE complex in *trans*, so there must be one or more transmembrane proteins at the leading edge of each cell that bridge this interaction. Previous work has shown that the receptor tyrosine phosphatase Lar is part of this bridge—Fat2 recruits Lar to each follicle cell's leading edge (Barlan et al., 2017), and in Lar's absence both WAVE complex levels and cell protrusions are reduced (Barlan et al., 2017; Squarr et al., 2016) (Fig. 2.14G). However, the WAVE complex that persists at the leading edges of *lar* cells still colocalizes with Fat2 (Fig. 2.14A,B). Therefore, there must be at least one other transmembrane protein that works alongside Lar to mediate the Fat2-WAVE complex interaction. Identifying the missing leading edge protein(s) will be important to fully understand how Fat2 shapes WAVE complex activity.

Fat2 is localized in puncta along each cell's trailing edge (Barlan et al., 2017; Viktorinová & Dahmann, 2013), and we show here that these puncta correspond 1:1 with regions of high WAVE complex enrichment just across the leading-trailing cell-cell interface. Fat2's punctate distribution and its levels along cell-cell interfaces are unaffected by loss of the WAVE complex (Barlan et al., 2017), indicating that Fat2 puncta shape the distribution of the WAVE complex and protrusions, not the reverse. We further show that the puncta sit at the tips of filopodia that form within the lamellipodial actin network. Filopodia are a prominent feature of the long-lived protrusive regions that form in wild-type epithelia, but appear to be disproportionately reduced in the short-lived, fluctuating protrusive regions that form in *fat2* epithelia. We therefore propose that by concentrating the WAVE complex and/or stabilizing its distribution, Fat2 also facilitates filopodia formation. It should be noted, however, that the filopodia are dispensable for collective follicle cell migration (Cetera et al., 2014), so the reason these structures form remains to be determined.

Why, and how, is Fat2 localized in puncta? Cadherins commonly form puncta, though the causes and functions of this organization vary (Li et al., 2021; Rubinstein et al., 2017; Truong

Quang et al., 2013). For example, Flamingo (or mammalian Celsr1), an atypical cadherin and central component of the core planar cell polarity pathway, is stabilized by clustering, and this clustering is important for its planar polarization (Cho et al., 2015; Stahley et al., 2021; Strutt et al., 2011). In future work, it will be important to determine how Fat2 assembles in puncta, and whether this local clustering is important for its polarization to trailing edges or its effect on the organization of leading edges. More broadly, it will be critical to determine how Fat2 achieves its trailing edge localization, a necessary step in the polarization of the tissue.

2.6 Methods

Materials, data, and code availability

New plasmids and *Drosophila* lines reported in this paper are available upon request to Sally Horne-Badovinac. The code necessary to reproduce core aspects of data analysis, along with example datasets, are available at $https://github.com/a9w/Fat2_polarizes_WAVE$. Image and movie data are available from https://doi.org/10.6084/m9.figshare.20759314.v1.

Drosophila sources, care, and genetics

The genotypes of animals used in each experiment and associated figure panels are listed in Table 2.1. *Drosophila* were raised at 25°C and fed cornmeal molasses agar food. Females 0-3 days post-eclosion were aged on yeast with males prior to dissection. In most cases, they were aged for 2-3 days at 25°C. Temperatures and yeasting times used for each experiment are reported in Table 2.2. In all RNAi experiments, *traffic jam*>Gal4 (*tj*>Gal4) (Hayashi et al., 2002) was used to drive RNAi expression in follicle cells and not in germ cells. Sra1-GFP and *fat2* mosaic epithelia were generated using the Flp/FRT method (Golic, 1991; Golic & Lindquist, 1989), using FRT82B and FRT80B recombination sites, respectively. In both

cases *tj*>Gal4 was used to drive expression of *UAS*>Flp recombinase.

Generation of Sra1-GFP

Endogenous Sra1 was tagged C-terminally with enhanced GFP (GFP) following the general approaches described in Gratz et al., 2013 and Gratz et al., 2014. The guide RNA target sequence 5'-GCTTAAATGCATCCCTTTCC**GGG**-3' was chosen with flyCRISPR Target Finder (Gratz et al., 2014). The underlined sequence was cloned into the pU6-BbsI-chiRNA plasmid, and the bold sequence is the adjacent PAM motif. For homologous recombination, homology arms approximately 2 kb long flanking the insertion target site were amplified from genomic DNA from the y1 M{nos-Cas9.P}ZH-2A w* (nanos>Cas9) (Port et al., 2014) background. GFP was amplified from the pTWG plasmid. A linker with sequence encoding the amino acids 'GSGGSGGS' was added to the N-terminal side of GFP. Homology arms, linker, and GFP were inserted into donor plasmid pDsRed-attP, which contains 3xP3-DsRed flanked by loxP sites for insertion screening and subsequent removal. The linker-GFP insertion was made immediately before the Sra1 stop codon. Guide and homologous recombination plasmids were injected by Genetivision Inc. into the nanos>Cas9 background. F1 males were screened for 3xP3>DsRed and then 3xP3>DsRed was excised by crossing to Cre-expressing flies (MKRS hsFLP/TM6b Cre).

Egg chamber dissection

All data come from stage 6-7 egg chambers. To obtain these, ovaries were dissected into live imaging media (Schneider's *Drosophila* medium with 15% fetal bovine serum and 200 μg/mL insulin) in a spot plate using 1 set of Dumont #55 forceps and 1 set of Dumont #5 forceps. Ovarioles were removed from the ovary and from ovariole muscle sheathes with forceps. For live imaging, egg chambers older than the egg chamber to be imaged were removed from the ovariole strands by cutting through the stalk with a 27-gauge hypodermic needle. For fixed

imaging, egg chambers older than stage 9 were removed prior to fixation. Removal of older egg chambers allows more compression of the imaged egg chamber between the slide and coverslip so that the basal surface of a field of cells can be imaged in a single plane. For a more detailed description and movies of dissection, see Cetera et al., 2016.

Live imaging sample preparation

Following dissection, ovarioles were transferred to a fresh well of live imaging media. For membrane staining, CellMask Orange or Deep Red plasma membrane stain (Thermo Fisher Scientific, Waltham, MA, 1:500) was added and ovarioles incubated for 15 minutes, followed by a wash in live imaging media to remove excess stain before mounting. Ovarioles were then transferred to a glass slide with 20 μL of live imaging media. For CK-666 treatment, following plasma membrane staining, ovarioles were transferred to live imaging media with 750 μM CK-666 (Millipore Sigma, St. Louis, MO) and then mounted in the same media. Glass beads with diameter 51 μm were added to support the 22x22 mm #1.5 coverslip and limit egg chamber compression. Coverslip edges were sealed with melted petroleum jelly to prevent evaporation while imaging. Samples were checked for damage using the membrane stain or other fluorescent markers as indicators, and excluded if damage was observed. Slides were used for no more than 1 hour.

Immunostaining and F-actin staining

Following dissection, ovarioles were fixed in 4% EM-grade formaldehyde in PBT (phosphate buffered saline + 0.1% Triton X-100) and then washed 3x5 minutes in PBT at room temperature. Egg chambers were incubated with primary antibodies in PBT overnight at 4°C (anti-Scar, 1:200) or for 2 hours at room temperature (anti-Discs Large, 1:20) while rocking. Ovarioles were then washed 3x5 minutes in PBT and incubated in secondary antibody diluted 1:200 in PBT for two hours at room temperature while rocking. F-actin staining was

performed using either TRITC phalloidin (Millipore Sigma, 1:250) or Alexa Fluor 647 phalloidin (Thermo Fisher Scientific, 1:50). If TRITC phalloidin was the only stain or antibody used, it was added directly to the fixation media for 15 minutes of staining concurrent with fixation. Otherwise, TRITC phalloidin was added for 15-30 minutes at room temperature as the final staining step. Alexa Fluor 647 phalloidin staining was performed for two hours at room temperature while the sample was rocking, concurrent with secondary antibody staining where applicable. Ovarioles were then washed 3x5 minutes in PBT and mounted in 40 μL SlowFade Diamond antifade on a slide using a 22x50 mm #1.5 coverslip, sealed with nail polish, and stored at 4°C until imaged.

Microscopy

Laser scanning confocal microscopy

Laser scanning confocal microscopy was used for all fixed imaging and for live imaging of membrane-dyed egg chambers. Imaging was performed with a Zeiss LSM 800 upright laser scanning confocal with a 40x/1.3 NA EC Plan-NEOFLUAR oil immersion objective or a 63x/1.4 NA Plan-APOCHROMAT oil immersion objective, diode lasers (405, 488, 561, and 640 nm), and GaAsP detectors. The system was controlled with Zen 2.3 Blue acquisition software (Zeiss). Imaging was performed at room temperature. All images show the basal surface of stage 6-7 egg chambers except for Fig. 2.8A, bottom row, which shows follicle cells in cross-section. Cross-section images were used for egg chamber staging throughout. Laser scanning confocal microscopy was used to acquire the data in Figs. 2.1D,F; 2.2; 2.3; 2.6; 2.7B-F; 2.10A; 2.12A-C; 2.13A,C-G; 2.4A-C; 2.5A-C,E,F; 2.8; 2.9; 2.11; 2.14A-D,E-G.

TIRF microscopy

Near-TIRF microscopy was used to visualize Fat2-GFP, Sra1-GFP, Abi-mCherry, and F-Tractin-tdTomato (Spracklen et al., 2014) dynamics at the basal surface. Near-TIRF imaging was performed with a Nikon ECLIPSE-Ti inverted microscope with Ti-ND6-PFS Perfect Focus Unit, solid-state 50 mW 481 and 561 nm Sapphire lasers (Coherent technology), motorized TIRF illuminator, laser merge module (Spectral Applied Research), Nikon CFI 100x Apo 1.45 NA oil immersion TIRF objective with 1.5x intermediate magnification, and Andor iXon3 897 electron-multiplying charged-coupled device (EM-CCD) camera. Image acquisition was controlled using MetaMorph software. For two color imaging, frames were collected for each color consecutively with the TIRF illumination angle adjusted in between. Imaging was performed at room temperature. For display, movies were corrected for bleaching using the histogram matching method in Fiji (ImageJ) (Schindelin et al., 2012; Schindelin et al., 2015). TIRF microscopy was used to acquire the data in Figs. 2.10B,D-F; 2.13B; 2.5D; 2.14C.

Cell and protrusion segmentation from timelapses of cell membrane

Protrusions from timelapse datasets of the follicle cell basal surface stained with CellMask Orange (see Live imaging sample preparation) were segmented with the Python scikit-image and scipy libraries (Fig. 2.2)(van der Walt et al., 2014; Virtanen et al., 2020). First, each cell was segmented and tracked, with manual corrections to cell-cell interface placements made using napari (Sofroniew et al., 2022). Next, a watershed-based approach was used to segment the regions of high fluorescence intensity at the interface of each pair of neighboring cells. This segmented shape encompasses the cell-cell interface and any associated protrusions from either neighboring cell. Last, to assign protrusions to the cell from which they originated, the segmented region was divided in two by the shortest path between its bounding vertices that lay entirely within the region. This approximates the position of the interface between

the cells, and in subsequent steps we will call this line "the interface". Each of the two resulting protrusion shapes was assigned as originating from the cell on the opposite side of the interface, because protrusions extend from one cell and overlap the other. Using this approach, all of the protrusive structures that emerge from one cell, and that overlap a single neighboring cell, are grouped together as a single segmented region for subsequent analysis.

Measurement of membrane protrusivity, protrusion length, and protrusion orientation

After cell edges and associated protrusions were segmented, they were categorized as either protrusive or non-protrusive and their lengths and orientations using Python scikit-fmm, scikit-image, and scipy libraries. We use the term "membrane extensions" to refer to the cell edge shapes before the protrusive ones have been identified. To measure the length of a membrane extension, we used two different metrics, each of which provides a single length value per cell edge. In one, we calculated the "average length" of a membrane extension as the membrane extension's area divided by the length of the interface it extended across. As an alternate length measurement, we calculated its "longest length." To do so, we first found its "tip", defined as the pixel within the segmented region farthest from any point along the interface. We then found its "base", the pixel along the interface that was closest to the tip. We defined membrane extension longest length as the length of the shortest path between base and tip that lay entirely within the membrane extension. To categorize membrane extensions as *protrusive* or *non-protrusive* throughout the study, we used the "average length" metric. We measured the average length distribution in CK-666-treated epithelia, which are nearly non-protrusive and so provided a measure of the width of the cell-cell interface alone. For all conditions, we categorized a membrane extension as protrusive if its average length was greater than the 98th percentile of length of CK-666-treated epithelia. We then defined the protrusivity of an entire epithelium as the ratio of protrusive to total cell edges

in the field of view. We also report two alternate measurements of the protrusivity of an epithelium. In one, We calculate epithelial protrusivity as above, but substitute the longest length as our length measurement (Fig. 2.4A). In a second, cutoff-independent epithelial protrusivity measurement, we report the epithelium-mean average membrane extension length (Fig. 2.4B). Swarm plots of each of these analyses were generated using GraphPad Prism 9 (GraphPad, San Diego, CA), as were all other swarm plots.

For analysis of protrusion orientation, we included only the membrane extensions categorized as protrusive according to the "average length" metric. We defined a protrusion's orientation as the orientation of the vector from its base to its tip. Polar histograms, generated in Python with matplotlib (Hunter, 2007), show the distribution of protrusion orientations. In these plots, bar area is proportional to the number of protrusions in the corresponding bin. We note that cells of migratory epithelia often have rearward-pointing retraction fibers as well as protrusions, and our protrusion segmentation method does not distinguish these two types of membrane extensions. For this reason, the degree of protrusion polarity we measure for the migratory control epithelia is likely an underestimate.

Quantification of F-actin and Sra1-GFP cell-cell interface and non-interface basal surface fluorescence

Cells and cell-cell interfaces were segmented as described above. Cells and interfaces in contact with the tissue border or image border were excluded from analysis. For interface fluorescence intensity, interfaces were dilated by 5 pixels, and mean fluorescence intensity calculated from within this region. Non-interface basal surface fluorescence intensity was calculated as the mean of the remaining (non-interface) tissue surface. For F-actin cell-cell interface enrichment measurements, the overall brightness of the phalloidin staining varied between epithelia independent of genotype. To control for this variation we subtracted the mean intensity of the epithelium's non-interface basal surface from its mean interface

intensity measurement. This value, the degree of F-actin interface enrichment, was used as a proxy for F-actin protrusivity.

Quantification of F-actin and Sra1-GFP planar polarity

As a simple planar polarity measurement, we quantified mean F-actin (phalloidin) or Sra1-GFP fluorescence intensity along each cell-cell interface as a function of the interface's orientation with respect to the anterior-posterior axis. To do this, cells and cell-cell interfaces were segmented as described above. For interface angle measurements, the angular distance between the line defined by the interface-bounding vertices and the anterior-posterior (horizontal) axis was calculated. For interface fluorescence intensity measurements, interface regions were identified as segmented interfaces dilated by 5 pixels. Vertices, dilated by 10 pixels, were excluded from interface regions. Mean fluorescence intensity was calculated within each interface region, and background (the mean non-interface basal surface fluorescence intensity of all cells in the image) was subtracted. Polar bar plots, generated in Python with matplotlib, show the mean interface intensity as a function of interface angle. In these plots, bar area is proportional to intensity, and Control and *fat2* datasets are rescaled separately so that each have a mean value of one. As a summary statistic for the degree of planar polarization of F-actin or Sra1-GFP in each egg chamber, we found the average fluorescence intensities of interfaces with angles between 0°and 10°and between 80°and 90°. These correspond with leading-trailing and side interfaces, respectively, in migratory epithelia. The *leading-trailing interface enrichment* is the ratio of these numbers.

Autonomy analysis in mosaic epithelia

Egg chambers were stained with Alexa Fluor 647 phalloidin to mark protrusions, which indicate migration direction, and to determine whether egg chambers were planar polarized. We analyzed only S6-7 egg chambers with mixtures of control and *fat2* cells that had global

stress fiber alignment orthogonal to the anterior-posterior axis, indicating global planar polarity. Since migration is required to maintain planar polarity (Cetera et al., 2014), this also indicates that the epithelium was migratory. We then measured the Sra1-GFP fluorescence intensity at leading-trailing interfaces and medial basal surfaces to determine whether changes in Sra1-GFP levels coincided with the genotype of the Sra1-containing cell, or the genotype of the cell ahead. To select leading-trailing interface regions to measure, we drew 10 pixel-wide segmented lines along leading edges of individual cells, assigning them to a condition based on their own genotype and the genotype of the cell just ahead. If a cell had both control and *fat2* cells ahead of it, we measured those leading edge segments separately, assigning each to the applicable condition. Lines were drawn along all visible, in-focus *fat2*-control and control-*fat2* boundaries and a similar number of control-control and *fat2*-*fat2* boundaries. Epithelia were excluded if two or more interfaces of each of the four genotype combinations were not present. From these regions, we measured mean Sra1-GFP fluorescence intensity for each cell, and then took the mean of these as the fluorescence intensity per egg chamber. For a diagram of this method, see Barlan et al., 2017, which we have modified here to allow measurement of individual cells. To quantify medial basal surface Sra1-GFP fluorescence intensity, we used the same approach with the following exceptions: we measured polygonal regions of the basal surface of individual cells away from cell-cell interfaces, and cells were excluded if their leading edge contacted both control and *fat2* cells.

Quantification of migration rate

Egg chambers were dissected, dyed with CellMask Orange, and mounted for live imaging as described above. Several ovarioles were mounted on each slide, with each ovariole terminating in a S6-7 egg chamber. Timelapse imaging was performed for 30 minutes with frames acquired every 30 seconds. Multi-point acquisition was used to obtain movies of up to 5 egg chambers simultaneously. To generate a kymograph, a line was drawn along the axis of migration at

the center of the anterior-posterior egg chamber axis in Fiji. In these kymographs, cell-cell interfaces are visible as lines, and their slope gives a measurement of cell migration rate. Egg chamber migration rates were calculated from the average of 4 cell interface slopes from each kymograph. Egg chambers that clearly slowed down over the course of the timelapse, visible as curvature in the interface lines in the kymographs, were excluded. For an illustration of this method, see Barlan et al., 2017.

Cell perimeter kymograph generation and interpretation

To visualize the distribution of Sra1-GFP along cell-cell interfaces over time, we generated kymographs of cell perimeters from timelapses of Sra1-GFP-expressing epithelia obtained using near-TIRF microscopy. Perimeters were drawn manually in Fiji in each frame with the pencil tool, and then these perimeters were used to generate kymographs in Python. Perimeters were thinned to 1 pixel and then perimeter pixels were sequenced with Python scikit-image and scipy libraries. Kymographs were generated with matplotlib. Kymograph rows were constructed by linearizing the perimeters from each frame, starting with the pixel directly above the cell centroid (the center of the trailing edge in control cells) and continuing counter-clockwise. Each row shows the fluorescence intensity of the perimeter pixels in sequence. Cell perimeter lengths varied between frames, so kymograph row lengths varied and were aligned to their center position.

At the spatial and temporal resolution of the timelapses and corresponding kymographs, we cannot evaluate differences in the dynamics the puncta-scale WAVE complex accumulations highlighted in Fig. 2.13. Instead, we focus on the "region"-scale distribution of Sra1-GFP, and the stability of that distribution over time. The regions we refer to here are approximately the length of a cell-cell interface, with variation. Because the kymographs are generated from epithelia in which all cells express Sra1-GFP, we need additional information to identify the cell to which a region of Sra1-GFP enrichment belongs. We infer that

Sra1-GFP is predominantly at leading edges in polarized, migratory epithelia based on the Sra1-GFP distribution in epithelia with mosaic Sra1-GFP expression (Fig. 2.7B). Based on consistent correlation between Sra1-GFP enrichment and the presence of protrusions (Figs. 2.10A, 2.11), and its known role building lamellipodia as part of the WAVE complex (Miki et al., 1998; Miki et al., 2000; Steffen et al., 2004), we also infer that regions of Sra1-GFP enrichment belong to the cell that is protruding outward regardless of genotype. Our interpretations of Sra1-GFP enrichment patterns in movies and corresponding kymographs are made with these assumptions.

Quantification of the stability of interface protrusion polarity

As a measurement of the stability of protrusive regions over time, we quantified the frequency with which the direction of protrusion switched across a cell-cell interface. These switching events occur when one cell and then its neighbor protrude across their shared interface, and they serve as a score-able indicator of a change in the polarity state of the cells that bound the interface. To determine the switching frequency, we counted the number of switching events that occurred in each timelapse, and then determined an interface protrusion polarity switching rate by dividing the number of switches by the number of interfaces identified with cell and protrusion segmentation. We chose a hand-counting method because the protrusion segmentation error rate from the inclusion of retraction fibers and other sources (see Measurement of membrane protrusivity, protrusion length, and protrusion orientation) was sufficiently high that automated measurement of dynamic features of protrusions was unreliable.

Colocalization of proteins along the leading-trailing interface

Data used for colocalization analysis were collected with 63x/1.4 NA Plan-APOCHROMAT oil immersion objective to minimize chromatic aberration. Linescans were generated in Fiji

by manually drawing a 10 pixel-wide segmented line along rows of leading-trailing interfaces at the follicle cell basal surface. At least 20 leading-trailing interfaces were included per egg chamber. For the Fat2$^{\Delta ICD}$ condition, in which the distribution of Fat2 expands beyond leading-trailing interfaces, we measured colocalization either along randomly oriented interfaces (Fig. 2.13E) or leading-trailing interfaces (Fig. 2.14B) and obtained very similar results. Fluorescence intensities along the linescans were obtained with the PlotProfile function, which averages pixel intensities along the width of the line and reports a list of averaged values along the line's length. Spearman's correlation coefficients were calculated for each egg chamber in Python with the scipy.stats module. Failure to exactly follow leading-trailing interfaces and cusps in the segmented lines will artificially inflate the measured correlation, so we used correlation between E-cadherin-GFP (Huang et al., 2009) and Abi-mCherry as a negative control that is also subject to this inflation. Abi-mCherry and E-cadherin-GFP are slightly displaced from each other (anticorrelated) along the length of protrusions (the width of the linescans), but averaging across the line width collapses this displacement, resulting in measured intensity signals that are roughly uncorrelated. Spearman's correlation coefficients $\pm$ standard deviation are reported in the text. Linescans of leading-trailing interfaces were plotted using the fluorescence intensities from along the leading-trailing interfaces of two cells. Intensities from each fluorophore were rescaled between 0 and 1 and plotted with matplotlib in Python.

Protrusion profile generation

Viewing only the F-actin channel in Fiji, we drew 1 pixel-wide lines down the length of F-actin bundles at the leading edge. Fluorescence intensities along these lines were obtained for all fluorophores with the Fiji PlotProfile function. In Python, these traces were aligned to the pixel with highest Fat2-3xGFP or Ena-GFP intensity (Fig. 2.13G, 2.14F). To calculate standard deviation, all traces were first rescaled individually so that their values ranged

between 0 and 1. To plot "protrusion profiles," the mean fluorescence was determined for each fluorophore at each pixel position, and then average values were rescaled between 0 and 1. Plots of protrusion profiles were generated with matplotlib.

Reproducibility and statistical analysis

Visibly damaged egg chambers were excluded from all analyses. At least two biological replicates were performed for each experiment, and results confirmed to be qualitatively consistent. Each biological replicate included egg chambers pooled from multiple flies. Experiments and analysis were not randomized or performed blinded. Sample sizes were not predetermined using a statistical method. The number of biological replicates (n), statistical tests performed, and their significance can be found in figures or figure legends. Based on visual inspection, all data on which statistical tests were performed followed an approximately normal distribution, so tests assuming normalcy were used. Alpha was set to 0.05 for all statistical tests. Paired statistical tests were used for comparisons of cells of different genetic conditions within mosaic epithelia. All t-tests were two-tailed. One-sample t-tests were used when comparing a distribution of ratios to a null expectation of one. A one-way ANOVA was used when more than two conditions were compared. Welch's corrections were performed for the t-tests or ANOVAs of data plotted in Figs. 2.3C, 2.12C, 2.4A,B, and 2.5C, for which the variance did not appear consistent between conditions. For post-hoc comparison tests, all pairs of conditions present in the corresponding plot were compared using post-hoc Tukey's multiple comparisons test with the following exceptions: the data plotted in Figs. 2.13E and 2.14B were analyzed together, and all conditions were compared to Fat2-Abi and E-cadherin-Abi only, and in Fig. 2.9C only data from the same region (total, interface, or non-interface) were compared. For these, Šidák's multiple comparisons tests were used. For Welch's ANOVA, Dunnet's T3 multiple comparisons tests were used. P-values reported for all post-hoc tests were adjusted for multiple comparisons. All statistical tests except for the

calculation of Spearman's correlation coefficients were performed in GraphPad Prism 9.

Table 2.1: Experimental genotypes for Chapter 2

Figure	Panel	Name	Genotype
2.1	D	F-actin + Ena + Abi	*w*; ubi>GFP-Ena$^{\text{BDSC:28798}}$/ubi>Abi-mCherry$^{\text{BDSC:58729}}$
2.1	F	Control	*w*; tj>Gal4$^{\text{DGRC:104055}}$/+
2.1	F	*ena*-RNAi	*w*; tj>Gal4$^{\text{DGRC:104055}}$/UAS-*ena*-RNAi$^{\text{VDRC:43058}}$
2.1	F	*abi*-RNAi	*w*; tj>Gal4$^{\text{DGRC:104055}}$/+; UAS-*abi*-RNAi$^{\text{NIG:9749R-3}}$
2.2	Top row	Protrusion in 1 direction	w^{1118}
2.2	Bottom row	Protrusion in both directions	*w*; $fat2^{N103\text{-}2}$ FRT80B
2.3	A-C	Control	w^{1118}
2.3	A-C	*fat2*	*w*; $fat2^{N103\text{-}2}$ FRT80B
2.3	A-C	CK-666	w^{1118}
2.3	D	Control	w^{1118}
2.3	D	*fat2*	*w*; $fat2^{N103\text{-}2}$ FRT80B
2.4	A	Control	w^{1118}
2.4	A	*fat2*	*w*;; $fat2^{N103\text{-}2}$ FRT80B
2.4	A	CK-666	w^{1118}
2.4	B	Control	w^{1118}
2.4	B	*fat2*	*w*;; $fat2^{N103\text{-}2}$ FRT80B
2.5	A-C	Control	*w*; tj>Gal4$^{\text{DGRC:104055}}$/+
2.5	A-C	*fat2*	*w*; tj>Gal4$^{\text{DGRC:104055}}$/+; $fat2^{N103\text{-}2}$ FRT80B
2.5	A-C	*abi*-RNAi	*w*; tj>Gal4$^{\text{DGRC:104055}}$/+ UAS-*abi*-RNAi$^{\text{NIG:9749R-3}}$/+
2.5	D	Control	*w*; tj>Gal4DGRC:104055/UAS>F-Tractin-tdTomato$^{\text{BDSC:58989}}$
2.5	D	*fat2*	*w*; tj>Gal4$^{\text{DGRC:104055}}$/UAS>F-Tractin-tdTomato$^{\text{BDSC:58989}}$; $fat2^{N103\text{-}2}$ FRT80B
2.5	D	*abi*-RNAi	*w*; tj>Gal4$^{\text{DGRC:104055}}$/UAS>F-Tractin-tdTomato$^{\text{BDSC:58989}}$; UAS-*abi*-RNAi$^{\text{NIG:9749R-3}}$/+
2.5	E,F	Control	w^{1118}
2.5	E,F	*fat2*	*w*;; $fat2^{N103\text{-}2}$ FRT80B

Table 2.1: Experimental genotypes for Chapter 2 (continued)

2.6	A,B	*fat2* mosaic	*w*; tj>Gal4$^{\text{DGRC:104055}}$, UAS>Flp$^{\text{BDSC:4539}}$/+; *fat2*$^{N103\text{-}2}$ FRT80B/ubi>GFP-NLS FRT80B$^{\text{BDSC1620}}$
2.7	B	Sra1-GFP mosaic	*w*; tj>Gal4$^{\text{DGRC:104055}}$, UAS>Flp$^{\text{BDSC:4539}}$/+; FRT82B Sra1-GFP/FRT82B ubi>mRFP-NLS$^{\text{BDSC:30555}}$
2.7	C	*fat2* mosaic	*w*; tj>Gal4$^{\text{DGRC:104055}}$, UAS>Flp$^{\text{BDSC:4539}}$/+; *fat2*$^{N103\text{-}2}$ FRT80B/ubi>GFP-NLS FRT80B$^{\text{BDSC1620}}$
2.7	D-F	Sra1-GFP mosaic	*w*; tj>Gal4$^{\text{DGRC:104055}}$, UAS>Flp$^{\text{BDSC:4539}}$/+; *fat2*$^{N103\text{-}2}$ FRT80B Sra1-GFP/ubi>mRFP-NLS FRT80$^{\text{BDSC:30852}}$
2.8	A	Sra1-GFP	*w*;; Sra1-GFP
2.8	A	anti-SCAR	*w*;; Sra1-GFP
2.8	A	ubi>Abi-mCherry	*w*;; ubi>Abi-mCherry$^{\text{BDSC:58729}}$/+
2.8	B	Control	*w*; tj>Gal4$^{\text{DGRC:104055}}$/+
2.8	B	*abi*-RNAi	tj>Gal4$^{\text{DGRC:104055}}$/+; UAS-*abi*-RNAi$^{\text{NIG:9749R-3}}$/+
2.8	C	Control	*w*^{1118}
2.8	C	Sra1-GFP x1	*w*;; Sra1-GFP/+
2.8	C	Sra1-GFP x2	*w*;; Sra1-GFP
2.8	C	*sra1*-RNAi	*w*; tj>Gal4$^{\text{DGRC:104055}}$/+; UAS>sra1-RNAi$^{\text{BDSC:38294}}$/+
2.8	D	Control	*w*^{1118}
2.8	D	Sra1-GFP x1	*w*;; Sra1-GFP/+
2.8	D	Sra1-GFP x2	*w*;; Sra1-GFP
2.9	A, C-E	Control	*w*;; Sra1-GFP/+
2.9	A, C-E	*fat2*	*w*;; *fat2*$^{N103\text{-}2}$ FRT80B Sra1-GFP/*fat2*$^{N103\text{-}2}$ FRT80B
2.10	A	Sra1-GFP mosaic + *fat2*	*w*; tj>Gal4$^{\text{DGRC:104055}}$, UAS>Flp$^{\text{BDSC:4539}}$/+; *fat2*$^{N103\text{-}2}$ FRT80B Sra1-GFP/*fat2*$^{N103\text{-}2}$ FRT80B FRT82B
2.10	B,D	Control	*w*;; Sra1-GFP/+
2.10	B,D	*fat2*	*w*;; *fat2*$^{N103\text{-}2}$ FRT80B Sra1-GFP/*fat2*$^{N103\text{-}2}$ FRT80B

Table 2.1: Experimental genotypes for Chapter 2 (continued)

2.10	E,F	*fat2* mosaic + Sra1	*w*; tj>Gal4$^{\text{DGRC:104055}}$, UAS>Flp$^{\text{BDSC:4539}}$/+; *fat2*$^{N103\text{-}2}$ FRT80B Sra1-GFP/ubi>mRFP-NLS FRT80$^{\text{BDSC:30852}}$
2.11		Control	*w*;; Sra1-GFP/+
2.11		*fat2*	*w*;; *fat2*$^{N103\text{-}2}$ FRT80B Sra1-GFP/*fat2*$^{N103\text{-}2}$ FRT80B
2.12	A,C	Control	*w*^{1118}
2.12	A,C	*fat2*	*w*;; *fat2*$^{N103\text{-}2}$ FRT80B
2.12	B	Example of switch	*w*;; *fat2*$^{N103\text{-}2}$ FRT80B
2.13	A,E	Fat2 + Abi	*w*;; ubi>Abi-mCherry$^{\text{BDSC:58729}}$, Fat2-3xGFP FRT80B/Fat2-3xGFP FRT80B
2.13	A,E	Fat2$^{\Delta\text{ICD}}$ + Abi	*w*;; ubi>Abi-mCherry$^{\text{BDSC:58729}}$, Fat2$^{\Delta\text{ICD}}$-3xGFP FRT80B/Fat2$^{\Delta\text{ICD}}$-3xGFP FRT80B
2.13	B	Fat2 + Abi	*w*;; ubi>Abi-mCherry$^{\text{BDSC:58729}}$, Fat2-3xGFP FRT80B/Fat2-3xGFP FRT80B
2.13	C,D,F,G	Fat2 + Abi + F-actin	*w*;; ubi>Abi-mCherry$^{\text{BDSC:58729}}$, Fat2-3xGFP FRT80B/Fat2-3xGFP FRT80B
2.14	A,B	Control Fat2 + Abi	*w*;; ubi>Abi-mCherry$^{\text{BDSC:58729}}$, Fat2-3xGFP FRT80B/Fat2-3xGFP FRT80B
2.14	A,B	Fat2$^{\Delta\text{ICD}}$ + Abi	*w*;; ubi>Abi-mCherry$^{\text{BDSC:58729}}$, Fat2$^{\Delta\text{ICD}}$-3xGFP FRT80B/Fat2$^{\Delta\text{ICD}}$-3xGFP FRT80B
2.14	A,B	*ena*-RNAi, Fat2 + Abi	*w*; tj>Gal4$^{\text{DGRC:104055}}$/UAS>ena-RNAi$^{\text{VDRC:43058}}$; ubi>Abi-mCherry$^{\text{BDSC:58729}}$, Fat2-3xGFP FRT80B/Fat2-3xGFP FRT80B
2.14	A,B	Control Fat2 + Abi	*w*; lar^{bola1} $^{\text{BDSC:91654}}$/lar$^{13.2}$ $^{\text{BDSC8774}}$ FRT40A; ubi>Abi-mCherry$^{\text{BDSC:58729}}$, Fat2-3xGFP FRT80B/Fat2-3xGFP FRT80B
2.14	C	Fat2 + Abi	*w*;; ubi>Abi-mCherry$^{\text{BDSC:58729}}$, Fat2-3xGFP FRT80B/Fat2-3xGFP FRT80B

Table 2.1: Experimental genotypes for Chapter 2 (continued)

2.14	D-F	Ena + Abi + F-actin	*w*; ubi>GFP-Ena$^{\text{BDSC:28798}}$/ubi>Abi-mCherry$^{\text{BDSC:58729}}$
2.14	G	Control	*w*;; ubi>Abi-mCherry$^{\text{BDSC:58729}}$, Fat2-3xGFP FRT80B/Fat2-3xGFP FRT80B
2.14	G	*lar*	*w*; lar^{bola1} $^{\text{BDSC:91654}}$/lar$^{13.2}$ $^{\text{BDSC8774}}$ FRT40A; ubi>Abi-mCherry$^{\text{BDSC:58729}}$, Fat2-3xGFP FRT80B/Fat2-3xGFP FRT80B

Table 2.2: *Drosophila* culture conditions for Chapter 2

Figure	Panel	Days on yeast	Temp. (°C)
2.1	D	2-3	25
2.1	F	3	29
2.2		2-3	25
2.3	A-D	2-3	25
2.4	A-C	2-3	25
2.5	A-C,E,F	2-3	29
2.5	D	2-3	29
2.6	A,B	2-3	25
2.7	B	7	25
2.7	C	3	25
2.7	D-F	3	25
2.8	A	2-3	25
2.8	B	3	29
2.8	C	3	29
2.8	D	2-3	25
2.9	A-E	2-3	25
2.10	A	5	25
2.10	B,D	2-3	25
2.10	E	2-3	25
2.12	A-C	2-3	25
2.11		2-3	25
2.13	A,E	2-3	25
2.13	B	2-3	25
2.13	C,D,F,G	2-3	25
2.14	A,B,F	3	29
2.14	C	2-3	25
2.14	D-F	2-3	25

CHAPTER 3

FAT2 POLARIZES LAR AND SEMA5C TO COORDINATE THE MOTILITY OF COLLECTIVELY MIGRATING EPITHELIAL CELLS

3.1 Preface

This chapter primarily includes work made available as a preprint with the following citation:

Williams, A. M., & Horne-Badovinac, S. (2023). Fat2 polarizes Lar and Sema5c to coordinate the motility of collectively migrating epithelial cells. https://doi.org/10.1101/2023.02.28.530349

There are minor changes to the figures and text relative to the preprint, and several figures have been added here for which this was the most fitting home (Figs. 3.2, 3.8, 3.9, A.2).

3.2 Abstract

Migrating epithelial cells globally align their migration machinery to achieve tissue-level movement. Biochemical signaling across leading-trailing cell-cell interfaces can promote this alignment by partitioning migratory behaviors like protrusion and retraction to opposite sides of the interface. However, how the necessary signaling proteins become organized at this site is poorly understood. The follicular epithelial cells of *Drosophila melanogaster* have two signaling modules at their leading-trailing interfaces—one composed of the atypical cadherin Fat2 and the receptor tyrosine phosphatase Lar, and one composed of Semaphorin 5c and its receptor Plexin A. Here we show that these modules form one interface signaling system with Fat2 at its core. Trailing edge-enriched Fat2 concentrates both Lar and Semaphorin 5c at cells' leading edges, likely by slowing their local turnover. Once localized, Lar and

Semaphorin 5c act in parallel to promote collective migration. Our data suggest a model in which Fat2 couples and polarizes the distributions of multiple effectors that work together to align the migration machinery of neighboring cells.

3.3 Introduction

Epithelial cells migrate collectively during animal development, wound healing, intestinal turnover, and cancer metastasis (Friedl & Gilmour, 2009; Krndija et al., 2019; Rørth, 2012; Shaw & Martin, 2016; Theveneau & Mayor, 2013). To do so, they must polarize within the epithelial plane at both the individual and tissue scales. At the individual scale, cells polarize along a leading-trailing axis. Protrusion and adhesion formation are biased to cells' leading edges, and contractility and adhesion removal to their trailing edges, much as in cells migrating solo (Sherrard et al., 2021; Soans et al., 2022; Stock & Pauli, 2021). At the tissue scale, cells throughout the epithelium are polarized such that their leading edges preferentially point in the direction of migration, and trailing edges in the opposite direction, a form of planar cell polarity. At the intersection of these scales are the cell-cell interfaces that link the trailing edge of one cell to the leading edge of the cell behind. These leading-trailing interfaces can act as sites of biochemical or mechano-chemical signaling that polarize motility behaviors across the interface (Gupta & Yap, 2021; Jain et al., 2020; Roberto & Emery, 2022; Venhuizen & Zegers, 2017) However, we know little about how the necessary signaling proteins become organized along these interfaces.

The rotational migration of the follicle cells in *Drosophila melanogaster* has proven to be a fruitful system for identifying signaling mechanisms that coordinate epithelial cell movements. Follicle cells are somatic cells of the egg chamber, the multicellular structure within the ovary that gives rise to an egg. They form a continuous monolayer epithelium around a central cluster of germ cells, and they are surrounded in turn by a basement membrane extracellular matrix that encapsulates the entire egg chamber. The follicle cells' apical

surfaces adhere to the germ cells, and their basal surfaces adhere to and crawl along the basement membrane (Haigo & Bilder, 2011). Migration in this topologically-closed configuration causes the entire egg chamber to rotate within the stationary basement membrane. This motion changes the basement membrane's structure, ultimately helping give the egg its elongated shape (Crest et al., 2017; Gutzeit et al., 1991; Haigo & Bilder, 2011; Isabella & Horne-Badovinac, 2016). Follicle cell migration requires WAVE complex-dependent lamellipodia, which are polarized to the leading edge of each cell and planar-polarized across the epithelium (Cetera et al., 2014; Gutzeit et al., 1991) (Fig. 3.1A,B). Polarity emerges tissue-autonomously, without input from extrinsic directional cues. This simplifying feature allows us to more easily isolate the contribution of within-group coordination to collective migration. It likely also makes these cells particularly reliant on such coordination for movement.

Two biochemical signaling modules operate at leading-trailing interfaces, where they coordinate the migratory behaviors of neighboring follicle cells. The first module is composed of the atypical cadherin Fat2 and the receptor tyrosine phosphatase Leukocyte-antigen-related-like (Lar). Fat2 is enriched along the trailing edge of each cell, where it acts in trans to concentrate Lar and the WAVE complex across the cell-cell interface, at the leading edge of the cell behind (Barlan et al., 2017; Viktorinová & Dahmann, 2013; Williams et al., 2022) (Fig. 3.1C,D). Lar also contributes to WAVE complex localization, but not as strongly as Fat2, implying the existence of additional unidentified Fat2 effectors (Barlan et al., 2017; Squarr et al., 2016). Together, these proteins restrict cell protrusive activity to a single leading edge domain and orient all the cells' protrusions in a uniform direction across the tissue (Williams et al., 2022). The second module is composed of a transmembrane semaphorin (ligand) and plexin (receptor) pair, Semaphorin 5c (Sema5c) and Plexin A (PlexA), which are enriched at leading and trailing edges respectively (Stedden et al., 2019) (Fig. 3.1C,D). In other contexts, semaphorin-plexin signaling can lower integrin-based adhesion and/or inhibit protrusivity on the plexin-containing cell side (Alto & Terman, 2017; Hung & Terman,

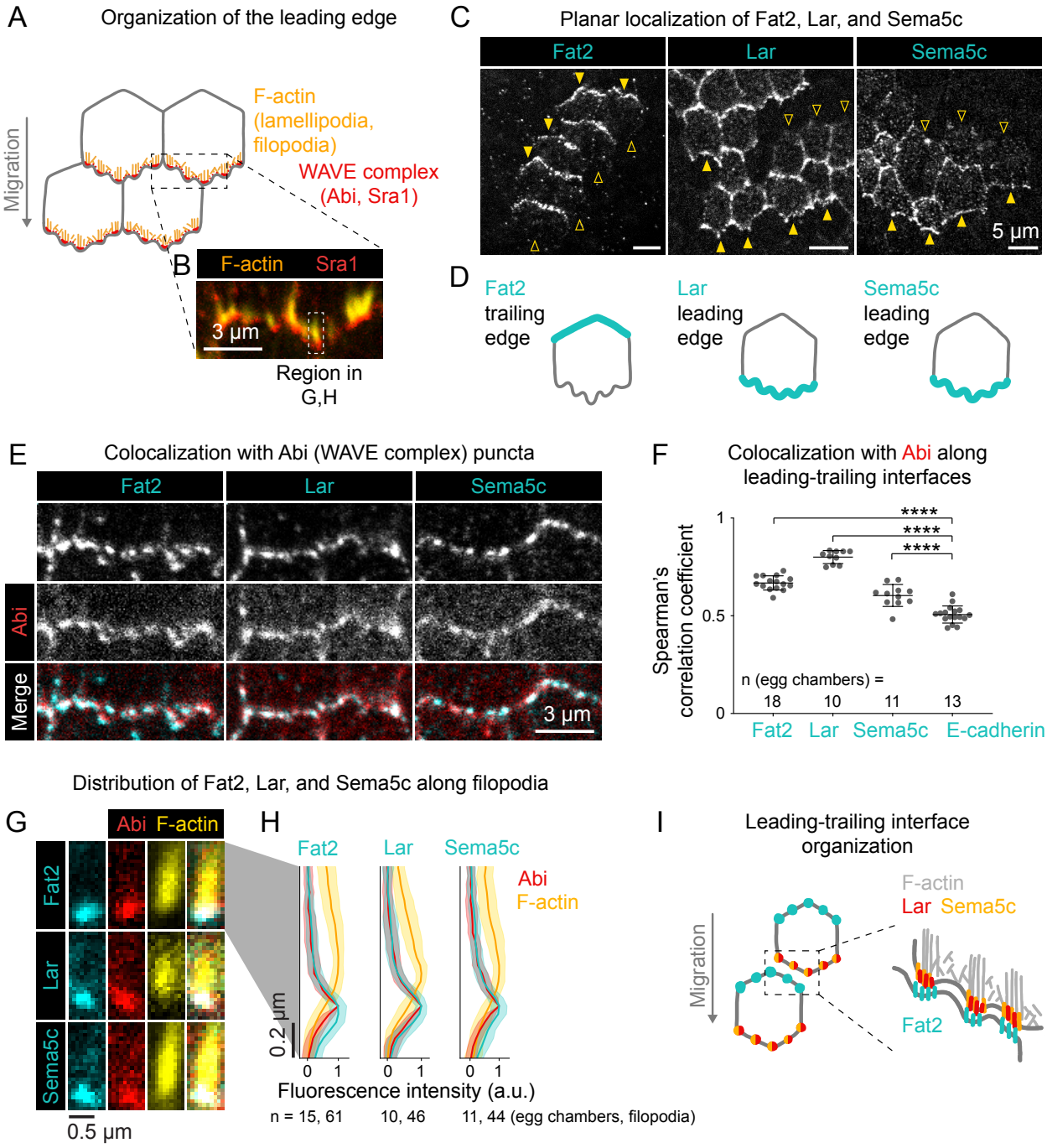

Figure 3.1: **Introduction to the organization of Fat2, Lar, and Sema5c at the follicle cell basal surface.** Continued on next page.

Figure 3.1: **Introduction to the organization of Fat2, Lar, and Sema5c at the follicle cell basal surface (continued).** **A**, Diagram of protrusion organization at the basal surface of four follicle cells. The WAVE complex (including subunits Abi and Sra1, labeled in this study) is enriched at the tips of filopodia and lamellipodia along the leading edge of each cell. **B**, Image of the leading edge of one cell with Sra1 (Sra1-GFP) and F-actin (phalloidin) labeled. Filopodia, including a boxed example, are the most prominent F-actin structures. **C**, Images of the basal surfaces of epithelia with mosaic expression of Fat2-3xGFP, Lar-3xGFP, or Sema5c-3xGFP, showing the cell side to which each is polarized. Arrows point to leading-trailing interfaces at the boundary between 3xGFP-labeled and unlabeled cells. Arrows are filled where the labeled protein is enriched and hollow elsewhere. **D**, Diagrams of Fat2, Lar, and Sema5c localization at the basal surface, as shown in (C). Fat2 is polarized to the trailing edge; Lar and Sema5c to the leading edge. **E**, Images of leading-trailing interfaces labeled with Abi-mCherry and Fat2-3xGFP, Lar-3xGFP, or Sema5c-3xGFP. **F**, Plot of colocalization (Spearman's correlation coefficient) between Abi-mCherry and Fat2-3xGFP, Lar-3xGFP, Sema5c-3xGFP, or E-cadherin-GFP along leading-trailing interfaces. Fat2, Lar, and Sema5c all colocalize with Abi more strongly than do Abi and E-cadherin. One-way ANOVA ($F(3,49)=104.0$, $p<0.0001$ with post-hoc Tukey's test; ****$p<0.0001$. **G,H**, Images and plots showing distributions of Fat2-3xGFP, Lar-3xGFP, and Sema5c-3xGFP along the length of filopodia. All three proteins are enriched along with Abi-mCherry at filopodia tips. **I**, Diagram showing the organization of a leading-trailing interface. Fat2, Lar, and Sema5c molecules reside together in puncta that span leading and trailing edges, with Fat2 enriched at the trailing edge and Lar and Sema5c at the leading edge.

2011; Verhagen & Pasterkamp, 2020). Similarly, overexpression of Sema5c in one follicle cell reduces the protrusivity of its neighbors in a PlexA-dependent manner (Stedden et al., 2019). This led to the model that Sema5c signals through PlexA to maintain a non-protrusive state at cells' trailing edges.

Despite their distinct depletion and overexpression phenotypes, several lines of evidence suggest that the Fat2-Lar and Sema5c-PlexA modules function within one interface-polarizing signaling system. A series of pairwise comparisons show that Fat2, Lar, and Sema5c all colocalize with the WAVE complex in interface-spanning puncta that sit at the tips of filopodia within a broader lamellipodium (Barlan et al., 2017; Squarr et al., 2016; Stedden et al., 2019; Williams et al., 2022) (Fig. 3.1E-I). For reasons that are not yet clear, PlexA only rarely colocalizes with the other proteins (Stedden et al., 2019). Loss of Lar also reduces

Sema5c's enrichment at leading edges, implying functional interaction between the two modules in addition to their shared spatial organization (Stedden et al., 2019). In this study, we investigated the hierarchy of interactions between Fat2, Lar, and Sema5c by which they form interface-spanning puncta, and asked how the three proteins work together to promote collective migration.

We found that Fat2 forms the core of both the Lar- and Sema5c-containing signaling modules. Trailing edge-enriched Fat2 concentrates both Lar and Sema5c at leading edges in trans and is continuously required for them to maintain this localization. Fat2 performs this function, at least in part, by slowing Lar's and likely Sema5c's turnover from the leading edge. We further found that Lar and Sema5c act in parallel to promote collective migration. From these data, we propose that Fat2 acts as a central organizer of follicle cells' interface-polarizing signaling system, serving to couple and polarize the distributions of multiple effectors that together align the motility machinery of neighboring cells.

3.4 Results

Fat2 maintains both Lar and Sema5c's enrichment at leading edges

Fat2, Lar, and Sema5c all colocalize in interface-spanning puncta along leading-trailing interfaces along the basal surface, with Fat2 at trailing edges and Lar and Sema5c at leading edges (Barlan et al., 2017; Stedden et al., 2019; Viktorinová & Dahmann, 2013). They also all localize in puncta at tricellular junctions away from the basal surface (Barlan et al., 2017; Stedden et al., 2019; Viktorinová & Dahmann, 2013). These puncta exhibit similar spatial organization to the basal surface ones, as these also sit at the tips of filopodia and have polarized compositions with Fat2 enriched at the trailing edges side (Fig. 3.2). At the basal surface, Fat2 acts in trans to concentrate Lar at leading edges (Barlan et al., 2017), a result we confirmed in this study using a new endogenous 3xGFP tag on Lar (Fig. 3.3).

To ask if Fat2 has the same effect on Sema5c, we generated epithelia with mosaic expression of *fat2*-RNAi and measured Sema5c-3xGFP levels along leading-trailing interfaces. Sema5c levels were reduced wherever a *fat2*-RNAi cell was present ahead of the interface, regardless of the genotype of the cell behind the interface (Fig. 3.4C,D), again indicating a local trans interaction. Since Lar also contributes to Sema5c's enrichment at leading edges (Stedden et al., 2019), we asked if Fat2 localizes Sema5c indirectly through Lar. We confirmed that Sema5c levels were indeed reduced at leading-trailing interfaces between control cells and cells with a null *lar* allele ($lar^{13.2}$, Fig. 3.4E,F). However, this reduction was not as great as at interfaces between *fat2*-RNAi cells (Fig. 3.4G). We conclude that Fat2 acts in trans to concentrate Sema5c at leading edges at least partly independently of Lar (Fig. 3.4H).

We next asked whether Fat2 is continuously required for Lar and Sema5c's enrichment at leading edges, or whether it becomes dispensable after interface polarity is established. Because calcium ions are integral to the structure of cadherin extracellular domains (Kim et al., 2011; Nagar et al., 1996; Tsukasaki et al., 2014), calcium removal should disrupt any Fat2 function that depends directly or indirectly on its extracellular domain. Treating egg chambers with the cell-impermeable calcium chelator ethylene glycol-O,O′-bis(2-aminoethyl)-N,N,N′,N′-tetraacetic acid (EGTA, 20 mM) for five minutes reduced the levels of protrusion-associated F-actin (Fig. 3.5A), consistent with loss of Fat2 function (Barlan et al., 2017; Squarr et al., 2016) (compare to Figs. 3.4A, 3.3D). It did not, however, cause other obvious changes to cell morphology, and protrusions returned within one hour after EGTA washout (Fig. 3.5A), suggesting that this method rapidly and reversibly inhibits Fat2 without generally disrupting tissue architecture. Notably, the five minute EGTA treatment substantially reduced Lar and Sema5c levels along leading-trailing interfaces (Lar fluorescence intensity by 50%, Sema5c by 25%, Fig. 3.5B,C). Fat2 levels were nearly unchanged after five minutes, but its distribution became even more punctate, and by 30 minutes of EGTA treatment its levels had substantially decreased (Fig. 3.5B-D). Thus, Fat2 is contin-

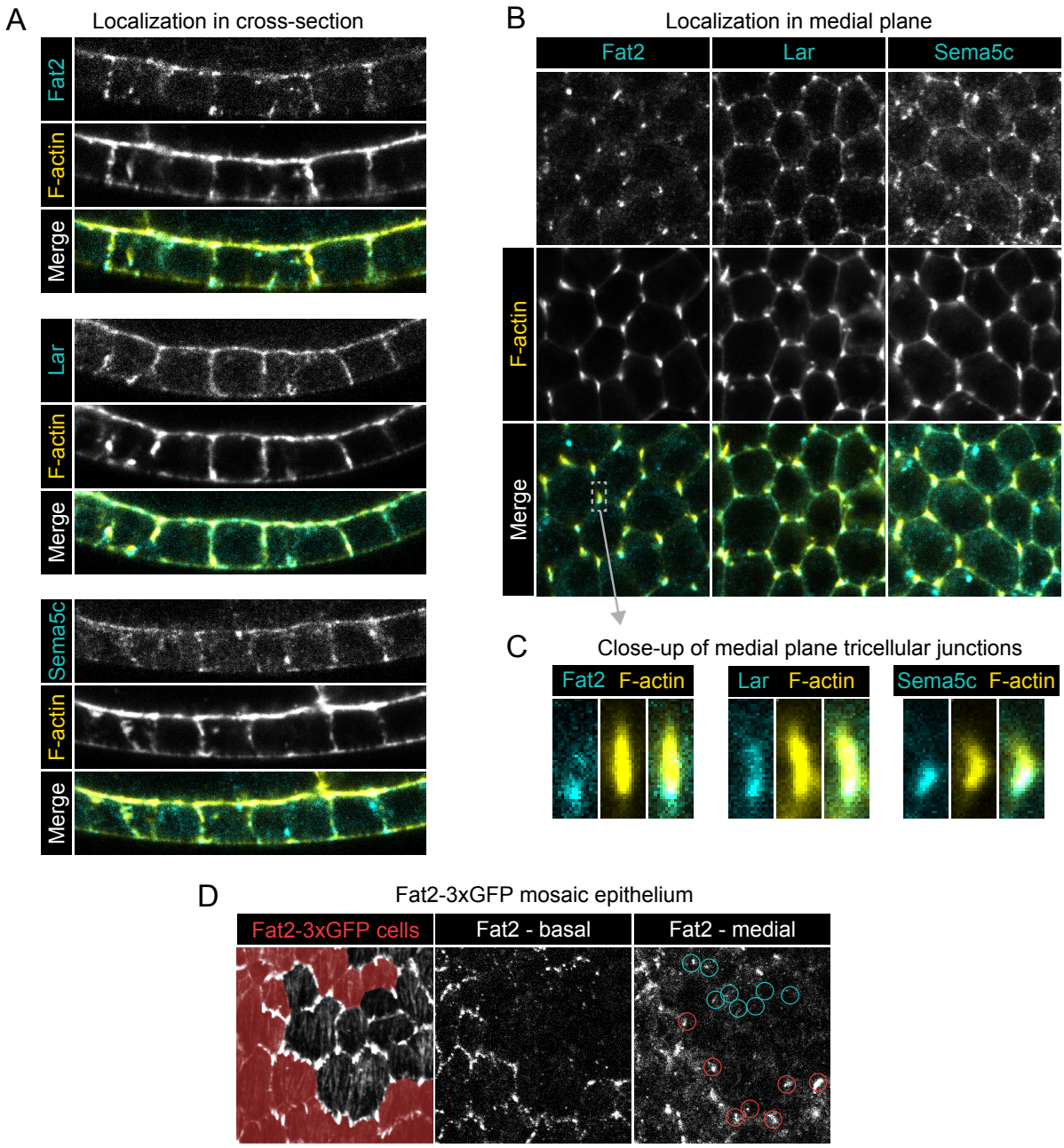

Figure 3.2: **Fat2, Lar, and Sema-5c are enriched at actin protrusion tips away from the basal surface.** Continued on next page.

Figure 3.2: **Fat2, Lar, and Sema-5c are enriched at actin protrusion tips away from the basal surface (continued). A-C**, Follicle cells expressing endogenously-tagged Fat2-3xGFP, Lar-3xGFP, or Sema5c-3xGFP, with F-actin stained by phalloidin. **A**, Images show follicle cells in cross-section. Fat2, Lar, and Sema-5c localize in puncta at cell-cell interfaces away from the basal surface. **B**, Images show the medial plane between apical and basal cell surfaces. Fat2, Lar, and Sema5c are enriched at tricellular junctions along with F-actin-rich protrusions. **C**, Expanded views of tricellular junction regions from (B). The puncta of Fat2, Lar, and Sema5c sit at the tips of F-actin-rich protrusions at tricellular junctions as they do at the basal surface. **D**, Images of a mosaic epithelium mosaic for expression of Fat2-3xGFP and wild-type Fat2, with F-actin stained with phalloidin (white in left image). Fat2-3xGFP-containing cells are pseudocolored based on Fat2-3xGFP expression. Red circles indicate tricellular junctions where Fat2-3xGFP-expressing cells are ahead of unlabeled ones; blue circles where unlabeled cells are ahead of Fat2-3xGFP-expressing ones. Fat2 is polarized to the trailing edge side of tricellular junctions away from the basal surface as it is at the basal surface.

uously required to maintain the enrichment of Lar and Sema5c at leading edges.

To probe the limits of Fat2's capacity to position the leading-edge proteins, we used GrabFP-A^{Int} to create an ectopic Fat2 population (Harmansa et al., 2017) (Fig. 3.6A), and asked if this could relocalize Lar. At present, we lack a functional Sema5c antibody, and so could not check for its relocalization. Fat2 and Lar normally colocalize in puncta at the basal surface and along tricellular junctions that span the apical-basal axis (Bateman et al., 2001; Viktorinová et al., 2009). Expression of GrabFP-A^{Int} caused Fat2-3xGFP to accumulate all around adherens junctions as well, and increased Fat2-3xGFP levels overall (Fig. 3.6B-F). The ectopic Fat2 had no effect on the distribution of Lar, which remained restricted to tricellular junctions in the adherens junction plane despite Fat2's presence all around cell perimeters (Fig. 3.6D-F). These data show that Fat2 is limited in its ability to recruit Lar, and that there must be some other feature(s) of basal cell-cell interfaces and tricellular junctions that are required for Lar's enrichment and perhaps for puncta assembly in general.

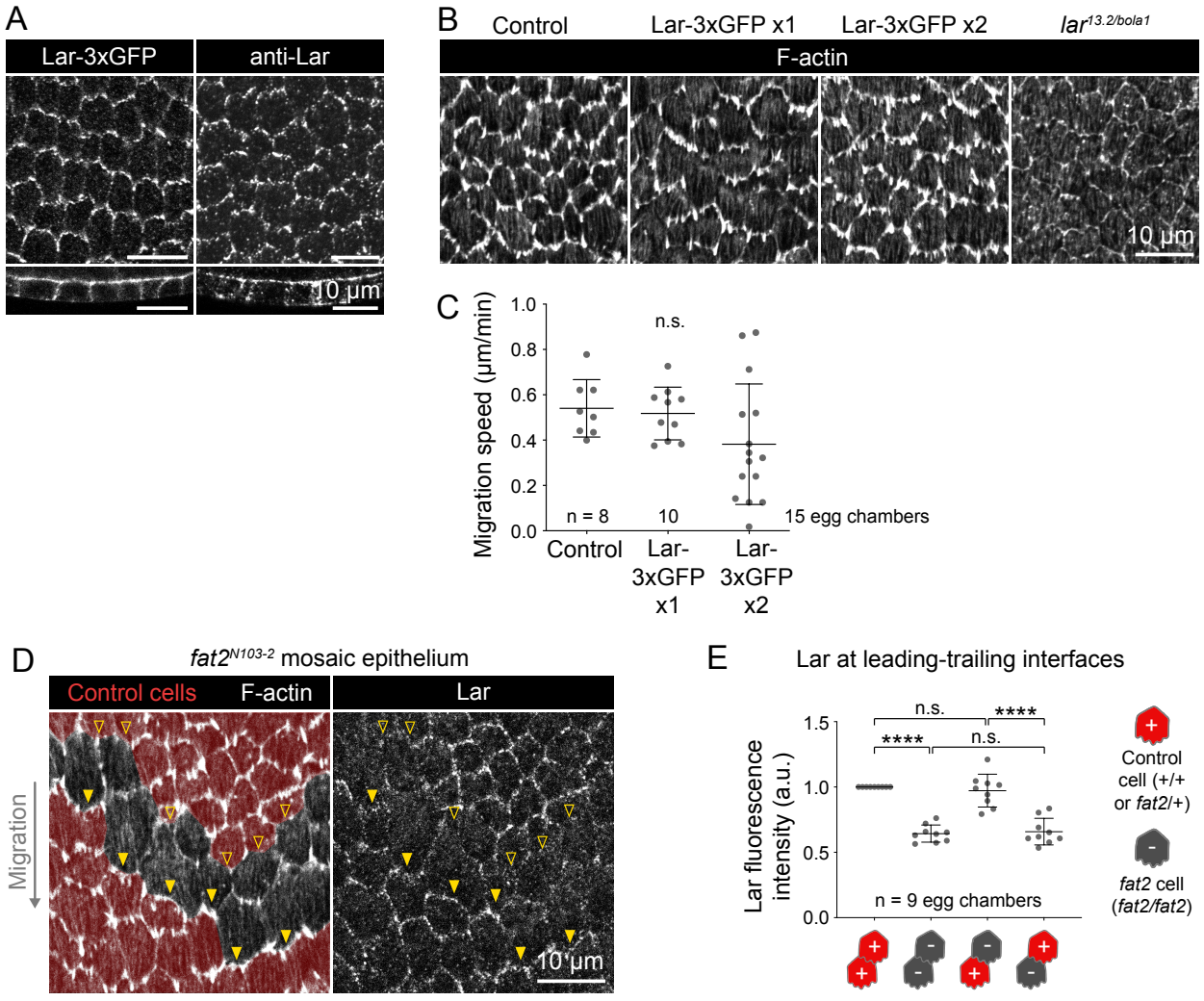

Figure 3.3: **Lar remains largely functional with an endogenous 3xGFP tag.** Continued on next page.

Figure 3.3: **Lar remains largely functional with an endogenous 3xGFP tag (continued).** **A**, Images showing Lar's distribution at the basal surface (top row) or in cross-section (bottom row) as detected using either Lar-3xGFP or a Lar antibody. Lar localization patterns are similar between the two markers. **B**, Images showing F-actin (phalloidin) structures at the basal surface in epithelia with wild-type Lar, one or two Lar-3xGFP alleles, or with no Lar expression. F-actin protrusions appear normal in epithelia expressing Lar-3xGFP, in contrast to the reduced F-actin protrusions in epithelia without Lar. **C**, Plot of follicle cell migration speeds in control epithelia or epithelia with one or two Lar-3xGFP copies. Average migration speeds are similar to controls when one copy of Lar-3xGFP is present, but they are more variable and possibly slower in Lar-3xGFP homozygotes. Welch's ANOVA ($W(2.00,19.01)=1.92$, $p=0.17$). **D**, Images of a $fat2^{N103\text{-}2}$ mosaic epithelium expressing Lar-3xGFP, with F-actin stained using phalloidin. Control cells are pseudocolored based on a genetically-encoded fluorescent marker. Filled arrows indicate the leading edges of $fat2^{N103\text{-}2}$ cells behind control cells, hollow arrows indicate the leading edges of control cells behind $fat2^{N103\text{-}2}$ cells. **E**, Plot of Lar-3xGFP fluorescence intensity at leading-trailing interfaces between different combinations of control and $fat2^{N103\text{-}2}$ cells. Lar-3xGFP enrichment is reduced at leading edges of cells of any genotype behind $fat2^{N103\text{-}2}$ cells, showing that the trans interaction between Fat2 and Lar that was identified using Lar antibody staining (Barlan et al., 2017) is preserved with Lar-3xGFP. Repeated measures one-way ANOVA ($F(3, 24)=60.38$, $p<0.0001$ with post-hoc Tukey's test; n.s. (left to right) $p=0.66$, 0.96, ****$p<0.0001$.

Lar and Sema5c play only a minor role in the localization of Fat2

Given Fat2's importance for localizing Lar and Sema5c, we asked if they play a reciprocal role in localizing Fat2. To this end, we measured the average level of Fat2-3xGFP along all cell-cell interfaces at the basal surface of epithelia lacking Lar (*lar*-RNAi), Sema5c ($Sema5c^{K175}$), or both proteins together (*lar*-RNAi, $Sema5c^{K175}$) and compared these values to control epithelia. Full basal cell perimeters were used instead of leading-trailing interfaces because Fat2 loses its planar polarization when migration is disrupted (Barlan et al., 2017), as occurs in some of these backgrounds (see Fig. 3.11). Fat2 levels were normal in epithelia lacking Lar and mildly reduced in epithelia lacking Sema5c (Fig. 3.7A-C). Importantly, Fat2 levels were not further reduced in epithelia lacking both proteins compared to those lacking Sema5c alone (Fig. 3.7A,B). We validated these findings in $Sema5c^{K175}$ mosaic epithelia, again finding that Fat2-3xGFP levels were reduced at the $Sema5c^{K175}$ interfaces relative to control ones, and

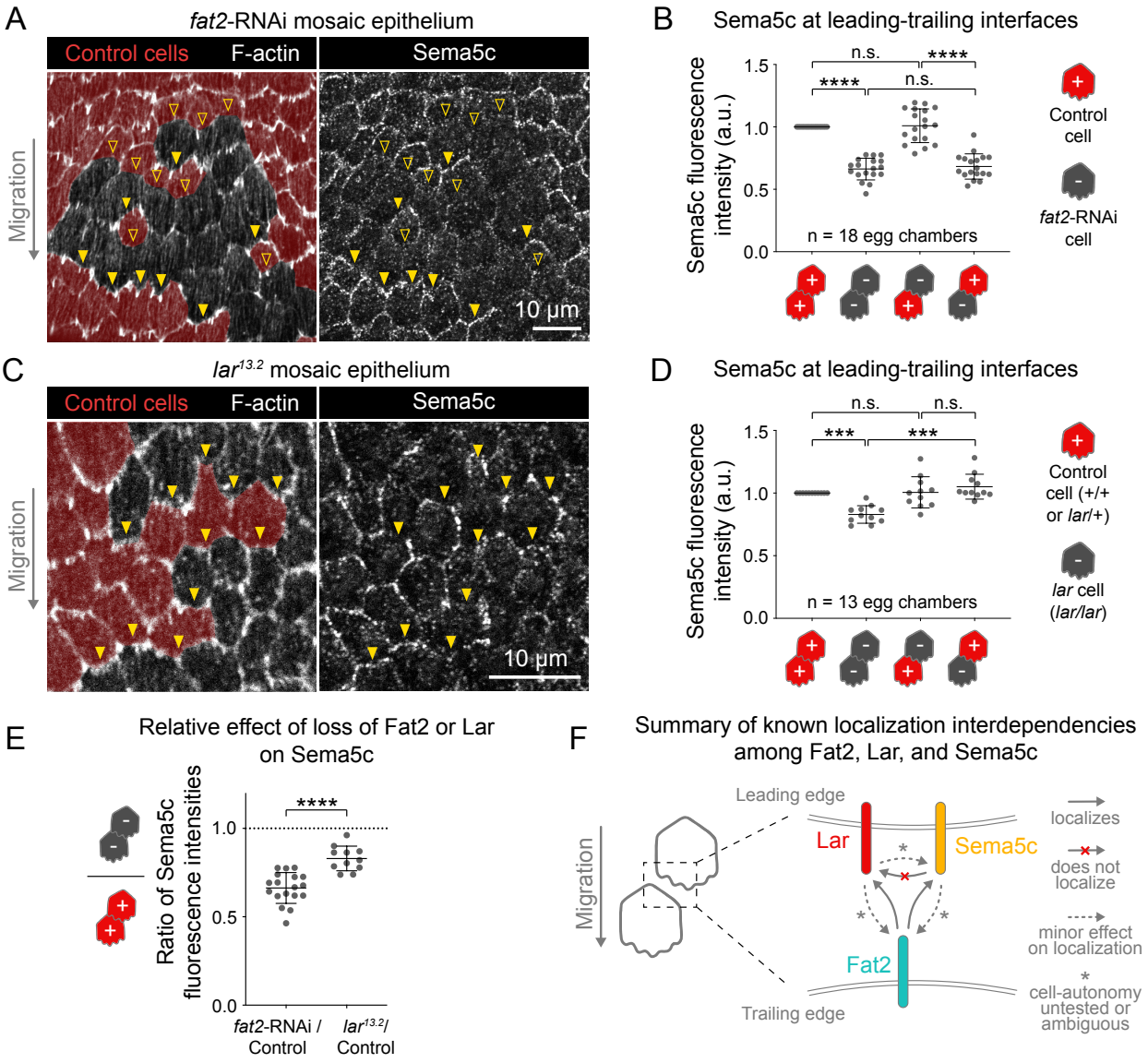

Figure 3.4: **Fat2 concentrates Sema5c in trans at the leading edge.** Continued on next page.

Figure 3.4: **Fat2 concentrates Sema5c in trans at the leading edge (continued).** **A**, Images of a *fat2*-RNAi mosaic epithelium expressing Sema5c-3xGFP, with F-actin stained using phalloidin. Control cells are pseudo-colored based on genetically-encoded markers. Filled arrows indicate leading edges of *fat2*-RNAi-expressing cells behind control cells, which have normal Sema5c-3xGFP enrichment. Hollow arrows indicate the leading edges of control cells behind *fat2*-RNAi-expressing cells, which have reduced Sema5c-3xGFP enrichment. **B**, Plot of Sema5c-3xGFP fluorescence intensity at leading-trailing interfaces between different combinations of control and *fat2*-RNAi-expressing cells. Bars indicate mean ± SD. Sema5c-3xGFP enrichment is reduced at the leading edge of cells of any genotype behind *fat2*-RNAi cells. Repeated measures one-way ANOVA ($F(2.42, 41.07)=96.23$, $p<0.0001$ with post-hoc Tukey's test; n.s. (left to right) $p=0.99$, 0.79, ****$p<0.0001$. **C**, Images of a $lar^{13.2}$ mosaic epithelium expressing Sema5c-3xGFP, with F-actin stained using phalloidin. Control cells are pseudo-colored based on genetically-encoded markers. Arrows indicate leading-trailing interfaces at boundaries between control and $lar^{13.2}$ cells in either order, both of which are enriched for Sema5c-3xGFP. **D**, Plot of Sema5c-3xGFP fluorescence intensity at leading-trailing interfaces between different combinations of control and $^{13.2}$ cells. Bars indicate mean ± SD. Sema5c-3xGFP enrichment is reduced at leading-trailing interfaces between two $lar^{13.2}$ cells, but not at interfaces with a control cell either ahead or behind, which is inconsistent with Lar simply recruiting Sema5c locally to their shared leading edge. Repeated measures one-way ANOVA ($F(2.24, 22.41)=19.93$, $p<0.0001$ with post-hoc Tukey's test; n.s. (left to right) $p>0.99$, 0.77, ***$p=0.003$, ****$p<0.0001$. **E**, Plot comparing the effects of loss of Fat2 and Lar on Sema5c-3xGFP enrichment at leading-trailing interfaces. Data replotted from (B) and (D). Both *fat2*-RNAi and $lar^{13.2}$ reduce Sema5c-3xGFP enrichment (fluorescence intensity ratios below dotted line at $y=1$), but *fat2*-RNAi causes a greater reduction. Unpaired t-test; ****$p<0.0001$. **F**, Diagram showing dependencies among Fat2, Lar, and Sema5c for localization to the leading-trailing interface, summarizing findings from this and previous studies (Barlan et al., 2017; Stedden et al., 2019) (see also Figs. 3.7, 3.3D,E). Fat2 concentrates Lar and Sema5c at the leading edge in trans, and Lar and Sema5c play minor, perhaps non-interface-local roles in the distribution of the three proteins.

that the severity of reduction was not altered by depletion of Lar throughout the epithelium using *lar*-RNAi (Fig. 3.8A-E). These epithelia unexpectedly lacked planar polarity, so we could not assess the cell autonomy of this interaction with respect to leading and trailing edges. Fat2-3xGFP levels were intermediate when Sema5c was only present on one side of the cell-cell interface (Fig. 3.8B), showing that in this unpolarized context, Sema5c from both sides of the interface contributes to the localization of Fat2-3xGFP. We conclude that whereas Fat2 plays a major role in the localization of Lar and Sema5c, Lar and Sema5c play at most a minor role in localizing Fat2 (Fig. 3.4B).

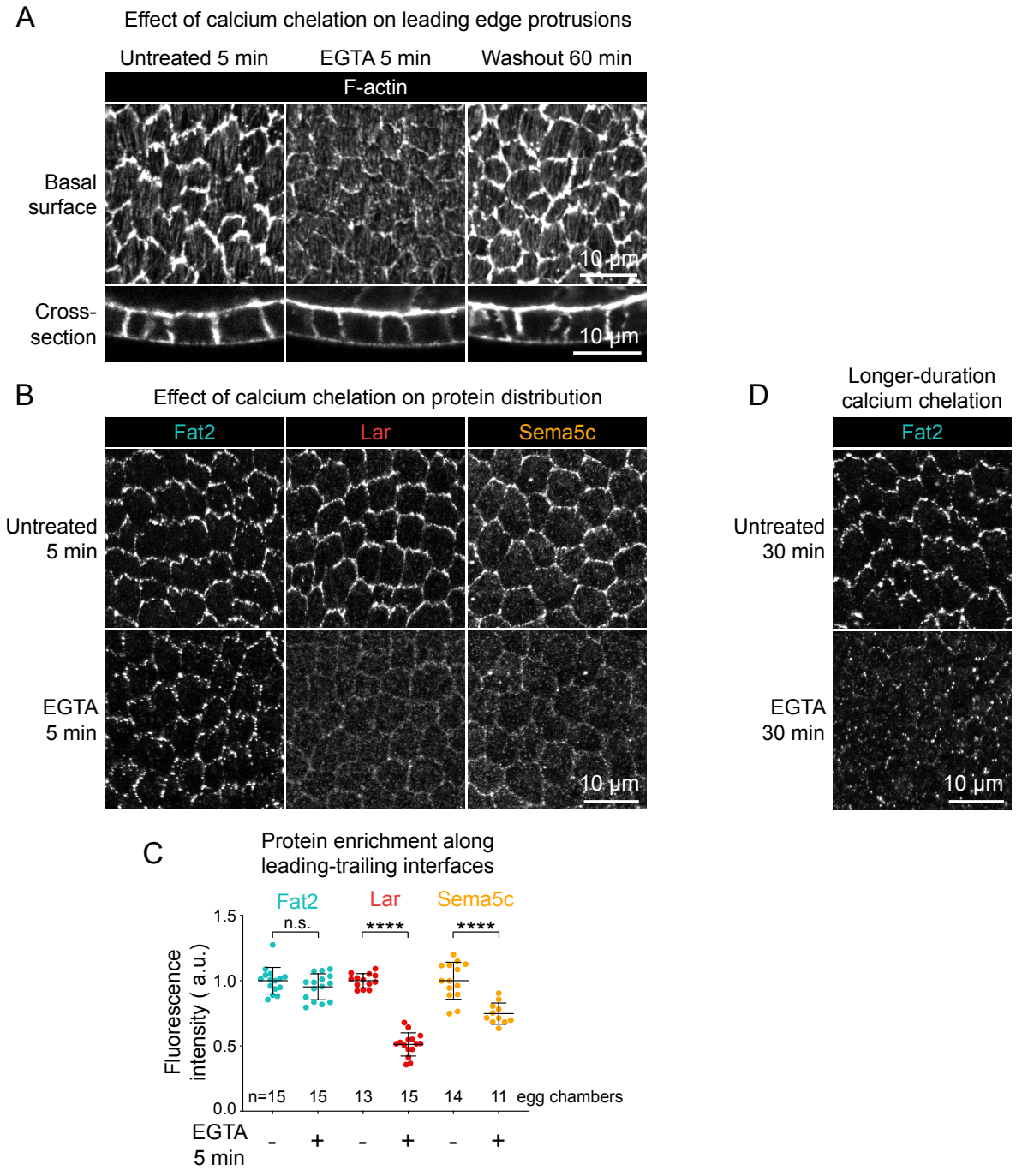

Figure 3.5: **Calcium chelation causes rapid loss of Lar and Sema5c from the leading edge.** Continued on next page.

Figure 3.5: **Calcium chelation causes rapid loss of Lar and Sema5c from the leading edge (continued).** **A**, Images of the basal surfaces of the follicle cells with F-actin stained by phalloidin after being left untreated for 5 minutes, treated with 20 mM EGTA (an extracellular calcium chelator) for 5 minutes, or treated with EGTA for 5 minutes followed by washout and 60 minutes of recovery. F-actin-rich protrusions are reduced by EGTA treatment, but return following washout. Cross-section images show no apparent changes to follicle cell shape or epithelial integrity caused by EGTA treatment or treatment and washout. **B**, Images of Fat2-, Lar-, or Sema5c-3xGFP at the basal surfaces of epithelia left untreated or treated with 20 mM EGTA for 5 minutes, representative of data quantified in (C). **C**, Plot of the mean fluorescence intensity of Fat2-3xGFP, Lar-3xGFP, and Sema5c-3xGFP along leading-trailing interfaces at the basal surface, with or without 5 minutes of EGTA treatment. EGTA treatment causes a reduction in Lar- and Sema5c-3xGFP levels, but no significant change in Fat2-3xGFP levels. Bars indicate mean ± SD. Unpaired t-tests; n.s. $p=0.21$, ****$p<0.0001$. **D**, Images of Fat2-3xGFP at the basal surface of epithelia left untreated or treated with 20 mM EGTA for 30 minutes. Unlike in (B) and (C), this longer treatment results in nearly-complete clearance of Fat2-3xGFP from the basal surface.

Since Sema5c did minorly alter the localization of Fat2, we asked whether this in turn affected the localization of Lar or the WAVE complex, both of which are localized by Fat2. We tested this using $Sema5c^{K175}$ mosaic epithelia expressing either Lar-3xGFP or Sra1-GFP. We found no reduction in the levels of either protein at leading-trailing interfaces between $Sema5c^{K175}$ cells compared to interfaces between control cells (Figs. 3.8A,B; 3.9A,B). The lack of a change in Lar-3xGFP levels is consistent with a previous finding made using a Lar antibody (Stedden et al., 2019). Together, these data indicate that Sema5c is dispensable for the enrichment of Lar and the WAVE complex at leading edges. They further suggest that Sema5c plays a sufficiently minor role in Fat2's localization that its loss does not cause indirect effects on the localization of Lar or the WAVE complex. Alternatively, it is possible that the altered localization of Fat2-3xGFP in $Sema5c^{K175}$ cells is an artifact caused by Fat2's 3xGFP tag and does not occur in these other backgrounds.

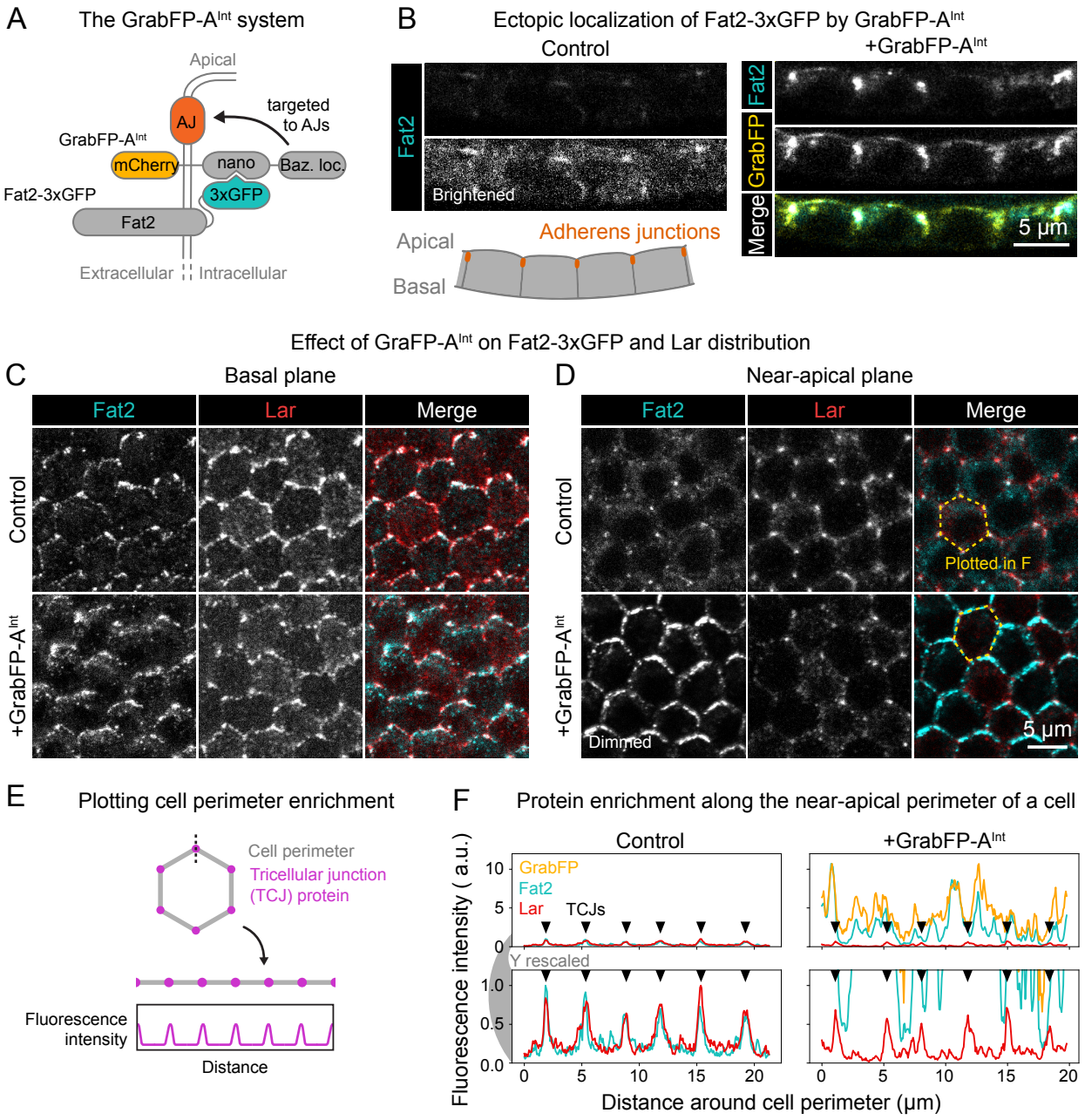

Figure 3.6: **Fat2 is not sufficient to relocalize Lar away from the basal surface or tricellular junctions.** Continued on next page.

Figure 3.6: **Fat2 is not sufficient to relocalize Lar away from the basal surface or tricellular junctions (continued). A**, Diagram showing how the GrabFP-A^{Int} protein is used to recruit Fat2-3xGFP to adherens junctions (AJs). GrabFP-A^{Int} binds intracellularly GFP-tagged proteins with a GFP nanobody (nano), and is targeted to AJs, along with any bound proteins, by a domain of Bazooka (Baz. loc.). **B**, Images of Fat2-3xGFP-expressing follicle cells in cross-section with or without expression of GrabFP-A^{Int}. The diagram shows the imaging plane, with the adherens junctions to which GrabFP-A^{Int} is targeted indicated. Fat2-3xGFP is present in control cells, but its enrichment at adherens junctions and overall levels are strongly increased in the presence of GrabFP-A^{Int}. **C,D**, Images of Fat2-3xGFP-expressing epithelia with or without co-expression of GrabFP-A^{Int}, stained with a Lar antibody. Images in (C) show the basal planes of a group of cells; images in (D) show a near-apical plane through their adherens junctions. Fat2-3xGFP is displayed more dimly in the +GrabFP-A^{Int} image in (D) relative to other images to allow the Fat2-3xGFP distribution to be clear in each. **E**, Diagram illustrating the "unrolling" process by which the perimeters of cells such as those outlined in (D) are linearized for plotting in (F). **F**, Plots of the fluorescence intensity distribution of Fat2-3xGFP, anti-Lar, and GrabFP-A^{Int} (if present) along the cell perimeters outlined in (D). The upper row shows the full range of intensities, and the lower row shows an expanded view of the lower intensities. Triangles correspond to tricellular junctions (TCJs), to which Fat2 and Lar are normally largely restricted in this plane. GrabFP-A^{Int} expression causes a large increase in Fat2-3xGFP levels and their expansion around the entire cell perimeter, but Lar remains restricted to tricellular junctions.

Slowly-exchanging Fat2 molecules decrease the turnover of the leading edge proteins

We hypothesized that Fat2's ability to concentrate Lar and Sema5c across their shared interface might be due to Fat2 slowing their turnover from cells' leading edges. To test this idea, we first used fluorescence recovery after photobleaching (FRAP) to measure the turnover rates of all three proteins along leading-trailing interfaces at the basal surface of control epithelia. Within 6 minutes after photobleaching, Fat2-3xGFP fluorescence had only recovered to $29\% \pm 10\%$ of its initial levels, whereas Lar-3xGFP and Sema5c-3xGFP fluorescence had recovered to $70\% \pm 21\%$ and $90\% \pm 26\%$, respectively (Fig. 3.10A-E). During a longer recovery period of 28 minutes, Fat2-3xGFP fluorescence increased to $59\% \pm 25\%$ of initial levels, still lower than the maximum recovery seen for Lar and Sema5c (Fig. 3.10F,G). These data show that Fat2 molecules reside at leading-trailing interfaces for tens of minutes,

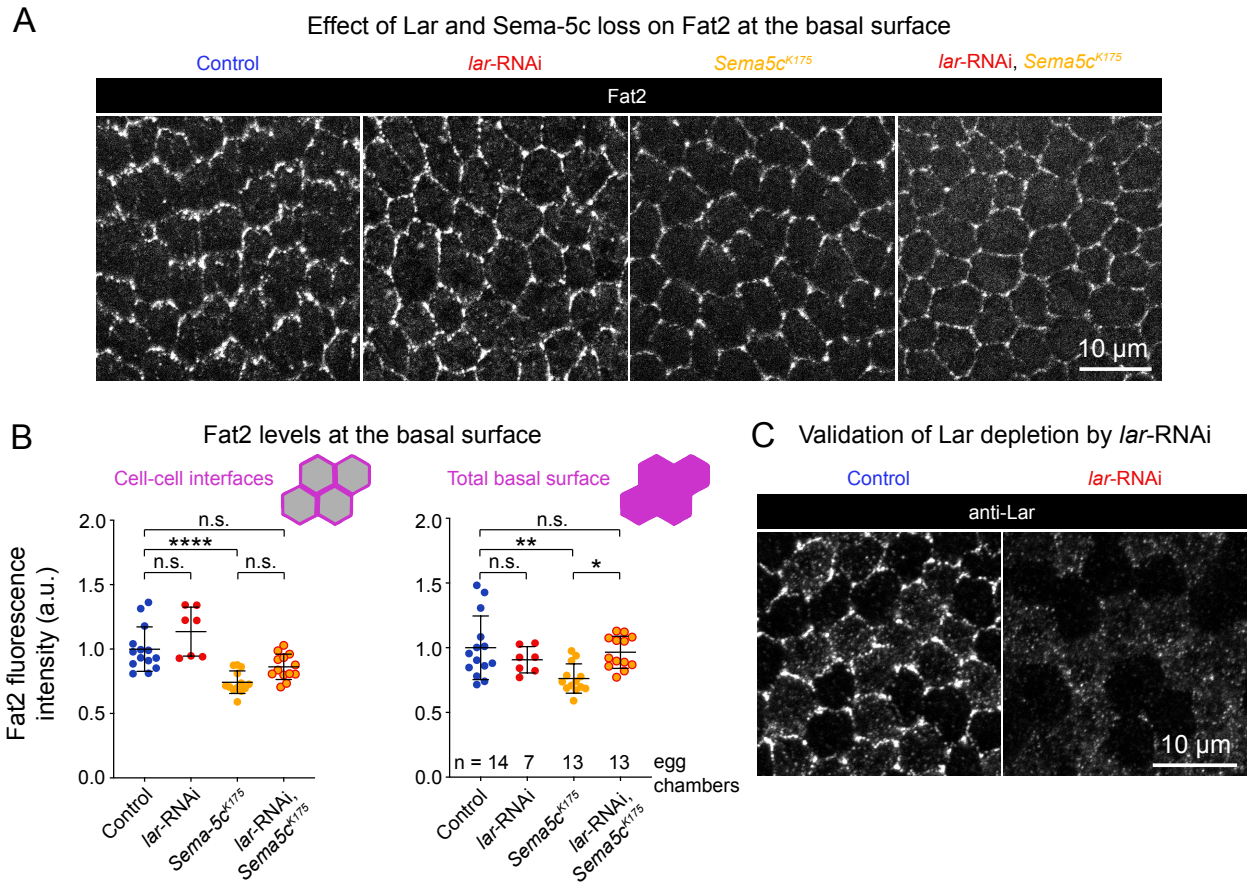

Figure 3.7: **Fat2's enrichment at interfaces shows only a mild dependence on Lar and Sema5c. A**, Images of Fat2-3xGFP at the basal surface in control epithelia, *lar*-RNAi-expressing or $Sema5c^{K175}$ epithelia, and in a combined $Sema5c^{K175}$ *lar*-RNAi-expressing epithelium. **B**, Plots of Fat2-3xGFP levels at cell-cell interfaces (left) or the entire basal surface (right) of epithelia exemplified in (A). Fat2-3xGFP levels are slightly reduced at interfaces and across the basal surface in $Sema5c^{K175}$ epithelia. Lar depletion causes no additional reduction in Fat2-3xGFP levels at these locations. Bars indicate mean ± SD. Cell-cell interfaces: One-way ANOVA ($F(3,43)=15.18$, $p<0.0001$ with post-hoc Tukey's test; ****$p<0.0001$, n.s. (left to right) $p=0.16$, 0.059, 0.14. Total basal surface: One-way ANOVA ($F(3,43)=5.31$, $p=0.0033$ with post-hoc Tukey's test; **$p=0.0030$, *$p=0.016$, n.s. (left to right) $p=0.63$, 0.95. **C**, Images of Lar antibody staining at the basal surface, demonstrating the strength of Lar depletion by *lar*-RNAi.

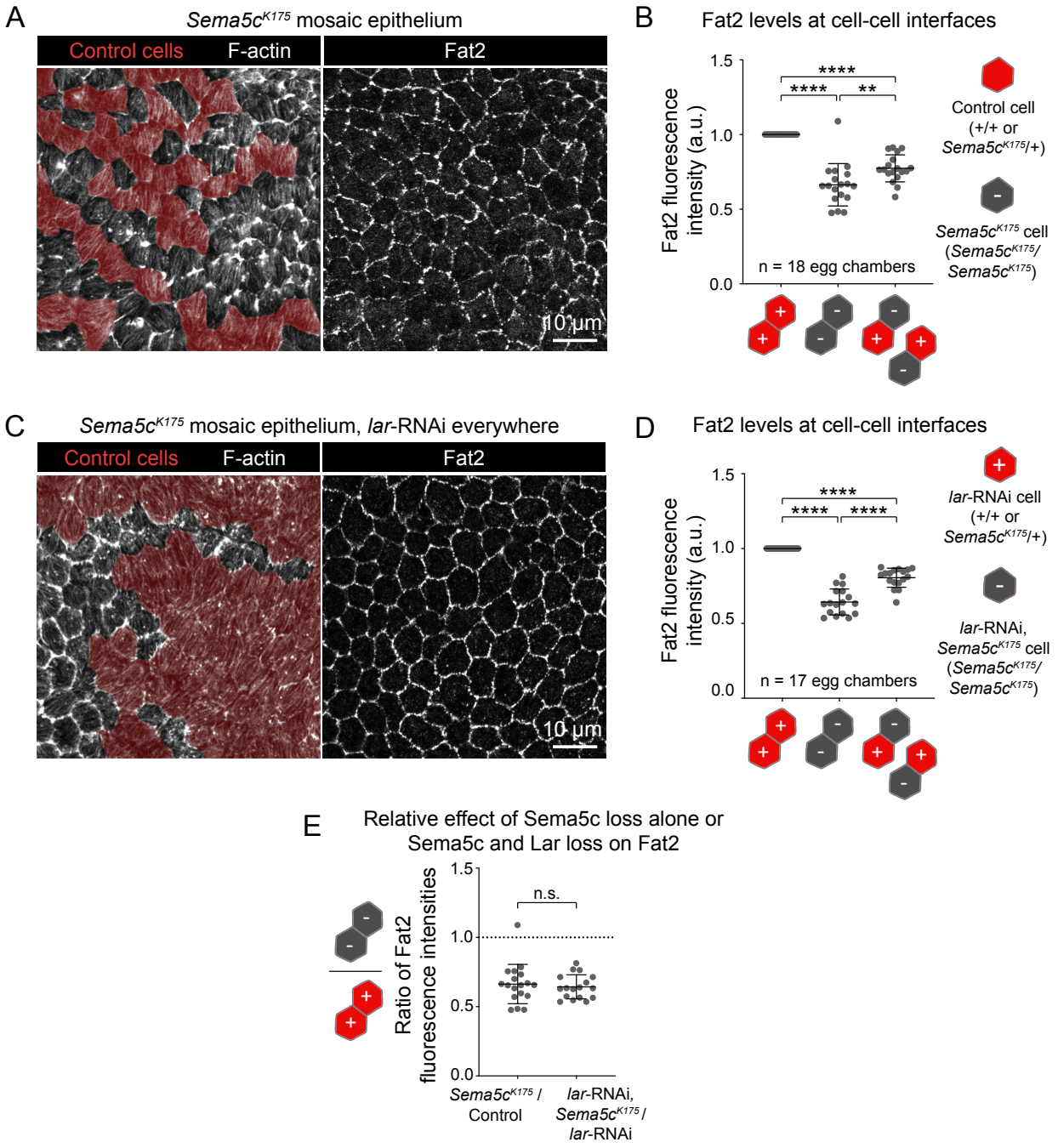

Figure 3.8: **Sema5c contributes to the localization of Fat2.** Continued on next page.

Figure 3.8: **Sema5c contributes to the localization of Fat2 (continued).** **A**, Images of a *Sema5c*^{K175} mosaic epithelium expressing Fat2-3xGFP, with F-actin stained using phalloidin. These epithelia lack planar polarity. Control cells are pseudo-colored red based on genetically encoded markers. **B**, Plot of Fat2-3xGFP mean fluorescence intensity along cell-cell interfaces of different genotype pairs from data exemplified in (A). Fat2-3xGFP levels were reduced at interfaces between *Sema5c*^{K175} cells relative to ones between control cells, and levels were intermediate at genotype boundaries. Repeated measures ANOVA ($F(2,34)=57.47$, $p<0.0001$) with post-hoc Tukey's test; **p=0.0030, ****p<0.0001. **C**, Images of a *Sema5c*^{K175} mosaic epithelium expressing Fat2-3xGFP and *lar*-RNAi in all cells and with F-actin stained using phalloidin. These epithelia lack planar polarity. Control cells are pseudo-colored red based on genetically encoded markers. **D**, Plot of Fat2-3xGFP mean fluorescence intensity along cell-cell interfaces of different genotype pairs from data exemplified in (C). Fat2-3xGFP levels were reduced at interfaces between *Sema5c*^{K175} *lar*-RNAi cells relative to ones between *lar*-RNAi-only cells, and levels were intermediate at genotype boundaries. Repeated measures ANOVA ($F(2,32)=107.5$, $p<0.0001$) with post-hoc Tukey's test; ****p<0.0001. **E**, Plot comparing the change in Fat2-3xGFP enrichment caused by loss of Sema5c in epithelia expressing *lar*-RNAi to epithelia with normal Lar levels. Depletion of Lar does not change the severity of the reduction in Fat2-3xGFP enrichment at cell-cell interfaces. Unpaired t-test, n.s. p=0.62.

and Lar and Sema5c only minutes, under normal conditions.

We then asked if Fat2 regulates the turnover of Lar and Sema5c at interfaces by performing the same FRAP experiment in epithelia lacking Fat2 (Fig. 3.10B,E,F). If Fat2 concentrates Lar and Sema5c by slowing their departure from leading edges, their turnover should increase in its absence. Conversely, if Fat2 concentrates Lar and Sema5c by speeding up their rate of arrival to leading edges, turnover should decrease in its absence. We found that the time to half recovery of fluorescence was faster on average in *fat2*$^{N103\text{-}2}$ epithelia for both Lar-3xGFP and Sema5c-3xGFP (Fig. 3.10H,I). However, this difference was not statistically significant in the case of Lar-3xGFP, and in the case of Sema5c-3xGFP it was contributed to by a decrease in overall recovery as well as an increase in the rate of recovery. We note that Sema5c-3xGFP levels at interfaces were lower than those of Lar-3xGFP normally (Fig. 3.10J,K), and even lower in *fat2*$^{N103\text{-}2}$ epithelia, which may have contributed to the lower recovery fraction. Altogether, these data favor a model in which Fat2 has a stabilizing effect on Lar and Sema5c. However, additional work will be needed to show this

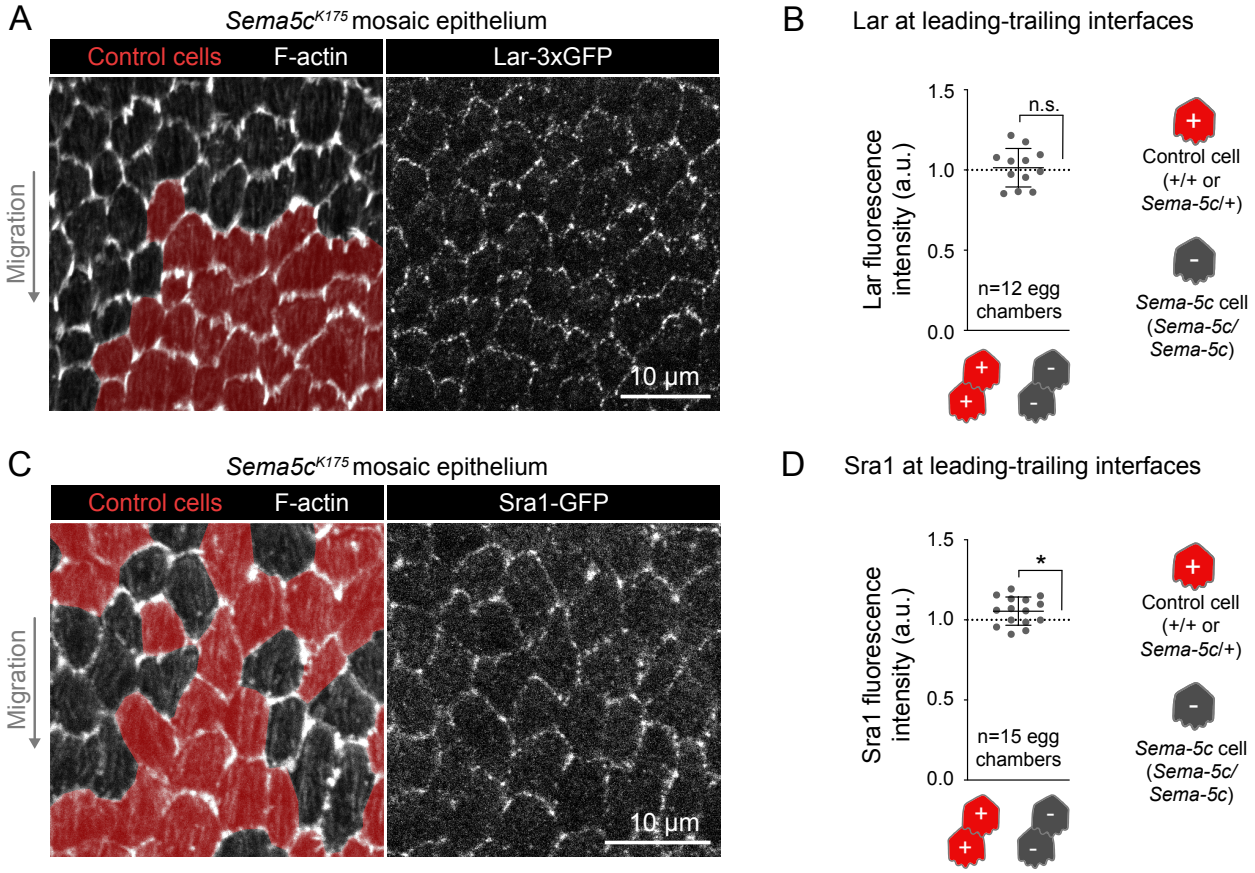

Figure 3.9: **Sema5c does not regulate the localization of Lar or the WAVE complex.** **A**, Images of a $Sema5c^{K175}$ mosaic epithelium expressing Lar-3xGFP, with F-actin stained using phalloidin. Control cells are pseudo-colored red based on genetically encoded markers. **B**, Plot showing the effect of $Sema5c^{K175}$ on Lar-3xGFP enrichment at leading-trailing interfaces, expressed as the ratio of Lar-3xGFP mean fluorescence intensity at $Sema5c^{K175}$ and control interfaces. Lar-3xGFP levels are not affected by loss of Sema5c. One sample t-test, n.s. p=0.6752. **C**, Images of a $Sema5c^{K175}$ mosaic epithelium expressing Sra1-GFP, with F-actin stained using phalloidin. Control cells are pseudo-colored red based on genetically encoded markers. **Control cells are pseudo-colored red based on genetically encoded markers (Make this be true). D, Plot showing the effect of $Sema5c^{K175}$ on Sra1-GFP enrichment at leading-trailing interfaces, expressed as the ratio of Lar-3xGFP mean fluorescence intensity at $Sema5c^{K175}$ and control interfaces. Loss of Sema5c causes little or no change in Sra1-GFP levels. One sample t-test, n.s. p=0.0297.**

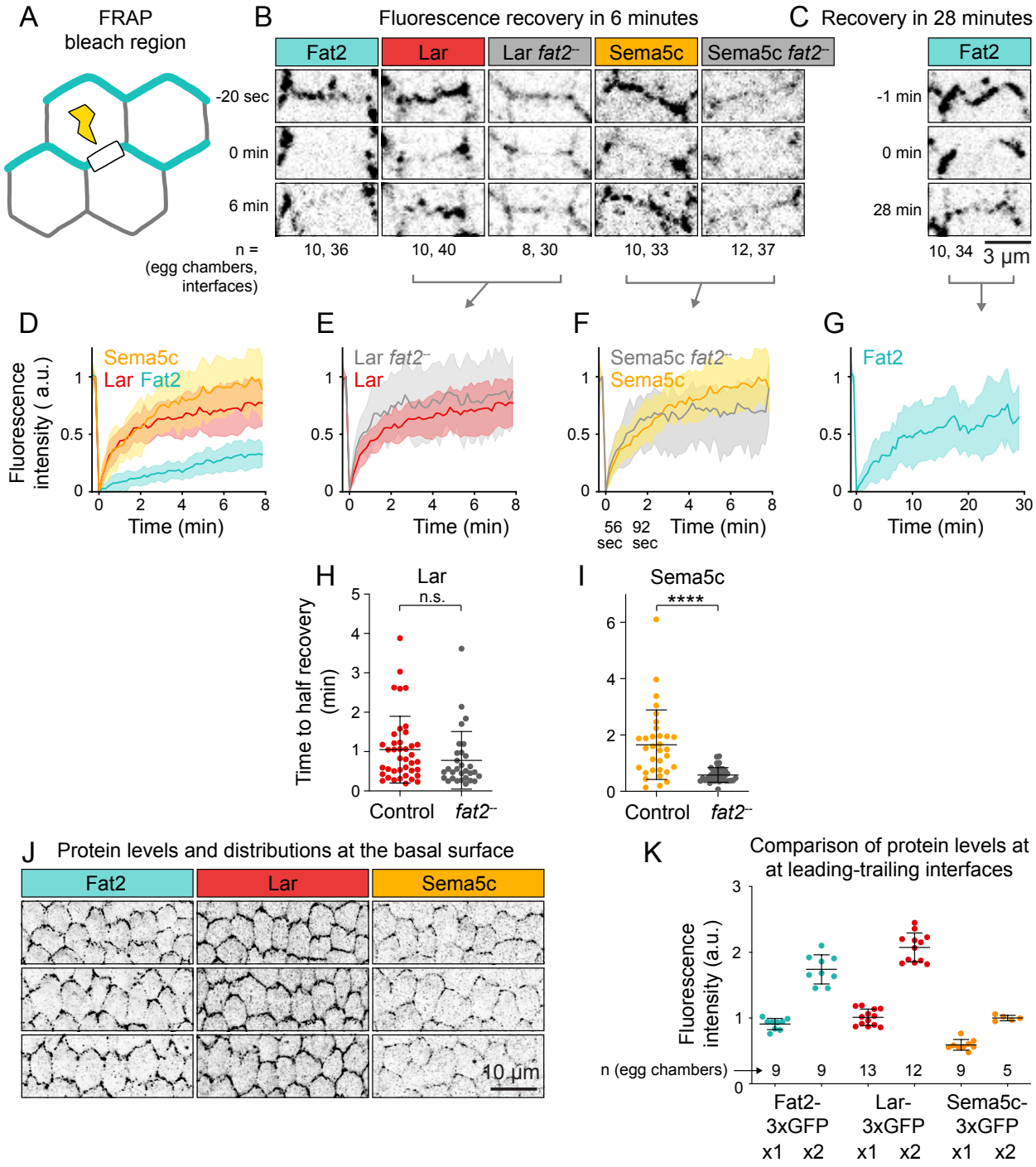

Figure 3.10: **Fat2 is relatively stable at the trailing edge, and slows the departure of Lar and Sema5c from the leading edge.** Continued on next page.

Figure 3.10: **Fat2 is relatively stable at the trailing edge, and slows the departure of Lar and Sema5c from the leading edge (continued).** **A**, Diagram of the photobleached regions: leading-trailing interfaces at the basal surface excluding the two bounding tricellular junctions. **B**, Images of Fat2-3xGFP, Lar-3xGFP, and Sema5c-3xGFP at individual leading-trailing interfaces shortly before, immediately after, and 6 minutes after photobleaching. The $fat2^{N103\text{-}2}$ were non-migratory and lacked planar polarity so interfaces of any angle were used. **C**, Images of Fat2-3xGFP at a leading-trailing interface shortly before, immediately after, and 28 minutes after photobleaching. **D**, Plot comparing recovery of Fat2-3xGFP, Lar-3xGFP, and Sema5c-3xGFP fluorescence intensity to leading-trailing interfaces over 8 minutes following photobleaching, exemplified in (B). Solid lines and filled regions show mean ± SD. Fat2 recovers more slowly than Lar or Sema5c. **E,F**, Plots comparing recovery of Lar-3xGFP and Sema5c-3xGFP in control epithelia (reproduced from (D)) and $fat2^{N103\text{-}2}$ epithelia. **G**, Plot showing recovery of Fat2-3xGFP fluorescence intensity to leading-trailing interfaces over 28 minutes following photobleaching, exemplified in (C). In that time, its fluorescence had still only recovered to 65% of its initial level, less than Lar-3xGFP or Sema5c-3xGFP did within 8 minutes. **H,I**, Plots of the time to half fluorescence recovery calculated by fitting single exponential equations to data in (E,F). **H**, Lar-3xGFP half recovery time showed an average decrease in $fat2^{N103\text{-}2}$ epithelia that was not statistically significant. Welch's t-test, p=0.15.**I**, Sema5c-3xGFP half recovery time decreased in $fat2^{N103\text{-}2}$ due to both increased average recovery rate and decreased percent recovery. Welch's t-test, <0.0001. **J**, Images of Fat2-3xGFP, Lar-3xGFP, and Sema-5c-3xGFP at the basal surfaces of rows of cells from multiple epithelia acquired and displayed using uniform settings. **K**, Plot comparing the levels of Fat2-3xGFP, Lar-3xGFP, and Sema-5c-3xGFP at leading-trailing interfaces, expressed in two copies or with a wild-type allele. Interface enrichment differed across the three proteins, and Sema-5c-3xGFP levels were approximately half those of Fat2-3xGFP and Lar-3xGFP. No correction for background fluorescence was performed.

more conclusively.

Lar and Sema5c promote collective migration in parallel downstream of Fat2

Fat2, Lar, and Sema5c are all required for normal collective migration, but whereas loss of Fat2 prevents migration entirely, loss of Lar only slows migration, and loss of Sema5c both slows it and delays its onset (Barlan et al., 2017; Stedden et al., 2019; Viktorinová & Dahmann, 2013) (Fig. 3.11A,B). These milder migration phenotypes suggest that Lar and

Sema5c may act in parallel downstream of Fat2 to regulate cell motility. If true, analysis of the cell-scale phenotypes caused by loss of Lar or Sema5c could help us understand the two "arms" of the interface signaling system that Fat2 assembles. Fat2 promotes epithelial migration both by increasing cell protrusivity and by polarizing cells' protrusions in the direction of tissue movement (Barlan et al., 2017; Squarr et al., 2016; Williams et al., 2022), so we asked if Lar or Sema5c play similar roles in protrusion formation and polarity. These roles have previously been studied using F-actin labeling (Barlan et al., 2017; Squarr et al., 2016; Stedden et al., 2019), but we recently found that this approach misses much of the protrusive activity in $fat2^{N103\text{-}2}$ epithelia (Williams et al., 2022). We therefore used live imaging and membrane labeling to re-examine the protrusion phenotypes caused by loss of Lar or Sema5c alone, and to build on this by determining the effect of losing both proteins together.

First, we examined Lar's role in protrusion formation and polarity. F-actin staining had suggested that cells lacking Lar are less protrusive than normal (Barlan et al., 2017; Squarr et al., 2016). However, using membrane labeling, we detected no reduction in protrusivity in $lar^{13.2/bola1}$ epithelia (Fig. 3.11C,D). This suggests that Lar increases F-actin enrichment within protrusions, but is not required for protrusion formation. Loss of Lar did, however, disrupt protrusion polarity. Whereas control epithelia had most protrusions pointed in the direction of migration, epithelia lacking Lar had a sizeable minority pointed rearwards, and their protrusions were less aligned with migration overall (Figs. 3.11C,E; 3.12). These data show that Lar helps polarize protrusions across the tissue, and suggest that Fat2's role in this process is due in part to its ability to localize Lar.

We then performed the same analysis for Sema5c. $Sema5c^{K175}$ epithelia initiate migration later in development than normal, and their migration is slow and difficult to preserve ex vivo (Stedden et al., 2019). Consistently, about 1/2 of the $Sema5c^{K175}$ epithelia were migrating detectably, albeit slowly, and several others had a degree of protrusion polarity

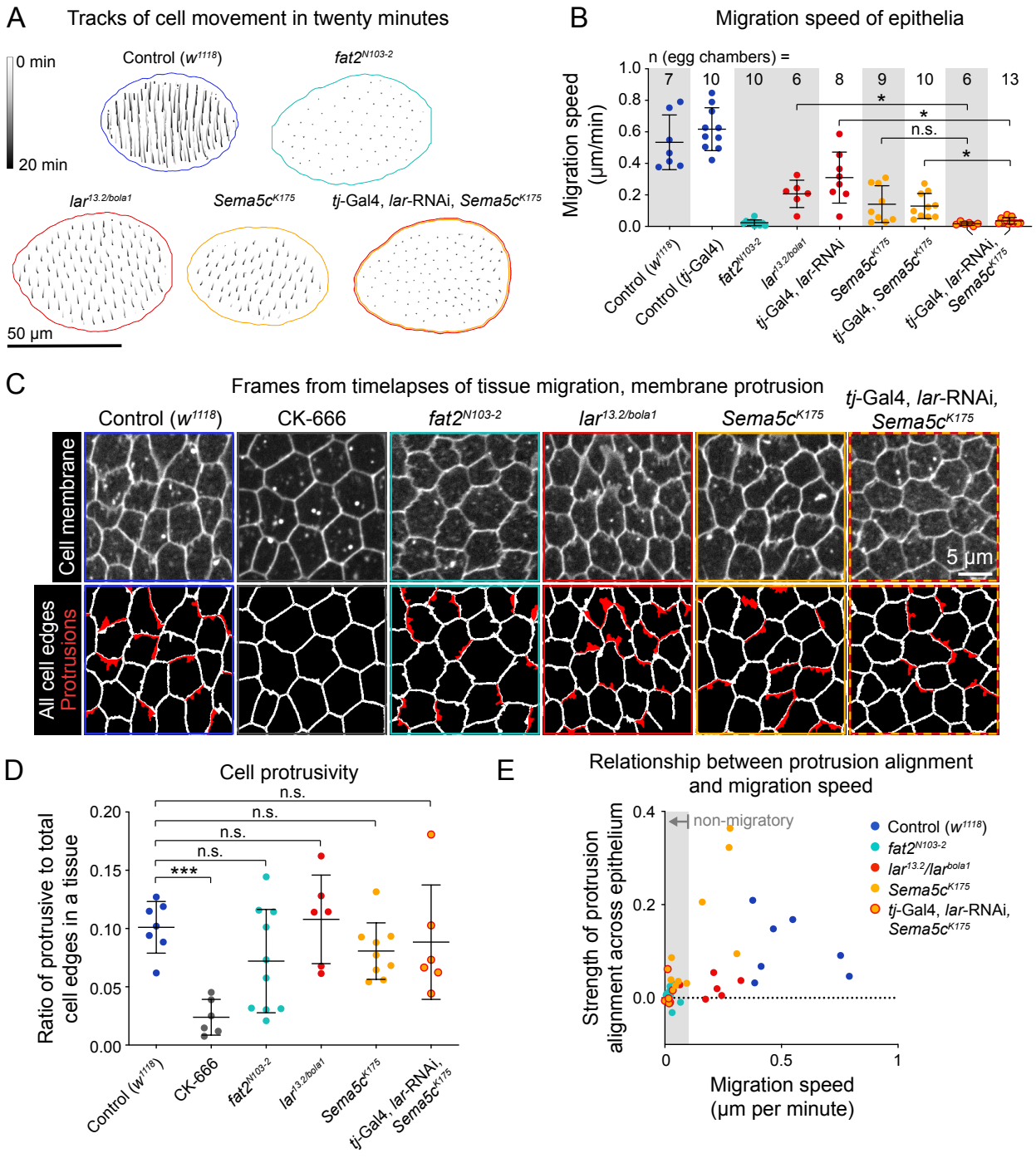

Figure 3.11: **Lar and Sema5c act in parallel to polarize cell migratory machinery and promote collective migration.** Continued on next page.

Figure 3.11: **Lar and Sema5c act in parallel to polarize cell migratory machinery and promote collective migration (continued). A**, Tracks of cell movement over twenty minutes in individual epithelia. The in-focus tissue region is outlined. **B**, Plot of tissue migration speeds. Movies of conditions with white backgrounds on the graph were taken at medial planes through the follicle cells. Movies of conditions with gray backgrounds were taken at the basal surface and used for analysis of membrane protrusion traits in addition to migration speed. Whereas loss of Lar or Sema5c slows migration, simultaneous loss of both Lar and Sema5c stops it entirely. Gray backgrounds: Welch's ANOVA ($W(3.000,14.31)=64.11$, $p<0.0001$) with post-hoc Dunnet's T3 multiple comparisons test; *p=0.021, n.s. p=0.099. White backgrounds: Welch's ANOVA ($W(4.00,14.30)=21.64$, $p<0.0001$) with post-hoc Dunnet's T3 multiple comparisons test; * (left to right) p=0.0.011, n.s. p=0.025. **C**, Frames from timelapse movies used for measurement of migration speed and protrusion traits. Control epithelia treated with CK-666 are used as a non-protrusive control. The top row shows cell membranes labeled with CellMask. The bottom row shows the segmented cell edges and protrusions. Edges categorized as protrusive based on their average lengths of extension are shown in red. **D**, Plot of the level of cell protrusivity per epithelium, defined as the ratio of protrusive to total cell edges. Edges are categorized as protrusive if their average length is greater than that of 98% of edges in CK-666-treated epithelia. Unlike CK-666 treatment, loss of Fat2, Lar, or Sema5c causes only minor changes to the level of cell protrusivity, if any. Welch's ANOVA ($W(5.000,16.43)=12.83$, $p<0.0001$) with post-hoc Dunnet's T3 multiple comparisons test; ***p=0.0002, n.s. (left to right) p=0.69, >0.99, 0.70, >0.99. **E**, Plot showing the relationship between migration speed and the strength of protrusion alignment. An alignment of one indicates perfect alignment of all protrusions, and zero indicates either random protrusion orientations or symmetrical protrusion in two opposite directions. The gray region indicates non-migratory epithelia (speed < 0.1 um/min). Protrusions of slowly-migrating $Sema5c^{K175}$ epithelia (but not $lar^{13.2/bola1}$ epithelia) are poorly aligned with one another.

that likely indicated they had been migrating prior to dissection Figs. 3.11A,B; 3.12B). In agreement with previous findings based on F-actin staining (Stedden et al., 2019), we did not observe a difference in the membrane protrusivity of $Sema5c^{K175}$ epithelia. In the detectably-migrating subset of epithelia, protrusion polarity also appeared normal (Figs. 3.11C-E; 3.12). The slow migration speeds of these epithelia therefore do not seem to be caused by protrusion defects, although it is possible that Sema5c regulates protrusions in ways we did not detect. Alternatively, Sema5c may primarily regulate other aspects of cell motility such as contractility or adhesion.

Finally, we asked whether Lar and Sema5c work in parallel to promote collective mi-

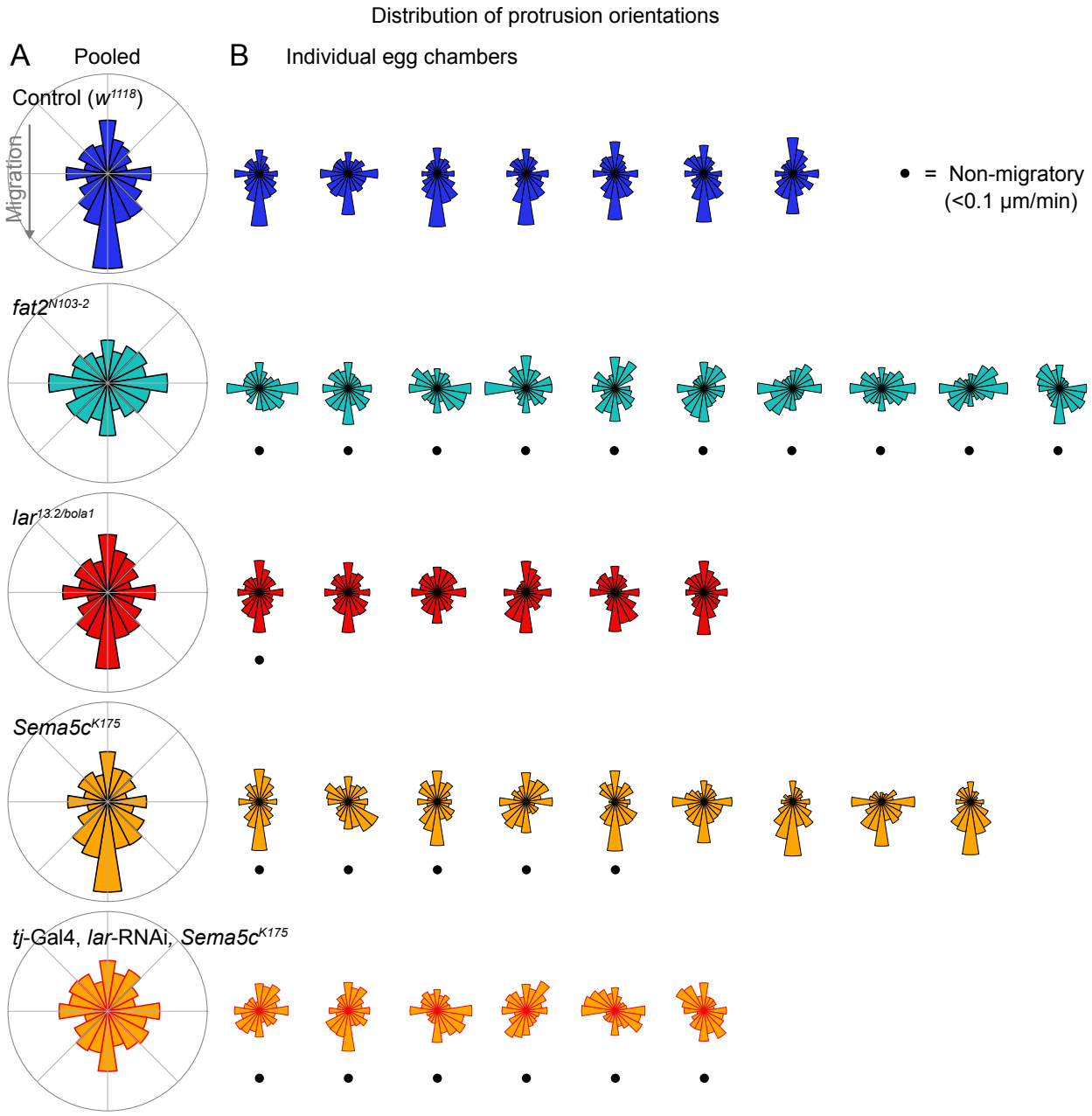

Figure 3.12: **Loss of either Fat2, Lar, or Sema5c have different effects on the polarity of membrane protrusions. A,B**, Polar histograms showing the distribution of protrusion orientations in epithelia pooled by genotype (A) or plotted individually (B). In (B), dots under histograms indicate that the epithelium was not migrating (speed <0.1 μm/min). Anterior is left, posterior is right, and data has been flipped vertically as needed such that the migration direction (where applicable) is downwards. $lar^{13.2/bola1}$ epithelia have excess rearwards protrusions, and removal of both Lar and Sema5c causes protrusions to be unpolarized, as is seen upon loss of Fat2.

gration as suggested by the distinct loss-of-function phenotypes. To test this, we expressed *lar*-RNAi in follicle cells of $Sema5c^{K175}$ egg chambers. These epithelia failed to migrate and had unpolarized protrusions in all cases, making them indistinguishable from $fat2^{N103\text{-}2}$ epithelia (Figs. 3.11A-C,E; 3.12). We conclude that Lar and Sema5c act in parallel to regulate cell motility, likely through distinct effectors. These data further suggest that Fat2's polarization of both Lar and Sema5c to leading edges is a major means by which it regulates the collective migration of follicle cells.

3.5 Discussion

The follicle cells use biochemical signaling across their leading-trailing interfaces to polarize their migration machinery at interface, cell, and tissue scales. Here we have shown that Fat2 is a central organizer of this signaling system. Fat2 acts at the trailing edge of each cell to concentrate both Lar and Sema5c at the leading edge of the cell behind, and it appears to do so, at least in part, by slowing their turnover at this site. By contrast, Lar and Sema5c play at most minor roles in the localization of Fat2. In this way, Fat2 coordinates the activities of two effector proteins with distinct functions, allowing them to work synergistically to promote highly persistent collective migration.

One defining feature of this Fat2-based signaling system is that most of the component proteins colocalize in interface-spanning puncta. Cadherins often self-organize into clusters (Brasch et al., 2019; Stahley et al., 2021; Truong Quang et al., 2013; Wu et al., 2015), making it likely that this punctate organization stems from Fat2. However, whether Fat2 recruits Lar and Sema5c into the puncta through direct binding or through intermediary proteins is unknown. An ectopic Fat2 pool did not cause redistribution of Lar, suggesting that additional inputs are necessary for recruitment. We also do not know how Sema5c's receptor, PlexA, fits into this model. Like Fat2, PlexA is enriched at cells' trailing edges and helps to localize Sema5c, and yet antibody staining indicates that PlexA only partially

colocalizes with the Fat2-based puncta. The biggest open question is how Fat2 becomes localized to the trailing edge, as this appears to be the key event that polarizes the entire signaling system. Mechanical feedback from collective migration itself is required for Fat2's polarization to trailing edges (Barlan et al., 2017), but the nature of this feedback, and whether Fat2 has a trans binding partner that further stabilizes its localization, will be important areas for future investigation.

This work also sheds light on how Lar and Sema5c work together to promote collective migration. Loss of either protein alone impairs migration but does not stop it (Barlan et al., 2017; Stedden et al., 2019). By contrast, removing both proteins together fully blocks migration in a way that is indistinguishable from loss of Fat2. These data suggest that once Fat2 concentrates Lar and Sema5c to cells' leading edges, they then act in parallel to promote collective migration, likely by polarizing distinct aspects of the migration machinery.

What aspects of the migration machinery do Lar and Sema5c each control? In the case of Lar, it seems to be part of the bridge between Fat2 and WAVE complex-dependent protrusions—both Fat2 and Lar increase protrusive F-actin enrichment at leading edges (Fat2 in trans and Lar in cis), and both also help polarize protrusions in the direction of migration. In addition, Lar acts in trans to promote retraction of the trailing edge of the cell ahead (Barlan et al., 2017), but the mechanistic basis for this trans function, and the degree to which it is separable from Lar's cis function, remain undetermined. In the case of Sema5c, cell-scale loss-of-function phenotypes have proven more elusive, but enrichment of PlexA at trailing edges and the ability of overexpressed Sema5c to suppress protrusion in trans both point to the trailing edge as the likely site of regulation (Stedden et al., 2019).

By positioning both Lar and Sema5c, Fat2 integrates two features of interface signaling systems known to operate in other collectively migrating cell types but not yet seen together. The first feature is the use of a trailing edge-associated mechanical cue to orient protrusions in the cell behind (Das et al., 2015; Hayer et al., 2016). Mechanical localization of Fat2 to

trailing edges polarizes protrusions in the following cell, in part by localizing Lar (Barlan et al., 2017). The second feature is the use of contact inhibition of locomotion (Carmona-Fontaine et al., 2008; Smeets et al., 2016; Zimmermann et al., 2016), which causes cells to polarize away from one another by suppressing protrusion and/or increasing contractility at the point of contact (Roycroft & Mayor, 2016; Stramer & Mayor, 2017). By localizing Lar and Sema5c to leading edges, Fat2 positions them to enforce trailing edge behavior at the contacting edge of the cell ahead. Therefore, Fat2 translates a mechanical cue into bi-directional signaling across leading-trailing interfaces to coordinate cell migratory behaviors for collective migration.

3.6 Methods

Materials, data, and code availability

Code used in data analysis, all numerical datasets, and plasmid maps are available at *https://github.com/a9w/epithelial_migration_signaling*. Images and movies are available upon request to Sally Horne-Badovinac.

Drosophila sources, care, and genetics

The genotypes of animals used in each experiment and associated figure panels are listed in Table 3.1. *Drosophila* were raised on a diet of cornmeal molasses agar food at 25°C. Experimental females were collected 0-3 days post-eclosion and aged in the presence of males with a diet of the same cornmeal molasses agar supplemented with finely powdered active dry yeast before dissection. In most experiments, they were aged for two to three days at 25°C. Higher temperatures were used to increase the expression of Gal4-driven transgenes in some cases, and longer aging times (up to 5 days) were used to obtain more FRT recombination events in some mosaic epithelia. The temperatures and yeasting times

used in each experiment are listed in Table 3.2. Epithelia mosaic for RNAi expression were generated using the Flp-out system with Gal4 expressed under control of a heat shock promoter. To heat shock, experimental females were aged while undergoing the following 12 hr temperature cycle: 1 hr 37°C, 1 hr 25°C, 1 hr 37°C, 9 hr 25°C. After 5 cycles (2.5 days), they were then transferred to 29°C and given fresh yeast for an additional 12 hrs prior to dissection to increase RNAi expression strength and uniformity across clones.

Generation of the Lar-3xGFP line

Endogenous Lar was tagged C-terminally with three enhanced GFP proteins in tandem separated by short linker sequences (3xGFP) using CRISPR following the general approaches described in Gratz et al. (2013, 2014) (Gratz et al., 2013; Gratz et al., 2014). The same 3xGFP sequence had been used to generate Fat2-3xGFP and Sema5c-3xGFP proteins in previous studies (Barlan et al., 2017; Stedden et al., 2019). The guide RNA target sequence 5'-GCTTCTGCTATCGCGCTGCACTGG-3' was chosen with flyCRISPR Target Finder (Gratz et al., 2014). The underlined sequence was cloned into the pU6-BbsI-chiRNA plasmid, the upstream G added for efficient U6-driven expression, and the bold sequence is the adjacent PAM motif. The homologous recombination donor plasmid contained homology arms approximately 2 kb in length flanking the insertion target site, acquired by amplification of genomic DNA from the y1 Mnos-Cas9.PZH-2A w* (nanos-Cas9) background (Port et al., 2014). The 3xGFP sequence was amplified from the pDsRed-Fat2-3xGFP plasmid (Barlan et al., 2017). A linker with a sequence encoding the amino acids GSGGSTVPRARDPP-VAT connects the Lar C-terminus with the N-terminus of 3xGFP. Homology arms, linker, and 3xGFP DNA fragments were inserted into donor plasmid pDsRed-attP, which contains 3xP3-DsRed flanked by loxP sites for insertion screening and subsequent removal (Gratz et al., 2014). The linker-3xGFP insertion was made immediately before the Lar stop codon. Guide and homologous recombination plasmids were injected by Genetivision in the nanos-

Cas9 background, providing a germline Cas9 source. F1 males were screened for 3xP3-DsRed, which is expressed in the eye, and then 3xP3-DsRed was excised by crossing to Cre-expressing flies (MKRS hsFLP/TM6b Cre). Successful insertion was confirmed with genomic DNA sequencing of the lar C-terminus and 3xGFP insertion region following 3xP3-DsRed excision. This insertion strategy leaves a loxP "scar" downstream of the *lar* protein-coding region.

Egg chamber dissection

Ovaries were dissected into 500 μL of live imaging media (Schneider's *Drosophila* medium with 15% fetal bovine serum and 200 μg/mL insulin) in a spot plate using one set of Dumont #55 forceps in the experimenters' dominant hand and 1 set of Dumont #5 forceps in the non-dominant hand. A more detailed description and images of this dissection protocol are available in Cetera et al. (2016) (Cetera et al., 2016). Ovarioles were removed from both the ovary and their individual muscle sheaths by pinching the germarium with forceps and pulling anteriorly. For fixed imaging, egg chambers older than stage 9 were removed prior to fixation. For live imaging, egg chambers older than the egg chamber to be imaged were removed from the ovariole strands by slicing through the adjoining stalk cells with a 27-gauge hypodermic needle. Removal of older egg chambers results in more compression of the younger egg chambers between the slide and the coverslip.

Live imaging sample preparation

Immediately after dissection, ovarioles were transferred to a fresh well of live imaging media using a p10 pipettor. For samples with membrane staining, CellMask Orange (Thermo Fisher Scientific, Waltham, MA, 1:500) was added and samples incubated for 15 minutes, and then samples were washed in live imaging media to remove excess dye before mounting. For samples treated with CK-666, following plasma membrane staining, ovarioles were instead transferred to live imaging media with 750 μM CK-666 (Millipore Sigma, St. Louis, MO)

and then mounted immediately after in the same CK-666-containing media. Samples were mounted along with 51 μm beads on standard glass slides, and covered with 22x22 mm #1.5 coverslips. The beads support the coverslip, controlling the amount of tissue compression. Some compression enables imaging of the basal surface of a field of cells in a single plane, but too much interferes with the migration process. Coverslip edges were sealed with petroleum jelly to prevent evaporation during imaging. Samples were checked for damage using the membrane stain or other available fluorescent markers as indicators, and excluded if damage was present. Slides were imaged for one hour or less.

EGTA treatment

Egg chambers were dissected into live imaging media, and then half were transferred into spot plate wells with 250 μL of live imaging media (the "control" treatment), and the other half into 250 μL of live imaging media containing 20 mM EGTA (Thermo Fisher Scientific). They were incubated for 5 or 30 minutes, depending on the experiment, with wells covered by a slide to slow evaporation, and then fixed and stained with phalloidin as detailed below.

Immunostaining and F-actin staining

After dissection, ovarioles were fixed at room temperature for 15 minutes in 4% EM-grade formaldehyde in PBT (phosphate-buffered saline with 0.1% Triton X-100 detergent), and then washed for 3x5 minutes in PBT. For antibody staining, egg chambers were incubated in primary antibody (mouse anti-Lar monoclonal, 1:200, or mouse anti-Dlg monoclonal, 1:20) overnight at 4°C, washed 3x5 minutes in PBT, and then incubated in secondary antibody (Donkey anti-mouse polyclonal, 1:200) for 2-3 hours at room temperature. For phalloidin staining, samples were incubated in TRITC phalloidin (Millipore Sigma, 1:250) for 15 minutes at room temperature, or with 647 AlexaFluor phalloidin (Thermo Fisher Scientific, 1:100) for 2-3 hours at room temperature. For a more detailed phalloidin staining protocol,

see Anderson et al. (2023) (Anderson et al., 2023). Phalloidin and secondary antibody incubations were performed concurrently where applicable. Samples were then washed for 3x5 minutes in PBT and mounted on a slide in a drop (∼40 μL) of SlowFade Diamond antifade (Invitrogen), covered in a 22x50 mm #1.5 coverslip sealed with nail polish, and stored at 4°C until imaged. This mounting strategy results in compression of stage 6-7 egg chambers, allowing imaging of the basal surfaces of many cells in a single plane.

Microscopy

All micrograph images collected are of egg chambers at either stage 6 or 7, as assessed by their size and by the size and shape of their oocyte in cross-section. Images were acquired using a Zeiss LSM800 upright laser scanning confocal microscope with either a 40x/1.3 NA EC 386 Plan-NEOFLUAR or 63x/1.4 NA Plan-APOCHROMAT oil immersion objective. The system was controlled with Zen 2.3 Blue acquisition software (Zeiss). Imaging was performed at room temperature. All images and measurements are of a single Z-slice of the follicle cells' basal surfaces unless otherwise noted. Exceptions are Fig. 3.6B and the bottom rows of Figs. 3.5A and 3.3A, which show cross-sections through the apical-basal axis; Fig. 3.6D, which show a near-apical plane (the plane of the adherens junctions); and the timelapse movies used to measure the migration speeds plotted in Fig. 3.11B on a white background, which were taken at a medial plane through the cells with respect to their apical-basal axis. Unless noted, imaging settings were held constant for all images of the same fluorescent protein shown in the same image panel and any corresponding plot panels, but settings affecting image brightness were optimized separately for each fluorophore when multiple are present in the same panel, or for data shown in separate panels. The exceptions are in Fig. 3.4A,B and 3.4C,D, which were collected with the same imaging settings to enable the comparison in 3.4E, and Fig. 3.10H,I, in which Fat2-3xGFP, Lar-3xGFP, and Sema5c-3xGFP were imaged and displayed in the same manner to enable comparison of their levels.

Cell tracking and migration speed measurement

Twenty minute-long timelapse movies were acquired of stage 6-7 egg chambers stained with CellMask membrane dye. These were taken at either the medial epithelial plane (used for migration speed measurement only, conditions with white background in Fig. 3.11B) or the basal plane (for migration speed and protrusion trait measurement, conditions with gray backgrounds). In either case, cells were segmented in each frame using the pretrained "cytoplasm" model in Cellpose (Stringer et al., 2021). Subsequent analysis steps were performed in Python using scikit-image and scipy libraries (van der Walt et al., 2014; Virtanen et al., 2020). The gaps between segmented cells were closed with a watershed algorithm seeded by the initial segmented regions. Segmented cells were then tracked by linking regions of high overlap in consecutive frames. Errors in segmentation and tracking were corrected manually using napari (Sofroniew et al., 2022). Migration speed was measured from a 22 μm-wide band of cells around the egg chamber's "equator," half-way between anterior and posterior poles, where linear cell migration speed is fastest in migratory epithelia. The displacement vector of the centroid of each cell present in consecutive pairs of frames was calculated, and these vectors averaged to obtain a vector whose length and direction were used to determine the tissue migration speed and direction.

Measurement of membrane protrusivity and protrusion alignment with migration

Protrusions were identified from timelapse movies of epithelia stained with CellMask membrane dye, which yield rich information about protrusion characteristics including their sizes and distributions, and often allow detection of more protrusive activity than is detectable by F-actin labeling. Protrusions were segmented using a watershed-based approach, and their average lengths and orientations measured, as described in Williams et al. (2022) (Williams et al., 2022) and briefly here. Protrusion segmentation and trait measurement were per-

formed in Python using scikit-image and scipy libraries. Following cell segmentation, the region of high membrane fluorescence at the interface between each pair of neighboring cells was segmented. This region includes the cell-cell interface and any protrusions that extend across it from either of the neighboring cells. We then approximated the cell-cell interface position running through this region by drawing the shortest path through the region that connects its bounding vertices. This divides the region into two portions belonging to each of the neighboring cells, which we call "edges."

To obtain a benchmark for the width of non-protrusive cell edges, we identified the average width (area divided by interface length) of edges from CK-666-treated epithelia, which are nearly non-protrusive. Edges from all conditions were considered protrusive if their width (corresponding with their average length of membrane extension from the interface) was greater than that of 98% of those of CK-666-treated epithelia. We then calculated the average cell protrusivity of each epithelium, defined as its ratio of protrusive to total edges.

To measure protrusion polarity, we took the protrusive edges ("protrusions"), identified their "tip" and "base" as in Williams et al. (2022) (Williams et al., 2022), and then assigned their orientation as the direction of the vector from base to tip. As a metric for protrusion alignment across an epithelium, we found the dot product of each pair of protrusions present in the same frame, and then took the mean of all dot products. For each protrusion pair, the dot product will be 1 if they have the same orientation, 0 if they are orthogonal to one another, and -1 if they have opposite orientations. Averaging these for an epithelium would yield an alignment score of 1 if all protrusions were perfectly aligned (high vectorial polarity), but could have a score of zero either if protrusions were randomly oriented (no polarity), or if half pointed in each direction along one axis (high axial polarity, no vectorial polarity). We report protrusions' alignment with one another, rather than with the direction of migration, because this is still meaningful in non-migratory epithelia (whether truly non-migratory or only non-migratory ex vivo). In migrating epithelia, protrusion-protrusion alignment and

protrusion-migration alignment measurements were highly correlated.

Quantification of Fat2-3xGFP fluorescence at cell-cell interfaces and the basal surface

Egg chambers expressing Fat2-3xGFP were stained with anti-Dlg to label cell edges, stage 6-7 egg chambers were imaged, and the cells were segmented using the pretrained "cytoplasm" model in Cellpose applied to the Dlg channel. Subsequent analysis steps were performed in Python using scikit-image and scipy libraries. Gaps between segmented cells were closed with a watershed algorithm seeded by the initial segmented regions, and segmentation errors were then manually corrected using napari. Mean fluorescence intensity was calculated at cell-cell interfaces (boundaries between segmented cells dilated by 10 px) and the entire in-focus basal surface.

Measurement of fluorescence intensity at leading-trailing interfaces

Leading-trailing interface regions were annotated by hand based on phalloidin staining using Fiji (ImageJ) (Schindelin et al., 2012; Schindelin et al., 2015): 10 px-wide segmented lines were drawn along leading-trailing interfaces and then the mean fluorescence intensity across those interfaces was calculated. In experiments with non-mosaic epithelia, at least 10 leading-trailing interfaces were measured. For more information about measurement in mosaic epithelia, see the next section. Note that no correction was performed for background fluorescence, so the proportional relationship between fluorescence intensity measurements should not be interpreted as corresponding directly to the proportional relationship between protein levels.

Analysis of localizing interactions and their cell autonomy

Analysis of protein localization in genetically mosaic epithelia was used to disentangle cell- and interface-scale protein-localizing interactions from the tissue-wide effects of genotype on planar polarity and migration. It was also used to determine the cell autonomy of localizing interactions. Interpretations of the cell autonomy of effects on Lar or Sema5c's localization were made based on the much greater enrichment of Lar and Sema5c at leading edges than trailing edges in normal circumstances (Barlan et al., 2017; Stedden et al., 2019) (see Fig. 3.1C). In epithelia mosaic for a loss-of-function mutation (generated using the Flp/FRT system), cells with the chromosome containing the wild-type allele were marked with a nucleus-enriched fluorophore, and "control" cells include both homozygous wild-type and heterozygous cells. In epithelia mosaic for RNAi expression (generated using the Flp-out system), RNAi-expressing cells were marked with a nucleus-enriched fluorophore. F-actin staining with AlexaFluor 647 phalloidin was used to visually assess whether epithelia were planar-polarized and migratory (based on stress fiber alignment across the epithelium), their migration direction (based on the orientation of leading edge protrusions), and to check for regions of tissue damage that could otherwise be misinterpreted as genetic clones. Egg chambers were included in subsequent analysis if they were within stage 6-7, had planar-polarized actin stress fibers, and had both control and mutant/RNAi-expressing cells in view with at least three leading-trailing interfaces between cells of each genotype combination. Mean fluorescence intensity at individual leading-trailing interfaces was then measured as described in the previous section, with all leading-trailing interfaces at genotype boundaries, and a similar number of clone-internal ones, included. Plots show intensities rescaled per sample such that the mean fluorescence intensity at leading-trailing interfaces between control cells is equal to 1, and were made using GraphPad Prism 9.

Plotting of protein intensity along an "unrolled" cell perimeter

Plots of "unrolled" cell perimeters were used to display the distributions of Fat2, Lar, and GrabFP-AInt fluorescence around cell perimeters and the correspondence between those distributions. 10 px-wide segmented lines were drawn around the perimeter of cells in Fiji, and fluorescence intensities measured. Using Python, intensities were rescaled for ease of comparison and plotted. Specifically, Fat2-3xGFP and anti-Lar intensities were rescaled such that they had a range of 0 to 1 in the control dataset. GrabFP-AInt was rescaled proportionally to Fat2-3xGFP.

Colocalization of proteins along the leading-trailing interface

Multi-channel confocal imaging was performed, and resulting images analyzed, to determine the degree of colocalization between pairs of fluorophore-tagged proteins (Abi-mCherry and Fat2-3xGFP, Lar-3xGFP, Sema5c-3xGFP, E-cadherin(Shg)-GFP) along leading trailing interfaces. Images of the basal plane of follicle cells were acquired with a 63x/1.4 NA Plan-APOCHROMAT oil immersion objective to minimize chromatic aberration. In Fiji, 10 px-wide segmented lines were drawn along rows of leading-trailing interfaces. At least 20 leading-trailing interfaces were included per egg chamber, and fluorescence intensities at each position along the lines measured. Spearman's correlation coefficients were calculated for each egg chamber using the scipy statistics module in Python. As E-cadherin is fairly uniformly distributed along all cell-cell interfaces, correlation between E-cadherin-GFP and Abi-mCherry serves as a baseline for spurious correlation caused by the measurement region-drawing method and correlated effects of interface shape on the intensity distribution of both fluorophores. The plot was made using GraphPad Prism 9.

Quantification of fluorescence distributions along filopodia

The fluorescence intensity distributions of proteins along the lengths of many filopodia were used to obtain representations of their typical distribution. Epithelia expressing Abi-mCherry and either Fat2-3xGFP, Lar-3xGFP, or Sema5c-3xGFP were stained with AlexaFluor 647 phalloidin. In Fiji, for one cell per egg chamber, 1 px-wide lines were drawn along the lengths of each filopodium identified phalloidin staining. Subsequent data processing and plotting was all performed in Python. Fluorescence intensity traces from along different filopodia were registered using the highest-intensity Abi-mCherry pixels, a proxy for the filopodia tips. Standard deviations were calculated for each fluorophore after rescaling traces so that their values each ranged from 0 to 1. For plotting, data were first averaged, then rescaled from 0 to 1.

FRAP analysis of protein exchange at leading-trailing interfaces

Photobleaching was performed on samples mounted and imaged as described in previous sections using the timed bleaching tool in Zen Blue. Focusing at the basal surface plane, leading-trailing interface regions between two vertices, excluding those vertices, were selected for bleaching. Lar-3xGFP, $fat2^{N103\text{-}2}$ and Sema5c-3xGFP, $fat2^{N103\text{-}2}$ epithelia were non-migratory and lacked planar polarity, so any interfaces were used. Up to four interfaces were bleached per egg chamber, always from non-neighboring cells. Two frames were acquired before bleaching, bleaching performed once, and then timelapse acquisition continued for a total of either 8 minutes (at 10 sec/frame) or 30 minutes (at 30 sec/frame). Bleached interfaces were excluded from analysis if the majority of the interface length was not bleached, the bleached region encompassed a cell vertex, or the bleached interface was not in view throughout the timelapse. Fluorescence intensity measurements were made using Fiji. Rectangular regions were drawn around the bleached interfaces and the same number of non-bleached interfaces, the positions of these regions were translated in each time point as needed to fol-

low interface movement, and the mean intensity of each was measured. Subsequent analysis and plotting was performde using Python. Mean fluorescence per time point was calculated separately for bleached and unbleached regions, and the mean of the unbleached regions used to rescale the bleached regions to correct for the effects of progressive photobleaching and region selection inaccuracy. The bleach-corrected values were then rescaled so that the time point just before bleaching had a value of one, and the time point just after bleaching zero. Standard deviations were calculated for each time point from the mean intensities of individual bleached regions after they were rescaled in the same manner. For calculation of the time to half recovery, single exponential curves of the form $I(t) = A(1 - e^{-\tau * t})$ were fit to data from individual interfaces, where I is fluorescence intensity, t is time, and the parameters A (the immobile fraction) and τ are fit. Time to half recovery ($\tau_{1/2}$, $\frac{ln(0.5)}{-\tau}$) was then calculated for each interface. In each of the Sema5c-3xGFP and Lar-3xGFP $fat2^{N103\text{-}2}$ datasets there was one interface with a time to half recovery that was higher than the others by 3-4 orders of magnitude, and these were excluded.

Reproducibility and statistical analysis

Two or more biological replicates were performed for each experiment, with each containing egg chambers pooled from multiple flies, and results confirmed to be qualitatively consistent between them. Visibly damaged egg chambers were excluded from all analyses. No randomization of treatment groups was performed, and experiments were not performed with blinding. Sample sizes were not predetermined using a statistical method. The number of egg chambers, interfaces, and/or filopodia (n) analyzed for each experiment can be found in the associated figure or figure legend. Statistical tests performed and their significance can also be found in figures or figure legends. An alpha of 0.05 was used to determine significance in all cases, but we have also attempted to plot data distributions in ways that allow the reader to weigh their similarities and differences for themselves. Statistical testing was

all conducted using GraphPad Prism 9. Based on visual inspection, all datasets appeared normally distributed, and statistical tests assuming normalcy were used throughout. All t-tests were two-tailed. A one-way ANOVA was used when more than two conditions were compared. A repeated measures one-way ANOVA was used for analysis of genetic mosaic epithelia, in which multiple genetic conditions were present in the same tissue. Welch's corrections were performed and Dunnet's T3 multiple comparison tests used for datasets in which the variance did not appear consistent between conditions (indicated in figure legends). Otherwise, post-hoc Tukey's multiple comparison tests were used. Initial and post-hoc multiple comparisons testing was conducted on all data present in the corresponding plots with two exceptions: in Fig. 3.5C, only data including the same fluorophore were compared, and in Fig. 3.11B, data from conditions with gray and white background shading were collected and analyzed separately.

Table 3.1: Experimental genotypes for Chapter 3

Figure	Panel	Name	Genotype
3.1	B	Sra1	w1118 ;; Sra1-GFP/+
3.1	C	Fat2	w1118 ; tj>Gal4, UAS>Flp/+; Fat2-3xGFP FRT80B/FRT80B
3.1	C	Lar	w1118 ; Lar-3xGFP FRT40A/FRT40A; t155>Gal4, UAS>Flp/+
3.1	C	Sema5c	w1118 ; tj>Gal4, UAS>Flp/+; Sema5c-3xGFP FRT80B/FRT80B
3.1	E-G	Fat2	w1118 ; ubi>Abi-mCherry, Fat2-3xGFP FRT80B/Fat2-3xGFP FRT80B
3.1	E-G	Lar	w1118 ; Lar-3xGFP FRT40A ; ubi>Abi-mCherry/+
3.1	E-G	Sema5c	w1118 ; ubi>Abi-mCherry, Sema5c-3xGFP FRT80B/Sema5c-3xGFP FRT80B
3.1	F	E-cadherin	w1118 ; Shg-GFP/+ ; ubi>Abi-mCherry/+
3.2	A-C	Fat2	w1118 ;; Fat2-3xGFP FRT80B
3.2	A-C	Lar	w1118 ; Lar-3xGFP FRT40A

Table 3.1: Experimental genotypes for Chapter 3 (continued)

3.2	A-C	Sema5c	w1118 ;; Sema5c-3xGFP FRT80B
3.2	D	Fat2-3xGFP mos.	w1118 ; tj>Gal4, UAS>Flp/+ ; Fat2-3xGFP FRT80B/FRT80B
3.3	A	Lar-3xGFP	w1118 ; Lar-3xGFP FRT40A
3.3	A	anti-Lar	w1118
3.3	B,C	Control	w1118
3.3	B,C	Lar-3xGFP x1	w1118 ; Lar-3xGFP FRT40A/+
3.3	B,C	Lar-3xGFP x2	w1118 ; Lar-3xGFP FRT40A
3.3	B	$lar^{13.2/bola1}$	w1118 ; $lar^{13.2}$ FRT40A/lar^{bola1}
3.3	D,E	Lar in $fat2^{N103-2}$ mos.	w1118 ; Lar-3xGFP FRT40A/tj>Gal4, UAS>Flp ; $fat2^{N103-2}$ FRT80B/ubi>mRFP-NLS FRT80B
3.4	A,B	Sema5c in fat2-RNAi mos.	hs>Flp, w1118 ; UAS>fat2-RNAi/+ ; Sema5c-3xGFP FRT80/act5c>CD2>Gal4, UAS>mRFP-NLS
3.4	C,D	Sema5c in fat2-RNAi mos.	w1118 ; lar13.2 FRT40A/ubi>mRFP-NLS FRT40A ; Sema5c-3xGFP FRT80B/ t155>Gal4, UAS>Flp
3.4	E	fat2-RNAi/Control	hs>Flp, w1118 ; UAS>fat2-RNAi/+ ; Sema5c-3xGFP FRT80/act5c>CD2>Gal4, UAS>mRFP-NLS
3.4	E	$lar^{13.2}$/Control	w1118 ; lar13.2 FRT40A/ubi>mRFP-NLS FRT40A ; Sema5c-3xGFP FRT80B/ t155>Gal4, UAS>Flp
3.5	A	All images	w1118
3.5	B,C,D	Fat2	w1118 ;; Fat2-3xGFP FRT80B
3.5	B,C	Lar	w1118 ; Lar-3xGFP FRT40A
3.5		Sema5c	w1118 ;; Sema5c-3xGFP FRT80B
3.6	B-D,F	Control	w1118 ; tj>Gal4/+ ; Fat2-3xGFP FRT80/+
3.6	B-D,F	+GrabFP-A^{Int}	w1118 ; tj>Gal4/+ ; Fat2-3xGFP FRT80/UAS>GrabFP-AInt-mCherry
3.7	A,B	Control	w1118 ; tj>Gal4/+
3.7	A,B	lar-RNAi	w1118 ; tj>Gal4/UAS>lar-RNAi

Table 3.1: Experimental genotypes for Chapter 3 (continued)

3.7	A,B	Sema5c^{K175}	w1118 ; tj>Gal4/+ ; Sema5cK175 FRT80B
3.7	A,B	lar-RNAi, Sema5c^{K175}	w1118 ; tj>Gal4/UAS>lar-RNAi ; Sema5cK175 FRT80B
3.7	C	Control	w1118 ; tj>Gal4/+
3.7	C	lar-RNAi	w1118 ; tj>Gal4/UAS>lar-RNAi
3.8	A,B,E	Sema5c^{K175} mos.	w1118 ; tj>Gal4, UAS>Flp/+; Sema5c^{K175} Fat2-3xGFP FRT80B/ubi>mRFP-NLS Fat2-3xGFP FRT80B
3.8	C,D,E	Sema5c^{K175} mos. lar-RNAi	w1118 ; tj>Gal4, UAS>Flp/UAS>lar-RNAi; Sema5c^{K175} Fat2-3xGFP FRT80B/ubi>mRFP-NLS Fat2-3xGFP FRT80B
3.9	A,B	Sema5c^{K175} mos. Lar	w1118 ; tj>Gal4, UAS>Flp/Lar-3xGFP FRT40A ; Sema5c^{K175} FRT80B/ubi>mRFP-NLS FRT80B
3.9	C,D	Sema5c^{K175} mos. Sra1	w1118 ; tj>Gal4, UAS>Flp/+ ; Sema5c^{K175} FRT80B Sra1-GFP/ubi>mRFP-NLS FRT80B
3.10	B-I	Fat2	w1118 ;; Fat2-3xGFP FRT80B
3.10	B-I	Lar	w1118 ; Lar-3xGFP FRT40A
3.10	B-I	Lar fat2^{-}	w1118 ; Lar-3xGFP FRT40A ; fat2N103-2 FRT80B
3.10	B-I	Sema5c	w1118 ;; Sema5c-3xGFP FRT80B
3.10	B-I	Sema5c fat2^{-}	w1118 ;; Sema5c-3xGFP fat2N103-2 FRT80B
3.10	J,K	Fat2-3xGFP x1	w1118 ;; Fat2-3xGFP FRT80B/+
3.10	J,K	Fat2-3xGFP x2	w1118 ;; Fat2-3xGFP FRT80B
3.10	J,K	Lar-3xGFP x1	w1118 ; Lar-3xGFP FRT40A/+
3.10	J,K	Lar-3xGFP x2	w1118 ; Lar-3xGFP FRT40A
3.10	J,K	Sema5c-3xGFP x1	w1118 ;; Sema5c-3xGFP FRT80B/+
3.10	J,K	Sema5c-3xGFP x2	w1118 ;; Sema5c-3xGFP FRT80B
3.11	A-E	Control (w^{1118})	w1118
3.11	A-E	fat2^{N103-2}	w1118 ;; fat2N103-2 FRT80B
3.11	A-E	lar$^{13.2/bola1}$	w1118 ; lar13.2 FRT40A/larbola1
3.11	A-E	Sema5c^{K175}	w1118 ;; Sema5cK175 FRT80B
3.11	A-E	tj>Gal4, lar-RNAi, Sema5c^{K175}	w1118 ; tj>Gal4/UAS>lar-RNAi ; Sema5cK175 FRT80B
3.11	B	Control (tj>Gal4)	w1118 ; tj>Gal4/+

Table 3.1: Experimental genotypes for Chapter 3 (continued)

3.11	B	tj>Gal4, lar-RNAi	w1118 ; tj>Gal4/UAS>lar-RNAi
3.11	B	tj>Gal4, Sema5c^{K175}	w1118 ; tj>Gal4/+ ; Sema5cK175 FRT80B
3.11	C,D	CK-666	w1118
3.12	A,B	Control (w^{1118}	w1118
3.12	A,B	fat2$^{N103\text{-}2}$	w1118 ; fat2$^{N103\text{-}2}$ FRT80B
3.12	A,B	lar$^{13.2/bola1}$	w1118 ; lar$^{13.2}$ FRT40A/lar^{bola1}
3.12	A,B	Sema5c^{K175}	w1118 ; Sema5c^{K175} FRT80B
3.12	A,B	tj>Gal4, lar-RNAi, Sema5c^{K175}	w1118 ; tj>Gal4/UAS>lar-RNAi ; Sema5cK175 FRT80B

Table 3.2: *Drosophila* culture conditions for Chapter 3

Figure	Panel	Days on yeast	Temp. (°C)
3.1	B	2-3	25
3.1	C - Fat2	3	25
3.1	C - Lar	5	25
3.1	C - Sema5c	3	25
3.1	E-G	2-3	25
3.2	A-C	2-3	25
3.2	D	3	25
3.3	A	2-3	25
3.3	B,C	2	25
3.3	D,E	3	25
3.4	A,B	See methods for head shock protocol	
3.4	C,D	5	25
3.4	E	see A,B and C,D	
3.5	A-D	2-3	25
3.6	B-D,F	3	29
3.7	A-C	3	29
3.8	A,B	3	25
3.8	C,D	first 2	25
		then 1	29
3.8	E	see A,B and C,D	
3.9	A,B	3	25
3.9	C,D	3	25
3.10	B-I	2	25
3.10	J,K	2-3	25
3.11	A,C-E, B gray (except below)	2	25
3.11	tj>Gal4, lar-RNAi, $Sema5c^{K175}$ in A,C-E,B gray	2	29
3.11	B white	2	29
3.12	A,C-E, B gray (except below)	2	25
3.12	tj>Gal4, lar-RNAi, $Sema5c^{K175}$ in A,C-E,B gray	2	29

CHAPTER 4

TRANSIENT EXTRACELLULAR CALCIUM CHELATION REVERSES FOLLICLE CELLS' POLARITY AND MIGRATION DIRECTION

4.1 Preface

This chapter contains unpublished data from my work on the effects of treating egg chambers with the extracellular calcium chelator EGTA, and of restoration of normal calcium levels following EGTA treatment. The flow chamber design used in many of these experiments was developed with advice from Allison Zajac and published in the following book chapter:

Zajac, A. L., Williams, A. M., & Horne-Badovinac, S. (2023). A Low-Tech Flow Chamber for Live Imaging of Drosophila Egg Chambers During Drug Treatments. In M. S. Giedt & T. L. Tootle (Eds.), *Drosophila Oogenesis: Methods and Protocols* (pp. 277–289). Springer US.

4.2 Introduction

Across different organisms and tissues in which planar polarity has been studied, and across multiple protein signaling systems, basic features of the planar polarity signaling architecture remain the same. Planar polarity is achieved through positive feedback between local asymmetric signaling across cell-cell interfaces and mechanical or biochemical cues that align interface polarities across the tissue (Lavalou & Lecuit, 2022). The unconventional planar signaling that promotes follicle cell migration is no exception to this general architecture—local signaling between the leading and trailing edges of neighboring cells partitions motility behaviors to opposite sides of the interface, and mechanical feedback from tissue movement provides a global axis to which that interface signaling aligns (Barlan et al., 2017;

Cetera et al., 2014; Stedden et al., 2019; Viktorinová & Dahmann, 2013; Williams et al., 2022; Williams & Horne-Badovinac, 2023). The atypical cadherin Fat2 is a core part of this polarity circuit, acting to couple interface- and tissue-wide cues. From its position at the trailing edge of each cell, it localizes migration-regulating signaling proteins Lar and Sema5c in puncta at the leading edge, where they polarize motility behaviors across those interfaces (Barlan et al., 2017; Stedden et al., 2019; Williams & Horne-Badovinac, 2023) The resulting alignment of neighboring cells' motility machinery facilitates collective migration, and that movement in turn reinforces Fat2's polarization to trailing edges (Barlan et al., 2017; Williams et al., 2022).

This description of follicle cells' planar polarity circuit comes mainly from experiments using genetic manipulations such as loss-of-function fat2 mutations or protein depletion with RNAi. Because these approaches provide limited time resolution, we know little about the timescales over which Fat2 is polarized by tissue movement or maintains the planar organization of interfaces once polarized. Planar polarity arises gradually and during a stage of egg chamber development when the tissue is small and contains few cells (Cetera et al., 2014; Chen et al., 2016), making polarity detection challenging. Because of this, we have not yet been able to follow the emergence of planar polarization in individual epithelia. Acute pharmacological perturbations provide an avenue to overcome these limitations. One such perturbation is treatment with the small-molecule Arp2/3 inhibitor CK-666, which rapidly halts follicle cell migration through disruption of cells' leading edge protrusions (Cetera et al., 2014). CK-666 treatment was used to demonstrate that the alignment of stress fibers depends on ongoing collective migration in stage 5 egg chambers, but loses this dependence by stage 7 (Cetera et al., 2014). Complementing CK-666 treatment, I demonstrate in Chapter 3 (Williams & Horne-Badovinac, 2023) that the extracellular calcium chelator EGTA can be used to acutely disrupt Fat2 function. Ca^{2+} binding at sites between adjacent cadherin repeats contributes to the rigidity of the extracellular domains of both classical and atypical

cadherins, and removal of calcium causes these domains to become less structured and disrupts their ability to participate in binding interactions (Kim et al., 2011; Nagar et al., 1996; Tsukasaki et al., 2014). Upon treatment of follicle cells using EGTA, the planar polarity of Lar, Sema5c, and protrusions is rapidly lost, consistent with strong disruption of Fat2's ability to stabilize them at leading edges. Together, CK-666 and EGTA provide complementary tools for disrupting follicle cells' collective migration and planar polarity at the level of the cell motility machinery (CK-666) and Fat2-dependent planar signaling (EGTA).

The basic efficacy of CK-666 and EGTA has been demonstrated, but the potential for elucidation of follicle cells' polarization and depolarization dynamics using treatment and release from these inhibitors remains unrealized. After confirming that EGTA treatment stops follicle cell migration, I use a flow chamber mounting and media exchange method to demonstrate that migration can resume after either CK-666 or EGTA washout. Surprisingly, whereas CK-666-treated egg chambers resumed migration in their original direction after washout, EGTA-treated egg chambers consistently resumed migration in the opposite direction. I constrain possible reversal mechanisms by repeating the assay under different genetic, developmental, and inhibitor treatment conditions. I then investigate the dynamics of cell movement, protrusion, and the organization of planar signaling proteins during the reversal arc. These preliminary studies provide a general timeline for the repolarization of cell structures and proteins upon restoration of Fat2 function. They build a foundation for future studies of the assembly and polarization dynamics of Fat2-based puncta, and of the relationship between movement and planar organization in follicle cells. Finally, they hint at the presence of local negative feedback within the polar signaling circuit normally at work in follicle cells.

4.3 Results

Calcium chelation with EGTA rapidly and reversibly stops follicle cell migration

I previously showed that calcium removal with the extracellular calcium chelator EGTA causes phenotypes in fixed tissue that are similar to those of null fat2 mutations, consistent with EGTA strongly inhibiting Fat2 function (see Chapter 3; Williams and Horne-Badovinac, 2023). As a further test of Fat2 inhibition, I checked whether EGTA treatment stopped follicle cell migration. I began treating egg chambers with 20 mM EGTA and then mounted and imaged them within the EGTA-containing media, which introduced a delay of approximately five minutes between the start of treatment and the start of imaging. By the beginning of imaging, no EGTA-treated egg chambers were migrating (Fig. 4.1A,B). This shows that EGTA treatment rapidly blocks follicle cell migration and further supports the efficacy of EGTA as an inhibitor of Fat2 function.

I next wanted to know if, and how, follicle cell migration resumes from this stopped state. I previously found that aligned F-actin-rich protrusions return within approximately an hour after after washout from EGTA treatment, suggestive of resumed migration. Using live imaging of E-cadherin-labeled epithelia beginning 5 minutes after EGTA washout, I confirmed that the epithelia resume migration over the subsequent 1-2 hours (Fig. 4.1C,D). In the interim, some epithelia passed through periods of up to tens of minutes in which their protrusions were not planar polarized before these gradually aligned as migration accelerated (Fig. 4.1C,D). This period of poorly-polarized protrusive activity is also visible using F-actin staining (Fig. 4.1E).

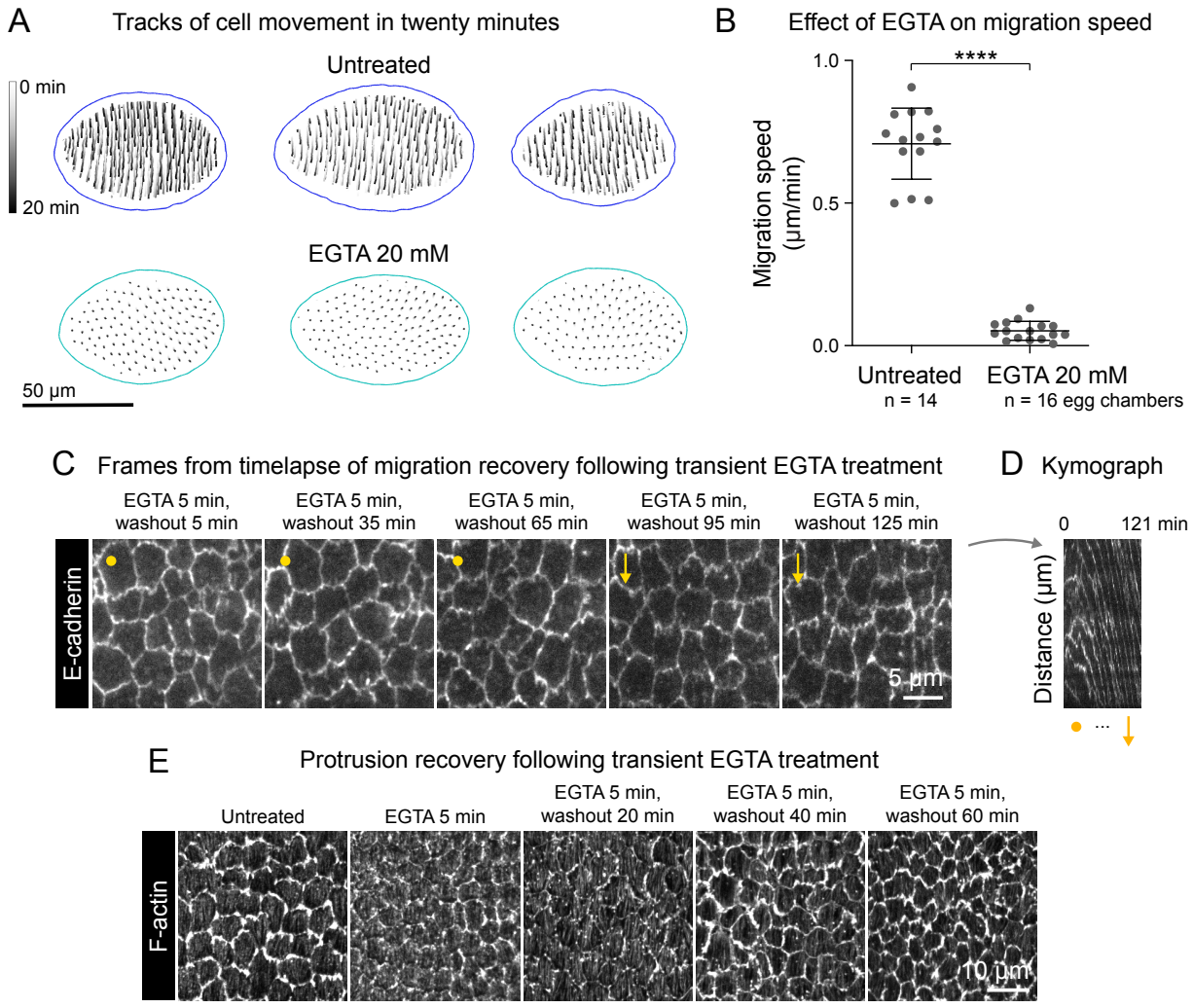

Figure 4.1: **Calcium chelation with EGTA rapidly, reversibly stops follicle cell migration.** **A**, Tracks of cell movement over twenty minutes in untreated epithelia and epithelia treated with EGTA. **B**, Plot of tissue migration speeds in EGTA-treated epithelia and untreated controls. EGTA treatment strongly inhibits follicle cell migration. Unpaired t-test; ****$p<0.0001$. **C**, Frames from a timelapse movie of the basal surface of follicle cells following washout from 5 minutes of EGTA treatment. Cells' lateral edges are labeled with E-cadherin-GFP. The planar polarity of cell protrusions increases, and migration begins, over 1-2 hours. **D**, Kymograph showing the acceleration of cells from the timelapse in (C). Steeper negative slope in the E-cadherin signal indicates faster migration, which accelerates from a non-migratory (horizontal) initial state. **E**, Images showing the basal surface of epithelia before and during EGTA treatment, and after different periods of EGTA washout. Phalloidin staining of F-actin shows the level and distribution of protrusive F-actin structures. These are reduced by EGTA treatment, and then progressively return and planar-polarize over 1-2 hours following EGTA washout.

Follicle cell migration reverses direction following transient EGTA treatment, but not CK-666 treatment

During normal egg chamber development, the direction of follicle cell migration is selected stochastically, but then maintained stably. Follicle cells' ability to repolarize their protrusions following EGTA treatment raised the question of whether they were undergoing a new stochastic polarity decision or their original polarity persisted through treatment. Testing this required a new mounting approach that would allow me to image the same egg chamber before and after EGTA treatment. I developed a simple flow chamber that holds an egg chamber in place using compression between a slide and a bead-supported coverslip while allowing exchange of the surrounding media and nearly-continuous imaging (Zajac et al., 2023). Using this flow chamber, I imaged the same egg chamber before, during, and after 5-10 minutes of EGTA treatment, with 1-2 minute imaging pauses between each phase during media exchange. Follicle cells were marked with either CellMask or a variety of genetically-encoded fluorescent markers. In each case, I found that follicle cells re-initiated migration in the opposite of their original direction following EGTA washout (n = 26/26, Fig. 2A-C). This surprising result shows that some form of leading edge-trailing edge polarity information persists through the EGTA treatment window, but that this information or its interpretation has an effect on polarity opposite that of untreated egg chambers, resulting in migration reversal.

To determine whether migration reversal is a general consequence of transient migration halt, I performed the same washout assay using the Arp2/3 inhibitor CK-666. Treatment with 0.75 μM CK-666 also stopped follicle cell migration. However, these epithelia resumed migration in their original direction in all cases (n = 4/4, Fig. 4.2A-C). Migration reversal is therefore a more specific consequence of calcium chelation rather than a general effect of stopping migration, and may be mediated specifically by Fat2 disruption.

Follicle cell migration is required for the planar polarity of the cells' migration-regulating

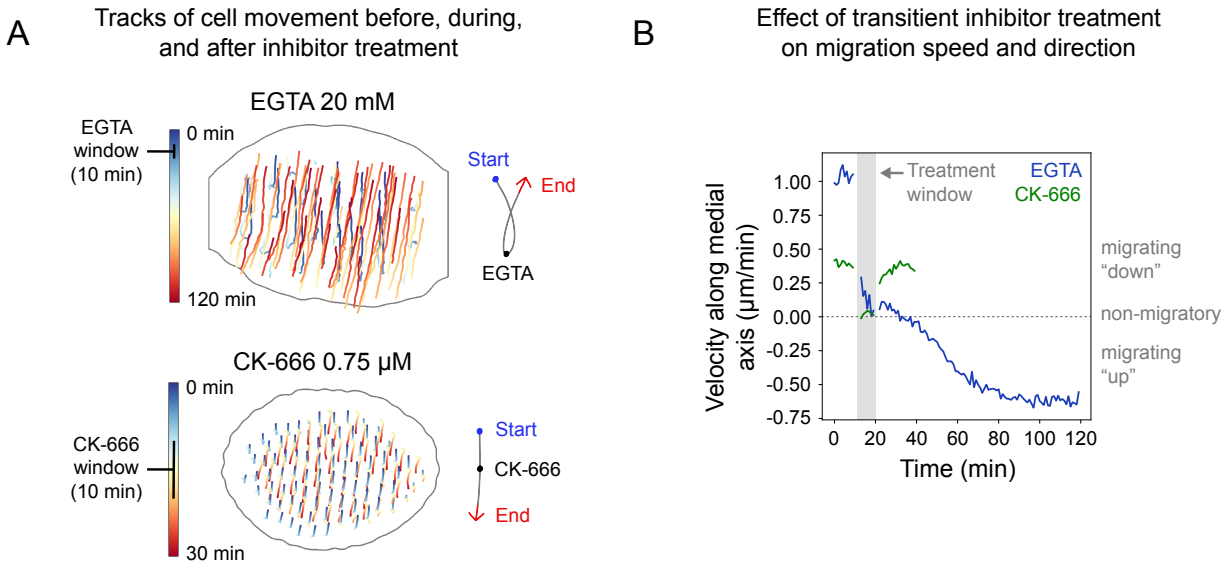

C Direction of migration resumption following inhibitor washout

Treatment	Original	Reverse
EGTA	0	26
CK-666	4	0

n (egg chambers)

D Effect of different genetic and treatment conditions on migration resumption following EGTA treatment

Genotype	Treatment	Initial state	After washout	n
fat2$^{\Delta ICD}$*-3xGFP*	5 min EGTA	Migratory	Reversed	1
fat2$^{\Delta ICD}$*-3xGFP*	5 min EGTA	Non-migratory	No migration	1
Sema5c^{K175}	5 min EGTA	Migratory	No migration	2
w^{1118}	30 min EGTA	Migratory	Reversed	1
w^{1118}, stage 3-5	5 min EGTA	Migratory	Reversed	2

Figure 4.2: **Transient EGTA treatment, but not CK-666 treatment, consistently reverses the direction of follicle cell migration.** **A**, Tracks of follicle cell movement from egg chambers before, during, and after EGTA or CK-666 treatment. The time after inhibitor washout differs between the two conditions. Manual image registration was used to correct for sample movement during media exchanges, but residual movement causes jogs in the tracks. **B**, Plot of the migration velocity of epithelia in (A). The original migration direction is "down" and has positive velocity. Migration resumes in the original direction rapidly after CK-666 washout, but more gradually and in the opposite direction after EGTA washout. **C**, Table showing the effect of transient EGTA or CK-666 treatment on the directionality of migration resumption relative to the original migration direction. Migration consistently reversed after EGTA treatment, but resumed in its original direction after CK-666 treatment. Samples are pooled from epithelia expressing a variety of different genetically encoded fluorescent markers or stained with CellMask. **D**, Table showing the effect of different genetic, treatment, and developmental conditions on the presence/absence and direction of migration resumption following EGTA washout. All data are from stage 6-7 egg chambers unless noted. Sample size (n) = egg chambers.

signaling proteins and motility machinery, but the timescale on which migration maintains planar polarity is not known. To see if longer periods of EGTA treatment and stopped migration would remove polarity information and lead to a new stochastic polarization outcome, I performed the transient EGTA treatment assay with the treatment window extended to 30 minutes. Migration reversed on a similar timescale to epithelia treated for 5-10 minutes following washout, suggesting that polarity information was still able to persist over this period. However, additional repetitions would be necessary to distinguish between this possibility and a new stochastic direction selection.

I next tested the involvement of planar polarity and migration-regulatory proteins in migration reversal, focusing on mutations that do not entirely prevent migration. In epithelia with a truncated form of Fat2 lacking its intracellular domain (Fat2$^{\Delta ICD}$-3xGFP), the Fat2$^{\Delta ICD}$ protein is poorly planar-polarized and migration is either slow or stopped. Performing the transient EGTA treatment assay in this background, I found that a slowly-migrating epithelium was still able to reverse its migration direction at a similar timescale to wild-type epithelia (n = 1) but an epithelium that was originally non-migratory remained so (n = 1). Performing the same assay with slowly-migrating epithelia lacking the migration-regulatory protein Sema5c ($Sema5c^{K175}$), migration did not resume following EGTA washout (n = 2). These preliminary experiments would need to be repeated to determine whether these outcomes were stochastic or deterministic. However, they show that the intracellular domain of Fat2 is not strictly required for polarity reversal, and that epithelia lacking Sema5c have a compromised ability to resume migration.

The experiments described so far in this chapter were all performed on egg chambers between developmental stages 6 and 7, at which point the cells' migration speed is at its fastest and egg chamber features such as the elongation of the tissue and the fibrillar structure of the basement membrane could serve as sources of axial polarity information. Performing the transient EGTA treatment assay at earlier stages with fewer cells, slower migration, and

lacking these axial polarity features, I found that they still reversed migration on a similar timescale to stage 6-7 egg chambers (n = 1x S3-4, 1x S4-5). This shows that developmental changes that occur between these stages are not likely to strongly influence the ability of the epithelium to resume or reverse migration.

Cells' planar polarity reverses with follicle cell migration

Fat2 orchestrates follicle cells' polarization and migration by signaling from the trailing edge of each cell to the leading edge of the cell behind (Barlan et al., 2017; Williams et al., 2022; Williams & Horne-Badovinac, 2023). Fat2 is progressively cleared from trailing edges during EGTA treatment (Chapter 3; Williams and Horne-Badovinac, 2023), implying that it must relocalize to cells' new trailing edges on the opposite side of the cell for migration to resume and reverse. To follow the dynamics of Fat2's relocalization at the basal surface after EGTA treatment, I generated epithelia mosaic for expression of Fat2-3xGFP, and imaged them through the transient EGTA treatment assay using TIRF microscopy. At clone boundaries, where it is possible to distinguish trailing edge from leading edge localization, Fat2-3xGFP was initially strongly enriched at trailing edges, had reduced basal surface enrichment following EGTA treatment, and then accumulated at cells' new trailing edges following EGTA washout (Fig. 4.3A). Following the repolarization timeline in more detail, I saw that Fat2-3xGFP levels at trailing edges at the basal surface decreased gradually during EGTA treatment, but then more rapidly in the minutes after washout (Fig. 4.3A). Fat2-3xGFP then gradually accumulated at the cells' new trailing edges during the tens of minutes following washout, and had not yet achieved clear enrichment at the new trailing edges until after tissue migration had clearly reversed and begun to accelerate (Fig. 4.3A). These observations show that migration reversal coincides with reorganization of the polarity of Fat2, and suggest that migration can resume, and reverse, with much less Fat2 enrichment and planar polarization than is present under normal circumstances. The rapid clearance

of Fat2 from (former) trailing edges following EGTA washout also hints that there is some source of calcium-dependent negative regulation of Fat2 at this site, which could contribute to migration reversal.

Fat2 regulates polarity and migration in large part by concentrating the effectors Lar and Sema5c at leading edges, and either loss of Fat2 or EGTA treatment eliminates Lar and Sema5c's enrichment at leading edges (Barlan et al., 2017; Williams & Horne-Badovinac, 2023). To determine how they then repolarize during migration resumption/reversal, I generated epithelia mosaic for Lar-3xGFP and followed its localization through transient EGTA treatment as I had with Fat2-3xGFP. Within the 1-2 minutes in which imaging was paused following EGTA treatment, Lar-3xGFP had lost planar polarization, consistent with data from fixed tissue (Chapter 3; Williams and Horne-Badovinac, 2023). Upon washout, its enrichment at cell-cell interfaces rapidly increased, although not to its initial levels and without any apparent planar polarization. It then progressively further increased in enrichment at basal cell-cell interfaces and in planar-polarization over tens of minutes as migration resumed (Fig. 4.3B), similar to Fat2-3xGFP. Interestingly, Lar-3xGFP was enriched at protrusion tips even during the early, pre-migratory phase of recovery in which protrusions formed transiently at positions away from eventual leading edges. The time resolution of these data (2-3 min/frame) was insufficient to determine whether Lar-3xGFP accumulation or protrusion formation preceded the other. Fat2-3xGFP did not appear to exhibit this dynamic protrusion tip association. This suggests that Lar has the ability to achieve a degree of enrichment at protrusion tips with little or no Fat2 present. Interestingly, in one case there was a transient Lar-3xGFP polarity "conflict" between two regions of the tissue, with one patch of cells polarized and protruding in the opposite direction from the other for a period of several minutes before resolving into coherent polarization (Fig. 4.3C). Altogether, the repolarization dynamics of Lar and Fat2 demonstrate that migration reversal coincides with wholesale leading edge-trailing edge polarity reversal, and that the repolarization mech-

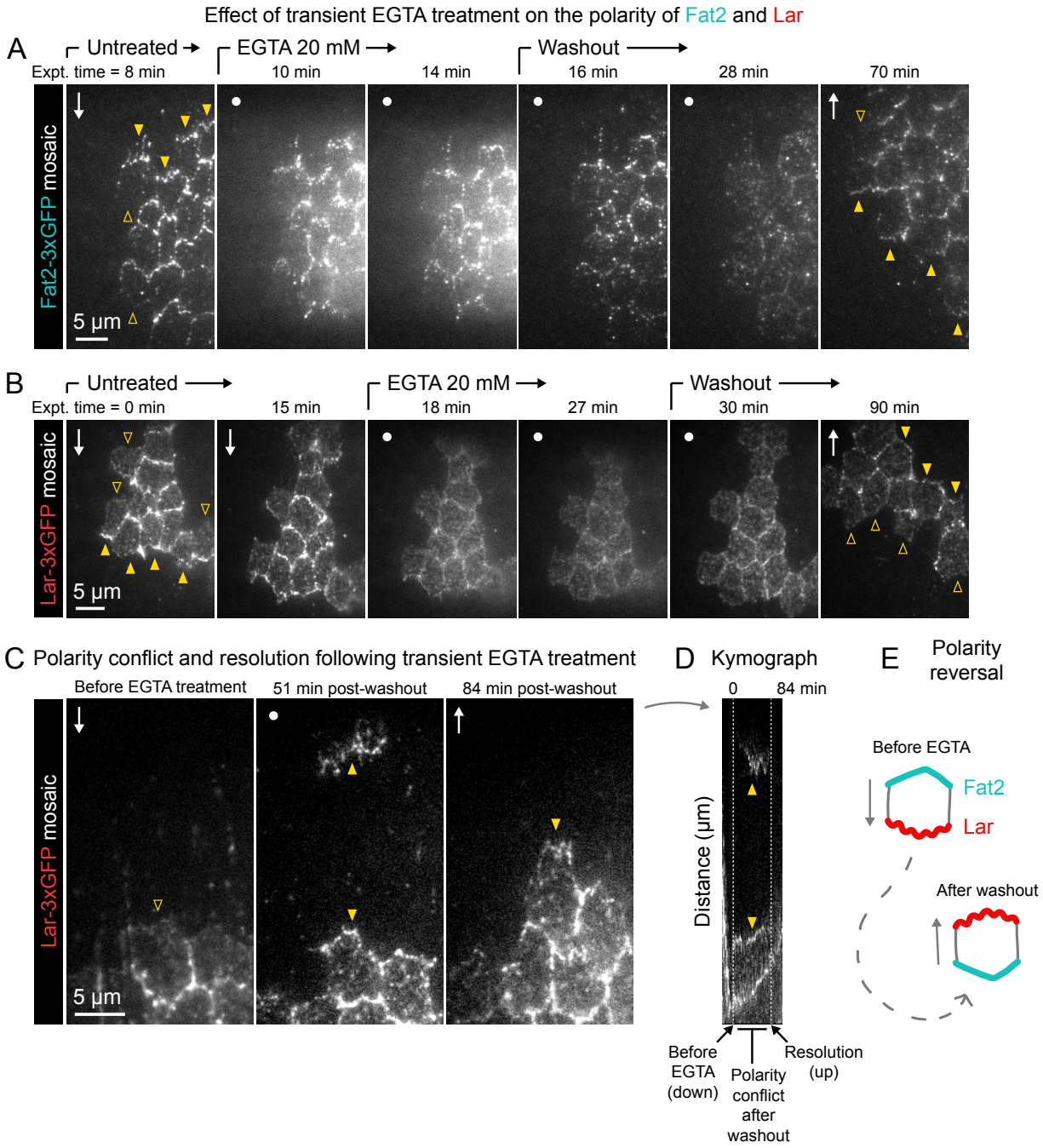

Figure 4.3: **The polarity of Fat2 and Lar reverses along with migration following transient EGTA treatment.** Continued on next page.

Figure 4.3: **The polarity of Fat2 and Lar reverses along with migration following transient EGTA treatment (continued). A-C**, Frames from timelapse movies of epithelia with mosaic expression of Fat2-3xGFP or Lar-3xGFP, acquired before, during, and after transient EGTA treatment. The migration state of the epithelium is indicated by white arrows (the migration direction) or circles (non-migratory) in the upper left corner of each image. Protein enrichment at clone boundaries is indicated with yellow arrowheads: filled arrowheads indicate high enrichment; hollow arrowheads indicate low enrichment. Image display brightness varies between treatment conditions. **A**, Fat2-3xGFP is enriched at trailing edges before EGTA treatment and this enrichment persists through 6 minutes of EGTA treatment, but is reduced following EGTA washout. It then accumulates at cells' new trailing edges as migration resumes in the reverse direction. **B**, Lar-3xGFP is enriched at leading edges before EGTA treatment, but loses that enrichment within 3 minutes of EGTA treatment. It regains some enrichment at cell-cell interfaces within 3 minutes of EGTA washout, and it increases in enrichment and polarization to cells new leading edges over the subsequent hour as migration resumes in the reverse direction. **C**, Frames from a timelapse movie showing that polarity "conflict" can occur within an epithelium, with cells in different tissue regions polarized in different directions. Filled yellow arrows in the center panel indicate Lar-3xGFP enrichment at oppositely-oriented leading edges. This conflict ultimately resolves with Lar-3xGFP polarized opposite its pre-treatment polarity. **D**, Kymograph from the timelapse movie in (C), showing the periods before, during, and after Lar-3xGFP polarity "conflict." Arrows indicate Lar-3xGFP enrichment at both downward-pointing and upward-pointing leading edges prior to migration resumption. **E**, Diagram showing the effects of transient EGTA treatment on the polarities of Fat2 and Lar along cells' leading edge-trailing edge axes. Arrows indicate migration direction.

anisms of these two proteins are partly distinct. The appearance of regions with different local polarities prior to global polarity establishment also shows that tissue-wide polarity reversal does not simply result from each cell independently reversing polarity. Instead, individual cells appear to polarize in variable directions but with a bias towards reversal, and the tissue then comes to consensus around reversal through subsequent cell-cell signaling.

In addition to Fat2 and Lar, a wide range of cytoplasmic proteins and organelles are planar-polarized at follicle cells' basal surfaces, and their planar organization is also reinforced by migration through unknown mechanisms. These include microtubules, which are aligned along cells' leading edge-trailing edge axes with their plus ends biased towards the trailing edge, and Rab10+ compartments, which are enriched at trailing edges through plus end-directed transport along those microtubules. Manipulating migration with EGTA

treatment and imaging using TIRF microscopy, I tested the timescale on which migration is required to maintain polarization of microtubules (*ubi*>Jupiter-mCherry) and Rab10+ compartments (*UAS*>YFP-Rab10). Within 10 minutes of EGTA treatment, the planar polarity of microtubules was reduced, and within 30 minutes it was not detectable (Fig. 4A). Over the same period, Rab10+ compartments progressively lost enrichment at trailing edges, and their overall levels at the basal surface were also gradually reduced (Fig. 4.4A). Upon washout from EGTA, microtubules regained their alignment along leading-trailing axes, and their dynamics suggested that they were anchored at cells' new trailing edges (Fig. 4.4B). Rab10+ compartments also repolarized as migration resumed, becoming enriched at cells' new trailing edges as microtubule alignment increased (Fig. 4.4B). These observations serve as a proof of principle that transient EGTA inhibition can be used to follow the reorganization of the cytoskeleton and organelles in response to changes in tissue movement.

Additional consequences of EGTA treatment

Beyond disrupting Fat2 function and migration, extracellular calcium chelation could disrupt a range of additional proteins and aspects of egg chamber homeostasis. This includes other cadherins such as N-cadherin and E-cadherin, which maintain cell-cell adhesion in follicle and nurse cells. To better understand any unintended effects of EGTA on cell adhesion and tissue architecture, I acquired timelapse movies of the crosssections of egg chambers expressing E-cadherin-GFP and bathed in fluorescent dextran, which labels extracellular space. There were no apparent changes in E-cadherin distribution or follicle cell architecture within 10 minutes of EGTA treatment (Fig. 4.5A), consistent with data from fixed tissue (Chapter 3; Williams and Horne-Badovinac, 2023). It is possible that follicle cells' E-cadherin and N-cadherin are not strongly affected by EGTA treatment, although I favor the explanation that their binding is inhibited, but that the follicle cells' confinement between a basement membrane and nurse cells in a pressurized tissue minimizes the short-term morphological

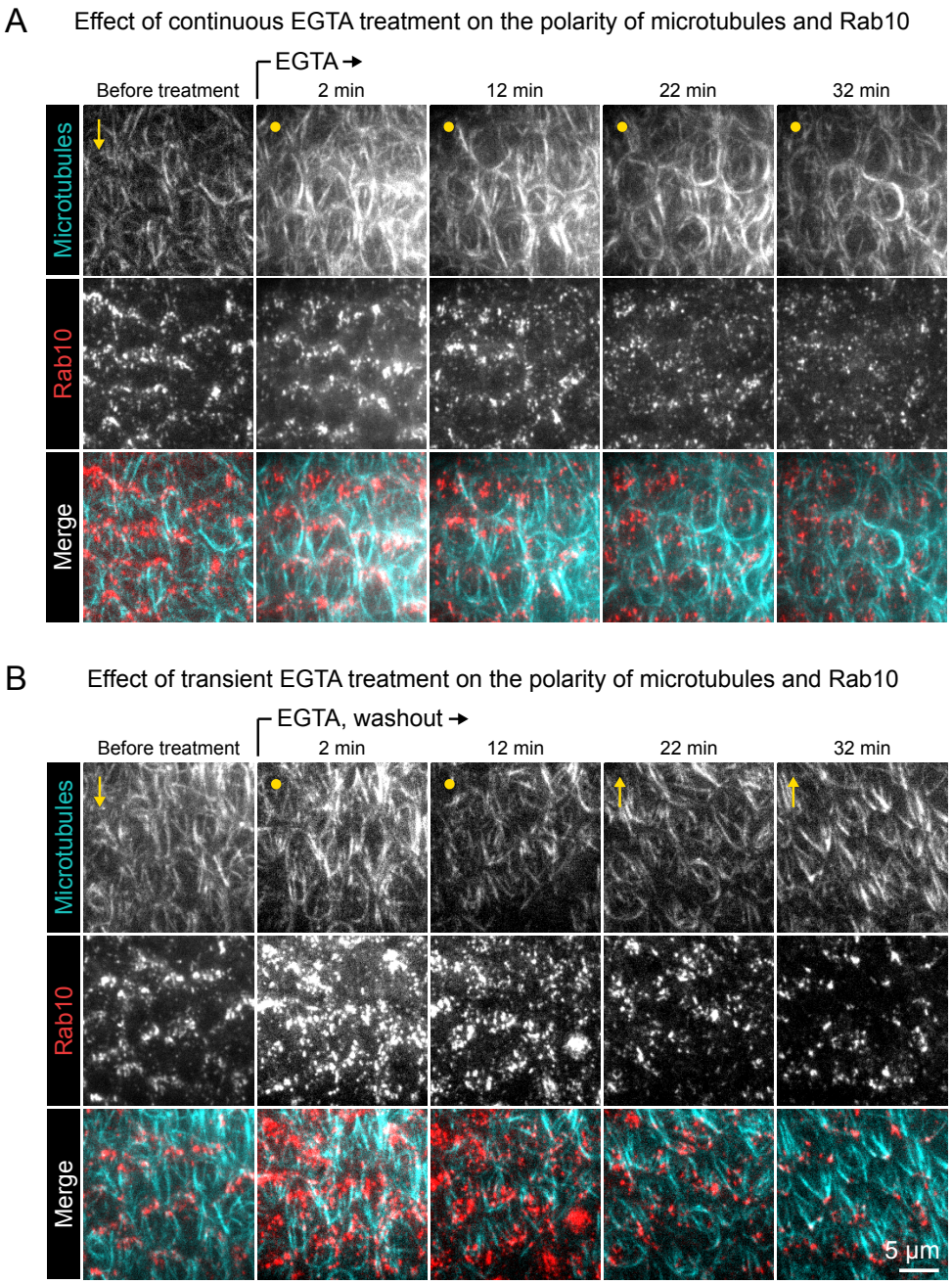

Figure 4.4: **The planar-polarization of microtubules and Rab10+ compartments is progressively lost when migration is stopped, and reversed along with migration reversal.** Continued on next page.

effects of this change. Nurse cell architecture, however, was altered by EGTA treatment–dextran-labeled gaps rapidly opened between the nurse cells (Fig. 4.5A). Interestingly, over the subsequent 10 minutes of continued treatment, the egg chamber contracted and the

Figure 4.4: **The planar-polarization of microtubules and Rab10+ compartments is progressively lost when migration is stopped, and reversed along with migration reversal (continued). A,B**, Frames from timelapse movies of the basal surfaces of epithelia expressing Rab10 and microtubule labels (*UAS*>YFP-Rab10 and *ubi*>Jupiter-GFP, respectively). The migration state of the epithelium is indicated by yellow arrows (the migration direction) or circles (non-migratory) in the upper left corner of each image. Image display brightness varies between treatment conditions. **A**, . **B**, Frames showing an epithelium before EGTA treatment and then during continuous EGTA treatment. The planar polarity of microtubules and Rab10 are both progressively lost during EGTA treatment. **C**, Frames showing an epithelium before EGTA treatment and then after washout from 5 minutes of EGTA treatment. The planar polarity of microtubules and Rab10 reverse along with migration.

gaps closed such that the tissue appeared smaller, but otherwise normal, by the end of the treatment window (Fig. 4.5A,B). The initial gap-opening is consistent with loss of cadherin-based adhesion, but the mechanism and significance of subsequent gap closing and tissue contraction is not clear. I also assessed changes in follicle cells' cytoplasmic calcium dynamics using the reporter GCaMP6m. Before EGTA treatment, follicle cells exhibited cytoplasmic calcium fluctuations that last for one to several minutes and exhibit no apparent spatiotemporal correlation across the epithelium (Fig. 4.5C). Upon EGTA treatment, those fluctuations stopped rapidly and cells exhibited uniform low GCamP6m fluorescence (Fig. 4.5C). Upon EGTA washout, calcium fluctuations resumed, beginning with an increase across many cells and then losing synchronization (Fig. 4.5C). This shows that extracellular calcium chelation does alter intracellular calcium dynamics, but that this effect is reversible.

Finally, I noticed that the brightness of a wide variety of fluorescent markers increased sharply upon EGTA treatment, but returned to its original levels after washout (see especially Figs. 4.3A; 4.4A,B). This change appeared to be driven by increased autofluorescence rather than a specific effect on an individual marker, and was especially pronounced for the collection of GFP data and during TIRF imaging. Consequently, to enable discernment of the subcellular distributions of labeled proteins, the display levels of frames from timelapse movies in several figure panels have been adjusted separately per treatment condition.

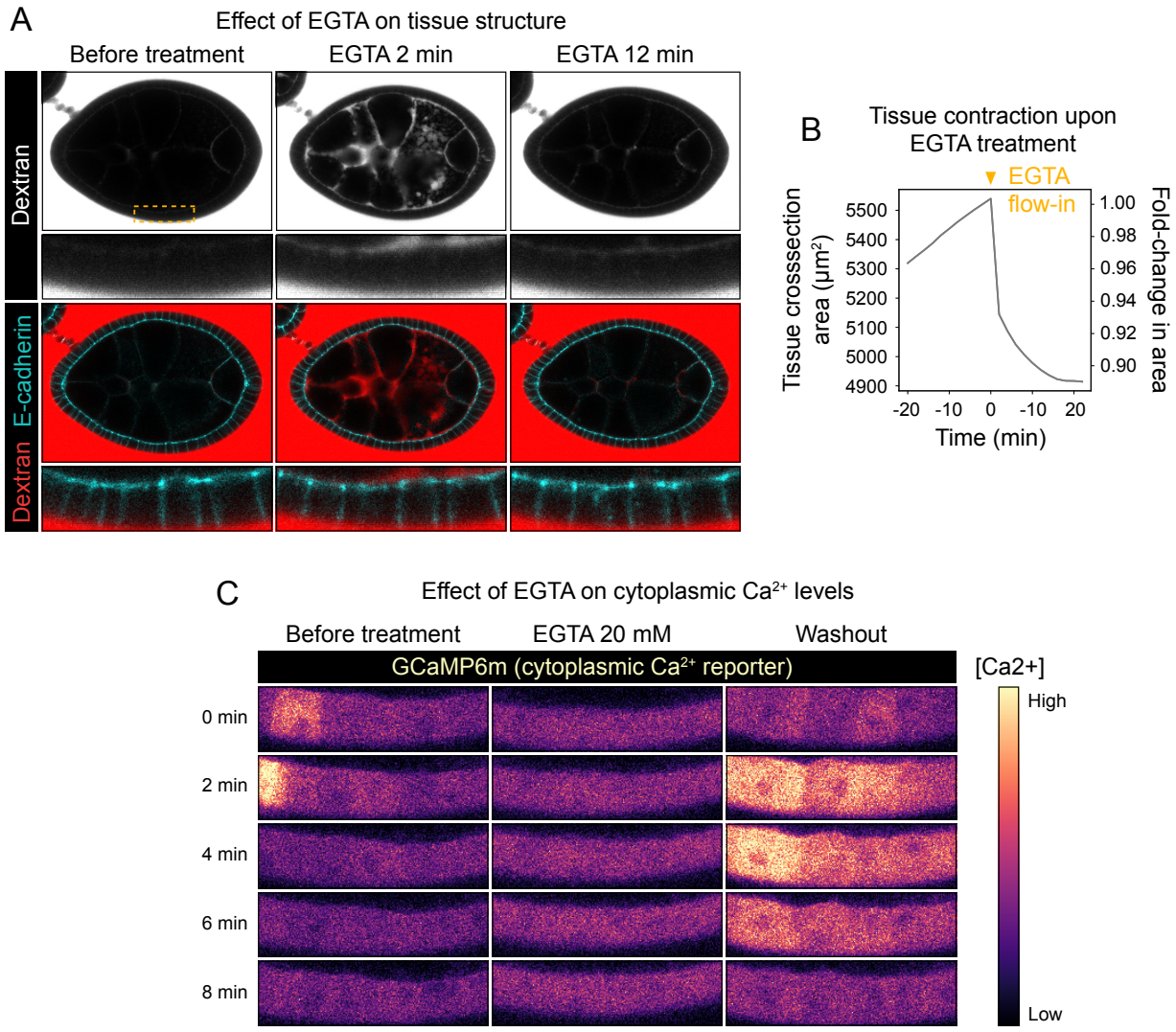

Figure 4.5: **EGTA treatment alters tissue architecture and cytoplasmic calcium dynamics.** **A**, Frames from a timelapse movie of the cross section of an egg chamber before and during EGTA treatment. The egg chamber is labeled with E-cadherin-GFP, and extracellular space is labeled with fluorescent dextran. EGTA treatment causes a rapid increase in the space between nurse cells, but no apparent changes in follicle cell architecture or E-cadherin distribution. The space between closes over 10 minutes of continuous EGTA treatment. **B**, Plot showing the cross-sectional area of the egg chamber shown in (A) over time. The tissue contracts rapidly during EGTA treatment, and this contraction coincides with the closing of the gaps between nurse cells. **C**, Frames from a timelapse movie showing a cytoplasmic calcium reporter (GCaMP6m) in cross sections of several follicle cells before, during, and after 10 minutes of EGTA treatment. Transient increases in cytoplasmic calcium stop rapidly following EGTA treatment, and resume more synchronously upon EGTA washout.

4.4 Discussion

This work demonstrates the efficacy of EGTA as a rapid, reversible inhibitor of Fat2 function and follicle cell migration. In addition, it shows that transient EGTA treatment can be used to change the planar polarity and migration direction of follicle cells after they have begun to migrate, the first condition known to do so. This enables mapping out of the reorganization of planar signaling proteins, the cell motility machinery, and other cell structures through transitions between migratory and non-migratory states, and through cells' polarity reversal. Although this reversal occurs under conditions that are not normally experienced by follicle cells, the fact of the reversal may nevertheless provide information about the polarity circuit normally at work. In addition, the mechanisms by which proteins and structures repolarize during reversal are likely to share important features with the mechanisms by which their polarity is normally maintained.

EGTA treatment has proven informative about the organization of Fat2-based planar signaling puncta, first in data presented in Chapter 3 and built upon using live imaging here. The rapid loss of Lar and Sema5c's punctate organization and planar polarization upon EGTA treatment suggests that Fat2 continuously maintains their enrichment by acting as a trap against diffusion within the plasma membrane. This is not a general effect of blocked migration, as CK-666 treatment does not disrupt Lar's planar polarity or punctate distribution (cetera diss). In contrast to Lar and Sema5c, Fat2 maintains its punctate organization following EGTA treatment and takes tens of minutes to lose its enrichment at trailing edges and the basal surface. This longer timescale, and the fact that entire Fat2 puncta are cleared at once, suggest that Fat2 is removed from the trailing edge by endocytosis when its extracellular domain structure or binding interactions are disrupted. Cadherins are often endocytosed more rapidly when their extracellular domains are unbound (cite), and it is possible that the same is true of Fat2. Alternately, the rate of endocytic turnover of Fat2 could be normal, and Fat2's gradual reduction at trailing edges could be caused by lower

rates of arrival there following EGTA treatment. The data reported here were collected at a time resolution of minutes to enable imaging of the entire repolarization arc while minimizing photobleaching and phytotoxicity. With faster TIRF imaging and sparse protein labeling, it should be possible to follow the arrival, disappearance, and movement of individual molecules of Fat2 and Lar at the basal surface under normal circumstances, and to determine how these dynamics are altered by Fat2 disruption with EGTA or protrusion/migration inhibition with CK-666. These data could provide information about how Fat2 polarizes Lar and Sema5c and about the mechanism of Fat2's polarization to trailing edges.

Curiously, although there was some remaining Fat2 enrichment at trailing edges after 5-10 minutes of EGTA treatment, its disappearance accelerated upon EGTA washout such that the period of lowest basal Fat2 enrichment occurred several minutes after EGTA was removed, not at the moment of washout. This suggests some source of negative regulation on Fat2 stability at the original trailing edges, and could also contribute to migration reversal. In addition, it suggests that migration reversal is driven by newly-secreted Fat2, rather than by movement of Fat2 across the basal surface from the original trailing edge to the new one. It is also notable that migration resumed before Fat2 had become clearly polarized to new trailing edges. This may indicate that the initial migration reversal is independent of polarized Fat2 signaling, or that a small degree of Fat2 polarization is sufficient to begin this process. Fat2 continued to accumulate at new trailing edges as migration accelerated, perhaps aided by tissue movement. Single-molecule TIRF imaging could be used to determine whether Fat2's accumulation at the new trailing edges results from polar secretion, stabilization, directed movement within the plasma membrane, or some combination of these.

The mechanism of migration reversal remains mysterious, but experiments reported here weigh (preliminarily) against several possibilities. One such possibility was that migration reversal was a general consequence of stopping migration transiently, for example mediated by elastic recoil of the basement membrane (cite theory paper). However, the fact that

migration does not reverse following CK-666 treatment argues against this, as does the ability of reversal to occur after 30 minutes of EGTA treatment, in which time it is likely that strain in the basement membrane or the epithelium would have dissipated. In addition, although the direction of follicle cell migration reliably reversed following transient EGTA treatment (+- 15° or so), there were indications that this reversal was not deterministic at the level of each individual cell. Protrusions sometimes re-formed directly at cells' new leading edges, but in several cases they first formed all around cell perimeters with no apparent planar polarity and then coalesced gradually to the new leading edges. In some epithelia, one patch of cells initially reformed Lar/protrusion polarity and started to move in its original direction before eventually reversing course, seemingly as a consequence of the overriding influence of neighbors' polarity and movement in the opposite direction. Once, a +1 topological defect formed away from the egg chamber poles, and cells moved rotationally around it. This set of observations is best explained by a model in which EGTA treatment biases each cell towards repolarization away from its initial direction, but that bias is not sufficiently strong to reliably repolarize every individual cell. Instead, it appears that a majority of cells reverse polarity, and these then drive the reversal of any remaining cells through some combination of biochemical and mechanical signaling. Transient EGTA treatment could therefore potentially be used to watch the propagation of polarity across an epithelium, although it would be challenging to disentangle cells' own bias towards reversal from the influence of their neighbors.

How might global EGTA treatment/Fat2 inhibition bias cells toward polarity and migration reversal? A recent study documented similar reversal in the migration of neutrophils in response to a global perturbation, in that case global ontogenetic upregulation of PIP3 production. There, they showed that reversal was driven by local negative feedback on Rac activity that is normally present but masked by sources of positive feedback. The global perturbation removed spatial variation in positive feedback on Rac, uncovering the local

negative feedback as the remaining polarized part of the circuit. Because of this negative feedback on Rac operating at the original leading edge, Rac activation and protrusion formation were biased elsewhere, and the cells tended to repolarize in the opposite direction (Town & Weiner, 2022). It is possible that follicle cells' polarity circuit similarly involves local negative feedback that is unmasked by EGTA treatment. Such feedback could operate on the cell motility machinery directly, as in the neutrophil example, or on Fat2 or other components of the planar signaling system. If it operates on the cell motility machinery, that might explain the ability of follicle cells to repolarize and begin to migrate in the reverse direction prior to apparent re-establishment of Fat2 polarity.

I also performed several preliminary experiments testing the role of different planar signaling proteins, or domains of those proteins, in migration reversal. The intracellular domain of Fat2 contributes to regulation of both its levels and planar polarity within the cell membrane. However, it does not appear to mediate repolarization of Fat2 to cells new trailing edges. Additional repetitions would be necessary to confirm that polarity consistently reverses, and to test whether the timescale of repolarization differs between wild-type Fat2 and Fat2dICD. In two cases, slowly-migrating epithelia lacking Sema5c failed to reverse, suggesting that Sema5c does play a role in migration reversal. However, Sema5cK175 epithelia normally undergo very slow migration that is difficult to preserve ex vivo, so although it is possible that Sema5c itself mediates polarity reversal, it is also possible that the failure of migration to resume was a more general consequence of the compromised motility of these epithelia in combination with the disruption of long-term ex vivo imaging.

I have mainly presented data on the effects of transient EGTA treatment here, and used transient CK-666 treatment only to test the generality of migration reversal following its disruption. However, CK-666 could be a more widely useful, complementary tool to EGTA. Because it stops follicle cell migration while leaving the planar signaling puncta intact, it provides an avenue for testing the mechanism by which tissue movement feeds back on cells'

planar polarity.Specifically, it could be informative to follow the distribution and dynamics of Fat2 in continuous CK-666 treatment to determine on what timescale, and how, its planar polarity decayed in the absence of migration. For example, it might be the case that puncta would gradually spread out along cell-cell interfaces without tissue movement, or that a loss of biased Fat2 secretion would lead to a gradual reduction in the number or size of puncta at the trailing edge and formation of new puncta elsewhere. In addition, it may be possible to treat epithelia with CK-666 for sufficiently long that planar polarity is lost, and then to observe a new stochastic polarization event upon CK-666 washout. To map out the arc of polarity reorganization, I performed many repetitions of the transient EGTA treatment assay with a variety of different genetically encoded markers and imaging modalities. Although these data collectively provide a consistent picture of the general trajectory of cell repolarization and migration reversal, this exploratory data collection mode makes it challenge to directly, quantitatively compare different datasets. As a simple extension of this work, it would be valuable to quantitatively compare the timelines of protein redistribution, the emergence of planar polarity, cell elongation (which correlates with migration) and cell movement itself. This would reveal the variation among different epithelia, and the temporal relationship between migration resumption and the polarization of different proteins and structures. I used a simple flow chamber design and wicking-based media exchange method to perform transient inhibitor treatments, which allowed imaging of one epithelium across different media treatments, but with a time delay of 1-2 minutes during which imaging was paused for media exchange. This approach cannot be used to follow events that unfold within tens of seconds following EGTA treatment or washout. For more detailed studies of protein dynamics that make use of this assay, it will be important to improve on the flow chamber design to eliminate this blind spot.

Finally, I note that although EGTA treatment conveniently does not cause major changes to the structure of the follicular epithelium, it does cause a range of consequences to the tissue

beyond effects on planar polarity and migration. For one, it transiently reduces the adhesion between nurse cells, which are then closed during ongoing EGTA treatment by what appears to be a global tissue contraction. The contraction and nurse cell gap closure could be caused by an upregulation of a non-cadherin-based adhesion program, or changes in the contractility or osmotic pressure of the cells. The contraction phenomenon points to an interesting tissue homeostasis mechanism, perhaps one that is engaged in contexts beyond this very unnatural one. EGTA treatment also alters cytoplasmic calcium dynamics, although since we do not know the importance of these dynamics under normal circumstances, it is unclear what the consequences of this change might be. Lastly, EGTA treatment led to a large increase in tissue autofluorescence during the treatment window, and this effect was particularly prominent in live imaging data collected using TIRF microscopy. The biological basis for this change is unclear, although one possibility is that it is caused by a change in the levels of NADH or NADPH, or by a shift in the localization of the mitochondria in which they are concentrated, as these molecules are major contributors to cells' autofluorescence. This autofluorescence may make it challenging to quantitatively compare the levels of fluorescent proteins across different phases of the transient EGTA treatment assay.

4.5 Methods

Drosophila sources, care, and genetics

The genotypes of animals used in each experiment are provided in Table 4.1. Note that data on the direction of migration resumption following transient EGTA and CK-666 are pooled from w^{1118} epithelia and ones expressing a number of different fluorophore-tagged proteins, listed in the table. *Drosophila* were raised as described in Chapter 2. Experimental females were given yeast and aged in the presence of males prior to dissection, generally for 2-3 days at 25°C. The specific temperature and number of days used for each experiment are listed

in Table 4.2.

Live imaging sample preparation

Ovarioles were dissected into live imaging media and, if applicable, stained with CellMask, as described in Chapter 2. For experiments in which EGTA treatment was performed prior to imaging, ovarioles were then transferred to a second well containing 20 mM EGTA in live imaging media. They were then mounted in the same media between a slide and a 22x22 mm #1.5 coverslip supported by glass beads and sealed with vaseline. For imaging of S3-5 egg chambers, 31 μm beads were used. For imaging of S6-7 egg chambers, 51 μm beads were used.

EGTA treatment with phalloidin staining

Ovarioles were dissected into live imaging media and then transferred to either new live imaging media ("untreated") or live imaging media with 20 mM EGTA (all other conditions). For "washout" samples, after 5 minutes of EGTA treatment they washed out of EGTA into live imaging media and left for 20, 40, or 60 min. Wells were covered with a slide to minimize evaporation during incubations. After the final treatment, ovarioles were fixed and stained with phalloidin as described in Chapter 2.

Flow chamber construction and media exchange

To image the same chamber during inhibitor treatment and before or after treatment, or both, egg chambers were mounted in a flow chamber. Flow chambers were constructed as described in Zajac et al., 2023. Briefly, two lines of vacuum grease were drawn in parallel $\sim$1 cm apart to form the walls of the flow channel. The sample was placed in the center, between the two lines, and 51 μm beads (for S6-7 egg chambers) or 31 μm beads (for S3-5 egg chambers) were added. A 22x30 mm#1.5 coverslip was placed over the channel and

depressed until it contacted the beads. For TIRF microscopy (inverted microscope), the vacuum grease lines and coverslip ran orthogonal to the long axis of the slide, such that the coverslip formed an overhang on either of the slide to enable media wicking. For confocal microscopy (upright microscope), the lines and coverslip ran parallel to the slide's long axis. Samples were then imaged. For media exchanges, imaging was paused and a 10 uL drop of the new media was placed next to and in contact with one open side of the channel. Whatman filter paper was placed in contact with the media on the other side of the channel such that old media was absorbed and the new droplet wicked into the channel. This was repeated two more times for a total of 30 uL exchanged. If no subsequent media exchanges were to be performed, the two open sides of the channel were sealed with vaseline. The sample was then re-centered within the field of view and the microscope focus corrected if necessary, and then imaging was resumed. There was typically a two minute pause in imaging during media exchange. For EGTA treatment, live imaging media with 20 mM EGTA was used. For CK-666 treatment, live imaging media with 0.75 μm CK-666 was used. Treatments were performed for 5-10 minutes unless otherwise stated, typically after 5-10 minutes of pre-treatment imaging. For imaging of extracellular space before and during EGTA treatment, 1:1000 AlexaFluor 647 dextran (10,000 MW) was added to the initial mounting media and to the EGTA-containing exchange media.

Microscopy

Imaging of all fixed samples was performed using a Zeiss LSM800. Imaging of live samples was performed using either a Zeiss LSM800 or a Nikon TIRF microscope. Laser scanning microscopy was used in Figs. 4.1A,B,E; 4.2A-C (CK-666); 4.5A-C. TIRF microscopy was used in Figs. 4.1C,D; 4.2A-C (EGTA) , 4.2D; 4.3A-D; 4.4A,B. See Chapter 2 for more detailed information about these microscopes. For timelapse movies acquired across media exchanges, the sample often shifted during media exchange, so portions of the movie acquired before

and after media exchange were registered manually using ImageJ (Fiji). With the exception of the S3-5 egg chambers in Fig. 2D, all data were collected from S6-7 egg chambers.

Measurement of migration speed

Timelapse movies of the medial plane of S6-7 follicular epithelia were acquired using multipoint imaging. Cells were segmented and tracked, cells near the medial region identified, and their migration speeds measured as described in Chapter 3. Migration speeds were plotted using GraphPad Prism. For measurement of velocity change over time, the direction and speed of cell movements were measured for each pair of consecutive frames. Intervals spanning media exchanges were excluded due to sample movement caused by the media exchange. Velocity along the medial axis and tracks of cell centroid movement were plotted for one EGTA-treated and one CK-666-treated egg chamber.

Measurement of egg chamber cross-sectional area

The egg chamber was segmented in each frame of a timelapse movie taken in cross-section. The dextran channel (inverted) was used for segmentation. The area of the segmented tissue and its fold-change relative to the frame before EGTA treatment was then plotted over time using Python.

Reproducibility and statistical analysis

Although there are a large number of repetitions of the transient EGTA treatment assay, repetitions with any given marker or mutant condition are low, or in some cases only one. Aside from the dataset of migration speeds with and without EGTA treatment, or the pooled datasets showing the frequency of follicle cell migration reversal following EGTA washout, data presented here bear repeating prior to publication. All statistical testing was performed in GraphPad Prism.

Table 4.1: Experimental genotypes for Chapter 4

Figure	Panel	Name	Genotype
4.1	A,B	All	w^{1118}
4.1	C,D	E-cadherin	w; Shg-GFP$^{\text{BDSC:60584}}$;
4.1	E	All	w^{1118}
4.2	A,B	All	w; Shg-GFP$^{\text{BDSC:60584}}$;
4.2	C	Treatment: EGTA	y w Dlg-GFP$^{\text{BDSC:59417}}$ (n = 1)
4.2			w;; Fat2-3xGFP FRT80 (n = 2)
4.2			w; Lar-3xGFP FRT80 (n = 4)
4.2			w; Lar-3xGFP FRT40/FRT40; t155>Gal4, UAS>Flp/+ (n = 8)
4.2			w; Shg-GFP$^{\text{BDSC:60584}}$; (n = 6)
4.2			w; tj>Gal4, UAS>Flp/+; Fat2-3xGFP FRT80/FRT80 (n = 2)
4.2			w; tj>Gal4/UAS>MoeABD-mCherry (n = 1)
4.2			w; tj>Gal4/+; UAS>YFP-Rab10/ubi>mCherry-Jupiter (n = 1)
4.2		Treatment: CK-666	w; Shg-GFP$^{\text{BDSC:60584}}$; (n = 2)
4.2			w^{1118} (n = 2)
4.2	D	*fat2*$^{\Delta ICD}$*-3xGFP*	w; *fat2*$^{\Delta ICD}$*-3xGFP* FRT80
4.2		*Sema5c*^{K175}	w;; *Sema5c*^{K175} FRT80
4.2		w^{1118}	w^{1118}
4.3	A	Fat2-3xGFP mosaic	w; tj>Gal4, UAS>Flp/+; Fat2-3xGFP FRT80/FRT80
4.3	B-D	Lar-3xGFP mosaic	w; Lar-3xGFP FRT40/FRT40; t155>Gal4, UAS>Flp/+
4.4	A,B	All	w^{1118}
4.5	A,B	E-cadherin	w; Shg-GFP$^{\text{BDSC:60584}}$;
4.5	C	GCaMP6m	w;; 20xUAS>GCaMP6m$^{\text{BDSC:42750}}$

Table 4.2: *Drosophila* culture conditions for Chapter 4

Figure	Panel	Days on yeast	Temp. (°C)
4.1	A,B	2-3	25
4.1	C,D	2-3	25
4.1	E	2-3	25
4.2	A,B	2-3	25
4.2	C	Fat2-3xGFP mosaic: 3-5 Lar-3xGFP mosaic: 5-7 Other genotypes: 2-3	25
4.2	D	2-3	25
4.3	A	3-5	25
4.3	B-D	5-7	25
4.4	A,B	2-3	25
4.5	A,B	2-3	25
4.5	C	2-3	25

CHAPTER 5

CONCLUSIONS, DISCUSSION, AND FUTURE DIRECTIONS

5.1 Conclusions

During my dissertation work, I studied the planar signaling system that enables the collective migration of *Drosophila* follicle cells. These cells' migration occurs in a tissue, the egg chamber, that can be imaged intact ex vivo and in which the cell-substrate interface is accessible at the tissue surface. This afforded me the opportunity to perform live imaging of cell behaviors and protein distributions at the sub-micron-scale in the context of a collective migration whose tissue structure and substrate are faithful to its in vivo context. This experimental system therefore served as a bridge between the wealth of information about collective epithelial cell migrations from studies in two-dimensional tissue culture and the growing number of studies demonstrating the occurrence of these migrations in different in vivo contexts, in which spatial and temporal resolution are often limitations.

Collective cell migrations can be thought of as cell responses to cues in the extracellular environment that are refined by cell-cell interaction, or conversely as self-organized collective behaviors that can be influenced by those extrinsic cues. These different emphases are helpful in different contexts, and the degree to which the extrinsic cues and self-organized, emergent behavior shape the migration differ across migration models. Because of the unusual closed topology and rotational migration of the follicular epithelium and its stochastic choice of a rotation direction (Haigo & Bilder, 2011), we infer that there are no extrinsic cues that impose a migration directionality or even a bias towards one. This places follicle cell migration far on the self-organized side of the spectrum, which allowed me to isolate contributions tissue-intrinsic cell-cell coordination to collective migration. Although many collective migrations are influenced by extrinsic guidance cues, coordination among the migrating cells also strongly influences their collective response, so principles learned from the

follicle cells are likely to be relevant in collective migrations more broadly.

In the absence of extrinsic guidance cues, follicle cell migration is highly dependent on a planar signaling system that regulates cell motility behaviors and aligns them among neighboring cells. Several planar-polarized transmembrane proteins, Fat2, Lar, Sema5c, and Plexin A, have been identified as participants in the cells' planar signaling (Bateman et al., 2001; Frydman & Spradling, 2001; Stedden et al., 2019; Viktorinová & Dahmann, 2013; Viktorinová et al., 2009), but little was known about how they work together to orchestrate migration or become polarized in order to do so. Since very few distinct planar-polarity-regulating signaling systems have been identified, these proteins provided an opportunity to dissect the organization of an additional one, a step towards the broader aim of understanding commonalities and variations among the protein networks that give rise to planar-polarized tissue organization. This system also served as an opportunity to study the molecular and cellular functions of these proteins, and particularly Fat2, whose loss causes the most severe disruption of follicle cell migration. Fat2 is the sole fly member of the Fat-like cadherins, which have important morphogenetic functions in mammalian organogenesis and are widely implicated in cancer (Badouel et al., 2015; Chen et al., 2022; Morris et al., 2013; Saburi et al., 2012; Tanoue & Takeichi, 2005), but whose molecular functions (and particularly their extracellular domain and trans functions) are poorly understood. Fat2 had been shown to regulate follicle cell protrusion and Lar localization in trans in the follicle cells (Barlan et al., 2017), in which assessment of the cell-autonomy of protein functions is made tractable by fly genetic tools and subcellular imaging resolution. I therefore tackled the questions of how Fat2 regulates protrusions in trans, and more broadly how it polarizes protein composition across leading-trailing interfaces to polarize and align neighboring cells' motility behaviors. The initial characterization of Fat2's localization and function, and that of the other planar signaling proteins, had been performed using fixed imaging. Since polarity and motility are dynamic processes, I used live imaging approaches and a variety of new fly lines, tissue

mounting and imaging methods, and experimental manipulations to extend this work and investigate the stabilization of polarity of Fat2, Lar, Sema5c, and the cell motility behaviors they regulate.

Fat2 acts in trans to entrain WAVE complex activity to leading edges

Investigating Fat2's regulation of leading edge protrusions, I showed that Fat2 concentrates the WAVE complex along the leading edge of each cell through a trans interaction, and that this has the dual effects of polarizing the WAVE complex's distribution within the following cell and orienting the following cell's protrusions toward the Fat2-containing trailing edge of the leading cell (see Chapter 2). In the absence of Fat2, the level and planar polarity of the WAVE complex at basal cell-cell interfaces was reduced, and the remaining WAVE complex population had a less stable distribution around cell edges. Genetic mosaic experiments showed that these were not indirect consequences of loss of tissue-wide planar polarity and migration, as the WAVE complex exhibited similar changes in distribution and dynamics in *fat2*$^{-}$ clones within migratory epithelia. My findings extend previous data showing that Fat2 increases protrusive F-actin enrichment in trans (Barlan et al., 2017), and they further indicate that Fat2 regulates protrusions by positioning the WAVE complex. This recasts some of the findings of Squarr et al., 2016, including data showing that Fat2 localizes the WAVE complex to leading edges, which was interpreted as mediated by a cis binding interaction between the WAVE complex and Fat2's intracellular domain.

Fat2's trans entrainment of WAVE complex activity to leading edges has interesting commonalities with other motility-coordinating signaling systems. Contact-dependent polarization of WAVE complex activity or upstream Rac activity has been observed in a number of cell types and migratory contexts, including during the collective migrations of mammalian kidney epithelial and umbilical vein endothelial cells (Das et al., 2015; Hayer et al., 2016) and upon collision of migrating glial cells (Nakao et al., 2008). In the case of the glial cells,

the WAVE complex localizes symmetrically to either side of the cell-cell interface as a result of recruitment by Protocadherin-10, molecules of which bind homophilically in trans. In the other examples, Rac/WAVE complex recruitment is asymmetric and occurs as a consequence of physical and geometric asymmetries across the interface, further sharpening those asymmetries. Concentration of WAVE complex activity at cell-cell contacts therefore seems to be a versatile tool for modulating cells' motility responses to contact with one another, either promoting continued contact (overcoming a contact inhibition of locomotion response) or promoting contact-following depending on whether it occurs symmetrically or asymmetrically. Coupling the WAVE complex's distribution to the interface-asymmetric cue of trailing edge-polarized Fat2 is critical to follicle cells' contact following behavior.

Lar and Sema5c regulate cell motility behaviors in parallel downstream of Fat2

Fat2/Lar and Sema5c/Plexin A have been investigated largely as distinct sets of regulators of follicle cell migration (Barlan et al., 2017; Stedden et al., 2019), and one of my aims was to determine if, and how, these proteins work together to regulate migration. Using *lar*-RNAi expression in a *Sema5c*$^{-}$ background, I demonstrated that Lar and Sema5c contribute additively to migration speed, showing that they have parallel functions rather than acting strictly in series (see Chapter 3). This is in agreement with data about these two proteins' functions in follicle cells and their homologs' functions in other contexts. In follicle cells, loss of either Lar or Sema5c slows migration, but in other respects their phenotypes differ (Stedden et al., 2019). Sema5c mutant epithelia initiate migration at a later stage of egg chamber development than do wild-type or lar mutant epithelia (Barlan et al., 2017; Stedden et al., 2019). In *lar*$^{-}$ epithelia, cells' leading edges have reduced WAVE complex and F-actin enrichment, and cells frequently protrude rearwards, neither of which occurs in *Sema5c*$^{-}$ epithelia (Barlan et al., 2017; Squarr et al., 2016) (Figs. 3.11, 3.12, 3.9). In

addition, Sema5c overexpression inhibits protrusion in trans (Stedden et al., 2019), which Lar overexpression does not do (Fig. A.2). Together, these data suggest that Lar positively regulates leading edge behavior in cis, and that Sema5c likely antagonizes leading edge behavior in trans. Drawing on the broader literature about these proteins, Lar has been shown to regulate neuronal pathfinding and morphology in cis (Bali et al., 2022; Fukai & Yoshida, 2021; Takahashi & Craig, 2013), and semaphorins typically act in trans as repulsive cues by signaling through plexin receptors (Alto & Terman, 2017; Verhagen & Pasterkamp, 2020), consistent with their proposed cis and trans follicle cell functions, respectively.

There are, however, several pieces of data that complicate this picture of strictly-parallel Lar and Sema5c function at opposite sides of the interface. For one, Lar also regulates follicle cells' ability to retract their trailing edges in trans (Barlan et al., 2017). This phenotype does not appear to be entirely an indirect effect of cis changes to leading edge protrusions, as WAVE complex mutation does not fully reproduce it (Barlan et al., 2017). Lar therefore appears to have some trans role in the regulation of cell motility behavior at trailing edges. In addition, loss of Lar changes the distribution of Sema5c, slightly reducing its enrichment at leading edges (Stedden et al., 2019). The cell-autonomy of this interaction is complex and difficult to interpret from existing data (Fig. 3.4), but one possible explanation is that Lar plays a role in the polarization of Sema5c's distribution across leading-trailing interfaces, such that loss of Lar both reduces the enrichment of Sema5c at leading edges in cis and also enables its accumulation at trailing edges in trans. If Lar regulates interface polarity in this manner, that could also explain the rearwards protrusions and trans tail retraction defects observed in its absence. It is also important to note that although Lar and Sema5c function additively, Sema5c's abnormal localization in lar^{-} epithelia could still partially contribute to *lar* loss-of-function phenotypes. In the case of Sema5c, no cis loss-of-function or overexpression phenotypes have yet been documented in follicle cells (nor has any cellular loss-of-function phenotype), but semaphorin-plexin "reverse signaling" to the semaphorin-

containing cell has been documented in other tissues (Battistini & Tamagnone, 2016) and remains a possibility. Finally, removal of one copy of Lar in epithelia lacking Sema5c suppresses the Sema5c mutant round egg phenotype (Stedden et al., 2019), suggestive of an antagonistic relationship between these two proteins. Additional work will be required to understand how this finding relates to the localizing interaction between the two proteins, but it again suggests a functional interaction between them.

Fat2 organizes polar, interface-spanning protein assemblies

I showed that Fat2 positions the WAVE complex through a local trans interaction, concentrating it in puncta just across the interface from Fat2, and that these puncta sit at the tips of filopodia (see Chapter 2). I likewise found that Fat2 concentrates Sema5c in these puncta (see Chapter 3), as it was previously demonstrated to do for Lar (Barlan et al., 2017). Fat2 is therefore required for the polarization of all leading edge-enriched proteins identified so far, and it accomplishes this by concentrating them locally in trans. It is likely that Fat2 is required for the formation of the puncta, not just for concentration of these proteins within them, since there are no signs of their persistence in its absence. I further found that Sema5c and Lar play little or no role in the localization of Fat2, such that the major trans localizing interactions among polarity-regulating proteins identified so far all proceed from trailing to leading edges. If this pattern holds when we have a more comprehensive list of the proteins in this signaling system, it would be an interesting deviation from other planar cell polarity systems in which a physical interaction between transmembrane proteins on either side of the cell-cell interface is required to scaffold the rest of the protein assembly.

To extend this into a dynamic description of the puncta and the maintenance of their polarized composition, I turned to time-resolved and live imaging approaches (see Chapter 3). I found that Fat2 is required on a timescale of minutes or less to maintain the enrichment of Lar and Sema5c in puncta, and found weak support for a model in which it accomplishes

this by slowing their turnover. Acute calcium chelation with EGTA caused rapid loss of Lar and Sema5c enrichment at leading edges and their more uniform distribution around basal cell-cell interfaces, suggesting that Fat2 concentrates them in puncta by restricting their diffusion within the membrane. Fat2 molecules exchanged more slowly from trailing edges than did Lar or Sema5c from leading edges, consistent with a more central scaffolding role for Fat2, and the average turnover speed of both Lar and Sema5c at cell-cell interfaces increased in the absence of Fat2, indicating that Fat2 plays a stabilizing role. However, this trend was either insignificant (Lar) or complicated by other changes in the protein's fluorescence recovery dynamics (Sema5c), so additional work is needed to corroborate this finding. The FRAP experiments were also limited by my inability to reliably follow individual puncta post-bleaching, which meant that I instead bleached and measured fluorescence recovery along entire cell-cell interfaces. This precludes distinguishing between protein turnover within puncta and the appearance and disappearance of puncta. The EGTA experiments also have the caveat that extracellular calcium chelation likely affects other cadherins and cell processes in addition to Fat2, so it is possible that I was observing the consequences of these non-specific effects rather than of Fat2 inhibition. It will be important to validate my findings with a more specific acute Fat2 inhibition method. Despite these limitations, the combination of EGTA treatment and FRAP experiments allowed me to form the first dynamic description of follicle cells' planar polarity system.

Membrane labeling of protrusions provides rich phenotypic information distinct from F-actin labeling

An important methodological finding of my research has been that membrane labeling of follicle cell protrusions provides distinct, complementary information to F-actin labeling. I used membrane labeling to assess the distributions and dynamics of protrusions at follicle cells' basal surface, in some cases revisiting phenotypes that had been assessed previously using

phalloidin staining of F-actin. Interestingly, the view of protrusivity and protrusion distribution provided by these two approaches diverged in multiple mutant conditions. Whereas phalloidin staining of fat2 mutant epithelia suggested that they have substantially reduced protrusive activity (Barlan et al., 2017; Squarr et al., 2016), membrane labeling indicated a smaller reduction. Phalloidin staining of *lar*$^{-}$ epithelia suggested that they have somewhat reduced protrusivity (Barlan et al., 2017), but membrane labeling showed no reduction (and possibly an excess) of protrusive activity, and interestingly also revealed a population of rearwards protrusions that were not detected with phalloidin staining. These discrepancies are not simply caused by a failure to preserve protrusions through tissue fixation, as live imaging of protrusions in fat2 mutant epithelia labeled with a genetically-encoded F-actin probe showed a similar reduction in protrusive F-actin enrichment to phalloidin staining. Membrane labeling reports the shape of the protruding cell front, whereas F-actin labeling reports the level and distribution of F-actin within the protrusion, so it should perhaps not be surprising that changes to protrusions observed in different perturbation conditions with these two labeling approaches do not always agree. The discrepancy in *fat2*$^{-}$ epithelia shows that Fat2 both increases the level of protrusive activity at the basal surface and changes the architecture of these protrusions, causing them to have higher levels of F-actin enrichment. This could be a byproduct of Fat2's stabilization of the WAVE complex's distribution, which may allow more time for branched actin networks to grow in one region and recruit additional actin regulators such as filopodium-elongating Ena to these sites. Lar may likewise promote F-actin enrichment in protrusions, but to a lesser degree. The detectability of rearwards protrusions in *lar*$^{-}$ epithelia with membrane but not F-actin labeling indicates that these protrusions have very low levels of F-actin enrichment, perhaps again because they are shorter-lived than protrusions at other cell positions. In the future, I suggest using both F-actin and membrane labeling as paired approaches to assess follicle cell motility phenotypes. This likely also applies to studies of cell morphology and motility more broadly. I

would also advocate for live imaging of membrane protrusions as a way to obtain rich, dynamic information about protrusion traits such as their extension speeds and lifetimes while simultaneously collecting data on cell and tissue movement.

Transient extracellular calcium chelation reverses follicle cells' polarity and migration direction

I reported a new acute perturbation, extracellular calcium chelation using EGTA treatment, which rapidly disrupts follicle cells' planar polarity, stops their migration, and causes polarity and migration to reverse upon calcium restoration (see Chapter 4). Although EGTA treatment is not a specific manipulation, there is strong concordance between the acute consequences of EGTA treatment and fat2 mutant phenotypes on planar signaling protein localization, protrusion, and migration. This suggests that the polarity and motility-related consequences of EGTA treatment are mediated by Fat2 inhibition specifically. The development of more specific methods for acute Fat2 inhibition, such as cleavage of its extracellular domain at an engineered protease site, will be useful for confirming this specificity.

Transient EGTA treatment provides a method for watching de novo formation of Fat2-based puncta using live imaging. This had proven challenging using live imaging of unmanipulated epithelia, since the puncta are present even prior to egg chamber formation and the onset of migration, and it is challenging to distinguish the formation of new puncta from other splitting, merging, and moving events. Using this new tool, I performed initial qualitative characterization of the reformation of puncta, finding that the kinetics of Fat2 and Lar accumulation differ—Lar initially rapidly re-accumulated at cell-cell interfaces before migration had resumed, and then that distribution became focused at trailing edges over tens of minutes as migration accelerated. Fat2, in contrast, accumulated more gradually at trailing edges with no apparent mispolarized early accumulation and no detectable polarization until after collective migration was underway. In the future, quantitative studies of

the formation of Fat2-based puncta and their polarization dynamics will help us understand the mechanisms by which these structures assemble. In addition, we know that migration is required for the polarization of Fat2, but we do not understand the mechanism by which migration influences Fat2, and analyzing the relationship between cell movement and Fat2's polarization dynamics may provide valuable clues. Pairing transient EGTA treatment with single-molecule and other live imaging approaches may also be fruitful.

Transient EGTA treatment also provided clues about the circuit organization by which follicle cells maintain their polarity. The tendency of the cells to reverse polarity after EGTA washout is reminiscent of repolarization events in cells such as neutrophils migrating individually, which repolarize upon collision with a barrier or upon optogenetic flattening of their leading edge-trailing edge polarity (Town & Weiner, 2022; Weiner et al., 2007). Here, repolarization is the result of negative feedback that "wins out" once the leading edge is no longer moving forward (Graziano & Weiner, 2014; Weiner et al., 2007). In the case of the follicle cells, their tendency to reverse polarity once they have been stopped and their Fat2-based planar signaling disrupted suggests the presence of similar local negative feedback on their polarity, such that their re-formation of leading or trailing edge regions in the same orientation is disfavored. The fact that not all cells initially reverse suggests that this feedback acts at the level of individual interfaces or cells rather than being a tissue-scale phenomenon. Using CK-666 treatment, I showed that stopped migration alone is insufficient for reversal, perhaps because the still-present Fat2-based planar signaling can overcome this hypothesized local negative feedback. Using different genetic and developmental conditions, I ruled out the intracellular domain of Fat2 and the egg chambers developmental stage (and co-varying traits like size and elongation) as major factors in migration reversal, and therefore as negative feedback mediators. A remaining candidate reversal mediator is the WAVE complex or other parts of the lamellipodia circuit, which exhibits local negative feedback as a result of the tendency of branched actin networks to remove the WAVE complex from the

plasma membrane, and perhaps from additional sources as well (Graziano & Weiner, 2014; Huang et al., 2013; Millius et al., 2012; Weiner et al., 2007). This could give other regions of the plasma membrane a WAVE complex accumulation advantage after the disruption of positive regulation of the WAVE complex by Fat2-based signaling.

Because EGTA treatment causes the dissolution of Fat2-based puncta, it may serve as a useful assay for following the (re)assembly of follicle cells' planar signaling system and reorganization of the cells' polarity. Studies of this system (including my own) have largely focused on how its spatial organization is maintained and how it regulates cell motility behaviors long after polarity initially arises. The re-establishment of follicle cells' planar polarity within 1-2 hours of washout from EGTA treatment makes live imaging of the entire polarization process newly accessible. The fact that migration consistently reverses shows that this induced repolarization differs from normal symmetry breaking during egg chamber formation, but the molecular dynamics of puncta reassembly would likely still be informative about their normal assembly. The fact that a sizable minority of follicle cells first repolarized in their initial direction leading to epithelia with mixed polarity may afford an opportunity to study polarity propagation across the epithelium as well. Finally, using different pharmacological perturbations and treatment times, or other perturbations such as optogenetic ones, it may be possible to identify one that erases the tissue's planar polarity memory and makes it possible to follow symmetry breaking anew.

Broader relevance of this work

Although it is widely appreciated that cell-cell interfaces are critical sites of coordination during collective cell migrations, most example of coordination mechanisms are physical, for example mediated by the transmission of tension through adherens junctions or by asymmetric membrane curvature caused by one cell protruding into another. In part, this is due to the tools available in mammalian cell culture, the experimental context in which this

topic has been most extensively studied. Traction force microscopy, tension biosensors, and other biophysical methods are relatively accessible in these models, but genetic screening for new protein players is less so. My work and the follicle cell migration system more broadly therefore serves as a useful complement to mammalian cell culture studies, pointing to receptor-mediated biochemical signaling as another mechanism of cell-cell coordination. One of the main outputs of this signaling system is the polarization of excitable WAVE complex activity and lamellipodial protrusion, which has also been observed in response to mechanical asymmetries across cell-cell interfaces (Das et al., 2015; Hayer et al., 2016). Genetics and mechanics-focused studies and experimental systems may be uncovering two facets of the same underlying organizing principles by asymmetries in cell motility behavior across cell-cell interfaces are generated and stabilized. It is also notable that the follicle cells' planar signaling is bidirectional and includes both attractive and repulsive cues spatially integrated by Fat2. I suspect that this kind of bidirectional signaling is widespread in the context of collective cell migration, whether mediated by biochemical or other asymmetries. Interface polarization inevitably alters the molecular composition, mechanics, and geometry of neighboring cells at either side of the interface, and it is only a small step from there to the polarization of downstream responses. Beyond the context of collective cell migration, this has been observed in the case of interfaces polarized by the core planar cell polarity pathway, which has been shown to signal bidirectionally and which is used to polarize a wide variety of proteins, cell structures, and behaviors (Butler & Wallingford, 2017; Fisher et al., 2019; Goodrich & Strutt, 2011).

By studying follicle cell migration and the planar signaling system that regulates it, I have come to see planar polarity and collective cell migration (and particularly collective epithelial cell migration) as highly overlapping processes that must overcome similar organizational challenges. Planar cell polarity systems have long been understood as means for the interpretation of tissue-scale, graded cues into both cell polarity and cell alignment (Fisher

& Strutt, 2019; Lavalou & Lecuit, 2022). This is also the task of collective cell migrations, in which groups of cells move persistently despite shallow or variable directional cues, or ones felt directly by only part of the group. Planar signaling through intercellular bridges could sharpen these cues, making cue detection more sensitive and migration more persistent. In the core planar cell polarity system, local positive and negative feedback at the level of cell-cell interfaces also contributes to sharpening and stabilization of interface polarity (Harrison et al., 2020), and this feature is likely widespread in collective migrations as well, either stemming from the coupling of the excitable dynamics of motility machinery on either side of a cell-cell interface (Iglesias & Devreotes, 2012; Li et al., 2020), or from additional layers of regulation. Despite these parallels, I have experienced the fields of collective cell migration and planar cell polarity as largely separate, which I suspect is due in part to the conflation of planar cell polarity as a general tissue organization with the core and Fat/Dachsous planar cell polarity proteins that orchestrate it in many animal tissues. It may also be due in part to the fact that few collectively-migrating tissues exhibit planar polarity as striking as that of the follicle cells, and an outsized emphasis has been placed on the importance of leader cells. In addition, the core and Fat/Dachsous planar cell polarity systems both operate at apical surfaces and primarily regulate proteins and structures in this plane (Goodrich & Strutt, 2011; Sharma & McNeill, 2013), whereas crawling cell migrations are most often driven by the polarization of structures at cells' basal surfaces. Follicle cell migration stands as a clear challenge to each of these conceptions, as (1) there are no leader cells but rather each cell of the epithelium exhibits clear leading edge-trailing edge polarization, (2) this organization is enabled by a set of planar-polarized signaling proteins distinct from either the core or Fat-Dachsous planar cell polarity pathways, and (3) those proteins localize to and regulate behaviors at cells' basal sides. Inspired by the follicle cell system, I propose that the theoretical frameworks of planar cell polarity could be fruitfully applied to collective cell migrations. As more collective epithelial cell migrations are documented with subcellular resolution, it

will also be useful to test the view that planar polarity in these processes is widespread by looking for alignment of cells' motility machinery or cells' force generation patterns across the migrating group.

5.2 Future Directions

Dissecting Fat2's polarization mechanism using single-molecule imaging

By showing that Fat2 concentrates all known leading edge-enriched proteins in trans through a non-reciprocal interaction, I addressed only part of the follicle cells' polarization puzzle. It will now be important to determine how Fat2 itself becomes polarized to trailing edges. I performed an initial characterization of Fat2's dynamics (and those of Lar and Sema5c) at leading-trailing interfaces, but I suspect that there is still a lot we could learn about Fat2's polarization mechanism from further live imaging. In particular, single-molecule imaging of its dynamics at the basal surface could be used to distinguish between models of polarization by biased delivery to trailing edges, stabilization at trailing edges, polarized movement within the plasma membrane, or some combination of these. The causes of this spatial bias could then be tested in different perturbation conditions. For example, if directed transport along the cells' polarized microtubule networks is required for polarization, we would expect Fat2 molecules to exhibit faster rates of arrival at trailing edges than elsewhere along the basal surface, and for this bias to be lost when microtubules are disrupted. If Fat2 reaches trailing edges through a binding interaction with the basement membrane, it should exhibit biased movement towards trailing edges in migratory epithelia, but this should be abruptly lost when migration is stopped. To achieve single molecule imaging, Fat2 could be sparsely labeled by expression of one copy of Fat2-3xGFP and then its levels depleted using GFP-RNAi. Alternatively, Fat2 could be tagged with the HALO protein and then sparsely labeled

using low levels of HALO dye (Chang & Dickinson, 2022; Los et al., 2008). Single molecule imaging approaches could also be used to test the mechanism by which Fat2 concentrates Lar and Sema5c at leading edges. My FRAP data suggests that Fat2 does this by slowing their turnover locally within puncta, but the trend is not strong and additional evidence will be needed to verify this finding.

The organization of proteins of the core planar cell polarity pathway into puncta is important for their polarization (Cho et al., 2015; Stahley et al., 2021; Strutt et al., 2011), and the puncta in which Fat2, Lar, and Sema5c localize may similarly be important sites at which the molecular interactions that establish and/or maintain their polarization play out. To bridge these proteins' single-molecule dynamics with their higher-order organization into puncta, protein photoconversion approaches may be helpful. This would enable following individual puncta over time, which I was unable to do reliably from TIRF timelapse data or after photobleaching. It should then be possible to measure their lifetimes and the rate of dissociation of different proteins within them.

Dissecting Fat2's polarization mechanism using pulsed secretion and pulsed labeling approaches

It is possible that much of Fat2's polarization dynamics play out away from the basal surface, in which case approaches other than single-molecule TIRF imaging will be necessary to follow them. In this case, pulsed secretion or pulsed labeling methods could be used to follow Fat2 through the endomembrane system. For example, the RUSH system (Boncompain et al., 2012; Glashauser et al., 2023) could be used to follow Fat2 through the secretory pathway and determine whether its secretion is biased to trailing edges. Secretion site visualization using pH-sensitive fluorophore tagging may also be possible. Pulsed labeling of an extracellularly HALO-tagged Fat2 with a membrane-impermeable HALO dye could be used to follow Fat2 as it is internalized and moves through the endocytic pathway. As with single molecule imaging,

these pulsed labeling approaches could be paired with different genetic and pharmacological perturbations to determine how Fat2's trafficking and transport are regulated.

How does Fat2's intracellular domain regulate polarity, migration, and protein turnover?

The intracellular domain of Fat2 contributes to, but is not essential for, follicle cell migration, as its removal in the truncation mutant Fat2$^{\Delta ICD}$-3xGFP slows (and occasionally prevents) migration (Barlan et al., 2017). Fat2's trans interactions seem to be preserved and not responsible for this migration slowing, since it still concentrates Lar and the WAVE complex (Barlan et al., 2017; Williams et al., 2022). Fat2$^{\Delta ICD}$ has an expanded distribution around cell edges at the basal surface, and its overall planar polarity is reduced (Barlan et al., 2017), suggesting that the slow migration stems from a polarity defect. The levels of Fat2$^{\Delta ICD}$ are also higher than those of full-length Fat2 (Fig. A.1), so this domain may regulate Fat2's endocytic turnover. Fat2$^{\Delta ICD}$ therefore may provide a window into both Fat2's polarization and turnover mechanisms. It is possible that Fat2$^{\Delta ICD}$'s excess levels are the cause of its poor planar polarity, as protein polarization mechanisms are often sensitive to the levels of that protein. This can be seen for Sema5c and Lar, both of which accumulate ectopically at trailing edges when over expressed (Stedden et al., 2019) (Fig. A.2). If Fat2$^{\Delta ICD}$'s excess accumulation causes its expanded distribution, lowering of these levels using its heterozygous expression or partial depletion with RNAi should improve its planar polarity. It is also possible that the intracellular domain of Fat2 independently regulates polarity and endocytic turnover, in which case depletion of Fat2$^{\Delta ICD}$ to wild-type Fat2 levels will not fully restore its planar polarity. If so, finer structure-function studies of the intracellular domain could then potentially be used to separate these two domain roles and might also provide clues about the binding interactions that mediate them. Distinguishing between these possibilities will help us understand the various functions of Fat2's intracellular domain as well as its polarization

mechanism. It will also be useful to take an unbiased approach to identifying the binding interactions that Fat2's intracellular domain participates in. To do this, proximity labeling with TurboID or a similar system paired with mass spectrometry could be used (Branon et al., 2018). In addition, a variety of intracellular domain binding interactions have been identified for mammalian Fat-like cadherins, and could provide clues (Avilés et al., 2022; Cheng et al., 2016; Krol et al., 2016; Moeller et al., 2004; Schreiner et al., 2006; Tanoue & Takeichi, 2005). Some of these are mediated by binding sites (such as the Ena-binding EVH1 site) that are not conserved in *Drosophila* Fat2, but it would be useful to search for conservation of the others and test their relevance to Fat2 function if present.

What are the binding partners and functions of Fat2's extracellular domain?

By far the largest part of any Fat-like cadherin protein is extracellular, and there is strong reason to think that these domains are critical for the function of these proteins. However, their large size has made tackling their biochemistry fairly formidable, and no extracellular domain truncation mutants have been reported. Genetic and biochemical investigation of extracellular domain binding partners and functions is an important gap in our knowledge. To test for binding, the ELISA-based assay that was used to detect the binding interaction between extracellular domains of Sema5c and PlexA could be useful (Özkan et al., 2013; Ranaivoson et al., 2019; Stedden et al., 2019; Wojtowicz et al., 2007). This could be used to determine whether Fat2 binds Lar or Sema5c directly, and it could also be used to conduct an unbiased screen for binding partners using an existing library of the extracellular domains of transmembrane *Drosophila* proteins. The binding interactions of sub-regions of Fat2's extracellular domain could also be tested. For example, large atypical cadherins typically bind other cadherins with several of their N-terminal-most cadherin repeats only, as in the case of Fat and Dachsous whose binding interface includes just four of their respective

34 and 27 cadherin repeats (Medina et al., 2023; Sotomayor et al., 2014). They often bind homophillically in cis with more C-terminal cadherin repeats (Sotomayor et al., 2014). Truncations of the Fat2 extracellular domain could be used to test the applicability of these trends to Fat2, and to identify binding interactions specific to its mysterious EGF-like and Laminin G repeats at the plasma membrane-proximal base of the extracellular domain.

To complement these binding assays, structure-function experiments in follicle cells using a series of extracellular domain truncations would also be valuable. We now know a number of things that Fat2 does in follicle cells—concentrating different leading edge proteins in trans, polarizing protrusive activity, and itself achieving a polarized, punctate distribution at edges. Most of these still occur normally, or mostly normally, without its intracellular domain. The extracellular domain regions that mediate these different functions could be tested and related to binding partners identified for those regions. In addition, a number of point mutations in the extracellular domain of human Fat1 have been identified that result in kidney disease (Gee et al., 2016), and I have confirmed that the affected amino acids are conserved in *Drosophila* Fat2. Recreation of these disease mutations in Fat2 could serve as a second approach to testing the function of Fat2's extracellular domain, and could also shed light on the role of Fat1 in the kidney and the etiology of the mutant alleles' dysfunction.

What is the molecular basis for Fat2's polarization of the WAVE complex and protrusions?

I found that Fat2 concentrates the WAVE complex at leading edges through a trans interaction that plays out within sub-micron-scale puncta, but the molecular basis for this interaction remains unknown. I focused on the WAVE complex over other regulators of lamellipodia because of its demonstrated importance for follicle cell migration and known localization to their leading edges (Cetera & Horne-Badovinac, 2015). However, it is highly likely that lamellipodial protrusion in follicle cells depends on a similar regulatory circuit

as in other cell types, which includes regulators such as the small GTPases Rac and Arf and the phosphoinositide PI(3,4,5)P_3 (Graziano & Weiner, 2014). These molecules act in a positive feedback circuit along with the WAVE complex, so Fat2 could potentially intervene at any point in this circuit and thereby position both the WAVE complex and protrusions. For example, localization of Rac or Arf GEFs to the puncta could increase the activity of the GTPases and thereby WAVE complex enrichment, as could local inhibition of Rac or Arf GAPs. To better understand the regulation of lamellipodia by Fat2 and other parts of follicle cells' planar signaling, it will be useful to work back from the side of the lamellipodia circuit, and also to work forward from Lar and any other transmembrane proteins that mediate Fat2's interaction with the leading edge. On the lamellipodium side, my non-exhaustive RNAi screen targeting Rac GEFs did not reveal any promising candidates, but these remain a potential node through which planar signaling could regulate the WAVE complex. Another avenue into determining the point of Fat2's regulation of the lamellipodia circuit would be to image the distributions of active Rac and PI(3,4,5)P_3 relative to cells' leading-trailing axes. Their polarization is often more graded than that of the WAVE complex (Weiner et al., 2007), and if that holds in follicle cells and the colocalization of Fat2 and the WAVE complex is much higher than Fat2 and these other molecules, it would suggest that the WAVE complex is the more direct point of regulation. As a word of caution however, I was unable to detect polarization in the distributions of active Rac or PI(3,4,5)P_3 using available biosensors and non-exhaustive efforts. In addition, it will be useful to explore how both increases and decreases in lamellipodia circuit members aside from the WAVE complex change protrusion and migration dynamics, and how these manipulations interact with changes to the planar signaling proteins.

The interaction between Fat2 and the lamellipodia circuit must be mediated by one or more transmembrane proteins that localize to leading edges. Previous findings point to Lar as one such intermediary—its loss reduces protrusive F-actin enrichment at leading edges

in cis, and WAVE complex enrichment at leading edges with undetermined cell-autonomy (Barlan et al., 2017; Squarr et al., 2016). However, both of these phenotypes are milder than those caused by loss of Fat2, pointing to at least one missing intermediary between Fat2 and leading edge motility behaviors. Sema5c is one candidate, and data reported in this dissertation sends mixed messages about the likelihood that it plays this role. Weighing against this hypothesis, loss of Sema5c did not reduce WAVE complex enrichment at leading edges (Fig. 3.9). Weighing in favor, the combined loss of Sema5c and Lar caused changes to protrusion levels and distributions indistinguishable from loss of Fat2 (Figs. 3.11, 3.12). It would be interesting to see whether WAVE complex levels at basal cell-cell interfaces were reduced comparably to *fat2*$^{-}$ epithelia and more than in *lar*$^{-}$ epithelia in this context, which would support a model in which Lar and Sema5c together shape the distribution of the WAVE complex downstream of Fat2. It would also be useful to take a less biased approach to this question, for example by performing screens for transmembrane proteins that bind Fat2's extracellular domain.

Does interface-scale feedback contribute to the polarization of Fat2-based puncta?

Proteins of the core planar cell polarity system can become polarized across cell-cell interfaces even in the absence of tissue-scale polarity with which to align, and they accomplish this through a combination of positive and negative feedback interactions among these proteins within cells and across cell-cell interfaces (Lavalou & Lecuit, 2022). Proteins of the Fat/Dachsous planar cell polarity system do not seem to be capable of this, and removal of tissue-scale polarity causes them to lose polarity entirely (Lavalou & Lecuit, 2022). We do not yet know which of these categories the follicle cells' Fat2-based puncta fall into. Collective migration (a tissue-scale polarity cue) is required to maintain long-range planar polarity of Fat2 and other puncta components. However, it is possible that these proteins can still

achieve some degree of local polarity in the absence of migration, which would indicate the presence of as-yet-unidentified sources of negative feedback that contribute to polarity sorting. Alternately, the Fat2-based system could behave more like the Fat/Dachsous system, as suggested by the relatedness of Fat and Fat2. If capable of some local, migration-independent polarity, the Fat2-based puncta should still have compositions that are polarized across cell-cell interfaces in non-migratory epithelia. This could be tested by looking for spatial shifts in the peaks of Fat2-3xGFP puncta and those of leading edge proteins labeled in a second color in the context of epithelia that lack tissue-wide planar polarity. I was able to consistently detect a small shift between these peaks in planar-polarized, migratory epithelia. If these shifts persist in individual puncta even when the tissue lacks planar polarity, it would indicate that the composition of puncta can polarize across interfaces through local polarization mechanisms aside from collective migration. If the shift goes away, it would suggest no such capability. I measured puncta positions and their shifts using laser scanning confocal microscopy and a lens corrected for chromatic abberation, but this resolution could be improved using superresolution techniques such as AiryScan or structured illumination microscopy. An alternative approach for detection of punctum-scale polarity would be to label one protein with different fluorophores in neighboring cells, for example using the Flp/FRT system to generate clones with GFP or RFP-tagged Fat2. At clone boundaries, puncta with mixed fluorophore composition would indicate a lack of polarity, and the degree of polarity could be measured quantitatively. If puncta remain able to polarize without migration, it will be interesting to check for polarity at larger scales such as along interfaces or across cells, again aided by mosaic labeling, and to test the contributions of different puncta-resident proteins to that polarization.

Why is the migration direction always perpendicular to the anterior-posterior axis?

The collective migration of follicle cells is notable for maintaining its direction stably for approximately two days and many complete tissue revolutions without either reforming in a new direction or drifting gradually away from its initial one, at least the latter of which should occur in the absence of polarity stabilization by some extrinsic directional cue. Our current model of polarity maintenance is that positive feedback between polar signaling across leading-trailing interfaces and the tissue's rotational movement stabilizes collective alignment. However, this does not explain either how the initial polarity direction is restricted to the medial axis or how the cells avoid a gradual collective polarity drift away from that axis. To explain these migration features, some mechanism for restriction of the polarity axis is needed. This could be one mechanism that operates both during symmetry breaking and throughout migration, or distinct mechanisms could restrict the symmetry breaking axis and restrict rotational drift.

What are some candidate mechanisms by which the symmetry breaking direction could be restricted? Follicle cell precursors exhibit axial polarity of a number of traits prior to egg chamber formation, including having elongated cell shapes and high microtubule alignment along the ultimate migration axis. Cells' elongation and alignment with one another favors their migration along the axis of elongation (Park et al., 2015), and microtubules have been proposed to play a role in symmetry breaking (Chen et al., 2016; Viktorinová & Dahmann, 2013), so either of these could potentially contribute to migration axis restriction. However, ongoing research in the lab has shown that egg chambers can initiate migration even in the absence of these forms of axial polarity, so although they could contribute, they cannot be the sole axis restriction mechanism. These experiments have also shown that the constraint of transient adhesion between the anterior pole of the budding egg chamber and stalk cells is not required to set the rotational axis. Another possibility that has not yet been ruled

out is that physical properties of the polar cells or their biochemical signaling is responsible. Polar cells could restrict the migration axis by changing the motility behavior of the follicle cells close to the poles or through their own interaction with the basement membrane (e.g. by adhering more strongly than the follicle cells). These hypotheses could be tested by manipulating polar cell signaling or adhesion.

After they have begun to migrate, follicle cells maintain their directionality such that the egg chamber's rotational axis does not "tumble" over time. This differs from rotations of cultured epithelial cell cysts, whose rotation axes gradually shift. What causes this discrepancy between rotating tissues? Egg chambers have the distinction of having a number of different cell types whose position demarcates the anterior-posterior axis (polar cells, oocyte, nurse cells) and previous studies have argued that polar cells determine the migration axis (de la Loza et al., 2017; Frydman & Spradling, 2001). However, it seems unlikely that ongoing signaling from any of these cells could prevent tumbling, since they would tumble with the rest of the tissue and maintain their position relative to the migrating cells. Another contender is tissue geometry—egg chambers begin to elongate along their anterior-posterior axes very early in their development (Alégot et al., 2018), and once this has occurred, only rotation orthogonal to the axis of elongation can occur without tissue or basement membrane deformation. To test the necessity of tissue elongation for rotation axis stability, it will be important to prevent the early, migration-independent phase of egg chamber elongation using a manipulation that does not prevent follicle cell migration, which may prove challenging. JAK/STAT signaling from the polar cells initiates elongation (Alégot et al., 2018), so either the polar cells or this signaling pathway are potential targets. If this model is correct, it would represent an interesting example of polarity self-stabilization, with the polar cells setting an initial rotational axis and then the follicle cells continuing to reinforce it by increasing the anisotropy of the basement membrane and thereby further elongating the tissue.

Is follicle cell migration widespread among insects?

As part of a team in the Embryology course at the Marine Biological Laboratory including Kyle DeMarr, Jana Sipkova, and Sally Horne-Badovinac, and through work with rotation student Michael Wen, I recently found suggestive morphological evidence that the Hemipterans *Pagaronia minor* (a leafhopper) and *Oncopeltus fasciatus* (milkweed bug) have follicle cells that undergo a rotational migration during a period of their egg chamber development. In both cases, the follicle cells had parallel arrays of stress fibers polarized circumferentially orthogonal to the anterior-posterior axis. More compellingly, these cells exhibited a rotational chirality, with the hypothetical leading edges being concave and trailing edges convex from the cell's perspective. Within insects, Hemipterans and Dipterans are fairly distantly related, raising the possibility that follicle cell migration could be widespread among insects. However, additional work is required to document their migration or morphological evidence of the migration. Performing a survey of the chirality of a sampling of insects' follicle cells would provide useful information about the breadth of follicle cell migration in insects. This could be the basis for more in-depth comparative studies of follicle cell migration and related aspects of egg chamber development.

If follicle cell migration is widespread in insects, that raises the question of whether it also mediates basement membrane remodeling and egg chamber elongation as it does in *Drosophila*, whether it has distinct functions elsewhere, or whether it is an epiphenomenon of the biology of follicular epithelia that was co-opted for elongation in *Drosophila* relatives. Interestingly, both *Pagaronia* and *Oncopeltus* have elongated eggs, and in the case of *Pagaronia* we were able to detect basement membrane ridges interdigitated with stress fibers, much like in *Drosophila*. This suggests that *Pagaronia* (and perhaps also milkweed bugs) also use follicle cell migration as a means to polarize their basement membrane to drive egg elongation. Insect eggs' aspect ratios vary widely, and there have been many independent evolutionary transitions between round and elongated eggs, so it would be interesting to

determine whether the migratory state of follicular epithelia is a knob that has been turned throughout insect evolution to change egg chamber shape.

BIBLIOGRAPHY

Abercrombie, M., & Heaysman, J. E. M. (1954). Observations on the social behaviour of cells in tissue culture: II. "Monolayering" of fibroblasts. *Experimental Cell Research*, *6*(2), 293–306. https://doi.org/10.1016/0014-4827(54)90176-7

Adler, P. N. (2012). Chapter One - The frizzled/stan Pathway and Planar Cell Polarity in the Drosophila Wing. In Y. Yang (Ed.), *Current Topics in Developmental Biology* (pp. 1–31). Academic Press.

Aigouy, B., Farhadifar, R., Staple, D. B., Sagner, A., Röper, J.-C., Jülicher, F., & Eaton, S. (2010). Cell Flow Reorients the Axis of Planar Polarity in the Wing Epithelium of Drosophila. *Cell*, *142*(5), 773–786. https://doi.org/10.1016/j.cell.2010.07.042

Alégot, H., Pouchin, P., Bardot, O., & Mirouse, V. (2018). Jak-Stat pathway induces Drosophila follicle elongation by a gradient of apical contractility (E. Knust, Ed.). *eLife*, *7*, e32943. https://doi.org/10.7554/eLife.32943

Alto, L. T., & Terman, J. R. (2017). Semaphorins and their Signaling Mechanisms. *Methods in molecular biology (Clifton, N.J.)*, *1493*, 1–25. https://doi.org/10.1007/978-1-4939-6448-2_1

Anderson, M. T., Sherrard, K., & Horne-Badovinac, S. (2023). Optimized Fixation and Phalloidin Staining of Basally Localized F-Actin Networks in Collectively Migrating Follicle Cells. In M. S. Giedt & T. L. Tootle (Eds.), *Drosophila Oogenesis: Methods and Protocols* (pp. 179–191). Springer US. https://doi.org/10.1007/978-1-0716-2970-3_9

Anon, E., Serra-Picamal, X., Hersen, P., Gauthier, N. C., Sheetz, M. P., Trepat, X., & Ladoux, B. (2012). Cell crawling mediates collective cell migration to close undamaged epithelial gaps. *Proceedings of the National Academy of Sciences*, *109*(27), 10891–10896. https://doi.org/10.1073/pnas.1117814109

Arima, S., Nishiyama, K., Ko, T., Arima, Y., Hakozaki, Y., Sugihara, K., Koseki, H., Uchijima, Y., Kurihara, Y., & Kurihara, H. (2011). Angiogenic morphogenesis driven by dynamic and heterogeneous collective endothelial cell movement. *Development*, *138*(21), 4763–4776. https://doi.org/10.1242/dev.068023

Atia, L., Fredberg, J. J., Gov, N. S., & Pegoraro, A. F. (2021). Are cell jamming and unjamming essential in tissue development? *Cells & Development*, *168*, 203727. https://doi.org/10.1016/j.cdev.2021.203727

Aurich, F., & Dahmann, C. (2016). A Mutation in fat2 Uncouples Tissue Elongation from Global Tissue Rotation. *Cell Reports*, *14*(11), 2503–2510. https://doi.org/10.1016/j.celrep.2016.02.044

Avilés, E. C., Krol, A., Henle, S. J., Burroughs-Garcia, J., Deans, M. R., & Goodrich, L. V. (2022). Fat3 acts through independent cytoskeletal effectors to coordinate asymmetric cell behaviors during polarized circuit assembly. *Cell Reports*, *38*(5). https://doi.org/10.1016/j.celrep.2022.110307

Aw, W. Y., & Devenport, D. (2017). Planar cell polarity: Global inputs establishing cellular asymmetry. *Current Opinion in Cell Biology*, *44*, 110–116. https://doi.org/10.1016/j.ceb.2016.08.002

Aw, W. Y., Heck, B. W., Joyce, B., & Devenport, D. (2016). Transient Tissue-Scale Deformation Coordinates Alignment of Planar Cell Polarity Junctions in the Mammalian Skin. *Current Biology*, *26*(16), 2090–2100. https://doi.org/10.1016/j.cub.2016.06.030

Badouel, C., Zander, M., Liscio, N., Bagherie-Lachidan, M., Sopko, R., Coyaud, E., Raught, B., Miller, F., & McNeill, H. (2015). Fat1 interacts with Fat4 to regulate neural tube closure, neural progenitor proliferation and apical constriction during mouse brain development. *Development (Cambridge)*, *142*(16), 2781–2791. https://doi.org/10.1242/dev.123539

Bai, J., Uehara, Y., & Montell, D. J. (2000). Regulation of Invasive Cell Behavior by Taiman, a Drosophila Protein Related to AIB1, a Steroid Receptor Coactivator Amplified in Breast Cancer. *Cell*, *103*(7), 1047–1058. https://doi.org/10.1016/S0092-8674(00)00208-7

Bali, N., Lee, H.-K. (, & Zinn, K. (2022). Sticks and stones, a conserved cell surface ligand for the Type IIa RPTP Lar, regulates neural circuit wiring in Drosophila (K. VijayRaghavan, Ed.). *eLife*, *11*, e71469. https://doi.org/10.7554/eLife.71469

Barlan, K., Cetera, M., & Horne-Badovinac, S. (2017). Fat2 and Lar Define a Basally Localized Planar Signaling System Controlling Collective Cell Migration. *Developmental Cell*, *40*(5), 467–477.e5. https://doi.org/10.1016/j.devcel.2017.02.003

Barnhart, E. L., Lee, K.-C., Keren, K., Mogilner, A., & Theriot, J. A. (2011). An Adhesion-Dependent Switch between Mechanisms That Determine Motile Cell Shape. *PLOS Biology*, *9*(5), e1001059. https://doi.org/10.1371/journal.pbio.1001059

Bateman, J., Reddy, R. S., Saito, H., & Vactor, D. V. (2001). The receptor tyrosine phosphatase Dlar and integrins organize actin filaments in the Drosophila follicular ep-

ithelium. *Current Biology*, *11*(17), 1317–1327. https://doi.org/10.1016/S0960-9822(01)00420-1

Batson, J., Maccarthy-Morrogh, L., Archer, A., Tanton, H., & Nobes, C. D. (2014). EphA receptors regulate prostate cancer cell dissemination through Vav2–RhoA mediated cell–cell repulsion. *Biology Open*, *3*(6), 453–462. https://doi.org/10.1242/bio.20146601

Battistini, C., & Tamagnone, L. (2016). Transmembrane semaphorins, forward and reverse signaling: Have a look both ways. *Cellular and Molecular Life Sciences*, *73*(8), 1609–1622. https://doi.org/10.1007/s00018-016-2137-x

Benton, R., & Johnston, D. S. (2003). A Conserved Oligomerization Domain in Drosophila Bazooka/PAR-3 Is Important for Apical Localization and Epithelial Polarity. *Current Biology*, *13*(15), 1330–1334. https://doi.org/10.1016/S0960-9822(03)00508-6

Bieling, P., Hansen, S. D., Akin, O., Li, T.-D., Hayden, C. C., Fletcher, D. A., & R Dyche, M. (2018). WH2 and proline-rich domains of WASP-family proteins collaborate to accelerate actin filament elongation. *The EMBO Journal*, *37*(1), 102–121. https://doi.org/10.15252/embj.201797039

Bloch Qazi, M. C., Heifetz, Y., & Wolfner, M. F. (2003). The developments between gametogenesis and fertilization: Ovulation and female sperm storage in drosophila melanogaster. *Developmental Biology*, *256*(2), 195–211. https://doi.org/10.1016/S0012-1606(02)00125-2

Bodor, D. L., Pönisch, W., Endres, R. G., & Paluch, E. K. (2020). Of Cell Shapes and Motion: The Physical Basis of Animal Cell Migration. *Developmental Cell*, *52*(5), 550–562. https://doi.org/10.1016/j.devcel.2020.02.013

Boncompain, G., Divoux, S., Gareil, N., de Forges, H., Lescure, A., Latreche, L., Mercanti, V., Jollivet, F., Raposo, G., & Perez, F. (2012). Synchronization of secretory protein traffic in populations of cells. *Nature Methods*, *9*(5), 493–498. https://doi.org/10.1038/nmeth.1928

Branon, T. C., Bosch, J. A., Sanchez, A. D., Udeshi, N. D., Svinkina, T., Carr, S. A., Feldman, J. L., Perrimon, N., & Ting, A. Y. (2018). Efficient proximity labeling in living cells and organisms with TurboID. *Nature Biotechnology*, *36*(9), 880–887. https://doi.org/10.1038/nbt.4201

Brasch, J., Goodman, K. M., Noble, A. J., Rapp, M., Mannepalli, S., Bahna, F., Dandey, V. P., Bepler, T., Berger, B., Maniatis, T., Potter, C. S., Carragher, B., Honig, B., &

Shapiro, L. (2019). Visualization of clustered protocadherin neuronal self-recognition complexes. *Nature*, *569*(7755), 280–283. https://doi.org/10.1038/s41586-019-1089-3

Braun, G. S., Kretzler, M., Heider, T., Floege, J., Holzman, L. B., Kriz, W., & Moeller, M. J. (2007). Differentially Spliced Isoforms of FAT1 Are Asymmetrically Distributed within Migrating Cells*. *Journal of Biological Chemistry*, *282*(31), 22823–22833. https://doi.org/10.1074/jbc.M701758200

Brooun, M., Klimovich, A., Bashkurov, M., Pearson, B. J., Steele, R. E., & McNeill, H. (2020). Ancestral roles of atypical cadherins in planar cell polarity. *Proceedings of the National Academy of Sciences*, *117*(32), 19310–19320. https://doi.org/10.1073/pnas.1917570117

Burridge, K., & Guilluy, C. (2016). Focal adhesions, stress fibers and mechanical tension. *Experimental Cell Research*, *343*(1), 14–20. https://doi.org/10.1016/j.yexcr.2015.10.029

Butler, M. T., & Wallingford, J. B. (2017). Planar cell polarity in development and disease. *Nature Reviews Molecular Cell Biology*, *18*(6), 375–388. https://doi.org/10.1038/nrm.2017.11

Buttenschön, A., & Edelstein-Keshet, L. (2020). Bridging from single to collective cell migration: A review of models and links to experiments. *PLOS Computational Biology*, *16*(12), e1008411. https://doi.org/10.1371/journal.pcbi.1008411

Camley, B. A., Zhang, Y., Zhao, Y., Li, B., Ben-Jacob, E., Levine, H., & Rappel, W.-J. (2014). Polarity mechanisms such as contact inhibition of locomotion regulate persistent rotational motion of mammalian cells on micropatterns. *Proceedings of the National Academy of Sciences*, *111*(41), 14770–14775. https://doi.org/10.1073/pnas.1414498111

Campanale, J. P., Mondo, J. A., & Montell, D. J. (2022). A Scribble/Cdep/Rac pathway controls follower-cell crawling and cluster cohesion during collective border-cell migration. *Developmental Cell*, *57*(21), 2483–2496.e4. https://doi.org/10.1016/j.devcel.2022.10.004

Campanale, J. P., & Montell, D. J. (2023). Who's really in charge: Diverse follower cell behaviors in collective cell migration. *Current Opinion in Cell Biology*, *81*, 102160. https://doi.org/10.1016/j.ceb.2023.102160

Campos, F. C., Dennis, C., Alégot, H., Fritsch, C., Isabella, A., Pouchin, P., Bardot, O., Horne-Badovinac, S., & Mirouse, V. (2020). Oriented basement membrane fibrils provide a memory for F-actin planar polarization via the Dystrophin-Dystroglycan

complex during tissue elongation. *Development*, *147*(7). https://doi.org/10.1242/dev.186957

Cao, L. L., Riascos-Bernal, D. F., Chinnasamy, P., Dunaway, C. M., Hou, R., Pujato, M. A., O'Rourke, B. P., Miskolci, V., Guo, L., Hodgson, L., Fiser, A., & Sibinga, N. E. S. (2016). Control of mitochondrial function and cell growth by the atypical cadherin Fat1. *Nature*, *539*(7630), 575–578. https://doi.org/10.1038/nature20170

Carmona-Fontaine, C., Matthews, H. K., Kuriyama, S., Moreno, M., Dunn, G. A., Parsons, M., Stern, C. D., & Mayor, R. (2008). Contact inhibition of locomotion in vivo controls neural crest directional migration. *Nature*, *456*(7224), 957–961. https://doi.org/10.1038/nature07441

Case, L. B., & Waterman, C. M. (2015). Integration of actin dynamics and cell adhesion by a three-dimensional, mechanosensitive molecular clutch. *Nature Cell Biology*, *17*(8), 955–963. https://doi.org/10.1038/ncb3191

Cetera, M., & Horne-Badovinac, S. (2015). Round and round gets you somewhere: Collective cell migration and planar polarity in elongating Drosophila egg chambers. *Current opinion in genetics & development*, *32*, 10–15. https://doi.org/10.1016/j.gde.2015.01.003

Cetera, M., Lewellyn, L., & Horne-Badovinac, S. (2016). Cultivation and Live Imaging of Drosophila Ovaries. In C. Dahmann (Ed.), *Drosophila: Methods and Protocols* (pp. 215–226). Springer.

Cetera, M., Leybova, L., Joyce, B., & Devenport, D. (2018). Counter-rotational cell flows drive morphological and cell fate asymmetries in mammalian hair follicles. *Nature Cell Biology*, *20*(5), 541–552. https://doi.org/10.1038/s41556-018-0082-7

Cetera, M., Leybova, L., Woo, F. W., Deans, M., & Devenport, D. (2017). Planar cell polarity-dependent and independent functions in the emergence of tissue-scale hair follicle patterns. *Developmental Biology*, *428*(1), 188–203. https://doi.org/10.1016/j.ydbio.2017.06.003

Cetera, M., Ramirez-San Juan, G. R., Oakes, P. W., Lewellyn, L., Fairchild, M. J., Tanentzapf, G., Gardel, M. L., & Horne-Badovinac, S. (2014). Epithelial rotation promotes the global alignment of contractile actin bundles during Drosophila egg chamber elongation. *Nature Communications*, *5*(1), 5511. https://doi.org/10.1038/ncomms6511

Chang, Y., & Dickinson, D. J. (2022). Non-invasive chimeric HaloTag labeling to study clustering and diffusion of membrane proteins. *STAR Protocols*, *3*(4), 101857. https://doi.org/10.1016/j.xpro.2022.101857

Chen, B., Brinkmann, K., Chen, Z., Pak, C. W., Liao, Y., Shi, S., Henry, L., Grishin, N. V., Bogdan, S., & Rosen, M. K. (2014). The WAVE Regulatory Complex Links Diverse Receptors to the Actin Cytoskeleton. *Cell*, *156*(1), 195–207. https://doi.org/10.1016/j.cell.2013.11.048

Chen, D.-Y., Crest, J., & Bilder, D. (2017). A Cell Migration Tracking Tool Supports Coupling of Tissue Rotation to Elongation. *Cell Reports*, *21*(3), 559–569. https://doi.org/10.1016/j.celrep.2017.09.083

Chen, D.-Y., Lipari, K. R., Dehghan, Y., Streichan, S. J., & Bilder, D. (2016). Symmetry Breaking in an Edgeless Epithelium by Fat2-Regulated Microtubule Polarity. *Cell Reports*, *15*(6), 1125–1133. https://doi.org/10.1016/j.celrep.2016.04.014

Chen, X. J., Squarr, A. J., Stephan, R., Chen, B., Higgins, T. E., Barry, D. J., Martin, M. C., Rosen, M. K., Bogdan, S., & Way, M. (2014). Ena/VASP Proteins Cooperate with the WAVE Complex to Regulate the Actin Cytoskeleton. *Developmental Cell*, *30*(5), 569–584. https://doi.org/10.1016/j.devcel.2014.08.001

Chen, Z., Borek, D., Padrick, S. B., Gomez, T. S., Metlagel, Z., Ismail, A. M., Umetani, J., Billadeau, D. D., Otwinowski, Z., & Rosen, M. K. (2010). Structure and control of the actin regulatory WAVE complex. *Nature*, *468*(7323), 533–538. https://doi.org/10.1038/nature09623

Chen, Z. G., Saba, N. F., & Teng, Y. (2022). The diverse functions of FAT1 in cancer progression: Good, bad, or ugly? *Journal of Experimental & Clinical Cancer Research*, *41*(1), 248. https://doi.org/10.1186/s13046-022-02461-8

Cheng, H., Burroughs-Garcia, J., Birkness, J. E., Trinidad, J. C., & Deans, M. R. (2016). Disparate Regulatory Mechanisms Control Fat3 and P75NTR Protein Transport through a Conserved Kif5-Interaction Domain. *PLOS ONE*, *11*(10), e0165519. https://doi.org/10.1371/journal.pone.0165519

Chepizhko, O., Chiara Lionetti, M., Malinverno, C., Giampietro, C., Scita, G., Zapperi, S., & Porta, C. A. M. L. (2018). From jamming to collective cell migration through a boundary induced transition. *Soft Matter*, *14*(19), 3774–3782. https://doi.org/10.1039/C8SM00128F

Chien, Y.-H., Keller, R., Kintner, C., & Shook, D. R. (2015). Mechanical Strain Determines the Axis of Planar Polarity in Ciliated Epithelia. *Current Biology*, *25*(21), 2774–2784. https://doi.org/10.1016/j.cub.2015.09.015

Chlasta, J., Milani, P., Runel, G., Duteyrat, J.-L., Arias, L., Lamiré, L.-A., Boudaoud, A., & Grammont, M. (2017). Variations in basement membrane mechanics are linked to

epithelial morphogenesis. *Development*, *144*(23), 4350–4362. https://doi.org/10.1242/dev.152652

Cho, B., Pierre-Louis, G., Sagner, A., Eaton, S., & Axelrod, J. D. (2015). Clustering and Negative Feedback by Endocytosis in Planar Cell Polarity Signaling Is Modulated by Ubiquitinylation of Prickle. *PLOS Genetics*, *11*(5), e1005259. https://doi.org/10.1371/journal.pgen.1005259

Cornils, H., Kohler, R. S., Hergovich, A., & Hemmings, B. A. (2011). Human NDR Kinases Control G1/S Cell Cycle Transition by Directly Regulating p21 Stability. *Molecular and Cellular Biology*, *31*(7), 1382–1395. https://doi.org/10.1128/MCB.01216-10

Crest, J., Diz-Muñoz, A., Chen, D.-Y., Fletcher, D. A., & Bilder, D. (2017). Organ sculpting by patterned extracellular matrix stiffness (A. C. Spradling, Ed.). *eLife*, *6*, e24958. https://doi.org/10.7554/eLife.24958

Dang, T. T., Westcott, J. M., Maine, E. A., Kanchwala, M., Xing, C., & Pearson, G. W. (2016). DeltaNp63alpha induces the expression of FAT2 and Slug to promote tumor invasion. *Oncotarget*, *7*(19), 28592–28611. https://doi.org/10.18632/oncotarget.8696

Das, T., Safferling, K., Rausch, S., Grabe, N., Boehm, H., & Spatz, J. P. (2015). A molecular mechanotransduction pathway regulates collective migration of epithelial cells. *Nature Cell Biology*, *17*(3), 276–287. https://doi.org/10.1038/ncb3115

Davis, J. R., Huang, C.-Y., Zanet, J., Harrison, S., Rosten, E., Cox, S., Soong, D. Y., Dunn, G. A., & Stramer, B. M. (2012). Emergence of embryonic pattern through contact inhibition of locomotion. *Development*, *139*(24), 4555–4560. https://doi.org/10.1242/dev.082248

de la Loza, M. C. D., Díaz-Torres, A., Zurita, F., Rosales-Nieves, A. E., Moeendarbary, E., Franze, K., Martín-Bermudo, M. D., & González-Reyes, A. (2017). Laminin Levels Regulate Tissue Migration and Anterior-Posterior Polarity during Egg Morphogenesis in Drosophila. *Cell Reports*, *20*(1), 211–223. https://doi.org/10.1016/j.celrep.2017.06.031

Deady, L. D., Shen, W., Mosure, S. A., Spradling, A. C., & Sun, J. (2015). Matrix Metalloproteinase 2 Is Required for Ovulation and Corpus Luteum Formation in Drosophila. *PLOS Genetics*, *11*(2), e1004989. https://doi.org/10.1371/journal.pgen.1004989

Deans, M. R., Krol, A., Abraira, V. E., Copley, C. O., Tucker, A. F., & Goodrich, L. V. (2011). Control of Neuronal Morphology by the Atypical Cadherin Fat3. *Neuron*, *71*(5), 820–832. https://doi.org/10.1016/j.neuron.2011.06.026

Deng, W.-M., Althauser, C., & Ruohola-Baker, H. (2001). Notch-Delta signaling induces a transition from mitotic cell cycle to endocycle in Drosophila follicle cells. *Development*, *128*(23), 4737–4746. https://doi.org/10.1242/dev.128.23.4737

Dent, L. G., Manning, S. A., Kroeger, B., Williams, A. M., Hilmi, A. J. S., Crea, L., Kondo, S., Horne-Badovinac, S., & Harvey, K. F. (2019). The dPix-Git complex is essential to coordinate epithelial morphogenesis and regulate myosin during Drosophila egg chamber development. *PLOS Genetics*, *15*(5), e1008083. https://doi.org/10.1371/journal.pgen.1008083

Desai, R. A., Gopal, S. B., Chen, S., & Chen, C. S. (2013). Contact inhibition of locomotion probabilities drive solitary versus collective cell migration. *Journal of The Royal Society Interface*, *10*(88), 20130717. https://doi.org/10.1098/rsif.2013.0717

Devergne, O., Sun, G. H., & Schüpbach, T. (2017). Stratum, a Homolog of the Human GEF Mss4, Partnered with Rab8, Controls the Basal Restriction of Basement Membrane Proteins in Epithelial Cells. *Cell Reports*, *18*(8), 1831–1839. https://doi.org/10.1016/j.celrep.2017.02.002

Devergne, O., Tsung, K., Barcelo, G., & Schüpbach, T. (2014). Polarized deposition of basement membrane proteins depends on Phosphatidylinositol synthase and the levels of Phosphatidylinositol 4,5-bisphosphate. *Proceedings of the National Academy of Sciences*, *111*(21), 7689–7694. https://doi.org/10.1073/pnas.1407351111

Devreotes, P., & Horwitz, A. R. (2015). Signaling Networks that Regulate Cell Migration. *Cold Spring Harbor Perspectives in Biology*, *7*(8), a005959. https://doi.org/10.1101/cshperspect.a005959

Diz-Muñoz, A., Fletcher, D. A., & Weiner, O. D. (2013). Use the force: Membrane tension as an organizer of cell shape and motility. *Trends in Cell Biology*, *23*(2), 47–53. https://doi.org/10.1016/j.tcb.2012.09.006

Duhart, J. C., Parsons, T. T., & Raftery, L. A. (2017). The repertoire of epithelial morphogenesis on display: Progressive elaboration of Drosophila egg structure. *Mechanisms of Development*, *148*, 18–39. https://doi.org/10.1016/j.mod.2017.04.002

Duhart, J. C., & Raftery, L. A. (2020). Mob Family Proteins: Regulatory Partners in Hippo and Hippo-Like Intracellular Signaling Pathways. *Frontiers in Cell and Developmental Biology*, *8*.

Eaton, S., & Jülicher, F. (2011). Cell flow and tissue polarity patterns. *Current Opinion in Genetics & Development*, *21*(6), 747–752. https://doi.org/10.1016/j.gde.2011.08.010

Emoto, K., Parrish, J. Z., Jan, L. Y., & Jan, Y.-N. (2006). The tumour suppressor Hippo acts with the NDR kinases in dendritic tiling and maintenance. *Nature*, *443*(7108), 210–213. https://doi.org/10.1038/nature05090

Ewald, A. J., Brenot, A., Duong, M., Chan, B. S., & Werb, Z. (2008). Collective Epithelial Migration and Cell Rearrangements Drive Mammary Branching Morphogenesis. *Developmental Cell*, *14*(4), 570–581. https://doi.org/10.1016/j.devcel.2008.03.003

Farooqui, R., & Fenteany, G. (2005). Multiple rows of cells behind an epithelial wound edge extend cryptic lamellipodia to collectively drive cell-sheet movement. *Journal of Cell Science*, *118*(1), 51–63. https://doi.org/10.1242/jcs.01577

Fernández, P. A., Buchmann, B., Goychuk, A., Engelbrecht, L. K., Raich, M. K., Scheel, C. H., Frey, E., & Bausch, A. R. (2021). Surface-tension-induced budding drives alveologenesis in human mammary gland organoids. *Nature Physics*, *17*(10), 1130–1136. https://doi.org/10.1038/s41567-021-01336-7
Bandiera_abtest: a Cg_type: Nature Research Journals Primary_atype: Research Subject_term: Biological physics;Cellular motility;Fluid dynamics Subject_term_id: biological-physics;cellular-motility;fluid-dynamics

Fisher, K. H., & Strutt, D. (2019). A theoretical framework for planar polarity establishment through interpretation of graded cues by molecular bridges. *Development*, *146*(3), dev168955. https://doi.org/10.1242/dev.168955

Fisher, K. H., Strutt, D., & Fletcher, A. G. (2019). Experimental and Theoretical Evidence for Bidirectional Signaling via Core Planar Polarity Protein Complexes in Drosophila. *iScience*, *17*, 49–66. https://doi.org/10.1016/j.isci.2019.06.021

Forbes, A., & Lehmann, R. (1998). Nanos and Pumilio have critical roles in the development and function of Drosophila germline stem cells. *Development*, *125*(4), 679–690. https://doi.org/10.1242/dev.125.4.679

Friedl, P., & Gilmour, D. (2009). Collective cell migration in morphogenesis, regeneration and cancer. *Nature Reviews Molecular Cell Biology*, *10*(7), 445–457. https://doi.org/10.1038/nrm2720

Fritz, R. D., Menshykau, D., Martin, K., Reimann, A., Pontelli, V., & Pertz, O. (2015). SrGAP2-Dependent Integration of Membrane Geometry and Slit-Robo-Repulsive Cues Regulates Fibroblast Contact Inhibition of Locomotion. *Developmental Cell*, *35*(1), 78–92. https://doi.org/10.1016/j.devcel.2015.09.002

Frydman, H. M., & Spradling, A. C. (2001). The receptor-like tyrosine phosphatase Lar is required for epithelial planar polarity and for axis determination with Drosophila ovarian follicles. *Development*, *128*(16), 3209–3220.

Fukai, S., & Yoshida, T. (2021). Roles of type IIa receptor protein tyrosine phosphatases as synaptic organizers. *The FEBS Journal*, *288*(24), 6913–6926. https://doi.org/10.1111/febs.15666

Fulford, A. D., & McNeill, H. (2020). Fat/Dachsous family cadherins in cell and tissue organisation. *Current Opinion in Cell Biology*, *62*, 96–103. https://doi.org/10.1016/j.ceb.2019.10.006

Funderburk, S. F., Wang, Q. J., & Yue, Z. (2010). The Beclin 1–VPS34 complex – at the crossroads of autophagy and beyond. *Trends in Cell Biology*, *20*(6), 355–362. https://doi.org/10.1016/j.tcb.2010.03.002

Gardel, M. L., Sabass, B., Ji, L., Danuser, G., Schwarz, U. S., & Waterman, C. M. (2008). Traction stress in focal adhesions correlates biphasically with actin retrograde flow speed. *Journal of Cell Biology*, *183*(6), 999–1005. https://doi.org/10.1083/jcb.200810060

Gates, J. (2012). Drosophila egg chamber elongation. *Fly*, *6*(4), 213–227. https://doi.org/10.4161/fly.21969

Gee, H. Y., Sadowski, C. E., Aggarwal, P. K., Porath, J. D., Yakulov, T. A., Schueler, M., Lovric, S., Ashraf, S., Braun, D. A., Halbritter, J., Fang, H., Airik, R., Vega-Warner, V., Cho, K. J., Chan, T. A., Morris, L. G. T., ffrench-Constant, C., Allen, N., McNeill, H., … Hildebrandt, F. (2016). FAT1 mutations cause a glomerulotubular nephropathy. *Nature Communications*, *7*(1), 10822. https://doi.org/10.1038/ncomms10822

Geng, W., He, B., Wang, M., & Adler, P. N. (2000). The tricornered Gene, Which Is Required for the Integrity of Epidermal Cell Extensions, Encodes the Drosophila Nuclear DBF2-Related Kinase. *Genetics*, *156*(4), 1817–1828. https://doi.org/10.1093/genetics/156.4.1817

Giavazzi, F., Paoluzzi, M., Macchi, M., Bi, D., Scita, G., Manning, M. L., Cerbino, R., & Marchetti, M. C. (2018). Flocking transitions in confluent tissues. *Soft Matter*, *14*(18), 3471–3477. https://doi.org/10.1039/C8SM00126J

Glashauser, J., Camelo, C., Hollmann, M., Backer, W., Jacobs, T., Sanchez, J. I., Schleutker, R., Förster, D., Berns, N., Riechmann, V., & Luschnig, S. (2023). Acute manipulation

and real-time visualization of membrane trafficking and exocytosis in Drosophila. *Developmental Cell*, *58*(8), 709–723.e7. https://doi.org/10.1016/j.devcel.2023.03.006

Golic, K. G. (1991). Site-Specific Recombination Between Homologous Chromosomes in Drosophila. *Science*, *252*(5008), 958–961. https://doi.org/10.1126/science.2035025

Golic, K. G., & Lindquist, S. (1989). The FLP recombinase of yeast catalyzes site-specific recombination in the drosophila genome. *Cell*, *59*(3), 499–509. https://doi.org/10.1016/0092-8674(89)90033-0

González-Reyes, A., & Johnston, D. S. (1998). Patterning of the follicle cell epithelium along the anterior-posterior axis during Drosophila oogenesis. *Development*, *125*(15), 2837–2846. https://doi.org/10.1242/dev.125.15.2837

Goodrich, L. V., & Strutt, D. (2011). Principles of planar polarity in animal development. *Development*, *138*(10), 1877–1892. https://doi.org/10.1242/dev.054080

Gratz, S. J., Cummings, A. M., Nguyen, J. N., Hamm, D. C., Donohue, L. K., Harrison, M. M., Wildonger, J., & O'Connor-Giles, K. M. (2013). Genome Engineering of Drosophila with the CRISPR RNA-Guided Cas9 Nuclease. *Genetics*, *194*(4), 1029–1035. https://doi.org/10.1534/genetics.113.152710

Gratz, S. J., Ukken, F. P., Rubinstein, C. D., Thiede, G., Donohue, L. K., Cummings, A. M., & O'Connor-Giles, K. M. (2014). Highly Specific and Efficient CRISPR/Cas9-Catalyzed Homology-Directed Repair in Drosophila. *Genetics*, *196*(4), 961–971. https://doi.org/10.1534/genetics.113.160713

Graziano, B. R., & Weiner, O. D. (2014). Self-organization of protrusions and polarity during eukaryotic chemotaxis. *Current Opinion in Cell Biology*, *30*, 60–67. https://doi.org/10.1016/j.ceb.2014.06.007

Gupta, S., & Yap, A. S. (2021). How adherens junctions move cells during collective migration. *Faculty Reviews*, *10*, 56. https://doi.org/10.12703/r/10-56

Gutzeit, H. O., Eberhardt, W., & Gratwohl, E. (1991). Laminin and basement membrane-associated microfilaments in wild-type and mutant Drosophila ovarian follicles. *Journal of Cell Science*, *100*(4), 781–788.

Haigo, S. L., & Bilder, D. (2011). Global Tissue Revolutions in a Morphogenetic Movement Controlling Elongation. *Science*, *331*(6020), 1071–1074. https://doi.org/10.1126/science.1199424

Hammond, M. P., & Laird, C. D. (1985). Chromosome structure and DNA replication in nurse and follicle cells of Drosophila melanogaster. *Chromosoma*, *91*(3), 267–278. https://doi.org/10.1007/BF00328222

Harmansa, S., Alborelli, I., Bieli, D., Caussinus, E., & Affolter, M. (2017). A nanobody-based toolset to investigate the role of protein localization and dispersal in Drosophila (K. VijayRaghavan, Ed.). *eLife*, *6*, e22549. https://doi.org/10.7554/eLife.22549

Harrison, C., Shao, H., Strutt, H., & Strutt, D. (2020). Molecular mechanisms mediating asymmetric subcellular localisation of the core planar polarity pathway proteins. *Biochemical Society Transactions*. https://doi.org/10.1042/BST20190404

Hayakawa, M., Hiraiwa, T., Wada, Y., Kuwayama, H., & Shibata, T. (2020). Polar pattern formation induced by contact following locomotion in a multicellular system (T. Mignot, A. M. Walczak, T. Mignot, & S. Tans, Eds.). *eLife*, *9*, e53609. https://doi.org/10.7554/eLife.53609

Hayashi, S., Ito, K., Sado, Y., Taniguchi, M., Akimoto, A., Takeuchi, H., Aigaki, T., Matsuzaki, F., Nakagoshi, H., Tanimura, T., Ueda, R., Uemura, T., Yoshihara, M., & Goto, S. (2002). GETDB, a database compiling expression patterns and molecular locations of a collection of gal4 enhancer traps. *genesis*, *34*(1-2), 58–61. https://doi.org/10.1002/gene.10137

Hayashi, S., Inoue, Y., Kiyonari, H., Abe, T., Misaki, K., Moriguchi, H., Tanaka, Y., & Takeichi, M. (2014). Protocadherin-17 Mediates Collective Axon Extension by Recruiting Actin Regulator Complexes to Interaxonal Contacts. *Developmental Cell*, *30*(6), 673–687. https://doi.org/10.1016/j.devcel.2014.07.015

Hayer, A., Shao, L., Chung, M., Joubert, L.-M., Yang, H. W., Tsai, F.-C., Bisaria, A., Betzig, E., & Meyer, T. (2016). Engulfed cadherin fingers are polarized junctional structures between collectively migrating endothelial cells. *Nature Cell Biology*, *18*(12), 1311–1323. https://doi.org/10.1038/ncb3438

He, Y., Fang, X., Emoto, K., Jan, Y.-N., & Adler, P. N. (2005). The Tricornered Ser/Thr Protein Kinase Is Regulated by Phosphorylation and Interacts with Furry during Drosophila Wing Hair Development. *Molecular Biology of the Cell*, *16*(2), 689–700. https://doi.org/10.1091/mbc.e04-09-0828

Hergovich, A., Stegert, M. R., Schmitz, D., & Hemmings, B. A. (2006). NDR kinases regulate essential cell processes from yeast to humans. *Nature Reviews Molecular Cell Biology*, *7*(4), 253–264. https://doi.org/10.1038/nrm1891

Hino, N., Rossetti, L., Marín-Llauradó, A., Aoki, K., Trepat, X., Matsuda, M., & Hirashima, T. (2020). ERK-Mediated Mechanochemical Waves Direct Collective Cell Polarization. *Developmental Cell*, *53*(6), 646–660.e8. https://doi.org/10.1016/j.devcel.2020.05.011

Hirata, E., Ichikawa, T., Horike, S.-i., & Kiyokawa, E. (2018). Active K-RAS induces the coherent rotation of epithelial cells: A model for collective cell invasion in vitro. *Cancer Science*, *109*(12), 4045–4055. https://doi.org/10.1111/cas.13816

Horne-Badovinac, S. (2017). Fat-like cadherins in cell migration—leading from both the front and the back. *Current Opinion in Cell Biology*, *48*, 26–32. https://doi.org/10.1016/j.ceb.2017.04.003

Horne-Badovinac, S., & Bilder, D. (2005). Mass transit: Epithelial morphogenesis in the Drosophila egg chamber. *Developmental Dynamics*, *232*(3), 559–574. https://doi.org/10.1002/dvdy.20286

Horne-Badovinac, S., Hill, J., Gerlach, G., Menegas, W., & Bilder, D. (2012). A Screen for Round Egg Mutants in Drosophila Identifies Tricornered, Furry, and Misshapen as Regulators of Egg Chamber Elongation. *G3: Genes, Genomes, Genetics*, *2*(3), 371–378. https://doi.org/10.1534/g3.111.001677

Hou, R., Liu, L., Anees, S., Hiroyasu, S., & Sibinga, N. E. (2006). The Fat1 cadherin integrates vascular smooth muscle cell growth and migration signals. *Journal of Cell Biology*, *173*(3), 417–429. https://doi.org/10.1083/jcb.200508121

Houk, A. R., Jilkine, A., Mejean, C. O., Boltyanskiy, R., Dufresne, E. R., Angenent, S. B., Altschuler, S. J., Wu, L. F., & Weiner, O. D. (2012). Membrane Tension Maintains Cell Polarity by Confining Signals to the Leading Edge during Neutrophil Migration. *Cell*, *148*(1), 175–188. https://doi.org/10.1016/j.cell.2011.10.050

Hu, S., & Zhu, L. (2018). Semaphorins and Their Receptors: From Axonal Guidance to Atherosclerosis. *Frontiers in Physiology*, *9*.

Huang, C.-H., Tang, M., Shi, C., Iglesias, P. A., & Devreotes, P. N. (2013). An excitable signal integrator couples to an idling cytoskeletal oscillator to drive cell migration. *Nature Cell Biology*, *15*(11), 1307–1316. https://doi.org/10.1038/ncb2859

Huang, J., Zhou, W., Dong, W., Watson, A. M., & Hong, Y. (2009). Directed, efficient, and versatile modifications of the Drosophila genome by genomic engineering. *Proceedings of the National Academy of Sciences*, *106*(20), 8284–8289. https://doi.org/10.1073/pnas.0900641106

Hulpiau, P., Gul, I. S., & van Roy, F. (2013). Chapter Four - New Insights into the Evolution of Metazoan Cadherins and Catenins. In F. van Roy (Ed.), *Progress in Molecular Biology and Translational Science* (pp. 71–94). Academic Press.

Humphreys, D., Liu, T., Davidson, A. C., Hume, P. J., & Koronakis, V. (2012). The Drosophila Arf1 homologue Arf79F is essential for lamellipodium formation. *Journal of Cell Science*, *125*(Pt 23), 5630–5635. https://doi.org/10.1242/jcs.108092

Hung, R.-J., & Terman, J. R. (2011). Extracellular inhibitors, repellents, and semaphorin / plexin / MICAL-mediated actin filament disassembly. *Cytoskeleton*, *68*(8), 415–433. https://doi.org/10.1002/cm.20527

Hunter, J. D. (2007). Matplotlib: A 2D Graphics Environment. *Computing in Science & Engineering*, *9*(03), 90–95. https://doi.org/10.1109/MCSE.2007.55

Iglesias, P. A., & Devreotes, P. N. (2012). Biased excitable networks: How cells direct motion in response to gradients. *Current Opinion in Cell Biology*, *24*(2), 245–253. https://doi.org/10.1016/j.ceb.2011.11.009

Isabella, A. J., & Horne-Badovinac, S. (2015). Dynamic regulation of basement membrane protein levels promotes egg chamber elongation in Drosophila. *Developmental Biology*, *406*(2), 212–221. https://doi.org/10.1016/j.ydbio.2015.08.018

Isabella, A. J., & Horne-Badovinac, S. (2016). Rab10-Mediated Secretion Synergizes with Tissue Movement to Build a Polarized Basement Membrane Architecture for Organ Morphogenesis. *Developmental Cell*, *38*(1), 47–60. https://doi.org/10.1016/j.devcel.2016.06.009

Isasti-Sanchez, J., Münz-Zeise, F., Lancino, M., & Luschnig, S. (2021). Transient opening of tricellular vertices controls paracellular transport through the follicle epithelium during Drosophila oogenesis. *Developmental Cell*. https://doi.org/10.1016/j.devcel.2021.03.021

Jain, S., Cachoux, V. M. L., Narayana, G. H. N. S., de Beco, S., D'Alessandro, J., Cellerin, V., Chen, T., Heuzé, M. L., Marcq, P., Mège, R.-M., Kabla, A. J., Lim, C. T., & Ladoux, B. (2020). The role of single-cell mechanical behaviour and polarity in driving collective cell migration. *Nature Physics*, *16*(7), 802–809. https://doi.org/10.1038/s41567-020-0875-z

Joffre, C., Dupont, N., Hoa, L., Gomez, V., Pardo, R., Gonçalves-Pimentel, C., Achard, P., Bettoun, A., Meunier, B., Bauvy, C., Cascone, I., Codogno, P., Fanto, M., Hergovich, A., & Camonis, J. (2015). The Pro-apoptotic STK38 Kinase Is a New Beclin1 Partner

Positively Regulating Autophagy. *Current Biology*, *25*(19), 2479–2492. https://doi.org/10.1016/j.cub.2015.08.031

Kim, J. H., Serra-Picamal, X., Tambe, D. T., Zhou, E. H., Park, C. Y., Sadati, M., Park, J.-A., Krishnan, R., Gweon, B., Millet, E., Butler, J. P., Trepat, X., & Fredberg, J. J. (2013). Propulsion and navigation within the advancing monolayer sheet. *Nature Materials*, *12*(9), 856–863. https://doi.org/10.1038/nmat3689
Bandiera_abtest: a Cg_type: Nature Research Journals Primary_atype: Research Subject_term: Biomaterials – cells;Biomedical engineering;Materials science Subject_term_id: biomaterials-cells;biomedical-engineering;materials-science

Kim, S. A., Tai, C.-Y., Mok, L.-P., Mosser, E. A., & Schuman, E. M. (2011). Calcium-dependent dynamics of cadherin interactions at cell–cell junctions. *Proceedings of the National Academy of Sciences*, *108*(24), 9857–9862. https://doi.org/10.1073/pnas.1019003108

Kirilly, D., & Xie, T. (2007). The Drosophila ovary: An active stem cell community. *Cell Research*, *17*(1), 15–25. https://doi.org/10.1038/sj.cr.7310123

Koronakis, V., Hume, P. J., Humphreys, D., Liu, T., Hørning, O., Jensen, O. N., & McGhie, E. J. (2011). WAVE regulatory complex activation by cooperating GTPases Arf and Rac1. *Proceedings of the National Academy of Sciences*, *108*(35), 14449–14454. https://doi.org/10.1073/pnas.1107666108

Krause, M., & Gautreau, A. (2014). Steering cell migration: Lamellipodium dynamics and the regulation of directional persistence. *Nature Reviews Molecular Cell Biology*, *15*(9), 577–590. https://doi.org/10.1038/nrm3861

Krndija, D., Marjou, F. E., Guirao, B., Richon, S., Leroy, O., Bellaiche, Y., Hannezo, E., & Vignjevic, D. M. (2019). Active cell migration is critical for steady-state epithelial turnover in the gut. *Science*, *365*(6454), 705–710. https://doi.org/10.1126/science.aau3429

Krol, A., Henle, S. J., & Goodrich, L. V. (2016). Fat3 and Ena/VASP proteins influence the emergence of asymmetric cell morphology in the developing retina. *Development*, *143*(12), 2172–2182. https://doi.org/10.1242/dev.133678

Krueger, N. X., Reddy, R. S., Johnson, K., Bateman, J., Kaufmann, N., Scalice, D., Vactor, D. V., & Saito, H. (2003). Functions of the Ectodomain and Cytoplasmic Tyrosine Phosphatase Domains of Receptor Protein Tyrosine Phosphatase Dlar In Vivo. *Molecular and Cellular Biology*, *23*(19), 6909–6921. https://doi.org/10.1128/MCB.23.19.6909-6921.2003

Krueger, N. X., Vactor, D. V., Wan, H. I., Gelbart, W. M., Goodman, C. S., & Saito, H. (1996). The Transmembrane Tyrosine Phosphatase DLAR Controls Motor Axon Guidance in Drosophila. *Cell*, *84*(4), 611–622. https://doi.org/10.1016/S0092-8674(00)81036-3

Kulawiak, D. A., Camley, B. A., & Rappel, W.-J. (2016). Modeling Contact Inhibition of Locomotion of Colliding Cells Migrating on Micropatterned Substrates. *PLOS Computational Biology*, *12*(12), e1005239. https://doi.org/10.1371/journal.pcbi.1005239

Lahrouchi, N., George, A., Ratbi, I., Schneider, R., Elalaoui, S. C., Moosa, S., Bharti, S., Sharma, R., Abu-Asab, M., Onojafe, F., Adadi, N., Lodder, E. M., Laarabi, F.-Z., Lamsyah, Y., Elorch, H., Chebbar, I., Postma, A. V., Lougaris, V., Plebani, A., … Sefiani, A. (2019). Homozygous frameshift mutations in FAT1 cause a syndrome characterized by colobomatous-microphthalmia, ptosis, nephropathy and syndactyly. *Nature Communications*, *10*. https://doi.org/10.1038/s41467-019-08547-w

Lavalou, J., & Lecuit, T. (2022). In search of conserved principles of planar cell polarization. *Current Opinion in Genetics & Development*, *72*, 69–81. https://doi.org/10.1016/j.gde.2021.11.001

Lavalou, J., Mao, Q., Harmansa, S., Kerridge, S., Lellouch, A. C., Philippe, J.-M., Audebert, S., Camoin, L., & Lecuit, T. (2021). Formation of polarized contractile interfaces by self-organized Toll-8/Cirl GPCR asymmetry. *Developmental Cell*, *56*(11), 1574–1588.e7. https://doi.org/10.1016/j.devcel.2021.03.030

Lebensohn, A. M., & Kirschner, M. W. (2009). Activation of the WAVE Complex by Coincident Signals Controls Actin Assembly. *Molecular Cell*, *36*(3), 512–524. https://doi.org/10.1016/j.molcel.2009.10.024

Lebo, D. P. V., & McCall, K. (2021). Murder on the Ovarian Express: A Tale of Non-Autonomous Cell Death in the Drosophila Ovary. *Cells*, *10*(6), 1454. https://doi.org/10.3390/cells10061454

Lerner, D. W., McCoy, D., Isabella, A. J., Mahowald, A. P., Gerlach, G. F., Chaudhry, T. A., & Horne-Badovinac, S. (2013). A Rab10-Dependent Mechanism for Polarized Basement Membrane Secretion during Organ Morphogenesis. *Developmental Cell*, *24*(2), 159–168. https://doi.org/10.1016/j.devcel.2012.12.005

Lewellyn, L., Cetera, M., & Horne-Badovinac, S. (2013). Misshapen decreases integrin levels to promote epithelial motility and planar polarity in Drosophila. *Journal of Cell Biology*, *200*(6), 721–729. https://doi.org/10.1083/jcb.201209129

Li, J. X. H., Tang, V. W., Boateng, K. A., & Brieher, W. M. (2021). Cadherin puncta are interdigitated dynamic actin protrusions necessary for stable cadherin adhesion. *Proceedings of the National Academy of Sciences*, *118*(24). https://doi.org/10.1073/pnas.2023510118

Li, X., Miao, Y., Pal, D. S., & Devreotes, P. N. (2020). Excitable networks controlling cell migration during development and disease. *Seminars in Cell & Developmental Biology*, *100*, 133–142. https://doi.org/10.1016/j.semcdb.2019.11.001

Lin, J., & Yue, Z. (2018). Coupling of apical-basal polarity and planar cell polarity to interpret the Wnt signaling gradient in feather development. *Development*, *145*(17), dev162792. https://doi.org/10.1242/dev.162792

Liu, J.-L. (2010). Intracellular compartmentation of CTP synthase in Drosophila. *Journal of Genetics and Genomics*, *37*(5), 281–296. https://doi.org/10.1016/S1673-8527(09)60046-1

Los, G. V., Encell, L. P., McDougall, M. G., Hartzell, D. D., Karassina, N., Zimprich, C., Wood, M. G., Learish, R., Ohana, R. F., Urh, M., Simpson, D., Mendez, J., Zimmerman, K., Otto, P., Vidugiris, G., Zhu, J., Darzins, A., Klaubert, D. H., Bulleit, R. F., & Wood, K. V. (2008). HaloTag: A Novel Protein Labeling Technology for Cell Imaging and Protein Analysis. *ACS Chemical Biology*, *3*(6), 373–382. https://doi.org/10.1021/cb800025k

Lu, H., & Bilder, D. (2005). Endocytic control of epithelial polarity and proliferation in Drosophila. *Nature Cell Biology*, *7*(12), 1232–1239. https://doi.org/10.1038/ncb1324

Ma, D., Yang, C.-H., McNeill, H., Simon, M., & Axelrod, J. (2003). Fidelity in planar cell polarity signalling. *Nature*, *421*(6922), 543–547. https://doi.org/10.1038/nature01366

Machesky, L. M., Mullins, R. D., Higgs, H. N., Kaiser, D. A., Blanchoin, L., May, R. C., Hall, M. E., & Pollard, T. D. (1999). Scar, a WASp-related protein, activates nucleation of actin filaments by the Arp2/3 complex. *Proceedings of the National Academy of Sciences*, *96*(7), 3739–3744. https://doi.org/10.1073/pnas.96.7.3739

Maines, J. Z., Stevens, L. M., Tong, X., & Stein, D. (2004). Drosophila dMyc is required for ovary cell growth and endoreplication. *Development*, *131*(4), 775–786. https://doi.org/10.1242/dev.00932

Matsuoka, S., & Ueda, M. (2018). Mutual inhibition between PTEN and PIP3 generates bistability for polarity in motile cells. *Nature Communications*, *9*(1), 4481. https://doi.org/10.1038/s41467-018-06856-0

Mayor, R., & Etienne-Manneville, S. (2016). The front and rear of collective cell migration. *Nature Reviews Molecular Cell Biology*, *17*(2), 97–109. https://doi.org/10.1038/nrm.2015.14

Mayor, R., & Theveneau, E. (2013). The role of the non-canonical Wnt–planar cell polarity pathway in neural crest migration. *Biochemical Journal*, *457*(1), 19–26. https://doi.org/10.1042/BJ20131182

McGregor, J. R., Xi, R., & Harrison, D. A. (2002). JAK signaling is somatically required for follicle cell differentiation in Drosophila. *Development*, *129*(3), 705–717. https://doi.org/10.1242/dev.129.3.705

McLaughlin, J. M., & Bratu, D. P. (2015). Drosophila melanogaster Oogenesis: An Overview. In D. P. Bratu & G. P. McNeil (Eds.), *Drosophila Oogenesis: Methods and Protocols* (pp. 1–20). Springer.

Medina, E., Easa, Y., Lester, D. K., Lau, E. K., Sprinzak, D., & Luca, V. C. (2023). Structure of the planar cell polarity cadherins Fat4 and Dachsous1. *Nature Communications*, *14*(1), 891. https://doi.org/10.1038/s41467-023-36435-x

Miki, H., Suetsugu, S., & Takenawa, T. (1998). WAVE, a novel WASP-family protein involved in actin reorganization induced by Rac. *The EMBO Journal*, *17*(23), 6932–6941. https://doi.org/10.1093/emboj/17.23.6932

Miki, H., Yamaguchi, H., Suetsugu, S., & Takenawa, T. (2000). IRSp53 is an essential intermediate between Rac and WAVE in the regulation of membrane ruffling. *Nature*, *408*(6813), 732–735. https://doi.org/10.1038/35047107

Millius, A., Dandekar, S. N., Houk, A. R., & Weiner, O. D. (2009). Neutrophils establish rapid and robust WAVE complex polarity in an actin-dependent fashion. *Current biology: CB*, *19*(3), 253–259. https://doi.org/10.1016/j.cub.2008.12.044

Millius, A., Watanabe, N., & Weiner, O. D. (2012). Diffusion, capture and recycling of SCAR/WAVE and Arp2/3 complexes observed in cells by single-molecule imaging. *Journal of Cell Science*, *125*(5), 1165–1176. https://doi.org/10.1242/jcs.091157

Mishra, A. K., Campanale, J. P., Mondo, J. A., & Montell, D. J. (2019). Cell interactions in collective cell migration. *Development*, *146*(23), dev172056. https://doi.org/10.1242/dev.172056

Moeller, M. J., Soofi, A., Braun, G. S., Li, X., Watzl, C., Kriz, W., & Holzman, L. B. (2004). Protocadherin FAT1 binds Ena/VASP proteins and is necessary for actin dynamics

and cell polarization. *The EMBO Journal*, *23*(19), 3769–3779. https://doi.org/10.1038/sj.emboj.7600380

Montell, D. J., Rorth, P., & Spradling, A. C. (1992). Slow border cells, a locus required for a developmentally regulated cell migration during oogenesis, encodes Drosophila CEBP. *Cell*, *71*(1), 51–62. https://doi.org/10.1016/0092-8674(92)90265-E

Morris, L. G. T., Kaufman, A. M., Gong, Y., Ramaswami, D., Walsh, L. A., Turcan, Ş., Eng, S., Kannan, K., Zou, Y., Peng, L., Banuchi, V. E., Paty, P., Zeng, Z., Vakiani, E., Solit, D., Singh, B., Ganly, I., Liau, L., Cloughesy, T. C., … Chan, T. A. (2013). Recurrent somatic mutation of FAT1 in multiple human cancers leads to aberrant Wnt activation. *Nature Genetics*, *45*(3), 253–261. https://doi.org/10.1038/ng.2538

Mullins, R. D., Bieling, P., & Fletcher, D. A. (2018). From solution to surface to filament: Actin flux into branched networks. *Biophysical Reviews*, *10*(6), 1537–1551. https://doi.org/10.1007/s12551-018-0469-5

Nagai, T., & Mizuno, K. (2014). Multifaceted roles of Furry proteins in invertebrates and vertebrates. *The Journal of Biochemistry*, *155*(3), 137–146. https://doi.org/10.1093/jb/mvu001

Nagar, B., Overduin, M., Ikura, M., & Rini, J. M. (1996). Structural basis of calcium-induced E-cadherin rigidification and dimerization. *Nature*, *380*(6572), 360–364. https://doi.org/10.1038/380360a0

Nakao, S., Platek, A., Hirano, S., & Takeichi, M. (2008). Contact-dependent promotion of cell migration by the OL-protocadherin–Nap1 interaction. *Journal of Cell Biology*, *182*(2), 395–410. https://doi.org/10.1083/jcb.200802069

Nakayama, M., Nakajima, D., Yoshimura, R., Endo, Y., & Ohara, O. (2002). MEGF1/fat2 Proteins Containing Extraordinarily Large Extracellular Domains Are Localized to Thin Parallel Fibers of Cerebellar Granule Cells. *Molecular and Cellular Neuroscience*, *20*(4), 563–578. https://doi.org/10.1006/mcne.2002.1146

Namekata, K., Harada, C., Taya, C., Guo, X., Kimura, H., Parada, L. F., & Harada, T. (2010). Dock3 induces axonal outgrowth by stimulating membrane recruitment of the WAVE complex. *Proceedings of the National Academy of Sciences*, *107*(16), 7586–7591. https://doi.org/10.1073/pnas.0914514107

Nishikawa, Y., Miyazaki, T., Nakashiro, K.-I., Yamagata, H., Isokane, M., Goda, H., Tanaka, H., Oka, R., & Hamakawa, H. (2011). Human FAT1 cadherin controls cell migration and invasion of oral squamous cell carcinoma through the localization of beta-catenin. *Oncology Reports*, *26*(3), 587–592. https://doi.org/10.3892/or.2011.1324

Norden, C., & Lecaudey, V. (2019). Collective cell migration: General themes and new paradigms. *Current Opinion in Genetics & Development*, *57*, 54–60. https://doi.org/10.1016/j.gde.2019.06.013

Norkett, R., del Castillo, U., Lu, W., & Gelfand, V. I. (2020). Ser/Thr kinase Trc controls neurite outgrowth in Drosophila by modulating microtubule-microtubule sliding (S. R. Pfeffer & J. G. DeLuca, Eds.). *eLife*, *9*, e52009. https://doi.org/10.7554/eLife.52009

Oikawa, T., Yamaguchi, H., Itoh, T., Kato, M., Ijuin, T., Yamazaki, D., Suetsugu, S., & Takenawa, T. (2004). PtdIns(3,4,5)P 3 binding is necessary for WAVE2-induced formation of lamellipodia. *Nature Cell Biology*, *6*(5), 420–426. https://doi.org/10.1038/ncb1125

Okajima, T., Gu, Y., Teruya, R.-i., Yano, S., Taketomi, T., Sato, B., Chiba, T., & Tsuruta, F. (2020). Atypical Cadherin FAT3 Is a Novel Mediator for Morphological Changes of Microglia. *eNeuro*, *7*(6). https://doi.org/10.1523/ENEURO.0056-20.2020

Olson, H. M., & Nechiporuk, A. V. (2018). Using Zebrafish to Study Collective Cell Migration in Development and Disease. *Frontiers in Cell and Developmental Biology*, *6*.

Özkan, E., Carrillo, R. A., Eastman, C. L., Weiszmann, R., Waghray, D., Johnson, K. G., Zinn, K., Celniker, S. E., & Garcia, K. C. (2013). An Extracellular Interactome of Immunoglobulin and LRR Proteins Reveals Receptor-Ligand Networks. *Cell*, *154*(1), 228–239. https://doi.org/10.1016/j.cell.2013.06.006

Park, D., Wershof, E., Boeing, S., Labernadie, A., Jenkins, R. P., George, S., Trepat, X., Bates, P. A., & Sahai, E. (2020). Extracellular matrix anisotropy is determined by TFAP2C-dependent regulation of cell collisions. *Nature Materials*, *19*(2), 227–238. https://doi.org/10.1038/s41563-019-0504-3

Park, J.-A., Kim, J. H., Bi, D., Mitchel, J. A., Qazvini, N. T., Tantisira, K., Park, C. Y., McGill, M., Kim, S.-H., Gweon, B., Notbohm, J., Steward Jr, R., Burger, S., Randell, S. H., Kho, A. T., Tambe, D. T., Hardin, C., Shore, S. A., Israel, E., ... Fredberg, J. J. (2015). Unjamming and cell shape in the asthmatic airway epithelium. *Nature Materials*, *14*(10), 1040–1048. https://doi.org/10.1038/nmat4357

Parsons, T. T., Mosallaei, S., & Raftery, L. A. (2023). Two phases for centripetal migration of Drosophila melanogaster follicle cells: Initial ingression followed by epithelial migration. *Development*, *150*(6), dev200492. https://doi.org/10.1242/dev.200492

Pastushenko, I., Mauri, F., Song, Y., de Cock, F., Meeusen, B., Swedlund, B., Impens, F., Van Haver, D., Opitz, M., Thery, M., Bareche, Y., Lapouge, G., Vermeersch, M., Van Eycke, Y.-R., Balsat, C., Decaestecker, C., Sokolow, Y., Hassid, S., Perez-Bustillo, A.,

... Blanpain, C. (2020). Fat1 deletion promotes hybrid EMT state, tumour stemness and metastasis. *Nature*, 1–8. https://doi.org/10.1038/s41586-020-03046-1

Perez-Vale, K. Z., & Peifer, M. (2020). Orchestrating morphogenesis: Building the body plan by cell shape changes and movements. *Development*, *147*(17), dev191049. https://doi.org/10.1242/dev.191049

Pipathsouk, A., Brunetti, R. M., Town, J. P., Breuer, A., Pellett, P. A., Marchuk, K., Tran, N.-H. T., Krummel, M. F., Stamou, D., & Weiner, O. D. (2019). WAVE complex self-organization templates lamellipodial formation. *bioRxiv*, 836585. https://doi.org/10.1101/836585

Poon, C. L. C., Liu, W., Song, Y., Gomez, M., Kulaberoglu, Y., Zhang, X., Xu, W., Veraksa, A., Hergovich, A., Ghabrial, A., & Harvey, K. F. (2018). A Hippo-like Signaling Pathway Controls Tracheal Morphogenesis in Drosophila melanogaster. *Developmental Cell*, *47*(5), 564–575.e5. https://doi.org/10.1016/j.devcel.2018.09.024

Port, F., Chen, H.-M., Lee, T., & Bullock, S. L. (2014). Optimized CRISPR/Cas tools for efficient germline and somatic genome engineering in Drosophila. *Proceedings of the National Academy of Sciences*, *111*(29), E2967–E2976. https://doi.org/10.1073/pnas.1405500111

Prasad, M., & Montell, D. J. (2007). Cellular and Molecular Mechanisms of Border Cell Migration Analyzed Using Time-Lapse Live-Cell Imaging. *Developmental Cell*, *12*(6), 997–1005. https://doi.org/10.1016/j.devcel.2007.03.021

Ramos-Lewis, W., & Page-McCaw, A. (2019). Basement membrane mechanics shape development: Lessons from the fly. *Matrix Biology*, *75–76*, 72–81. https://doi.org/10.1016/j.matbio.2018.04.004

Ranaivoson, F. M., Turk, L. S., Ozgul, S., Kakehi, S., von Daake, S., Lopez, N., Trobiani, L., De Jaco, A., Denissova, N., Demeler, B., Özkan, E., Montelione, G. T., & Comoletti, D. (2019). A Proteomic Screen of Neuronal Cell-Surface Molecules Reveals IgLONs as Structurally Conserved Interaction Modules at the Synapse. *Structure*, *27*(6), 893–906.e9. https://doi.org/10.1016/j.str.2019.03.004

Roberto, G. M., & Emery, G. (2022). Directing with restraint: Mechanisms of protrusion restriction in collective cell migrations. *Seminars in Cell & Developmental Biology*, *129*, 75–81. https://doi.org/10.1016/j.semcdb.2022.03.037

Robichaux, M. A., & Cowan, C. W. (2014). Signaling Mechanisms of Axon Guidance and Early Synaptogenesis. In S. L. Andersen & D. S. Pine (Eds.), *The Neurobiology of Childhood* (pp. 19–48). Springer. https://doi.org/10.1007/7854_2013_255

Rørth, P. (2012). Fellow travellers: Emergent properties of collective cell migration. *EMBO reports*, *13*(11), 984–991. https://doi.org/10.1038/embor.2012.149

Roycroft, A., & Mayor, R. (2015). Forcing contact inhibition of locomotion. *Trends in Cell Biology*, *25*(7), 373–375. https://doi.org/10.1016/j.tcb.2015.05.001

Roycroft, A., & Mayor, R. (2016). Molecular basis of contact inhibition of locomotion. *Cellular and Molecular Life Sciences*, *73*(6), 1119–1130. https://doi.org/10.1007/s00018-015-2090-0

Royzman, I., & Orr-Weaver, T. L. (1998). S phase and differential DNA replication during Drosophila oogenesis. *Genes to Cells*, *3*(12), 767–776. https://doi.org/10.1046/j.1365-2443.1998.00232.x

Rubinstein, R., Goodman, K. M., Maniatis, T., Shapiro, L., & Honig, B. (2017). Structural origins of clustered protocadherin-mediated neuronal barcoding. *Seminars in Cell & Developmental Biology*, *69*, 140–150. https://doi.org/10.1016/j.semcdb.2017.07.023

Saburi, S., Hester, I., Goodrich, L., & McNeill, H. (2012). Functional interactions between Fat family cadherins in tissue morphogenesis and planar polarity. *Development*, *139*(10), 1806–1820. https://doi.org/10.1242/dev.077461

Sadeqzadeh, E., de Bock, C. E., & Thorne, R. F. (2014). Sleeping Giants: Emerging Roles for the Fat Cadherins in Health and Disease. *Medicinal Research Reviews*, *34*(1), 190–221. https://doi.org/10.1002/med.21286

Scarpa, E., & Mayor, R. (2016). Collective cell migration in development. *Journal of Cell Biology*, *212*(2), 143–155. https://doi.org/10.1083/jcb.201508047

Schindelin, J., Arganda-Carreras, I., Frise, E., Kaynig, V., Longair, M., Pietzsch, T., Preibisch, S., Rueden, C., Saalfeld, S., Schmid, B., Tinevez, J.-Y., White, D. J., Hartenstein, V., Eliceiri, K., Tomancak, P., & Cardona, A. (2012). Fiji: An open-source platform for biological-image analysis. *Nature Methods*, *9*(7), 676–682. https://doi.org/10.1038/nmeth.2019

Schindelin, J., Rueden, C. T., Hiner, M. C., & Eliceiri, K. W. (2015). The ImageJ ecosystem: An open platform for biomedical image analysis. *Molecular Reproduction and Development*, *82*(7-8), 518–529. https://doi.org/10.1002/mrd.22489

Schmidt, E. F., Shim, S.-O., & Strittmatter, S. M. (2008). Release of MICAL Autoinhibition by Semaphorin-Plexin Signaling Promotes Interaction with Collapsin Response Mediator Protein. *Journal of Neuroscience*, *28*(9), 2287–2297. https://doi.org/10.1523/JNEUROSCI.5646-07.2008

Schmitz, C., Wacker, I., & Hutter, H. (2008). The Fat-like cadherin CDH-4 controls axon fasciculation, cell migration and hypodermis and pharynx development in Caenorhabditis elegans. *Developmental Biology*, *316*(2), 249–259. https://doi.org/10.1016/j.ydbio.2008.01.024

Schreiner, D., Müller, K., & Hofer, H. W. (2006). The intracellular domain of the human protocadherin hFat1 interacts with Homer signalling scaffolding proteins. *FEBS Letters*, *580*(22), 5295–5300. https://doi.org/10.1016/j.febslet.2006.08.079

Schulte, J., Sepp, K. J., Jorquera, R. A., Wu, C., Song, Y., Hong, P., & Littleton, J. T. (2010). DMob4/Phocein Regulates Synapse Formation, Axonal Transport, and Microtubule Organization. *The Journal of Neuroscience*, *30*(15), 5189–5203. https://doi.org/10.1523/JNEUROSCI.5823-09.2010

Schumacher, L. (2019). Collective Cell Migration in Development. In C. A. M. La Porta & S. Zapperi (Eds.), *Cell Migrations: Causes and Functions* (pp. 105–116). Springer International Publishing. https://doi.org/10.1007/978-3-030-17593-1_7

Servant, G., Weiner, O. D., Herzmark, P., Balla, T., Sedat, J. W., & Bourne, H. R. (2000). Polarization of chemoattractant receptor signaling during neutrophil chemotaxis. *Science (New York, N.Y.)*, *287*(5455), 1037–1040. https://doi.org/10.1126/science.287.5455.1037

Sharma, P., & McNeill, H. (2013). Chapter Ten - Fat and Dachsous Cadherins. In F. van Roy (Ed.), *Progress in Molecular Biology and Translational Science* (pp. 215–235). Academic Press. https://doi.org/10.1016/B978-0-12-394311-8.00010-8

Shaw, T. J., & Martin, P. (2016). Wound repair: A showcase for cell plasticity and migration. *Current Opinion in Cell Biology*, *42*, 29–37. https://doi.org/10.1016/j.ceb.2016.04.001

Shellard, A., & Mayor, R. (2019a). Supracellular migration – beyond collective cell migration. *Journal of Cell Science*, *132*(8), jcs226142. https://doi.org/10.1242/jcs.226142

Shellard, A., & Mayor, R. (2019b). Integrating chemical and mechanical signals in neural crest cell migration. *Current Opinion in Genetics & Development*, *57*, 16–24. https://doi.org/10.1016/j.gde.2019.06.004

Shellard, A., Szabó, A., Trepat, X., & Mayor, R. (2018). Supracellular contraction at the rear of neural crest cell groups drives collective chemotaxis. *Science*, *362*(6412), 339–343. https://doi.org/10.1126/science.aau3301

Sherrard, K. M., Cetera, M., & Horne-Badovinac, S. (2021). DAAM mediates the assembly of long-lived, treadmilling stress fibers in collectively migrating epithelial cells in Drosophila (D. Applewhite, A. Akhmanova, D. Applewhite, & G. Tanentzapf, Eds.). *eLife*, *10*, e72881. https://doi.org/10.7554/eLife.72881

Shimada, Y., Yonemura, S., Ohkura, H., Strutt, D., & Uemura, T. (2006). Polarized Transport of Frizzled along the Planar Microtubule Arrays in Drosophila Wing Epithelium. *Developmental Cell*, *10*(2), 209–222. https://doi.org/10.1016/j.devcel.2005.11.016

Shravage, B. V., Hill, J. H., Powers, C. M., Wu, L., & Baehrecke, E. H. (2013). Atg6 is required for multiple vesicle trafficking pathways and hematopoiesis in Drosophila. *Development*, *140*(6), 1321–1329. https://doi.org/10.1242/dev.089490

Smeets, B., Alert, R., Pešek, J., Pagonabarraga, I., Ramon, H., & Vincent, R. (2016). Emergent structures and dynamics of cell colonies by contact inhibition of locomotion. *Proceedings of the National Academy of Sciences*, *113*(51), 14621–14626. https://doi.org/10.1073/pnas.1521151113

Soans, K. G., Ramos, A. P., Sidhaye, J., Krishna, A., Solomatina, A., Hoffmann, K. B., Schlüßler, R., Guck, J., Sbalzarini, I. F., Modes, C. D., & Norden, C. (2022). Collective cell migration during optic cup formation features changing cell-matrix interactions linked to matrix topology. *Current Biology*, *32*(22), 4817–4831.e9. https://doi.org/10.1016/j.cub.2022.09.034

Sofroniew, N., Lambert, T., Evans, K., Nunez-Iglesias, J., Bokota, G., Winston, P., Peña-Castellanos, G., Yamauchi, K., Bussonnier, M., Doncila Pop, D., Can Solak, A., Liu, Z., Wadhwa, P., Burt, A., Buckley, G., Sweet, A., Migas, L., Hilsenstein, V., Gaifas, L., … McGovern, A. (2022). Napari: A multi-dimensional image viewer for Python. https://doi.org/10.5281/zenodo.7276432

Sossey-Alaoui, K., Li, X., Ranalli, T. A., & Cowell, J. K. (2005). WAVE3-mediated Cell Migration and Lamellipodia Formation Are Regulated Downstream of Phosphatidylinositol 3-Kinase*. *Journal of Biological Chemistry*, *280*(23), 21748–21755. https://doi.org/10.1074/jbc.M500503200

Sotomayor, M., Gaudet, R., & Corey, D. P. (2014). Sorting out a promiscuous superfamily: Towards cadherin connectomics. *Trends in Cell Biology*, *24*(9), 524–536. https://doi.org/10.1016/j.tcb.2014.03.007

Spracklen, A. J., Fagan, T. N., Lovander, K. E., & Tootle, T. L. (2014). The pros and cons of common actin labeling tools for visualizing actin dynamics during Drosophila oogenesis. *Developmental Biology*, *393*(2), 209–226. https://doi.org/10.1016/j.ydbio.2014.06.022

Spradling, A. C., de Cuevas, M., Drummond-Barbosa, D., Keyes, L., Lilly, M., Pepling, M., & Xie, T. (1997). The Drosophila Germarium: Stem Cells, Germ Line Cysts, and Oocytes. *Cold Spring Harbor Symposia on Quantitative Biology*, *62*, 25–34. https://doi.org/10.1101/SQB.1997.062.01.006

Spradling, A. C. (1993). Developmental genetics of oogenesis. *The development of Drosophila melanogaster*, *1*, 1–70.

Squarr, A. J., Brinkmann, K., Chen, B., Steinbacher, T., Ebnet, K., Rosen, M. K., & Bogdan, S. (2016). Fat2 acts through the WAVE regulatory complex to drive collective cell migration during tissue rotation. *Journal of Cell Biology*, *212*(5), 591–603. https://doi.org/10.1083/jcb.201508081

Stahley, S. N., Basta, L. P., Sharan, R., & Devenport, D. (2021). Celsr1 adhesive interactions mediate the asymmetric organization of planar polarity complexes (W. I. Weis & A. Akhmanova, Eds.). *eLife*, *10*, e62097. https://doi.org/10.7554/eLife.62097

Stedden, C. G. (2019). *Semaphorin Signaling Coordinates the Collective Migration of Epithelial Cells in the Drosophila Egg Chamber* (Doctoral dissertation). The University of Chicago. https://doi.org/10.6082/uchicago.1718

Stedden, C. G., Menegas, W., Zajac, A. L., Williams, A. M., Cheng, S., Özkan, E., & Horne-Badovinac, S. (2019). Planar-Polarized Semaphorin-5c and Plexin A Promote the Collective Migration of Epithelial Cells in Drosophila. *Current Biology*, *29*(6), 908–920.e6. https://doi.org/10.1016/j.cub.2019.01.049

Steffen, A., Rottner, K., Ehinger, J., Innocenti, M., Scita, G., Jürgen, W., & Stradal, T. E. (2004). Sra-1 and Nap1 link Rac to actin assembly driving lamellipodia formation. *The EMBO Journal*, *23*(4), 749–759. https://doi.org/10.1038/sj.emboj.7600084

Stock, J., & Pauli, A. (2021). Self-organized cell migration across scales – from single cell movement to tissue formation. *Development*, *148*(7). https://doi.org/10.1242/dev.191767

Stramer, B., & Mayor, R. (2017). Mechanisms and in vivo functions of contact inhibition of locomotion. *Nature Reviews Molecular Cell Biology*, *18*(1), 43–55. https://doi.org/10.1038/nrm.2016.118

Stramer, B., Moreira, S., Millard, T., Evans, I., Huang, C.-Y., Sabet, O., Milner, M., Dunn, G., Martin, P., & Wood, W. (2010). Clasp-mediated microtubule bundling regulates persistent motility and contact repulsion in Drosophila macrophages in vivo. *Journal of Cell Biology*, *189*(4), 681–689. https://doi.org/10.1083/jcb.200912134

Stringer, C., Wang, T., Michaelos, M., & Pachitariu, M. (2021). Cellpose: A generalist algorithm for cellular segmentation. *Nature Methods*, *18*(1), 100–106. https://doi.org/10.1038/s41592-020-01018-x

Strutt, H., Gamage, J., & Strutt, D. (2016). Robust Asymmetric Localization of Planar Polarity Proteins Is Associated with Organization into Signalosome-like Domains of Variable Stoichiometry. *Cell Reports*, *17*(10), 2660–2671. https://doi.org/10.1016/j.celrep.2016.11.021

Strutt, H., Langton, P. F., Pearson, N., McMillan, K. J., Strutt, D., & Cullen, P. J. (2019). Retromer Controls Planar Polarity Protein Levels and Asymmetric Localization at Intercellular Junctions. *Current Biology*, *29*(3), 484–491.e6. https://doi.org/10.1016/j.cub.2018.12.027

Strutt, H., & Strutt, D. (2008). Differential Stability of Flamingo Protein Complexes Underlies the Establishment of Planar Polarity. *Current Biology*, *18*(20), 1555–1564. https://doi.org/10.1016/j.cub.2008.08.063

Strutt, H., Warrington, S. J., & Strutt, D. (2011). Dynamics of Core Planar Polarity Protein Turnover and Stable Assembly into Discrete Membrane Subdomains. *Developmental Cell*, *20*(4), 511–525. https://doi.org/10.1016/j.devcel.2011.03.018

Styhler, S., Nakamura, A., Swan, A., Suter, B., & Lasko, P. (1998). Vasa is required for GURKEN accumulation in the oocyte, and is involved in oocyte differentiation and germline cyst development. *Development*, *125*(9), 1569–1578. https://doi.org/10.1242/dev.125.9.1569

Sundararajan, L., & Lundquist, E. A. (2012). Transmembrane proteins UNC-40/DCC, PTP-3/LAR, and MIG-21 control anterior-posterior neuroblast migration with left-right functional asymmetry in Caenorhabditis elegans. *Genetics*, *192*(4), 1373–1388. https://doi.org/10.1534/genetics.112.145706

Sundararajan, L., Norris, M. L., Schöneich, S., Ackley, B. D., & Lundquist, E. A. (2014). The fat-like cadherin CDH-4 acts cell-non-autonomously in anterior–posterior neuroblast migration. *Developmental Biology*, *392*(2), 141–152. https://doi.org/10.1016/j.ydbio.2014.06.009

Szabó, A., Theveneau, E., Turan, M., & Mayor, R. (2019). Neural crest streaming as an emergent property of tissue interactions during morphogenesis. *PLOS Computational Biology*, *15*(4), e1007002. https://doi.org/10.1371/journal.pcbi.1007002

Tada, M., & Heisenberg, C.-P. (2012). Convergent extension: Using collective cell migration and cell intercalation to shape embryos. *Development*, *139*(21), 3897–3904. https://doi.org/10.1242/dev.073007

Takahashi, H., & Craig, A. M. (2013). Protein tyrosine phosphatases PTPδ, PTPσ, and LAR: Presynaptic hubs for synapse organization. *Trends in Neurosciences*, *36*(9), 522–534. https://doi.org/10.1016/j.tins.2013.06.002

Tanentzapf, G., Smith, C., McGlade, J., & Tepass, U. (2000). Apical, Lateral, and Basal Polarization Cues Contribute to the Development of the Follicular Epithelium during Drosophila Oogenesis. *Journal of Cell Biology*, *151*(4), 891–904. https://doi.org/10.1083/jcb.151.4.891

Tanner, K., Mori, H., Mroue, R., Bruni-Cardoso, A., & Bissell, M. J. (2012). Coherent angular motion in the establishment of multicellular architecture of glandular tissues. *Proceedings of the National Academy of Sciences*, *109*(6), 1973–1978. https://doi.org/10.1073/pnas.1119578109

Tanoue, T., & Takeichi, M. (2004). Mammalian Fat1 cadherin regulates actin dynamics and cell–cell contact. *Journal of Cell Biology*, *165*(4), 517–528. https://doi.org/10.1083/jcb.200403006

Tanoue, T., & Takeichi, M. (2005). New insights into Fat cadherins. *Journal of Cell Science*, *118*(11), 2347–2353. https://doi.org/10.1242/jcs.02398

Terman, J. R., Mao, T., Pasterkamp, R. J., Yu, H.-H., & Kolodkin, A. L. (2002). MICALs, a Family of Conserved Flavoprotein Oxidoreductases, Function in Plexin-Mediated Axonal Repulsion. *Cell*, *109*(7), 887–900. https://doi.org/10.1016/S0092-8674(02)00794-8

Theveneau, E., & Mayor, R. (2013). Collective cell migration of epithelial and mesenchymal cells. *Cellular and Molecular Life Sciences*, *70*(19), 3481–3492. https://doi.org/10.1007/s00018-012-1251-7

Town, J., & Weiner, O. (2022). *Rac negative feedback links local PIP $_3$ rate-of-change to dynamic control of neutrophil guidance* (Preprint). Cell Biology. https://doi.org/10.1101/2022.12.30.521706

Trepat, X., & Sahai, E. (2018). Mesoscale physical principles of collective cell organization. *Nature Physics*, *14*(7), 671–682. https://doi.org/10.1038/s41567-018-0194-9

Trepat, X., Wasserman, M. R., Angelini, T. E., Millet, E., Weitz, D. A., Butler, J. P., & Fredberg, J. J. (2009). Physical forces during collective cell migration. *Nature Physics*, *5*(6), 426–430. https://doi.org/10.1038/nphys1269

Truong Quang, B.-A., Mani, M., Markova, O., Lecuit, T., & Lenne, P.-F. (2013). Principles of E-Cadherin Supramolecular Organization In Vivo. *Current Biology*, *23*(22), 2197–2207. https://doi.org/10.1016/j.cub.2013.09.015

Tsukasaki, Y., Miyazaki, N., Matsumoto, A., Nagae, S., Yonemura, S., Tanoue, T., Iwasaki, K., & Takeichi, M. (2014). Giant cadherins Fat and Dachsous self-bend to organize properly spaced intercellular junctions. *Proceedings of the National Academy of Sciences*, *111*(45), 16011–16016. https://doi.org/10.1073/pnas.1418990111

Tweedy, L., Thomason, P. A., Paschke, P. I., Martin, K., Machesky, L. M., Zagnoni, M., & Insall, R. H. (2020). Seeing around corners: Cells solve mazes and respond at a distance using attractant breakdown. *Science*, *369*(6507), eaay9792. https://doi.org/10.1126/science.aay9792

Ultanir, S. K., Hertz, N. T., Li, G., Ge, W.-P., Burlingame, A. L., Pleasure, S. J., Shokat, K. M., Jan, L. Y., & Jan, Y.-N. (2012). Chemical Genetic Identification of NDR1/2 Kinase Substrates AAK1 and Rabin8 Uncovers Their Roles in Dendrite Arborization and Spine Development. *Neuron*, *73*(6), 1127–1142. https://doi.org/10.1016/j.neuron.2012.01.019

van der Walt, S., Schönberger, J. L., Nunez-Iglesias, J., Boulogne, F., Warner, J. D., Yager, N., Gouillart, E., & Yu, T. (2014). Scikit-image: Image processing in Python. *PeerJ*, *2*, e453. https://doi.org/10.7717/peerj.453

Vasilyev, A., Liu, Y., Mudumana, S., Mangos, S., Lam, P.-Y., Majumdar, A., Zhao, J., Poon, K.-L., Kondrychyn, I., Korzh, V., & Drummond, I. A. (2009). Collective Cell Migration Drives Morphogenesis of the Kidney Nephron. *PLOS Biology*, *7*(1), e1000009. https://doi.org/10.1371/journal.pbio.1000009

Vecchio, S. L., Pertz, O., Szopos, M., Navoret, L., & Riveline, D. (2023). Spontaneous rotations in epithelia as an interplay between cell polarity and boundaries. https://doi.org/10.1101/2021.11.11.468187

Vedula, S. R. K., Leong, M. C., Lai, T. L., Hersen, P., Kabla, A. J., Lim, C. T., & Ladoux, B. (2012). Emerging modes of collective cell migration induced by geometrical constraints. *Proceedings of the National Academy of Sciences*, *109*(32), 12974–12979. https://doi.org/10.1073/pnas.1119313109

Venhuizen, J.-H., & Zegers, M. M. (2017). Making Heads or Tails of It: Cell–Cell Adhesion in Cellular and Supracellular Polarity in Collective Migration. *Cold Spring Harbor Perspectives in Biology*, *9*(11), a027854. https://doi.org/10.1101/cshperspect.a027854

Verhagen, M. G., & Pasterkamp, R. J. (2020). Axon guidance: Semaphorin/neuropilin/plexin signaling. In *Cellular Migration and Formation of Axons and Dendrites* (pp. 109–122). Elsevier. https://doi.org/10.1016/B978-0-12-814407-7.00005-5

Viktorinová, I., & Dahmann, C. (2013). Microtubule Polarity Predicts Direction of Egg Chamber Rotation in Drosophila. *Current Biology*, *23*(15), 1472–1477. https://doi.org/10.1016/j.cub.2013.06.014

Viktorinová, I., König, T., Schlichting, K., & Dahmann, C. (2009). The cadherin Fat2 is required for planar cell polarity in the Drosophila ovary. *Development*, *136*(24), 4123–4132. https://doi.org/10.1242/dev.039099

Villar-Cerviño, V., Molano-Mazón, M., Catchpole, T., Valdeolmillos, M., Henkemeyer, M., Martínez, L. M., Borrell, V., & Marín, O. (2013). Contact repulsion controls the dispersion and final distribution of Cajal-Retzius cells. *Neuron*, *77*(3), 457–471. https://doi.org/10.1016/j.neuron.2012.11.023

Virtanen, P., Gommers, R., Oliphant, T. E., Haberland, M., Reddy, T., Cournapeau, D., Burovski, E., Peterson, P., Weckesser, W., Bright, J., van der Walt, S. J., Brett, M., Wilson, J., Millman, K. J., Mayorov, N., Nelson, A. R. J., Jones, E., Kern, R., Larson, E., … van Mulbregt, P. (2020). SciPy 1.0: Fundamental algorithms for scientific computing in Python. *Nature Methods*, *17*(3), 261–272. https://doi.org/10.1038/s41592-019-0686-2

Vishwakarma, M., Di Russo, J., Probst, D., Schwarz, U. S., Das, T., & Spatz, J. P. (2018). Mechanical interactions among followers determine the emergence of leaders in migrating epithelial cell collectives. *Nature Communications*, *9*(1), 3469. https://doi.org/10.1038/s41467-018-05927-6

Wallingford, J. B. (2010). Planar cell polarity signaling, cilia and polarized ciliary beating. *Current Opinion in Cell Biology*, *22*(5), 597–604. https://doi.org/10.1016/j.ceb.2010.07.011

Wang, H., Lacoche, S., Huang, L., Xue, B., & Muthuswamy, S. K. (2013). Rotational motion during three-dimensional morphogenesis of mammary epithelial acini relates to laminin matrix assembly. *Proceedings of the National Academy of Sciences*, *110*(1), 163–168. https://doi.org/10.1073/pnas.1201141110

Wang, N., Dhumale, P., Chiang, J., & Püschel, A. W. (2018). The Sema3A receptor Plexin-A1 suppresses supernumerary axons through Rap1 GTPases. *Scientific Reports*, *8*, 15647. https://doi.org/10.1038/s41598-018-34092-5

Warrington, S., Strutt, H., Fisher, K., & Strutt, D. (2017). A Dual Function for Prickle in Regulating Frizzled Stability during Feedback-Dependent Amplification of Planar Polarity. *Current Biology*, *27*(18), 2784–2797.e3. https://doi.org/10.1016/j.cub.2017.08.016

Wehrle-Haller, B. (2012a). Structure and function of focal adhesions. *Current Opinion in Cell Biology*, *24*(1), 116–124. https://doi.org/10.1016/j.ceb.2011.11.001

Wehrle-Haller, B. (2012b). Assembly and disassembly of cell matrix adhesions. *Current Opinion in Cell Biology*, *24*(5), 569–581. https://doi.org/10.1016/j.ceb.2012.06.010

Weiner, O. D., Marganski, W. A., Wu, L. F., Altschuler, S. J., & Kirschner, M. W. (2007). An Actin-Based Wave Generator Organizes Cell Motility. *PLOS Biology*, *5*(9), e221. https://doi.org/10.1371/journal.pbio.0050221

Weiner, O. D., Rentel, M. C., Ott, A., Brown, G. E., Jedrychowski, M., Yaffe, M. B., Gygi, S. P., Cantley, L. C., Bourne, H. R., & Kirschner, M. W. (2006). Hem-1 Complexes Are Essential for Rac Activation, Actin Polymerization, and Myosin Regulation during Neutrophil Chemotaxis. *PLOS Biology*, *4*(2), e38. https://doi.org/10.1371/journal.pbio.0040038

Welch, M. D., Mallavarapu, A., Rosenblatt, J., & Mitchison, T. J. (1997). Actin dynamics in vivo. *Current Opinion in Cell Biology*, *9*(1), 54–61. https://doi.org/10.1016/S0955-0674(97)80152-4

Williams, A. M., Donoughe, S., Munro, E., & Horne-Badovinac, S. (2022). Fat2 polarizes the WAVE complex in trans to align cell protrusions for collective migration. *eLife*, *11*, e78343. https://doi.org/10.7554/eLife.78343

Williams, A. M., & Horne-Badovinac, S. (2023). Fat2 polarizes Lar and Sema5c to coordinate the motility of collectively migrating epithelial cells. https://doi.org/10.1101/2023.02.28.530349

Wojtowicz, W. M., Wu, W., Andre, I., Qian, B., Baker, D., & Zipursky, S. L. (2007). A Vast Repertoire of Dscam Binding Specificities Arises from Modular Interactions of Variable Ig Domains. *Cell*, *130*(6), 1134–1145. https://doi.org/10.1016/j.cell.2007.08.026

Wu, Y., Kanchanawong, P., & Zaidel-Bar, R. (2015). Actin-Delimited Adhesion-Independent Clustering of E-Cadherin Forms the Nanoscale Building Blocks of Adherens Junctions. *Developmental Cell*, *32*(2), 139–154. https://doi.org/10.1016/j.devcel.2014.12.003

Wu, Z., Sawada, T., Shiba, K., Liu, S., Kanao, T., Takahashi, R., Hattori, N., Imai, Y., & Lu, B. (2013). Tricornered/NDR kinase signaling mediates PINK1-directed mitochondrial quality control and tissue maintenance. *Genes & Development*, *27*(2), 157–162. https://doi.org/10.1101/gad.203406.112

Xie, T., & Spradling, A. C. (1998). Decapentaplegic Is Essential for the Maintenance and Division of Germline Stem Cells in the Drosophila Ovary. *Cell*, *94*(2), 251–260. https://doi.org/10.1016/S0092-8674(00)81424-5

Xiong, Y., Huang, C.-H., Iglesias, P. A., & Devreotes, P. N. (2010). Cells navigate with a local-excitation, global-inhibition-biased excitable network. *Proceedings of the National Academy of Sciences*, *107*(40), 17079–17086. https://doi.org/10.1073/pnas.1011271107

Yam, P. T., Wilson, C. A., Ji, L., Hebert, B., Barnhart, E. L., Dye, N. A., Wiseman, P. W., Danuser, G., & Theriot, J. A. (2007). Actin–myosin network reorganization breaks symmetry at the cell rear to spontaneously initiate polarized cell motility. *Journal of Cell Biology*, *178*(7), 1207–1221. https://doi.org/10.1083/jcb.200706012

Yang, Q., Xue, S.-L., Chan, C. J., Rempfler, M., Vischi, D., Maurer-Gutierrez, F., Hiiragi, T., Hannezo, E., & Liberali, P. (2021). Cell fate coordinates mechano-osmotic forces in intestinal crypt formation. *Nature Cell Biology*, *23*(7), 733–744. https://doi.org/10.1038/s41556-021-00700-2

Yip, Z. C., & Heiman, M. G. (2018). Ordered arrangement of dendrites within a C. elegans sensory nerve bundle (O. Hobert & D. Y. Stainier, Eds.). *eLife*, *7*, e35825. https://doi.org/10.7554/eLife.35825

Yolland, L., Burki, M., Marcotti, S., Luchici, A., Kenny, F. N., Davis, J. R., Serna-Morales, E., Müller, J., Sixt, M., Davidson, A., Wood, W., Schumacher, L. J., Endres, R. G., Miodownik, M., & Stramer, B. M. (2019). Persistent and polarized global actin flow is essential for directionality during cell migration. *Nature Cell Biology*, *21*(11), 1370–1381. https://doi.org/10.1038/s41556-019-0411-5

Zajac, A. L., & Horne-Badovinac, S. (2021). Kinesin-3 and kinesin-1 motors direct basement membrane protein secretion to a basal sub-region of the basolateral plasma membrane in epithelial cells. *bioRxiv*, 2021.01.31.429062. https://doi.org/10.1101/2021.01.31.429062

Zajac, A. L., Williams, A. M., & Horne-Badovinac, S. (2023). A Low-Tech Flow Chamber for Live Imaging of Drosophila Egg Chambers During Drug Treatments. In M. S. Giedt & T. L. Tootle (Eds.), *Drosophila Oogenesis: Methods and Protocols* (pp. 277–289). Springer US.

Zhang, Y., & Kalderon, D. (2001). Hedgehog acts as a somatic stem cell factor in the Drosophila ovary. *Nature*, *410*(6828), 599–604. https://doi.org/10.1038/35069099

Zhao, X.-F., Kohen, R., Parent, R., Duan, Y., Fisher, G. L., Korn, M. J., Ji, L., Wan, G., Jin, J., Püschel, A. W., Dolan, D. F., Parent, J. M., Corfas, G., Murphy, G. G., & Giger, R. J. (2018). PlexinA2 Forward Signaling through Rap1 GTPases Regulates Dentate Gyrus Development and Schizophrenia-like Behaviors. *Cell Reports*, *22*(2), 456–470. https://doi.org/10.1016/j.celrep.2017.12.044

Zhu, H., & Owen, M. R. (2013). Damped propagation of cell polarization explains distinct PCP phenotypes of epithelial patterning. *Scientific Reports*, *3*(1), 2528. https://doi.org/10.1038/srep02528

Zimmermann, J., Camley, B. A., Rappel, W.-J., & Levine, H. (2016). Contact inhibition of locomotion determines cell–cell and cell–substrate forces in tissues. *Proceedings of the National Academy of Sciences*, *113*(10), 2660–2665. https://doi.org/10.1073/pnas.1522330113

APPENDIX A

ADDITIONAL FINDINGS ON THE SPATIAL ORGANIZATION AND FUNCTION OF FAT2, LAR, AND SEMA5C IN FOLLICLE CELLS.

A.1 Introduction

Fat2, Lar, and Sema5c's ability to coordinate follicle cells' motility behaviors for persistent collective migration stems from their polarized distributions and a complex web of interactions with one another. I have laid out many of my findings regarding these proteins' spatial organization, interactions, and motility-regulating functions in Chapters 2-4, and particularly in 3. However, there were several pieces of data that did not fit into these chapters, but which may be informative for future studies of planar signaling and follicle cell migration. I have included those here.

One topic of these data is Fat2's intracellular domain. An endogenous Fat2 truncation lacking the intracellular domain (Fat2$^{\Delta ICD}$-3xGFP) has reduced planar polarity compared to full-length Fat2-3xGFP (Barlan et al., 2017) and its homozygosity causes an egg elongation defect intermediate between wild-type and *fat2*$^{N103\text{-}2}$ epithelia. Trans interactions between Fat2 and leading edge proteins seem to be preserved in Fat2$^{\Delta ICD}$-3xGFP, as it is still able to concentrate Lar and the WAVE complex in puncta. Here, I further explore the function of Fat2's intracellular domain using this truncation mutant.

Another set of findings explores the cell mixing phenotype seen in *Sema5c*^{K175} mosaic epithelia, first documented in Stedden, 2019, in which *Sema5c*^{K175} and control cells are spread out among one another rather than in large clusters of cells of the same genotype. This phenotype appears to be fairly specific to Sema5c, as it is not observed in epithelia mosaic for other migration-disrupting mutations (see for example Barlan et al., 2017). It remains unknown whether the cell mixing phenotype has the same origin as the migration

and polarity defects caused by tissue-wide loss of Sema5c, or whether it stems from disruption of a different Sema5c function.

The *Sema5c*^{K175} mosaic cell mixing phenotype also provided an opportunity to investigate the functional relationship between Lar and Sema5c. A variety of phenotypic and localization-related interactions between these proteins have been identified, but they paint a mixed picture of whether Lar and Sema5c positively regulate or antagonize one another. Favoring their synergistic function, Lar contributes to the enrichment of Sema5c at leading edges with a complex pattern of cell autonomy (Stedden et al., 2019; Williams & Horne-Badovinac, 2023) (Chapter 3), and whereas loss of either Lar or Sema5c individually only impairs follicle cell migration, loss of both prevents it (Williams & Horne-Badovinac, 2023) (Chapter 3). Favoring their antagonism, removal of one copy of Lar in the *Sema5c*^{K175} mutant background suppresses stress fiber alignment and egg elongation defects seen in *Sema5c*^{K175} homozygotes. Whether this suppression occurs for other *Sema5c*^{K175} phenotypes remains untested. I present data showing that loss of Lar can similarly suppress the cell mixing phenotype of *Sema5c*^{K175} mosaic epithelia, and that neither cell mixing nor its suppression depend on the presence of tissue planar polarity.

A.2 Results

Removal of the intracellular domain of Fat2 causes its levels to increase in follicle cells.

I generated epithelia homozygous for either Fat2-3xGFP or Fat2$^{\Delta ICD}$-3xGFP and evaluated the levels and distribution of these proteins in follicle cells. Measuring their mean fluorescence intensity from throughout cells in crosssection, I found that the levels of Fat2$^{\Delta ICD}$-3xGFP were more than 3-fold higher than Fat2-3xGFP (Fig. A.1A,B). Fat2$^{\Delta ICD}$-3xGFP mean levels along leading-trailing interfaces (or similarly-oriented cell-cell interfaces in unpolarized

epithelia) were also higher (Fig. A.1C,D). Fat2$^{\Delta ICD}$-3xGFP has an expanded distribution around cell sides at the basal surface (Barlan et al., 2017) (Fig. A.1C), so comparison of Fat2-3xGFP and Fat2$^{\Delta ICD}$-3xGFP levels along all cell-cell interfaces would likely show an even larger discrepancy. Together, I find that loss of Fat2's intracellular domain strongly increases its levels throughout follicle cells.

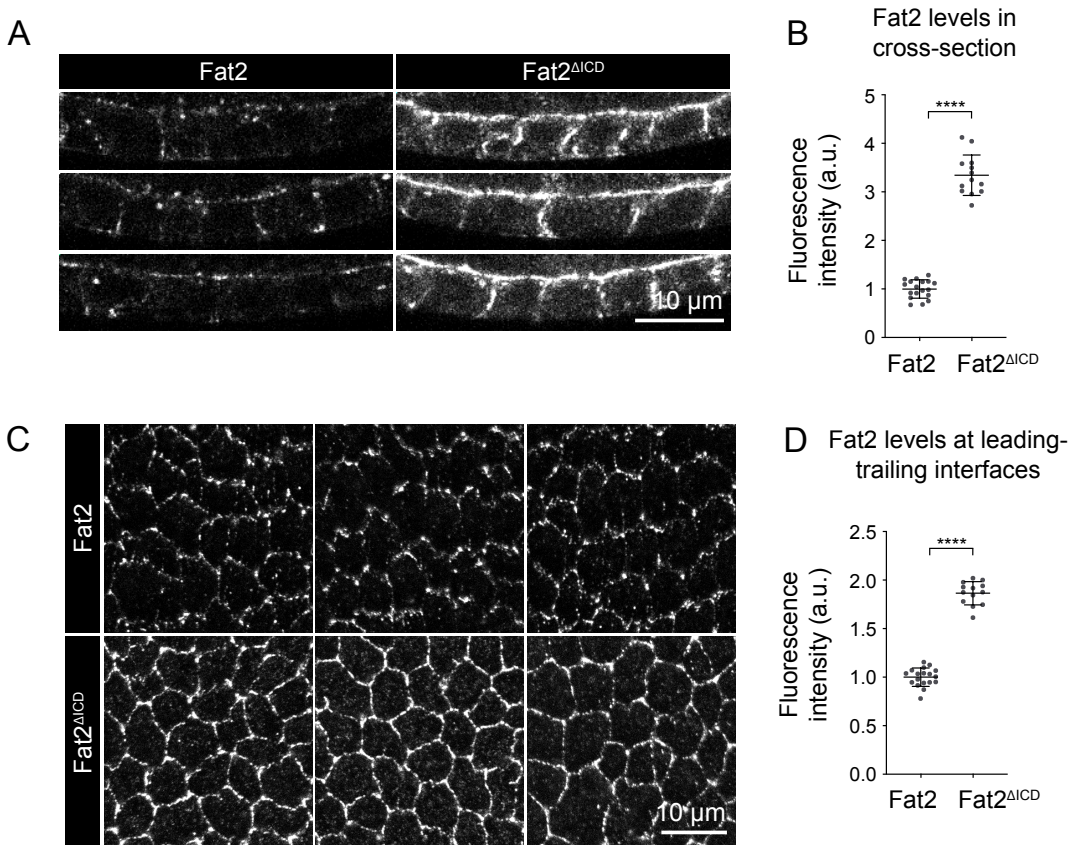

Figure A.1: **Removal of Fat2's intracellular domain sharply increases its levels throughout the cell.** **A**, Images of crosssections through epithelia homozygous for full-length Fat2 or Fat2 lacking its intracellular domain, tagged intracellularly with 3xGFP. **B**, Plot comparing the mean fluorescence intensity of Fat2-3xGFP or Fat2$^{\Delta ICD}$-3xGFP throughout follicle cell cross-sections. Fat2$^{\Delta ICD}$-3xGFP enrichment is higher throughout the cell than full-length Fat2-3xGFP. Unpaired t-test; ****$p<0.0001$. **C**, Images of the basal surface of epithelia homozygous for Fat2-3xGFP or Fat2$^{\Delta ICD}$-3xGFP. **D**, Plot comparing the mean fluorescence intensity of Fat2-3xGFP or Fat2$^{\Delta ICD}$-3xGFP at leading-trailing interfaces or similarly-oriented interfaces of unpolarized epithelia. Fat2$^{\Delta ICD}$-3xGFP enrichment is higher at leading-trailing interfaces than full-length Fat2-3xGFP. Unpaired t-test; ****$p<0.0001$.

Overexpression of Lar does not cause changes to basal F-actin structures

Overexpression of Sema5c causes loss of leading edge protrusions in trans (Stedden et al., 2019) (Fig. A.2A). To see if overexpression of Lar also causes changes to protrusions or other F-actin structures, I generated epithelia mosaic for expression of HA-tagged Lar, locating the Lar-overexpressing clones and confirming Lar's overexpression using anti-Lar staining. All the cells expressed endogenous Lar, but the Lar-overexpressing cells had higher levels of Lar staining around their perimeters at the basal surface as well as in large intracellular puncta. Using phalloidin staining, I did not detect any differences in F-actin protrusions or stress fibers caused by Lar overexpression (Fig. A.2B).

Loss of Lar suppresses the cell mixing phenotype of *Sema5c^{K175}* mosaic epithelia

In mosaic epithelia generated using the Flp/FRT system, clones of cells of the same genotype typically remain in contact with one another such that there are large groups of contiguous cells of each of the mosaic genotypes. However, in *Sema5c^{K175}* mosaic epithelia, *Sema5c^{K175}* and control cells are more interspersed with one another. The cell-biological cause of this cell mixing phenotype, and its relationship to other *Sema5c^{K175}* phenotypes, are unknown. In the course of testing the effects of loss of Sema5c on the levels of other planar-polarized proteins, I gained some clues about the cell mixing phenotype as well. Heightened cell mixing was readily apparent in *Sema5c^{K175}* mosaic epithelia expressing either Fat2-3xGFP (Fig. A.3A) or Sra1-GFP (Fig. 3.9). In the Fat2-3xGFP-expressing epithelia, tissue-wide planar polarity was consistently absent at least during Stages 6-7, with other stages not evaluated. Since collective cell migration and planar polarity are interdependent, this shows that the cell mixing phenotype is either independent of collective migration or that collective

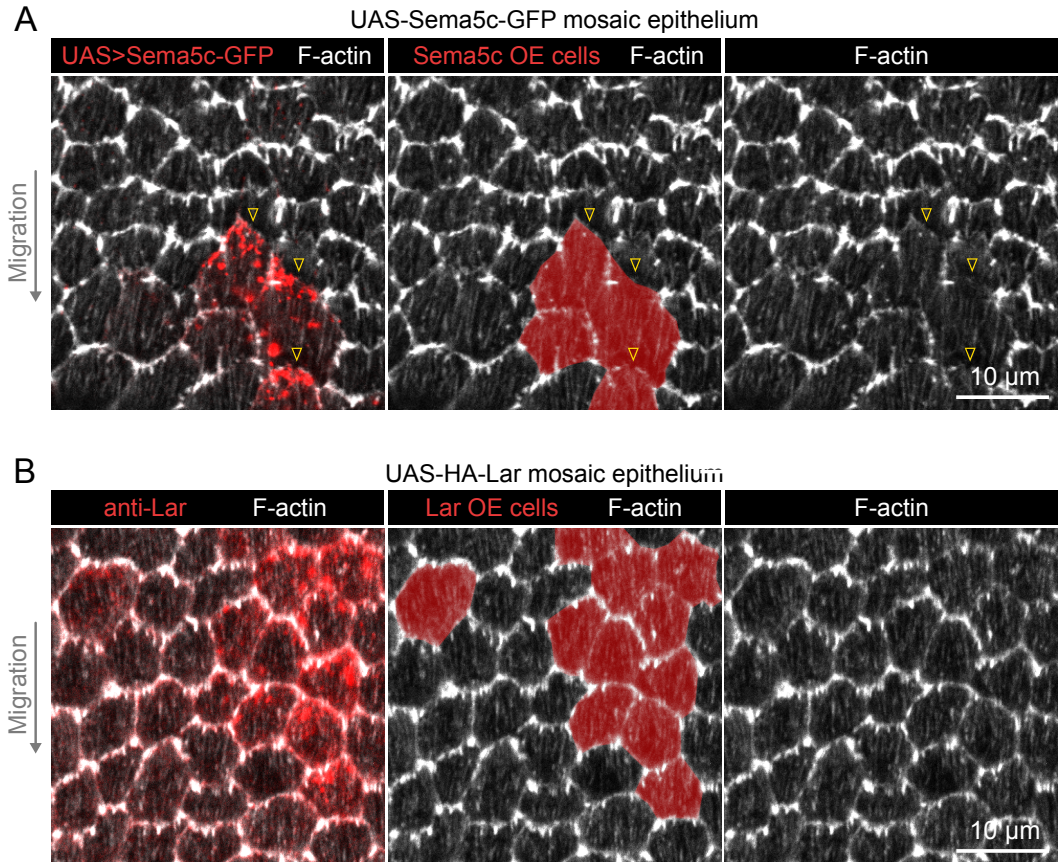

Figure A.2: **Unlike Sema5c overexpression, Lar overexpression does not inhibit protrusion. A**, Images of an epithelium mosaic for UAS>Sema5c-GFP expression, with F-actin labeled by phalloidin staining. F-actin-rich protrusions are reduced at leading edges of cells behind ones with Sema5c overexpression (hollow arrows). **B**, Images of an epithelium mosaic for UAS-driven HA-Lar expression, stained with Lar antibody and phalloidin (F-actin). All cells express Lar and exhibit Lar staining; Lar-overexpressing ones have increased Lar staining at membranes and Lar staining in endosomes. F-actin-rich protrusions are not altered by Lar overexpression.

migration becomes dispensable after an earlier stage of development.

In an effort to look at the effect of simultaneous loss of Lar and Sema5c on Fat2's localization, I also generated Fat2-3xGFP-expressing, $Sema5c^{K175}$ mosaic epithelia that expressed *lar*-RNAi throughout. Interestingly, the cell mixing phenotype was suppressed in these epithelia (but their planar polarity defect was not) (Fig. A.3B,C). Cell mixing was also suppressed in $Sema5c^{K175}$ mosaic epithelia in which one copy of Lar was tagged with 3xGFP (see Fig. 3.9A). It is possible that Lar-3xGFP is hypomorphic, as suggested by the slower migration speeds of Lar-3xGFP-homozygous epithelia (Fig. 3.3C). I conclude that the ability of reduced Lar levels or activity to suppress $Sema5c^{K175}$ phenotypes extends to the cell mixing phenotype.

A.3 Discussion

In this appendix, I presented three pieces of data furthering our understanding of Fat2-based puncta and the activities of their constituent proteins. One relates to protein turnover—I showed that loss of Fat2's intracellular domain causes a large increase in its levels in follicle cells. The others provide additional evidence that Lar and Sema5c have distinct, and in some cases antagonistic, functions in follicle cells.

I found that the $Fat2^{\Delta ICD}$-3xGFP was present at much higher levels in follicle cells than Fat2-3xGFP. It is possible that the intracellular domain mediates Fat2's endocytic turnover, and that proteins persist for longer in its absence and therefore accumulate to higher levels. $Fat2^{\Delta ICD}$ also had an expanded distribution around cell sides, in contrast to tightly trailing edge-localized full-length Fat2-3xGFP (Barlan et al., 2017; Viktorinová & Dahmann, 2013). It remains to be determined whether there is a causal link between these polarity and protein level phenotypes, but it is possible that the excess accumulation of $Fat2^{\Delta ICD}$-3xGFP is the cause of its expanded distribution. The mechanisms that drive the polarization of proteins are often sensitive to the amount of those proteins in the cell. Follicle cells' planar signal-

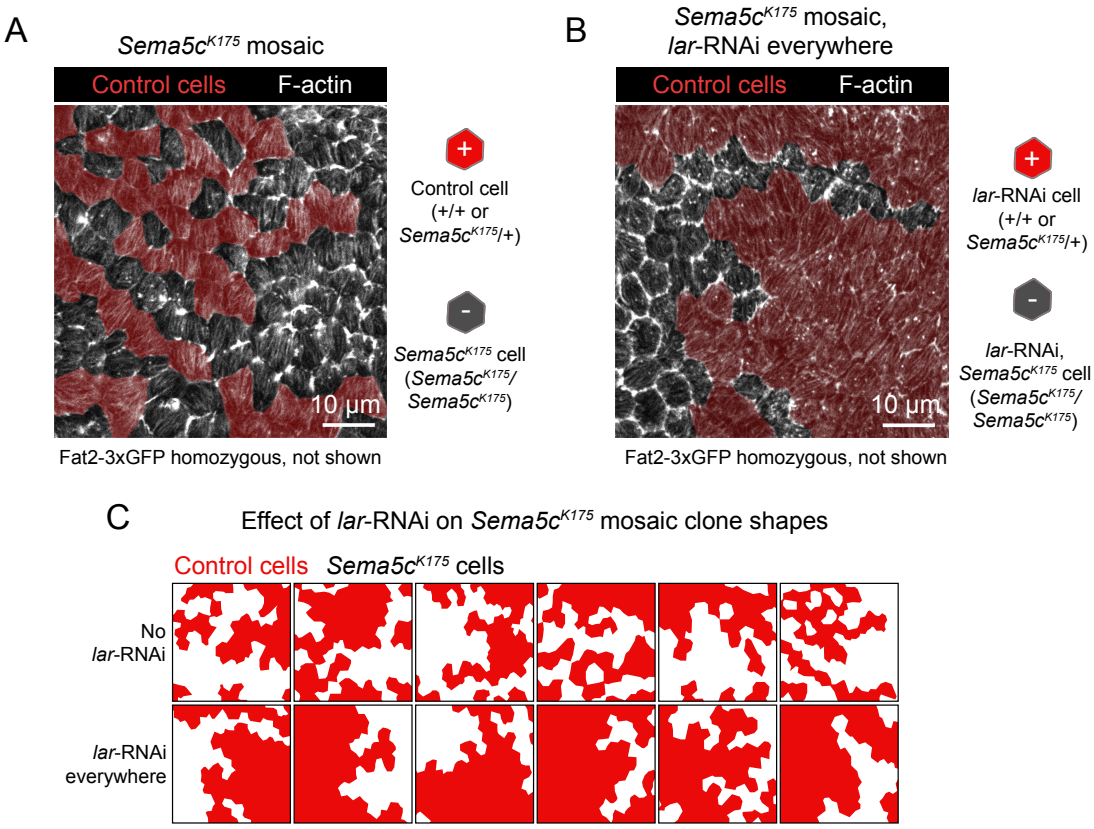

Figure A.3: **Tissue-wide depletion of Lar with RNAi suppresses the cell mixing phenotype of *Sema5c^{K175}* mosaic epithelia.** **A**, Image of a *Sema5c^{K175}* mosaic epithelium expressing Fat2-3xGFP (not shown), with F-actin stained using phalloidin. Control cells are pseudo-colored red based on genetically encoded markers. Image reproduced from Fig. 3.8. **B**, Image of a *Sema5c^{K175}* mosaic epithelium expressing Fat2-3xGFP (not shown) and *lar*-RNAi in all cells and with F-actin stained using phalloidin. Control cells are pseudo-colored red based on genetically encoded markers. Image reproduced from Fig. 3.8. **C**, Silhouettes of clone shapes from epithelia exemplified in (A) and (B). Planar polarity is consistently absent in both genotypes. Expression of *lar*-RNAi reduces the degree to which control and *Sema5c^{K175}* cells are interspersed.

ing system shows signs of this sensitivity as well, with the distributions of Sema5c and Lar expanding around the cells' perimeters when they are overexpressed (Stedden et al., 2019) (Fig. A.2). It will be important to determine whether Fat2$^{\Delta ICD}$'s mispolarization is entirely attributable to its excess accumulation, or whether the intracellular domain plays independent roles in the regulation of Fat2's levels and polarity. In addition to providing clues about the relationship between Fat2's levels and its polarization, this piece of information may be useful for future studies of Fat2's trafficking and turnover in cells.

An important remaining question about Fat2-based signaling is how the combined functions of Lar and Sema5c orchestrate collective migration. Genetic evidence points to these proteins functioning in parallel, and this is further supported by a range of distinct *lar*$^{-}$ and *Sema5c*$^{-}$ loss-of-function phenotypes. Here, I showed that the consequences of overexpression of these proteins also differ. Unlike Sema5c overexpression (Stedden et al., 2019), Lar overexpression caused no apparent change in protrusion morphology in either cis or trans. I have observed that visualizing protrusions with membrane labeling provides more detailed information about protrusion morphologies than does F-actin labeling, and that F-actin labeling can underestimate the presence of protrusions, so it remains possible that membrane labeling would reveal that Sema5c overexpression changes protrusion morphology rather than eliminating protrusions, or that Lar overexpression does indeed cause subtle protrusion changes. However, these data further supports independent functions for Lar and Sema5c in the regulation of cell motility. In the future, it will be important to gain molecular detail about what those functions are.

A long-standing puzzle in the lab has been the fact that epithelia mosaic for the *Sema5c*^{K175} mutation have different clone distributions than control mosaic epithelia, with mutant cells much more scattered among control ones (Stedden, 2019). I once again stumbled on this phenotype, finding it to occur even in a genetic condition in which tissue-wide planar polarity was lost. Cell clones should remain connected either if the epithelium undergoes perfectly

solid-like collective migration with no neighboring cell rearrangement, or if the cells are entirely non-motile and so no movement takes place. Clone organizations serve as a record of relative cell movements, and mixing phenotypes as indications of heightened cell rearrangement. It would be useful to verify this using live imaging of $Sema5c^{K175}$ mosaic epithelia, and then to determine how cell and tissue movement changes in Lar loss-of-function conditions that I found to suppress this phenotype.

It is curious that $Sema5c^{K175}$ mosaic epithelia exhibit heightened cell mixing, but not epithelia mosaic for genotypes that more strongly prevent migration such as $fat2^{N103\text{-}2}$ or *abi*-RNAi (personal observation). This may provide an important clue about *Sema5c* function, for example by (hypothetically) showing that their motility is intact but their tendency to align with their neighbors is reduced. $lar^{13.2}$ mosaic epithelia also exhibit unusual, elongated clone shapes, which may share a common mechanistic origin with quantitative differences, or be a distinct phenotype. It would be useful to undertake more systematic documentation of clone shape and size distributions that result from different migration-impacting genetic conditions. These data could provide a way to infer cell movement dynamics and the liquid-like or solid-like state of an epithelium without the need to perform long-term live imaging to capture infrequent neighbor rearrangement events. Studies of phase transitions in confluent epithelia will be helfpul for interpreting these data (Giavazzi et al., 2018).

A.4 Methods

Drosophila sources

The genotypes of animals used in each experiment, along with their stock center designations, are provided in Table A.1.

Egg chamber dissection

Egg chambers were dissected as described in Chapter 3.

Immunostaining and F-actin staining

F-actin (phalloidin) staining was performed as described in Chapter 3.

Microscopy

Microscopy was performed as described in Chapter 3. All figures show confocal microscopy images.

Quantification of Fat2 fluorescence levels

The levels of Fat2-3xGFP and Fat2$^{\Delta ICD}$-3xGFP levels at leading-trailing interfaces were measured from images of follicle cell basal surfaces by manually drawing 10 pixel-wide segmented lines along leading-trailing cell-cell interfaces in ImageJ and measuring mean fluorescence intensity within these regions. Mean intensity was measured per egg chamber. Where follicle cells lacked planar-polarity, similarly-oriented (approx. parallel to anterior-posterior axis) interfaces were used instead. For measurements of protein levels throughout the cell, crosssection images of egg chambers were obtained, polygonal regions outlining a set of 10 medial follicle cells (non-oocyte-contacting) were outlined manually in ImageJ, and mean fluorescence intensity measured within this region. These measurements likely include a small contribution of fluorescence from protein in nurse cells that localizes to the nurse cell-follicle cell interface.

Table A.1: Experimental genotypes for Appendix A

Figure	Panel	Name	Genotype
A.1	A-D	Fat2	w1118 ;; Fat2-3xGFP FRT80B
A.1	A-D	$Fat2^{\Delta ICD}$	w1118 ;; $Fat2^{\Delta ICD}$-3xGFP FRT80B
A.2	A	UAS-Sema5c-GFP mos.	hs>Flp, w1118 ; UAS>Sema5c-GFP/+ ; act5c>CD2>Gal4, UAS>mRFP-NLS
A.2	B	UAS-HA-Lar mos.	hs>Flp, w1118 ;; UAS>HA-Lar/act5c>CD2>Gal4, UAS>mRFP-NLS
A.3	A,C	$Sema5c^{K175}$ mosaic	w1118 ; tj>Gal4, UAS>Flp/+; $Sema5c^{K175}$ Fat2-3xGFP FRT80B/ubi>mRFP-NLS Fat2-3xGFP FRT80B
A.3	B,C	$Sema5c^{K175}$ mos., lar-RNAi ev.	w1118 ; tj>Gal4, UAS>Flp/UAS>lar-RNAi; $Sema5c^{K175}$ Fat2-3xGFP FRT80B/ubi>mRFP-NLS Fat2-3xGFP FRT80B

APPENDIX B

TRICORNERED AND FURRY ARE REQUIRED IN FOLLICLE CELLS FOR THEIR ROTATIONAL MIGRATION AND MEMBRANE HOMEOSTASIS

B.1 Introduction

The egg chamber is encapsulated in a basement membrane extracellular matrix, and anisotropic resistance from that basement membrane to the egg chamber's expansion causes the egg chamber to elongate as it grows (Gutzeit et al., 1991). Disruption of basement membrane proteins or their polarized secretion and assembly on the basal side of the follicle cells weakens the basement membrane's ability to channel growth along one axis and results in a failure of egg chamber elongation and the production of round eggs (Devergne et al., 2017; Isabella & Horne-Badovinac, 2016; Lerner et al., 2013; Zajac & Horne-Badovinac, 2021). Similarly, disruption of the follicle cells' migration, which is responsible for imbuing the basement membrane with its anisotropy, results in round eggs (Cetera et al., 2014; Haigo & Bilder, 2011; Viktorinová & Dahmann, 2013). A forward genetic screen for mutations that cause round eggs identified the proteins Tricornered (Trc) and Furry (Fry) as regulators of egg chamber elongation (Horne-Badovinac et al., 2012). When sufficient follicle cells were homozygous for mutations in these proteins, egg chambers were abnormally round as early as Stage 10. This suggests that Trc and Fry are important either for follicle cell migration or their polarized secretion of basement membrane proteins. These epithelia also had poorly-polarized stress fibers as early as Stage 7 (Horne-Badovinac et al., 2012), a sign that they were non-migratory.

Trc and its mammalian homolog NDR1/Stk38 have been shown to regulate several different cell-biological processes with a number of protein partners. The scaffold protein Fry activates Trc in many of these contexts (Nagai & Mizuno, 2014). Trc and Fry were first

identified for their importance for the formation of *Drosophila* hairs and bristles, as their absence caused hair splitting (Geng et al., 2000; He et al., 2005). Hair and bristle formation are highly F-actin-dependent processes, implicating Trc and Fry in F-actin regulation. Since then, the picture has grown more complicated, with Trc/NDR1/Stk38 kinases shown to positively regulate autophagy (Joffre et al., 2015), to act as part of the Hippo pathway (Emoto et al., 2006), to regulate mitochondrial quality (Wu et al., 2013), microtubule dynamics (Norkett et al., 2020), cell cycle progression (Cornils et al., 2011), and more. Many Trc phosphorylation targets have also been identified (Ultanir et al., 2012).

Early in my dissertation research, I set out to test the role of Trc and Fry in egg chamber morphogenesis, with the aims of (1) learning more about the molecular functions of these proteins and (2) identifying new cell-biological processes that are important for collective cell migration. I present data from my foray into this, in which I further characterize the follicle cell phenotypes caused by loss of Trc and Fry as well as their localization in follicle cells. I present evidence that Trc and Fry work together in follicle cells, where they are required for stalk and polar cell positioning and follicle cell migration, but not for polarized basement membrane secretion. In addition, I show that their role in migration is likely independent of Fat2-based signaling. Finally, I report several follicle cell phenotypes caused by disruption of proteins though to work together with Tricornered or its homologs in other contexts.

B.2 Results

To test the function of Trc and Fry in follicle cells, I first confirmed that large clones of *trcK23* caused loss of stress fiber planar polarity as reported in Horne-Badovinac et al., 2012. I then identified *trc*-RNAi and *fry*-RNAi lines that also caused stress fiber planar polarity defects (Fig. B.1A,B). The kinase GCKIII has been shown to activate Trc (Poon et al., 2018), and I found that GCKIII-RNAi expression caused a similar loss of planar polarity (Fig. B.1A), consistent with GCKIII activating Trc in follicle cells. The penetrance of RNAi

phenotypes varied among different *trc*-RNAi, *fry*-RNAi, and *GCKIII*-RNAi lines, and they caused milder egg elongation defects than did the roundest of eggs produced using trc^{-} or fry^{-} Flp/FRT clones, suggesting that knockdown is incomplete. In addition to the stress fiber alignment defect, F-actin-rich protrusions appeared to be midly reduced upon tissue-wide RNAi expression or in clones of trc^{K23} cells, but the penetrance of this phenotype was variable (Fig. B.1A,B). These data strongly suggest that Trc, Fry, and GCKIII are required for normal follicle cell migration. To test this more directly, I generated trc^{K23} or fry^{041} mosaic epithelia and performed live imaging of their CellMask-labeled cells' movements. In epithelia with large numbers of mutant cells, directional collective migration was lost and I instead observed movement of patches of cells in different directions, and sometimes the reversal of their movement directions (Fig. B.2). This shows that Trc and Fry are very likely required for follicle cell migration, although it would be useful to demonstrate this more straightforwardly with tissue-wide depletion using RNAi, or with incidences of whole-epithelium mutant clones.

Planar Fat2-based signaling is required for follicle cell migration, so I hypothesized that loss of Trc or Fry disrupted migration through disruption of this signaling. Fat2 and Lar act locally at leading-trailing interfaces to regulate cells' motility behaviors, so I asked whether loss of Trc or Fry disrupted their localization, and therefore their motility-regulating function. However, I found using Lar antibody staining that Lar's localization at the basal surface was unaltered in trc^{K23} or $fry^{H33\text{-}2}$ cells of mosaic epithelia that retained tissue-wide planar polarity (Fig. B.3A). I also found that Fat2-3xGFP was still enriched at basal cell-cell interfaces in a $fry^{H33\text{-}2}$ mosaic epithelium in which clones were unmarked, but planar-polarity was disrupted and therefore it is likely that a substantial fraction of cells were homozygous for $fry^{H33\text{-}2}$ (Fig. B.3B). The cells also have nearly-normal levels of F-actin-rich protrusions, a sign of intact Fat2-based signaling (Fig. B.1). These data suggest that the ability of Fat2 and Lar to localize to the sites at which they function remains intact without Trc or Fry,

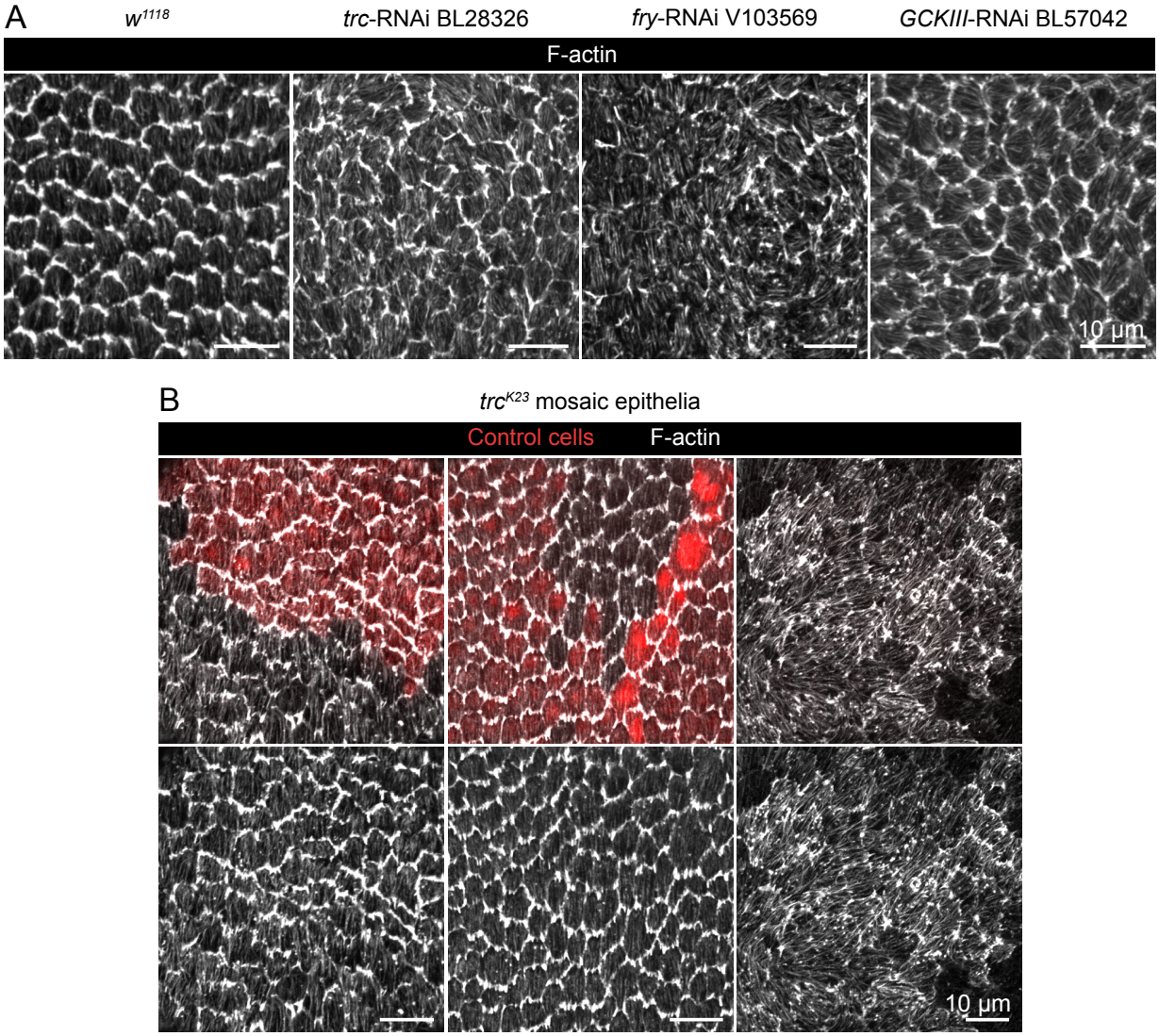

Figure B.1: **Loss of Trc, Fry, or GCKIII causes changes to basal F-actin organization. A**, Images of the basal surfaces of epithelia stained with phalloidin (F-actin). The epithelia expressing *trc*-RNAi, *fry*-RNAi, or *GCKIII*-RNAi have poorly planar-polarized stress fibers. **B**, Images of the basal surfaces of epithelia mosaic for the trc^{K23} mutation, with F-actin stained by phalloidin. F-actin-rich protrusions are reduced in the trc^{K23} clone in the left image, but not in the center image. Protrusions are reduced and stress fibers mispolarized in the whole-epithelium clone (right).

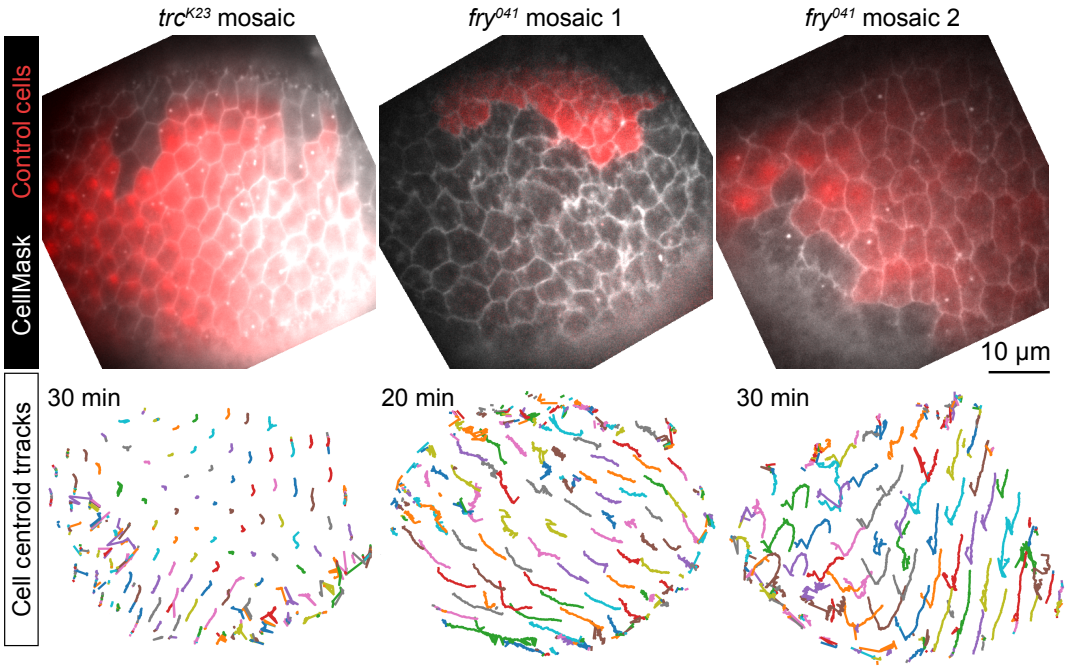

Figure B.2: **Mosaicism for *trc* or *fry* mutations decreases the persistence and coordination of follicle cell migration.** Top: Frames from timelapse movies of trc^{K23} or fry^{041} mosaic epithelia with cells labeled using CellMask. Bottom: Tracks of cell centroid movements over 20-30 minutes. Cell speeds and trajectories vary within epithelia and in some cases cells' movement direction reverses.

and that disruption of Fat2-based signaling is not the cause of their planar polarity and migration defects.

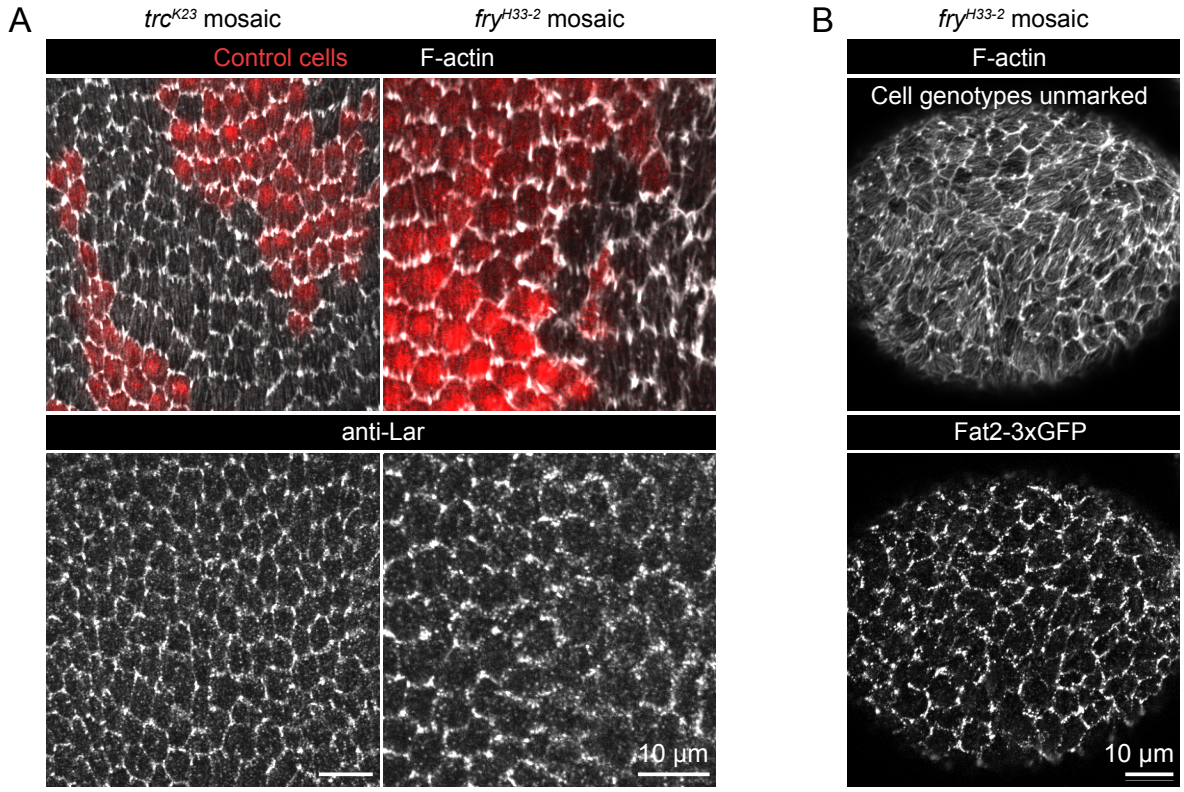

Figure B.3: **Fat2 and Lar are still able to localize to leading-trailing interfaces in the absence of Trc or Fry. A**, Images of epithelia mosaic for either trc^{K23} or $fry^{H33\text{-}2}$, stained with Lar antibody and phalloidin (F-actin). The localization of Lar is similar in control and mutant cells. **B**, Images of a $fry^{H33\text{-}2}$ mosaic epithelium expressing Fat2-3xGFP and stained with phalloidin (F-actin). Cell genotypes are unlabeled, but there were sufficient $fry^{H33\text{-}2}$ cells to disrupt tissue planar polarity. Fat2-3xGFP is mispolarized but still enriched at cell-cell interfaces.

Another potential cause of egg chamber elongation defects is disruption of polarized basement membrane secretion. Although my data point to failure of follicle cell migration as the mediator of the egg chamber elongation defects of trc^{-} and fry^{-}, it remained possible that basement membrane secretion defects could contribute as well. To test this, I generated epithelia mosaic for trc^{K23}, fry^{031}, or fry^{041} and evaluated the distribution of Collagen IV (Vkg-GFP), a major basemement membrane component. I detected no trapping of Vkg-

GFP within or between cells homozygous for these mutations (Fig. B.4A). I also detected no apical accumulation of Vkg-GFP, showing that these cells' ability to polarize Collagen IV secretion towards their basal surfaces is likely intact (Fig. B.4B). Finally, I evaluated the structure of the basement membrane in *trc*-RNAi expressing epithelia. In epithelia that had planar-polarized stress fibers and were likely migrating slowly, I observed that their basement membrane had a polarized structure as well, but lacked large fibrils and had only finer-scale polar structure (Fig. B.4C). This suggests that although basally-polarized secretion is intact, the fine structure of the basement membrane is altered by loss of Trc or Fry. This is most likely caused by their slowed or stopped migration.

In the course of these experiments, I noticed that egg chambers with disruptions in Trc, Fry, or GCKIII often had defects in their stalk and polar cells. Epithelia with depleted Trc, Fry, or GCKIII often had stalks with excess cells and cells that had not fully intercalated with one another (Fig. B.5A,B). They also often had polar cell clusters with more than two cells by Stage 6-7, after the normal period of polar cell pruning (Fig. B.5B), and those clusters were sometimes located away from the anterior and posterior poles (Fig. B.4C). It is possible that these defects contribute to follicle cell migration and planar polarity phenotypes. However, it is unlikely that they are solely responsible, as the penetrance of these defects was weaker than that of the migration-related defects.

To better understand the roles of Trc and Fry in follicle cell migration, I imaged their migratory basal surfaces stained with CellMask membrane dye, expecting to observe changes in their protrusion dynamics or cell movements. However, I instead found a large accumulation of CellMask-labeled membrane that was stationary with respect to the basement membrane, indicating that it was detached from the cells and sat between their basal surfaces and the basement membrane. I observed this membrane accumulation upon tissue-wide *trc*-RNAi or *fry*-RNAi expression, even in epithelia that were still migrating slowly (Fig. B.6A). I also observed it in a migratory fry^{041} mosaic epithelium, restricted to the pole of the egg

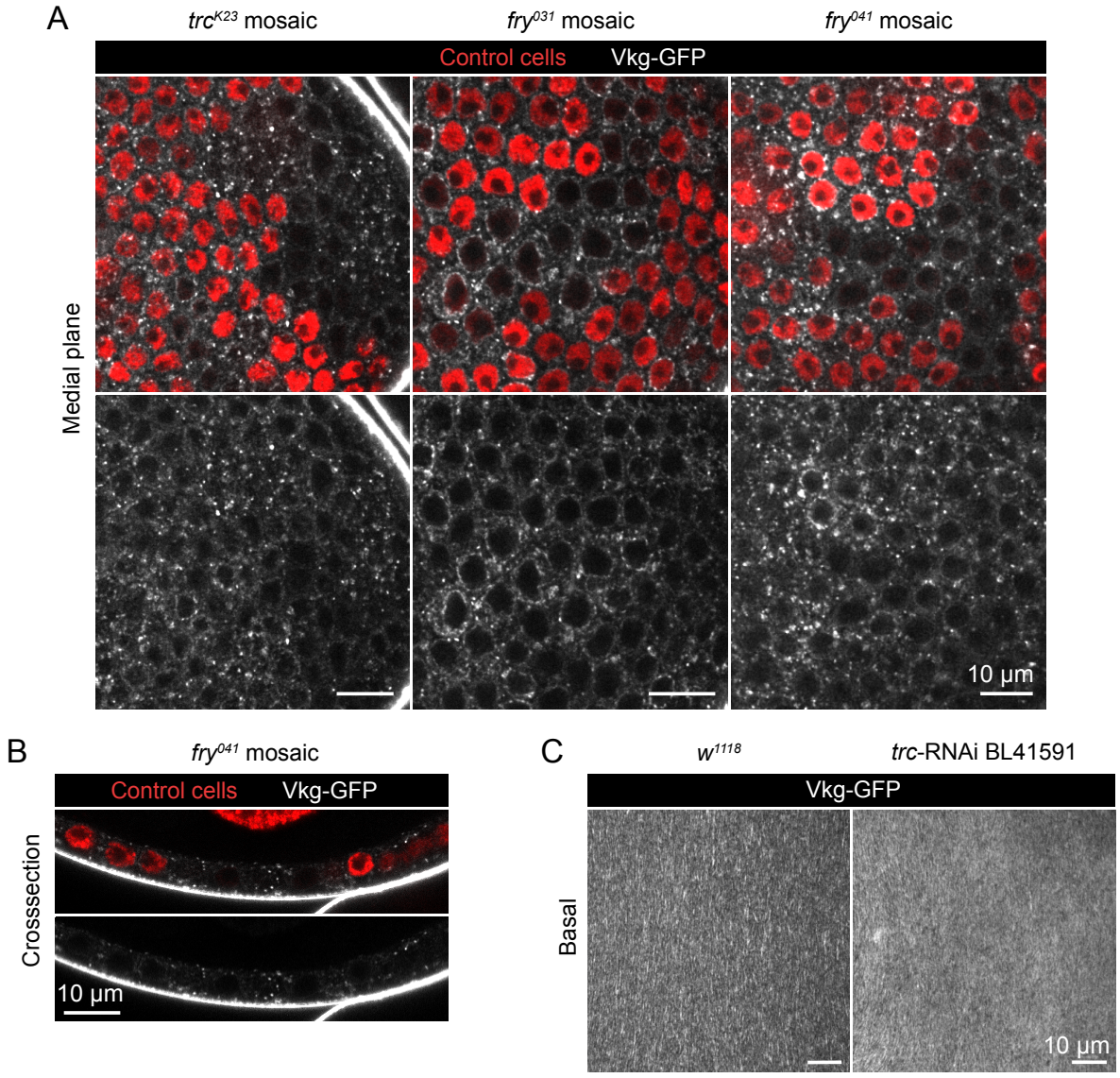

Figure B.4: **Loss of Trc or Fry does not disrupt polarized secretion of Collagen IV.** **A**, Images the medial planes of epithelia mosaic for *trc* or *fry* mutations, expressing Vkg-GFP (Collagen IV). The levels of VkgGFP within and between mutant cells are similar to control ones. **B**, Images of a fry^{041} mosaic epithelium in cross-section. There is no evidence of a defect in the polarized secretion of VkgGFP. **C**, Images of the basement membrane (Vkg-GFP) of w^{1118} epithelia and ones expressing *trc*-RNAi. The population of large fibrils is absent from the *trc*-RNAi-expressing epithelium.

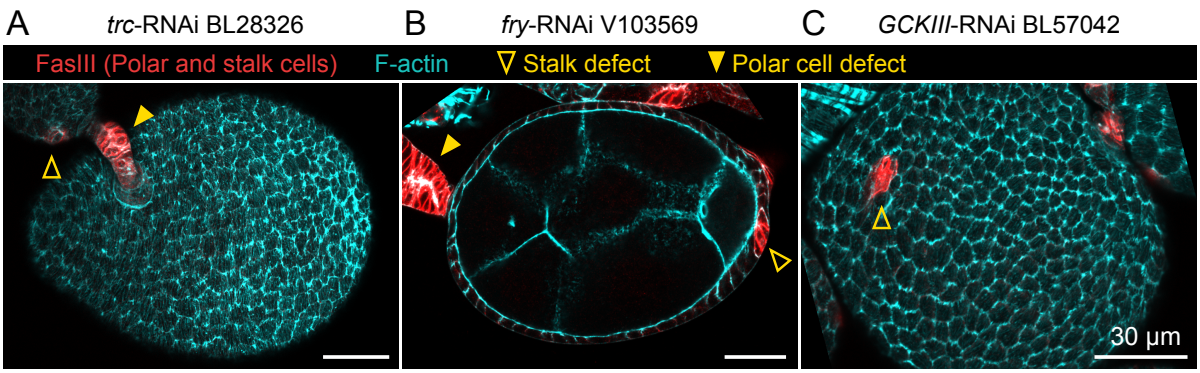

Figure B.5: **Loss of Trc, Fry, or GCKIII causes defects in stalk cells and polar cells. A,B,C**, Images of egg chambers stained with anti-FasIII (highly expressed in polar and stalk cells) and phalloidin (F-actin), expressing *trc*-RNAi (A), *fry*-RNAi and Dcr2 (B), or *GCKIII*-RNAi (C). **A**, Basal surface. The filled arrow points to a stalk with excess cells that have not fully intercalated. The hollow arrow points to mispositioned polar cells in the neighboring egg chamber. **B**, Crosssection. The filled arrow points to a stalk with excess cells that have not fully intercalated. The hollow arrow points to a mispositioned polar cell cluster with excess (>2) cells. **C**, Basal surface. The hollow arrow points to a mispositioned polar cell cluster.

chamber where fry^{041} cells predominated (Fig. B.6B). I conclude that loss of Trc or Fry causes cells to increase their deposition of membranes into the basement membrane, leading to membrane accumulation at positions along the basement membrane that those cells have contacted.

Mob-family proteins often act as allosteric activators of NDR kinases like Tricornered (Duhart & Raftery, 2020). To see if one of these, Mob4, activates Trc in follicle cells, I first asked whether loss of Mob4 caused egg chamber morphology and egg shape defects similar to those of loss of Trc. Expressing *mob4*-RNAi throughout follicle cells resulted in moderately round eggs and a number of follicle cell morphology and F-actin phenotypes (Fig. B.7A,B). At Stages 3-5 of egg chamber development, *mob4*-RNAi-expressing epithelia had poorly planar-polarized stress fibers and protrusions (Fig. B.7A). By Stages 6-7, the alignment of stress fibers was normal in most cases, but their F-actin-rich protrusions were unusually short (Fig. B.7A). The Stage 3-5 egg chambers had intact monolayered epithelia, but Stages 7-8 epithelia frequently had large holes (Fig. B.7A). These phenotypes indicate a

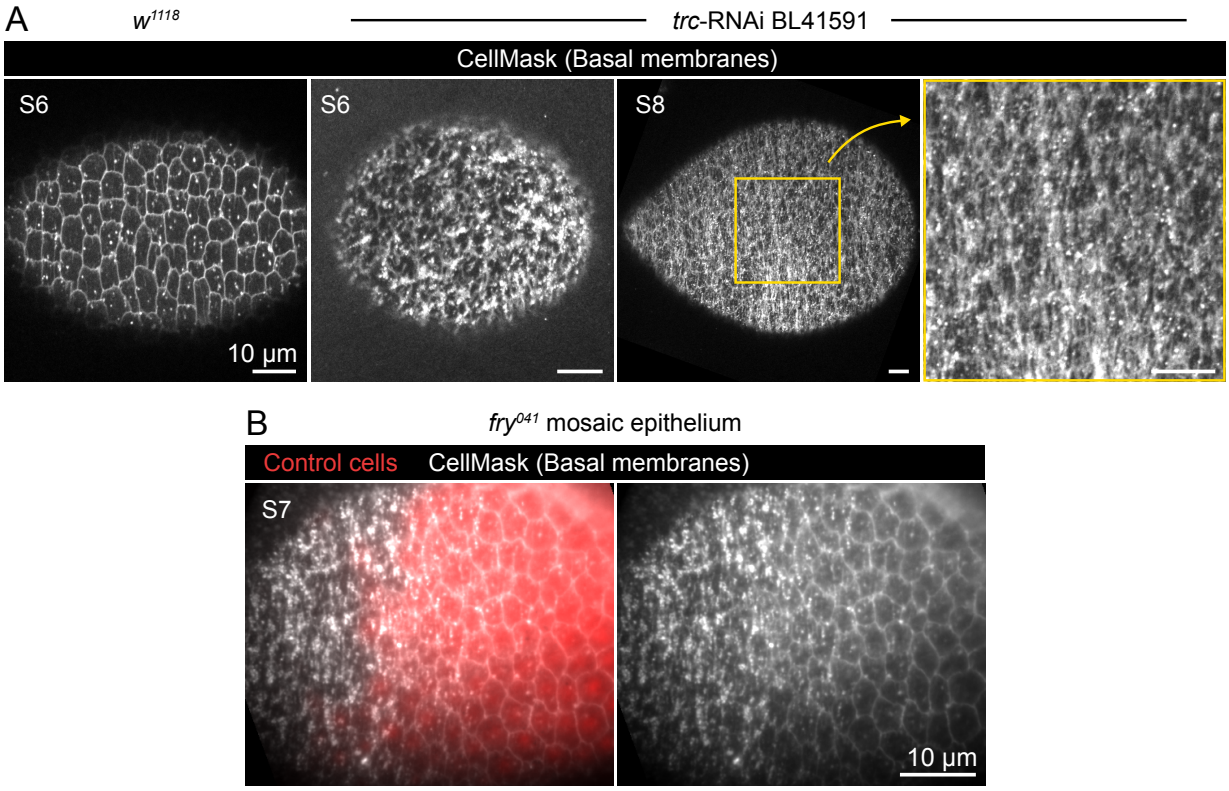

Figure B.6: **Loss of Trc or Fry causes excess membrane accumulation between cells' basal surfaces and the basement membrane. A**, Images of the basal surface of epithelia with cell membranes stained using CellMask, imaged using confocal microscopy. *trc*-RNAi-expressing follicle cells have large accumulations of membrane at their basal surfaces. **B**, Images of the basal surface of a fry^{041} mosaic epithelium stained with CellMask and imaged using TIRF microscopy. The side of the egg chamber with more fry^{041} cells has more basal membrane accumulation.

role for Mob4 in the integrity of the follicular epithelium and in egg chamber morphogenesis. They also suggest that Mob4 depletion causes a "delayed migration" phenotype similar to that of epithelia without Sema5c or Plexin A (Stedden et al., 2019). Although loss of either Mob4 or Trc causes changes in stress fiber alignment and egg shape, other aspects of their phenotypes differ, so my data do not support these proteins acting in a common pathway in the context of the follicular epithelium.

I next investigated the localization of Mob4 in follicle cells in search of clues about its function. Overexpressed Mob4 transgenes tagged either N- or C-terminally with mCherry localized throughout follicle cells, with slightly higher enrichment at cell membranes and in nuclei (Fig. B.8A). Mob4 antibody staining partly recapitulated this localization. Like transgenic Mob4, antibody staining was highest at cell membranes (Fig. B.8B). However, enrichment was low in nuclei, and the basal side of cells was stained more strongly than the apical side, likely because of poor antibody penetration. In addition, antibody staining revealed several microns-long filamentous structures not observed with transgenic Mob4 labeling (Fig. B.8B, dashed lines). The filamentous structures were close to the basal surface and were oriented orthogonal to the anterior-posterior axis in the the plane of the epithelium. Mob4 antibody penetration was poor, so it is possible that their basal localization simply reflects the range of antibody staining. Mob4 depletion with RNAi reduced cell membrane staining but not staining of the filamentous structures, suggesting that they are not composed of Mob4 and that they are non-specifically detected by the Mob4 antibody (Fig. B.8B). Interestingly, the planar-polarity of the filamentous structures was reduced in *mob4*-RNAi-expressing egg chambers during early developmental stages in which their stress fiber planar polarity was also poor. The filamentous structures did not colocalize with microtubules as detected by acetyl-tubulin or alpha-tubulin antibody staining (Fig. B.8C,D). Together, these data show that Mob4 is enriched at cell membranes and possibly in nuclei, and that the Mob4 antibody also stains a planar-polarized subcellular structure of unknown

composition.

The protein Atg6/Beclin1 interacts with Trc/NDR1 in both *Drosophila* larvae and mammalian cells (Joffre et al., 2015), so I wondered whether Atg6 also works with Trc in the context of follicle cell migration. To test this, I first asked whether loss of Atg6 caused changes in follicle cells' basal F-actin organization indicative of migration defects, as does loss of Trc. In epithelia mosaic for $atg6^{1}$, I saw no defects in actin architecture during migratory stages (Fig. B.9A), but note that I evaluated few clones and none that spanned the majority of the tissue. In wild-type epithelia, F-actin-rich protrusions are no longer present, and migration has stopped, by Stage 9. Intriguingly, in the one Stage 9 $atg6^{1}$ mosaic epithelium I evaluated, the $atg6^{1}$ cells but not the control cells retained prominent, planar-polarized F-actin protrusions (Fig. B.9A). The clone boundaries were also unusually straight, suggesting mechanical differences between $atg6^{1}$ and control cells. By Stage 10, no protrusions were present in either $atg6^{1}$ or control cells (Fig. B.9A). This phenotype is distinct from trc^{-} phenotypes (see Fig. B.1) and does not support my hypothesis that Atg6 and Trc regulate follicle cell migration as members of a shared pathway. However, this may provide clues about how follicle cells transition from motile to non-motile states as egg chambers develop. Atg6 is best known as a member of an autophagy-promoting complex, but it also participates in trafficking processes including secretion and endocytosis (Funderburk et al., 2010; Shravage et al., 2013). Disruption of one of these processes may hinder follicle cells' transition to a non-protrusive state.

In order to understand the cause of this protrusion persistence, I investigated the intracellular role of Atg6. It is an essential subunit of the VPS34 complex, which converts phosphatidylinositol (PI) into phosphatidylinositol 3-monophosphate (PI(3)P) in the endomembrane system (Funderburk et al., 2010). To verify this in follicle cells, I compared the localization of a GFP-myc-FYVE, a PI(3)P biosensor, in control follicular epithelia and ones expressing *atg6*-RNAi. GFP-myc-FYVE was highly enriched on a membrane compartment

in control epithelia, but was diffuse in *atg6*-RNAi-expressing epithelia, with very smaller puncta of GFP-myc-FYVE very sparsely present (Fig. B.9B). This shows that Atg6 plays a major role in PI(3)P production in follicle cells as has been demonstrated in other contexts, and that the *atg6*-RNAi line is effective. To identify the PI(3)P-enriched compartments, I stained GFP-myc-FYVE-expressing follicular epithelia with antibodies for several endomembrane compartments. I did not observe colocalization between GFP-myc-FYVE and Golgi (anti-GM130), Rab7 or Rab11-positive endosomes, or lysosomes (LAMP2), although Rab7-positive endosomes were fairly frequently contacting FYVE-positive ones (not shown). I did observe a close spatial relationship between FYVE and Notch-positive endosomes—FYVE-enriched compartments were always in close contact with Notch-enriched ones, although their shapes differed and they did not perfectly colocalize (Fig. B.9C). They likely mark endosomes that are attached to one another. Finally, I evaluated the localization of Atg6 using an Atg6-GFP transgene. Its expression level was variable, and when lowly-expressed it was diffuse, with slight nuclear enrichment. However, when more highly expressed, Atg6-GFP also formed large aggregates that colocalized with stress fibers, occasionally bridging two stress fibers in a manner that appeared akin to whetting (Fig. B.9D). This is unlikely to reflect the normal distribution of Atg6 in follicle cells, but it is possible that it is indicating a physical interaction between Atg6 and some stress fiber component.

B.3 Discussion

My data support Trc, Fry, and GCKIII acting in a common pathway in follicle cells, such as removal of any of these proteins disrupts some process required for follicle cell migration and planar polarity. I tested the hypotheses that Trc regulates Fat2-based signaling or basement membrane secretion, and thereby collective migration, but found support for neither of these—basement membrane secretion is still highly polarized to basal surfaces, and minor changes in the architecture of the basement membrane appear to be secondary to the

migration defect, not its cause. Fat2 and Lar localize normally in the absence of Trc, and F-actin-rich protrusions are only minorly altered, so disruption of Fat2-based signaling is also unlikely. More promisingly, loss of Trc or its activators caused the marked accumulation of membrane external to the cells' basal surfaces, and it is possible that sufficient membrane accumulation itself could have caused the cells' motility defects by disrupting their adhesion. However, it is also possible that the Trc signaling pathway is involved independently in follicle cell migration and membrane homeostasis. Trc is a kinase with many identified phosphorylation targets and cell functions (Hergovich et al., 2006; Ultanir et al., 2012), so this is plausible. Future studies will be needed to test the causal link between basal membrane accumulation and migration defects, and to determine how Trc regulates membrane homeostasis in follicle cells.

In the course of my research on Trc, I discovered that the scaffold protein Mob4 plays a role in follicle cells' epithelial architecture and planar polarity, and likely their collective migration. Based on their stress fiber orientation, it appears that Mob4 depletion causes a delayed migration phenotype akin to that of $Sema5c^{K175}$ epithelia, with epithelia restoring planar polarity and initiating collective migration around stage 5-6. Additional live imaging experiments will be required to confirm this. This condition also causes the appearance of holes in the epithelium at later stages of egg chamber development, as well as a moderate round egg defect. Whether the egg shape defect is caused by a migration defect or by defects in epithelial integrity remains to be determined. The pleiotropic effects of loss of Mob4 may make it difficult to study the role of this protein in follicle cell migration. Although I initially investigated Mob4 because of a link between Mob-family proteins and NDR kinases (Duhart & Raftery, 2020), F-actin phenotypes caused by Trc and Mob4 loss differed from one another, and it is not clear that they function together in follicle cells to regulate their migration.

While investigating Mob4's localization, I found that a Mob4 antibody detected a planar-polarized filamentous cell structure, with approximately one present per cell. These struc-

tures likely do not contain Mob4 or microtubules, and their planar-polarity likely depends on cell movement, as has been seen for a number of other organelles and cell structures (Chen et al., 2016; Lerner et al., 2013; Viktorinová & Dahmann, 2013). The composition and function of these structures is unclear. They bear a resemblance to cytooophidia made of CTP synthase (Liu, 2010), but unlike cytooophidia, they were not present in germline cells. The strong, albeit likely non-specific, affinity of these structures for the Mob4 antibody could enable the determination of their composition using immunoprecipitation-mass spectrometry should they become relevant to future studies.

B.4 Methods

Drosophila sources

The genotypes of animals used in each experiment, along with their stock center designations, are provided in Table B.1.

Egg chamber dissection

Egg chambers were dissected as described in Chapter 2.

Membrane labeling and live imaging

Egg chambers were dyed with CellMask and live imaging was performed as described in Chapter 2.

Immunostaining and F-actin staining

Immunostaining and F-actin (phalloidin) staining were performed as described in Chapter 2. Antibodies and their sources and concentrations were as follows:

- Lar: DSHB AB528202, mouse monoclonal, concentrate, 1:200
- FasIII: DSHB AB528238, mouse monoclonal, concentrate, 1:200
- Mob4: Guinea pig polyclonal, 1:200. From the Littleton Lab, Schulte et al., 2010
- acetyl-Tubulin: mouse 1:50
- α-tubulin (DM1α): SC 32293, mouse monoclonal, 1:100
- Notch: DSHB C458.2H, mouse monoclonal, supernatant, 1:20

Microscopy

Microscopy was performed as described in Chapter 2. All figures show confocal microscopy images except Figs. B.2 and B.6B, which were obtained using TIRF microscopy, and Fig. B.7B, which was obtained using the Fehon Lab dissection microscope with DSLR camera. Imaging conditions were not held constant in many of the image panels. Within-panel scale variation is indicated by the presence of scale bars on multiple panel images.

Table B.1: Experimental genotypes for Appendix B

Figure	Panel	Name	Genotype
B.1	A	w^{1118}	w1118
B.1	B	trc-RNAi BL28326	w1118 ; tj>Gal4/+ ; UAS>trc-RNAi BL28326/+
B.1	A	fry-RNAi V103569	w1118 ; tj>Gal4/UAS>fry-RNAi V103569
B.1	A	GCKIII-RNAi BL57042	w1118 ; tj>Gal4/UAS>GCKIII-RNAi BL57042
B.1	B	trc^{K23} mosaic	w1118 ; e22c>Gal4, UAS>Flp/+; trc^{K23} FRT80B/ubi>GFP-NLS FRT80B
B.2		trc^{K23} mosaic	w1118 ; e22c>Gal4, UAS>Flp/+; trc^{K23} FRT80B/ubi>GFP-NLS FRT80B

Table B.1: Experimental genotypes for Appendix B (continued)

B.2		fry^{041} mosaic	w1118 ; e22c>Gal4, UAS>Flp/+; fry^{041} FRT80B/ubi>GFP-NLS FRT80B
B.3	A	trc^{K23} mosaic	w1118 ; e22c>Gal4, UAS>Flp/+; trc^{K23} FRT80B/ubi>GFP-NLS FRT80B
B.3	A	$fry^{H33\text{-}2}$ mosaic	w1118 ; e22c>Gal4, UAS>Flp/+; $fry^{H33\text{-}2}$ FRT80B/ubi>GFP-NLS FRT80B
B.3	B	$fry^{H33\text{-}2}$ mos. (with Fat2-3xGFP)	w1118 ; e22c>Gal4, UAS>Flp/+; $fry^{H33\text{-}2}$ Fat2-3xGFP FRT80B/Fat2-3xGFP FRT80B
B.4	A	trc^{K23} mosaic	w1118 ; e22c>Gal4, UAS>Flp/Vkg-GFP; trc^{K23} FRT80B/ubi>GFP-NLS FRT80B
B.4	A	fry^{031} mosaic	w1118 ; e22c>Gal4, UAS>Flp/Vkg-GFP; fry^{031} FRT80B/ubi>GFP-NLS FRT80B
B.4	A	fry^{041} mosaic	w1118 ; e22c>Gal4, UAS>Flp/Vkg-GFP; fry^{041} FRT80B/ubi>GFP-NLS FRT80B
B.4	B	fry^{041} mosaic	w1118 ; e22c>Gal4, UAS>Flp/Vkg-GFP; fry^{041} FRT80B/ubi>GFP-NLS FRT80B
B.4	C	w^{1118}	w1118
B.4	C	trc-RNAi BL41591	w1118 ; tj>Gal4/Vkg-GFP; UAS>trc-RNAi BL41591/+
B.5	A	trc-RNAi BL28326	w1118 ; tj>Gal4/+ ; UAS>trc-RNAi BL28326/+
B.5	B	fry-RNAi V103569	w1118 ; tj>Gal4/UAS>fry-RNAi V103569
B.5	C	GCKIII-RNAi BL57042	w1118 ; tj>Gal4/UAS>GCKIII-RNAi BL57042
B.6	A	w^{1118}	w1118
B.6	A	trc-RNAi BL41591	w1118 ; tj>Gal4/+ ; UAS>trc-RNAi BL41591/+
B.6	B	fry^{041} mosaic	w1118 ; e22c>Gal4, UAS>Flp/+; fry^{041} FRT80B/ubi>GFP-NLS FRT80B
B.7	A	mob4-RNAi BL36488	w1118 ; tj>Gal4/+ ; UAS>mob4-RNAi BL36488/+

Table B.1: Experimental genotypes for Appendix B (continued)

B.7	B	w^{1118}	w1118
B.7	B	mob4-RNAi BL36488	w1118 ; tj>Gal4/+ ; UAS>mob4-RNAi BL36488/+
B.8	A	UAS>mCherry-Mob4	yv ; tj>Gal4/+ ; UAS>Mob4-N-mCherry BL36490/+
B.8	A	UAS>Mob4-mCherry	yv ; tj>Gal4/+ ; UAS>Mob4-C-mCherry BL36491/+
B.8	B	w^{1118}	w1118
B.8	B	mob4-RNAi BL36488	w1118 ; tj>Gal4/+ ; UAS>mob4-RNAi BL36488/+
B.8	C,D	All	w1118
B.9	A	$atg6^{1}$ mosaic	w1118 ; e22c>Gal4, UAS>Flp/+; FRT82B $atg6^{1}$/FRT82B ubi>GFP-NLS
B.9	B	Control	w1118 ; tj>Gal4/UAS>GFP-myc-2xFYVE BL42712
B.9	B	atg6-RNAi BL28060	w1118 ; tj>Gal4/UAS>GFP-myc-2xFYVE BL42712 ; UAS>atg6-RNAi BL28060/+
B.9	C	All	w1118 ; tj>Gal4/UAS>GFP-myc-2xFYVE BL42712
B.9	D	All	w1118 ; tj>Gal4/UAS>GFP-Atg6 (Baehrecke Lab 10.1242/dev.089490) ; Sb/+

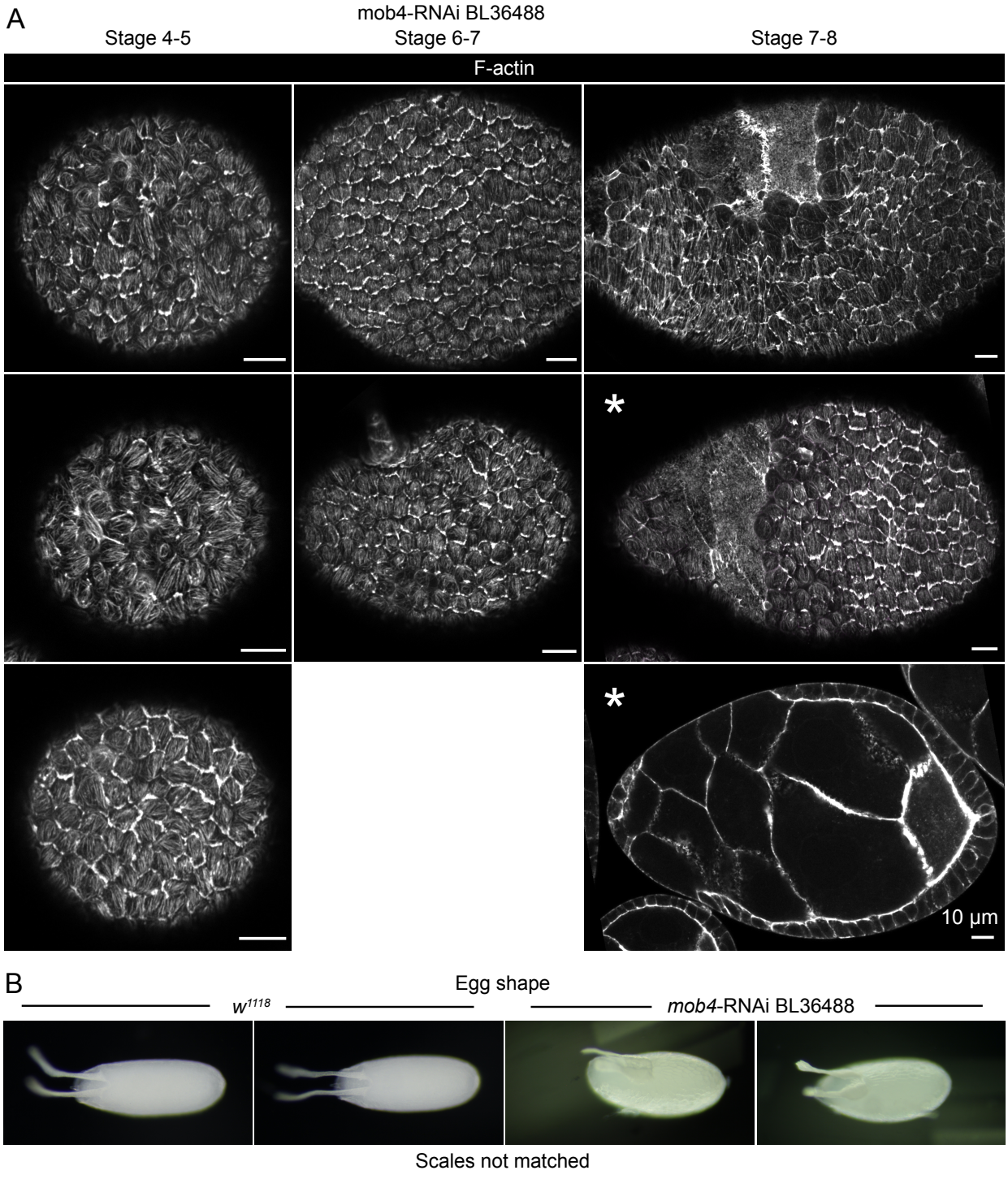

Figure B.7: **Depletion of Mob4 causes a range of egg chamber morphology defects.** Continued on next page.

Figure B.7: **Depletion of Mob4 causes a range of egg chamber morphology defects (continued).** **A**, Images of phalloidin-stained egg chambers with follicle cells expressing *mob4*-RNAi. Asterices mark basal and crosssection planes of the same egg chamber. Stage 4-5 follicle cells have poorly planar-polarized stress fibers. Stress fiber alignment is improved by Stage 6-8, but epithelial holes are increasingly prevalent. **B** Images of w^{1118} eggs or eggs from egg chambers with *mob4*-RNAi-expressed in follicle cells. The *mob4*-RNAi ones have a mild egg elongation defect and abnormally posterior placement of the bases of their dorsal appendages.

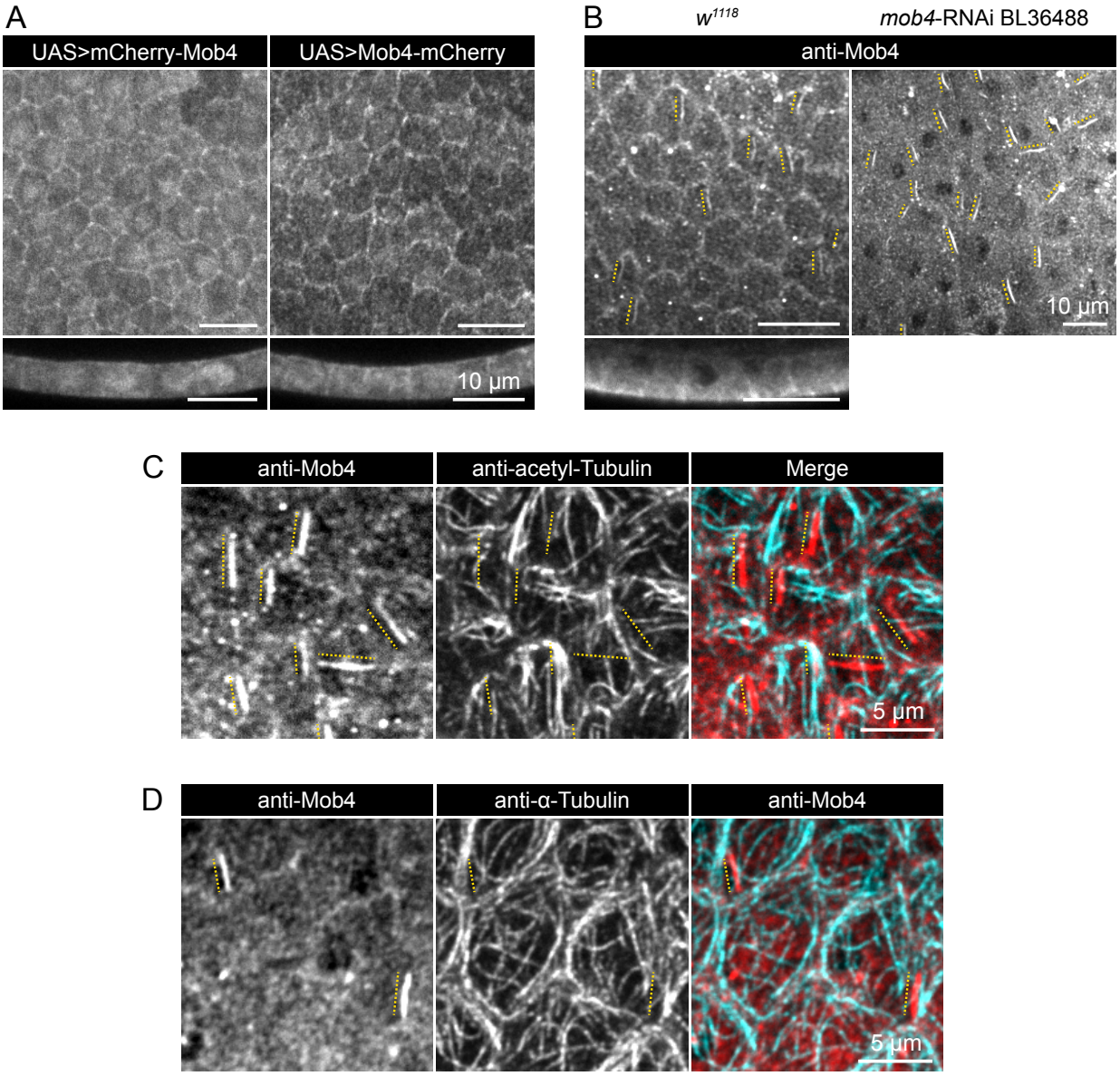

Figure B.8: **The Mob4 antibody stains large, sparse planar-polarized filamentous structures that do not contain Mob4 or microtubules.** Continued on next page.

Figure B.8: **The Mob4 antibody stains large, sparse planar-polarized filamentous structures that do not contain Mob4 or microtubules (continued). A**, Images of the basal surfaces (top) and crosssections (bottom) of follicle cells expressing Mob4 transgenes tagged with mCherry N-terminally (L) or C-terminally (R). Mob4 is present throughout the cell and slightly enriched in nuclei and on cell membranes. **B**, Images of the basal surfaces (top) and crosssections (bottom) of follicle cells stained with Mob4 antibody. In the w^{1118} epithelium, the Mob4 antibody stains cell membranes and filamentous structures several microns long that are planar-polarized near the basal surface. In *mob4*-RNAi-expressing epithelium, cell membrane staining is reduced but the filamentous structures are still prominent. Dashed yellow lines indicate filamentous structures (offset). **C,D**, Images comparing the relative localizations of Mob4 antibody-stained filamentous structures and anti-acetyl-tubulin or anti-α-tubulin-stained microtubules. Dashed yellow lines indicate filamentous structures (offset), which do not colocalize with the microtubules.

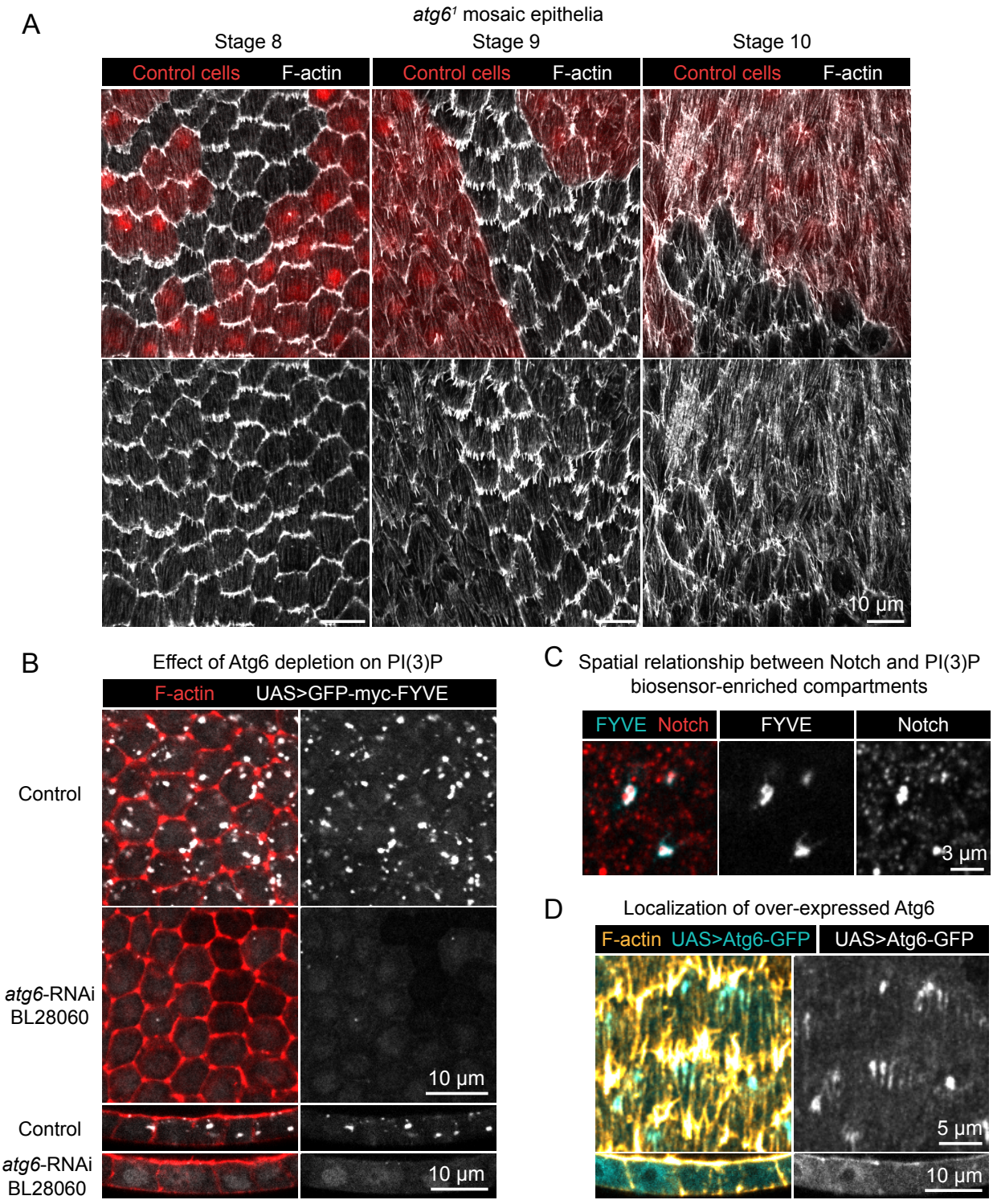

Figure B.9: **Loss of Atg6 causes protrusions to persist into Stage 9.** Continued on next page.

Figure B.9: **Loss of Atg6 causes protrusions to persist into Stage 9 (continued).** **A**, Images of the basal surfaces of epithelia mosaic for *atg6*^{1}, stained with phalloidin (F-actin). At Stage 8 and Stage 10, no differences in the F-actin structures of control and *atg6*^{1} cells are apparent. At Stage 9, control cells do not have F-actin-rich protrusions, but *atg6*^{1} cells retain their protrusions. Only one Stage 9 clone was evaluated. **B**, Images of Stage 7 follicle cells expressing the PI(3)P biosensor GFP-myc-FYVE, with or without *atg6*-RNAi expression. Images show either near-basal or cross-section planes. GFP-myc-FYVE is more diffuse in *atg6*-RNAi-expressing epithelia. **C**, Images of the near-basal surface of follicle cells expressing PI(3)P biosensor UAS>GFP-myc-FYVE, stained with a Notch antibody. FYVE-enriched and Notch-enriched compartments are closely associated with each other, but do not perfectly overlap. **D**, Images of Stage 7 follicle cells expressing transgenic Atg6-GFP and stained with phalloidin (F-actin). Overexpressed Atg6-GFP forms large aggregates that colocalize with stress fibers.